

Chapter 2: Plasma confinement and transport

E.J. Doyle¹ (Chair Transport Physics), W.A. Houlberg^{2,a} (Chair Confinement Database and Modelling), Y. Kamada³ (Chair Pedestal and Edge), V. Mukhovatov⁴ (co-Chair Transport Physics), T.H. Osborne⁵ (co-Chair Pedestal and Edge), A. Polevoi⁴ (co-Chair Confinement Database and Modelling), G. Bateman⁶, J.W. Connor⁷, J.G. Cordey⁷ (retired), T. Fujita³, X. Garbet⁸, T.S. Hahn⁹, L.D. Horton¹⁰, A.E. Hubbard¹¹, F. Imbeaux⁸, F. Jenko¹⁰, J.E. Kinsey⁵, Y. Kishimoto¹², J. Li¹³, T.C. Luce⁵, Y. Martin¹⁴, M. Ossipenko¹⁵, V. Parail⁷, A. Peeters¹⁰, T.L. Rhodes¹, J.E. Rice¹¹, C.M. Roach⁷, V. Rozhansky¹⁶, F. Ryter¹⁰, G. Saibene¹⁷, R. Sartori¹⁷, A.C.C. Sips¹⁰, J.A. Snipes¹¹, M. Sugihara⁴, E.J. Synakowski¹⁸, H. Takenaga³, T. Takizuka³, K. Thomsen¹⁷, M.R. Wade⁵, H.R. Wilson¹⁹, ITPA Transport Physics Topical Group, ITPA Confinement Database and Modelling Topical Group and ITPA Pedestal and Edge Topical Group

¹ Department of Electrical Engineering and PSTI, University of California, Los Angeles, CA, USA

² Oak Ridge National Laboratory, Oak Ridge, TN 37831, USA

³ Japan Atomic Energy Agency, Naka, Ibaraki-ken 311-0193, Japan

⁴ ITER Organization, 13108 Saint-Paul-Lez-Durance, France

⁵ General Atomics, San Diego, CA 92186-5608, USA

⁶ Physics Department, Lehigh University, Bethlehem, PA 18015, USA

⁷ EURATOM/UKAEA Fusion Association, Culham Science Centre, Abingdon, Oxfordshire OX14 3DB, UK

⁸ Association Euratom-CEA, Centre d' Etudes de Cadarache, Saint-Paul-Lez-Durance, France

⁹ Princeton Plasma Physics Laboratory, PO Box 451, Princeton, NJ 08543, USA

¹⁰ Max-Planck-Institut für Plasmaphysik, EURATOM Association, D-85748 Garching, Germany

¹¹ Massachusetts Institute of Technology, Plasma Science and Fusion Center, Cambridge, MA 02139, USA

¹² Graduate School of Energy Science, Kyoto University, Gokasho, Uji, Japan

¹³ Southwestern Institute of Physics, Chengdu, People's Republic of China

¹⁴ Centre de Recherches en Physique des Plasmas, Association Euratom-Confédération Suisse, Ecole Polytechnique Fédérale de Lausanne, CH-1015 Lausanne, Switzerland

¹⁵ Nuclear Fusion Institute, Russian Research Centre Kurchatov Institute, Moscow, 123182 Russia

¹⁶ St Petersburg State Polytechnical University, St Petersburg 195251, Russian Federation

¹⁷ European Fusion Development Agreement Close Support Unit, D-85748 Garching, Germany

¹⁸ Lawrence Livermore National Laboratory, Livermore, CA 94551, USA

¹⁹ University of York, Heslington, York, YO10 5DD, UK

E-mail: houlbergwa@ornl.gov

Received 12 June 2006, accepted for publication 12 April 2007

Published 1 June 2007

Online at stacks.iop.org/NF/47/S18

Abstract

The understanding and predictive capability of transport physics and plasma confinement is reviewed from the perspective of achieving reactor-scale burning plasmas in the ITER tokamak, for both core and edge plasma regions. Very considerable progress has been made in understanding, controlling and predicting tokamak transport across a wide variety of plasma conditions and regimes since the publication of the ITER Physics Basis (IPB) document (1999 *Nucl. Fusion* **39** 2137–2664). Major areas of progress considered here follow. (1) Substantial improvement in the physics content, capability and reliability of transport simulation and modelling codes, leading to much increased theory/experiment interaction as these codes are increasingly used to interpret and predict experiment. (2) Remarkable progress has been made in developing and understanding regimes of improved core confinement. Internal transport barriers and other forms of reduced core transport are now routinely obtained in all the leading tokamak devices worldwide. (3) The importance of controlling the H-mode edge pedestal is now generally recognized. Substantial progress has been made in extending high confinement H-mode operation to the Greenwald density, the demonstration of Type I ELM mitigation and control techniques and systematic explanation

^a Author to whom any correspondence should be addressed.

of Type I ELM stability. Theory-based predictive capability has also shown progress by integrating the plasma and neutral transport with MHD stability. (4) Transport projections to ITER are now made using three complementary approaches: empirical or global scaling, theory-based transport modelling and dimensionless parameter scaling (previously, empirical scaling was the dominant approach). For the ITER base case or the reference scenario of conventional ELMy H-mode operation, all three techniques predict that ITER will have sufficient confinement to meet its design target of $Q = 10$ operation, within similar uncertainties.

PACS numbers: 28.52.–s, 52.55.Fa, 52.25.Fi

(Some figures in this article are in colour only in the electronic version)

Contents

1. Introduction
2. Fundamental transport processes
 - 2.1. Theory of turbulent transport
 - 2.2. Turbulence simulation
 - 2.3. Turbulence measurements in tokamaks and comparison with theory/simulation
 - 2.4. Neoclassical transport
 - 2.5. Summary of issues
3. Core transport
 - 3.1. Enhanced core confinement regimes
 - 3.2. Ion thermal confinement
 - 3.3. Electron thermal transport
 - 3.4. Particle and impurity transport
 - 3.5. Toroidal momentum transport and spontaneous rotation
 - 3.6. Dimensionless parameter scaling experiments
 - 3.7. Improved core confinement regimes for advanced operation scenarios
 - 3.8. Summary and outstanding issues
4. Pedestal transport and dynamics
 - 4.1. Regimes of improved H-mode confinement at high density and operational limits
 - 4.2. Pedestal characteristics and structure
 - 4.3. L–H transitions
 - 4.4. Pedestal transport theory and modelling
 - 4.5. Modelling the pedestal structure
 - 4.6. Type I ELM structure, effects on the pedestal profiles and mitigation techniques
 - 4.7. Alternatives to Type I ELMy H-mode regime
 - 4.8. Pedestal stability
 - 4.9. Possible pedestal control scenarios
 - 4.10. Summary of pedestal structure and transport
5. Predictive capability and projections for ITER
 - 5.1. Improved database resources for modelling and scaling studies
 - 5.2. Pedestal and edge characteristics
 - 5.3. Global scaling
 - 5.4. Non-dimensional scaling
 - 5.5. Modelling codes, including edge modelling capability
 - 5.6. Summary of progress and remaining issues
6. Summary

1. Introduction

A fundamental feature of tokamak plasmas is that measured energy transport rates typically exceed those calculated for binary collisions in a toroidal plasma, i.e. transport is anomalously higher than that predicted by ‘classical’ (cylindrical geometry) or ‘neoclassical’ (toroidal geometry, including drift orbit effects) theory. The anomalous transport

is governed by highly non-linear turbulence processes, with multiple turbulence drives and suppression mechanisms, occurring on multiple scales. Due to this inherent complexity, understanding transport in fusion plasmas is generally regarded as a scientific ‘grand challenge.’ Despite this intrinsic complexity, very considerable progress has been made since the publication of the ITER Physics Basis (IPB) document [1] in understanding, controlling and predicting tokamak transport

across a wide variety of plasma conditions and regimes. It is the goal of this chapter to describe this progress in theory, in numerical simulation/modelling and in experiment, covering both plasma core and edge, and to present the current transport projections for ITER.

The structure and content of this chapter reflects both substantial changes in emphasis within the field since the IPB was published and also a desire to address the major outstanding issues that it identified. Major areas of change and progress since the IPB follow. (1) Substantial improvement in the physics content, capability and reliability of transport simulation and modelling codes, leading to much increased theory/experiment interaction as these codes are increasingly used to interpret and predict experiment. (2) Remarkable progress has been made in developing and understanding regimes of improved core confinement, which is relevant for the steady-state and hybrid scenarios that were not emphasized in the ITER design at the time of the IPB. Internal transport barriers and other forms of reduced core transport are now routinely obtained in all the leading tokamak devices worldwide. Reduced transport has been achieved in all four transport channels (ion and electron thermal, particle and momentum transport channels), sometimes simultaneously. (3) The importance of understanding and controlling the H-mode edge pedestal is now generally recognized, especially with regard to maximizing pedestal parameters while mitigating or eliminating Type I edge localized modes (ELMs). (4) Transport projections to ITER are now made using three complementary approaches: empirical or global scaling, theory-based transport modelling and dimensionless parameter scaling (previously, empirical scaling was the dominant approach). Projections to ITER using these three approaches show general agreement, though detailed differences remain between and within the three techniques.

Given these areas of emphasis within the current transport research, the remainder of this chapter is structured as follows: section 2 presents the progress in understanding fundamental transport processes, including analytic theory, numerical turbulence simulations and neoclassical transport theory, as well as progress in efforts to benchmark theory via direct comparisons with turbulence measurements. Section 3 presents the current understanding of tokamak core plasma transport, covering ion and electron thermal, particle and momentum transport, as well as dimensionless parameter scaling experiments and the transport properties of enhanced core confinement regimes. Progress in experiment and modelling are integrated in the descriptions and discussion of this section, reflecting the close and still evolving coupling between both. The transport and structure of the edge H-mode pedestal are considered in section 4. Topics covered here include obtaining high density with high confinement, pedestal characteristics and structure, L–H transitions, pedestal theory and modelling, ELM structure, ELM mitigation techniques and alternatives to operating in the Type I ELM regime and pedestal stability and control.

Confinement projections for ITER and the status of predictive transport capabilities are presented in section 5. Subsections here include a description of the improved database resources, both scalar and profile, now available for

global scaling and profile modelling studies, the status of predictive capabilities for the plasma edge and pedestal, the latest global scaling, non-dimensional scaling and modelling results and projections for ITER and the status of modelling capabilities in general. The chapter concludes with an overall summary (section 6), and in addition each main section concludes with an individual summary and a list of outstanding issues.

2. Fundamental transport processes

The purpose of this section is to provide a description of both the current level of understanding and the outstanding issues with regard to fundamental transport processes in tokamak plasmas. This section is structured into subsections as follows. Section 2.1 provides an introduction to turbulent transport theory, covering issues of current concerns such as turbulence correlation time and length, non-linear turbulence self-regulation via zonal flows, streamers, multiple-scale spatio-temporal transport, probabilistic transport and Bohm versus gyro-Bohm transport. In section 2.2, we detail the substantial progress made with turbulence simulation codes. Here, progress has been such that quantitative comparisons with experiment are now possible, and gyrokinetic simulations of electron as well as ion transport are being performed. The succeeding section 2.3 provides a review of quantitative experimental tests of theory and simulation, illustrating the substantial progress that has been made in experimentally testing and validating the standard theory of turbulent transport. Neoclassical transport theory, which describes drift and Coulomb collision-driven transport, is described in section 2.4. The routine achievement of regimes with reduced turbulent transport means that neoclassical ion transport is now often observed, and neoclassical theory is also widely used in bootstrap current and poloidal rotation calculations. Consequently, the validity and limits of neoclassical theory are being tested more rigorously than previously. Finally, section 2.5 provides a summary and a list of outstanding issues.

2.1. Theory of turbulent transport

Understanding turbulence-driven (anomalous) transport is one of the most important issues in present magnetized plasmas and future fusion reactors. As realized in previous years, plasma turbulence is driven by different free energy sources for micro-instabilities, mainly the inhomogeneity of plasma profiles including plasma temperature and density as well as the equilibrium magnetic field. The main instabilities that may contribute to anomalous transport in tokamaks were briefly reviewed in Chapter 2 of the ITER Physics Basis document [2]. There has been considerable progress since then in understanding and modelling turbulent transport in tokamaks. This has been greatly assisted by large increases in computational power, giving the ability to simulate turbulence and transport with ever more realistic plasma model equations, as discussed in section 2.2, enabling the construction of physics-based transport models. This has advanced our understanding of the complexity of plasma turbulence, of the formation of large-scale structures such

as zonal flows, streamers and their non-linear self-regulation processes and of the physical mechanisms of internal/edge transport barrier (ETB/ITB) formation as well as the L–H transition. Furthermore, new trends have become clear from the emphasis on some important issues such as the multiple-scale interaction between turbulence and structures, the spatial transport of turbulence and the coupling between core and edge, the underlying mechanism of electron transport, a new transport phenomenon in alpha particle heated burning plasmas such as ITER and transport feedback control.

Regulation of turbulent transport and the resultant confinement improvement in tokamak plasmas have been shown to be related to complex structures and dynamics [3]. Although plasma discharge conditions evolve gradually in space and time, such as the safety factor profile or the auxiliary heating power, distinct confinement improvements may abruptly occur and have prominent structures such as an ITB or/and an ETB. It is recognized that the formation of these high confinement modes, including potentially the L–H transition, may closely relate to the suppression of turbulence by sheared $E \times B$ or turbulence-driven zonal flows [4]. A change in magnetic topology, such as the formation of magnetic islands, is another plausible mechanism [5, 6]. Transport barriers can lead to higher confinement in an ITER burning plasma, although generating a core-sheared flow to trigger and sustain ITBs is a challenge for an ITER-scale device. The key questions are in regard to the mechanisms responsible for triggering and controlling transport barrier formation in the various channels, their strength, width and locations, impact on confinement, their dynamics and sustainment, and the roles of $E \times B$ flow shear and magnetic shear as well as the Shafranov shift in these processes [7]. Transport in tokamak plasmas is a rather complex process not only due to the highly non-linear dynamics of turbulence but also due to the dependence of the magnetic geometry and the device size. The shape of the plasma cross-section and the divertor design may influence the generation of sheared $E \times B$ or zonal flows in the central and edge regions. Synthesizing all these effects is a challenging task, but it may predict a transport scaling with Bohm or gyro-Bohm dependence for ITER or a future DEMO, which is still to be resolved.

Electron transport is a particularly important issue for ITER. Electron heating by the fusion-generated alpha particles will be dominant in ITER and future reactors, but energy transfer will lead to $T_i \approx T_e$. However, from the point of view of theory and modelling, electron heat transport has, so far, been less studied than ions. Sheared $E \times B$ flows with equilibrium scale or weak zonal flows are less effective for the short wavelength electron turbulence. Hence, the dynamics of other large-scale structures such as radially elongated eddies, for e.g. streamers, has attracted attention. Furthermore, fluctuations from the long wavelength ion scale to the intermediate skin depth scale may drive electron transport through various non-adiabatic responses by the electrons, such as trapped electrons and renormalized current diffusion.

Based on the realization of various linear and non-linear instability free energy sources which cover a wide spatio-temporal range from the ion to the electron gyro-radius, a new research direction that is essential for a comprehensive

understanding of turbulent transport has become evident. It emphasizes the dynamic non-linear interaction between the different scales and may reveal new channels of energy as well as particle and momentum transport, so that the plasma confinement can be experimentally controlled.

2.1.1. Physical mechanisms and description of turbulent transport. In a plasma, binary collisions are the basic mechanisms for the cross-field particle and heat transport based on the classic random walk model. It is generally described by a diffusion coefficient, χ :

$$\chi \sim \lambda^2 / \tau_c, \quad (1)$$

where the characteristic walking time τ_c and the step length λ are given by the collision time (i.e. inverse collision frequency) and the gyro-radius of the ions or the electrons, for ion or electron heat transport, respectively, in a cylindrical geometry. In a toroidal plasma this collisional transport is enhanced by particle drift orbit effects due to the inhomogeneous equilibrium magnetic field. This process is called neoclassical transport. For a typical tokamak plasma, neoclassical ion thermal conductivity is of the order $\chi_i \sim 0.1 \text{ m}^2 \text{ s}^{-1}$ and the electron counterpart is smaller by $\sqrt{m_e/m_i}$ (with m_e/m_i being the electron to ion mass ratio) [8]. However, the ion neoclassical transport level is much lower than the observed perpendicular transport in most tokamak plasmas, and the electron neoclassical transport level is never achieved. The higher observed transport level has traditionally been referred to as anomalous transport, which we now understand from theory, modelling and experimental analyses is caused by various turbulent fluctuations.

Description of turbulent transport and its properties. Turbulent transport in a tokamak plasma is mainly produced by micro-scale drift-type turbulence, which is driven by the gradients of temperature or density. The $E \times B$ convection due to the turbulent electric field rotates the plasma element along the electric potential contours across the magnetic field. Once the phase difference between potential and density perturbations is established, this process largely determines the radial particle and heat loss from a high temperature plasma. At the most general level, one can investigate what physical mechanisms may be involved in turbulent transport coefficients based on the dimensional analysis or the scaling properties of the governing equations. However, a specific form for these coefficients may be much preferred [9]. The analytical description of the net convective particle and the thermal fluxes across a given surface S , which are represented by $\Gamma_{i,e}$ and $q_{i,e}$, are given by [10]:

$$\Gamma_{i,e} = \frac{1}{S} \int_S n_{i,e} \vec{v}_E \cdot d\vec{a} = -D_{11} \frac{dn_{i,e}}{dx} - D_{12} \frac{dT_{i,e}}{dx}, \quad (2)$$

$$q_{i,e} = \frac{1}{S} \int_S n_{i,e} T_{i,e} \vec{v}_E \cdot d\vec{a} = -D_{21} \frac{dn_{i,e}}{dx} - D_{22} \frac{dT_{i,e}}{dx}, \quad (3)$$

where \vec{v}_E is the $\vec{E} \times \vec{B}$ convection velocity, \vec{a} is an area vector normal to the flux surface and $n_{i,e}$ and $T_{i,e}$ are the equilibrium density and the temperature of ions and electrons, respectively. These equations represent flux (particle or heat) versus gradient (density or temperature) relations. The matrices $D_{\alpha\beta}$ provide

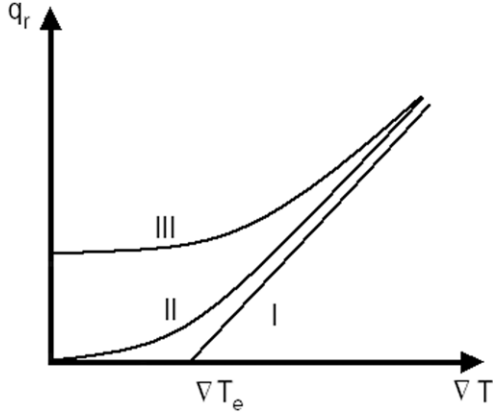


Figure 1. Three types of electron thermal flux versus electron temperature gradient. Type I exhibits a threshold, Type II represents a purely diffusive model where curvature is associated with a non-linear dependence on the temperature gradient, and Type III has contributions to the flux from other gradients. Reprinted with permission from [10]. © 2003 Institute of Physics.

physical insight into the important unstable modes. A phase shift between the fluctuating electrostatic potential, $\tilde{\phi}$, and the fluctuating density, $\delta\tilde{n}$, or the temperature, $\delta\tilde{T}$, can produce the particle or the heat transport. Different phase shift leads to the off-diagonal terms in the above equations. It may induce an inward heat flux contribution that gives a critical gradient above which the heat flux rises to a high level. Generally, different signs and parameter dependences of the off-diagonal terms D_{12} and D_{21} may lead to different types of flux-gradient relations that occur in plasmas. Figure 1 illustrates three different types, in which the electron heat transport is taken as an example with the flux $q_e = \chi_e \nabla T_e$ [10]. Type I represents a critical temperature gradient model above which the transport process starts. A rapid increase in transport when the critical gradient is exceeded anchors the profiles near the critical value; this property is referred to as profile stiffness. Type II describes a simplified turbulent transport model, where the flux vanishes when the gradient vanishes, although the flux can have a non-linear dependence on the gradient that produces curvature. Type III occurs when the turbulence is driven by other gradients, such as the ion temperature or the electron density gradient. Type III is extensively applied in transport modelling codes that implement theory-based models for predictive analysis [11–13], whereas Types I and II are typically employed in interpretive analyses.

Due to the complexity of the plasma turbulence, a comprehensive theoretical description of anomalous transport is still being developed. Turbulent transport models can generally predict a complicated relation between particle and heat transport and show the importance of the off-diagonal terms. However, one would prefer a simple model for the turbulent transport, in which the particle and energy fluxes have a form that is analogous to the classical or the neoclassical ones [14]. Thus, equations (2) and (3) for total particle and heat fluxes are expressed in terms of effective particle and thermal diffusivity coefficients, $D_{i,e}^{\text{eff}}$ and $\chi_{i,e}^{\text{eff}}$, as

follows:

$$\Gamma_{i,e} = \frac{1}{S} \int_S n_{i,e} \vec{v} \cdot d\vec{a} = -D_{i,e}^{\text{eff}} \frac{dn_{i,e}}{dx}, \quad (4)$$

$$q_{i,e} = \frac{1}{S} \int_S n_{i,e} T_{i,e} \vec{v} \cdot d\vec{a} = -\chi_{i,e}^{\text{eff}} \frac{dT_{i,e}}{dx}. \quad (5)$$

Calculating these diffusion coefficients is the objective of turbulent transport theory. They are determined by the properties of various micro-instabilities. The main instabilities that are possible underlying mechanisms for plasma turbulence in tokamaks are summarized in [2].

In a toroidal plasma, linear stability analyses predict the existence of a temperature gradient threshold for the ion or the electron temperature gradient driven instabilities, referred to as ITG or ETG modes, respectively (or $\eta_i(\eta_e)$ modes), which belong to Type I. Here $\eta_i = |L_n/L_{T_i}|$ ($\eta_e = |L_n/L_{T_e}|$) denotes the ratio of the scale length between the density and the ion (electron) temperature. Micro-tearing and current diffusive ballooning modes, where dissipative processes such as collisional resistivity or anomalous current diffusion play an essential role, may be categorized as Type III. TEM and TIM are sometimes driven by density gradients as well and can have behaviours ranging from Type I to Type III, depending on the value of the density gradient and the collisionality. At the edge, the drift-Alfvén mode and pressure (or resistivity and current) gradient driven modes may become more important.

Methods for describing diffusion. Generally speaking, turbulent transport is determined by two factors. One is the fluctuation level, i.e. the saturation amplitude of turbulence. Another is the phase relation of the turbulent structures. It is frequently described by an estimate using a random walk model as described in equation (1). There are two approaches to measure the turbulent diffusivity coefficients. The most widely invoked quasi-linear expression estimates the saturation amplitude by balancing the $E \times B$ non-linearity against the drift wave frequency, ω_* , leading to the familiar mixing length estimate,

$$D_{\perp} \sim (\gamma_L/k_{\perp}^2)_{\text{max}} k_{\perp}, \quad (6)$$

where γ_L is the linear growth rate of the instability and k_{\perp} is a characteristic perpendicular wavenumber of the turbulence [9]. Equation (6) can be interpreted as balancing the growth rate against the turbulent diffusion at saturation. This is an upper-bound: if the $E \times B$ non-linearity is balanced against the growth rate instead, then the weak turbulence result follows,

$$D_{\perp} \sim (\gamma_L/\omega_*)(\gamma_L/k_{\perp}^2). \quad (7)$$

When the linear or the non-linear growth of waves at longer wavelengths is balanced by the energy transfer to the short wavelength region by some dissipative processes such as viscosity, the growth rate and perpendicular wavenumber in equation (6) should be replaced by the inverse correlation time, τ_c , and the correlation length, L_c , respectively, in a quasi-steady turbulent plasma. Equation (6) is then expressed as follows:

$$D_{\perp} \sim L_c^2/\tau_c, \quad (8)$$

for the statistical analysis of turbulence, which may be linked to fluctuation diagnostics, i.e. with this formula the transport

level can be analysed by measuring the statistically averaged correlation time and length.

An alternative phenomenological point of view for determining self-consistently the instability saturation and the turbulent heat transport is that such turbulent diffusivity not only produces the observed anomalous transport but may also influence the stability properties of the mode itself and quench the instability through the non-linear damping rate, γ_d . The balance between non-linear and linear processes may lead to a specific form of turbulent diffusion coefficient which involves the instability [15]. For example, an electron heat diffusion coefficient based on the trapped electron mode is derived in this way to explain the formation of electron internal transport barriers (ITB) in strongly reversed shear plasmas [16]. An anomalous transport model has also been derived by balancing the non-linear growth of the current diffusion ballooning mode (CDBM) against other turbulent transport effects such as viscosity and thermal diffusion [17]. Under this quasi-linear estimate, the analyses of the linear or non-linear growth rates and the mode structures for the instabilities are necessary and useful.

The above relatively simple estimates are being superseded by the results of state-of-the-art computational models of turbulent transport. This approach takes the fundamental equations describing the plasma and computes the turbulent fluctuations and consequent transport. A hierarchy of plasma models can be considered. The most complete is at the level of the Vlasov or the Fokker–Planck equation, but this can be reduced to the somewhat simpler gyro-kinetic description that averages over the rapid gyro-motion [18]. Further approximations result from fluid closures, such as the gyro-Landau fluid moment equations that capture the kinetic effects of Landau damping or ultimately the two-fluid Braginskii equations, normally only applied in the plasma edge region [19]. In kinetic approaches one writes the distribution function $f = f_0 + \delta f$ and solves the dynamical equation for the turbulent fluctuation δf that responds to the perturbed electromagnetic fields. A radial transport equation can be obtained for the response of the flux surface averaged f_0 to sources and the turbulent radial fluxes. It is also possible to construct improved quasi-linear transport models by accurately determining the linear characteristics, e.g. γ_L and k_{\perp}^2 from kinetic stability calculations, and benchmarking them against computational turbulence models. A leading example of this approach is the GLF23 transport model [20]. Alternatively, one can obtain parametric fits to the outputs of the turbulence calculations; here a seminal example was the IFS/PPPL model [21].

2.1.2. Progress in turbulent transport theory.

Micro-instability and turbulent transport. Drift wave turbulence in tokamak plasmas is a highly complex non-linear system involving multiple-scale turbulence modes, non-linear self-regulation of sheared $E \times B$ or zonal flow and various stabilizing mechanisms influenced by the magnetic geometry and plasma compositions, as schematically shown in an outline summary in figure 2 [22]. The typical turbulent fluctuation in the ion regime is the so-called ITG mode, which mainly responds to ion heat transport. Correspondingly, the short

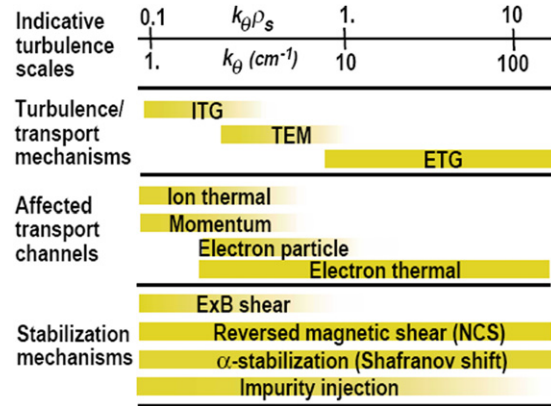


Figure 2. An outline summary of drift wave turbulence scales, with corresponding turbulence mechanisms, affected transport channels and stabilization mechanisms. Reprinted with permission from [22].

wavelength electron-scale fluctuation, the ETG mode, may produce large electron heat flux. ITG and ETG instabilities have critical temperature gradient thresholds, which categorize them as Type I transport models in figure 1. The trapped electron mode (TEM) with its intermediate spatial scale (meso-scale) can cause electron particle transport and also turbulent electron heat flux; it is categorized as Type II. Micro-tearing and current diffusive ballooning modes, in which dissipative processes such as collisional resistivity or anomalous current diffusion play essential roles, may be categorized as Type III. At the edge, the drift-Alfvén mode and the pressure (or resistivity and current) gradient driven modes may become more important.

Turbulent particle pinch. Particle transport is a central question in burning plasmas, since fusion power increases as the square of the density. Because of this, attention must be paid to the existence and nature of physical processes leading to density peaking. Recently the theory of turbulent pinches has made significant progress [23]. Based on equation (2), the additive term that is proportional to the logarithmic temperature gradient associated with thermo-diffusion, D_{12} , contributes to the turbulent particle pinch. In addition, the thermodynamic forces resulting from the coupling of the gradients of density and temperature and the magnetic field geometry also play an essential role in the particle pinch. TEM turbulence is one of the main mechanisms of particle transport. It has been shown that the magnetic shear can influence the pinch velocity and that collisionality decreases the density peaking factor. At high collisionality, the pinch velocity is close to the Ware value, whereas it is larger at low collisionality. It also suggests that density profiles in ITER may be more peaked than planned. However, it is not clear whether the passing electrons take part in the particle pinch, which calls for further theory and simulation studies. See section 3.4 for further discussion of pinches and density peaking.

Dynamics of sheared flow in ion-scale turbulence. Except for the dependence of plasma turbulence on complicated magnetic geometry and device parameters, remarkable progress has been made in understanding the suppression of turbulent transport by sheared $E \times B$ flows, which is thought to contribute to the

formation of internal (or edge) transport barriers in tokamak plasmas [24, 25]. As to the origin of $E \times B$ flows, besides externally and/or neoclassically driven macro-scale flows, the importance of self-generated zonal flows (with poloidal wavenumber $k_{\text{poloidal}} \cong 0$), which are convective cell modes non-linearly generated in turbulent plasmas that self-regulate the transport level, has been widely recognized. The model of turbulence decorrelation and stabilization by such sheared $E \times B$ and zonal flows [26, 27] has been extensively verified by large-scale turbulence simulations (see section 2.2) and has also been tested by different experiments (see section 2.3).

Large-scale ITG turbulence simulations based on gyro-kinetic or fluid (gyro-fluid) models not only predict the generation of zonal flows but also show the reduction of turbulent ion heat transport by such zonal flows (see section 2.2). The reduction of transport depends on the suppression of the fluctuation amplitude, the dephasing (cross-phase) of fluctuations or their synergetic changes. The physical mechanism for the dephasing of fluctuations is the randomization of the coherent structure, which is a complement to the flow shearing decorrelation of turbulence [27]. The transport reduction may be understood as a decrease in the correlation length of the turbulence in the model expressed by equation (8).

Transport scaling in tokamak plasmas. Based on the expression for the anomalous transport coefficient in equation (8), transport scaling is determined by the characteristic correlation length and time. When turbulent fluctuations are caused by low frequency drift waves with time scale $\tau_C^{-1} \sim \omega_{*i,e}$ and spatial scale $L_C \sim \rho_{i,e}$ (ion or electron gyro-radius), the transport coefficient is described by the so-called gyro-Bohm scaling, $D_{\perp} \sim (\rho_{i,e}/L_T)T/eB$, where L_T is the temperature gradient scale length. This is the expression expected from local drift wave turbulence theory [28–30]. If the turbulent fluctuations are characterized by the macroscopic size of the plasma, the transport has the conventional Bohm scaling, $D_{\perp} \sim T/eB$. In addition, the drift wave in toroidal geometry may form a radially extended non-local structure whose spatial length is approximately given by the geometrical mean between the ion Larmor radius, ρ_i , and the equilibrium scale length, L_T , or the plasma size, a , i.e. $L_C \sim \sqrt{\rho_i L_T / \hat{s}}$ (here \hat{s} is the magnetic shear). A Bohm-like (or large-scale non-local) scaling may occur in plasmas with peaked temperature [31, 32]. Recent ITG simulations show a transition of turbulent ion transport scaling from the Bohm-like dependence for a small system size to the gyro-Bohm scaling in larger plasma systems with $a/\rho_i > 300$ [33], as shown in figure 3. This trend has significant implications, since an accurate description of size scaling of transport is critical for the design of fusion reactors. The appearance of Bohm-like transport in an essentially gyro-Bohm model can result from the stabilizing effect of rotation shear arising from diamagnetic fluxes, represented by $\chi \sim \chi_{\text{gB}}(1 - \rho_*/\rho_*^{\text{crit}})$ [34], or from turbulence spreading in which there is radial propagation of turbulent fluctuations from unstable to stable regions of plasma [35, 36].

Electron thermal transport. Trapped electrons can produce high anomalous heat flux when either TEM or ITG modes

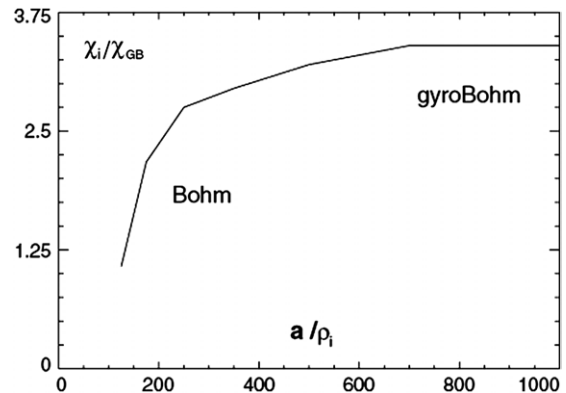


Figure 3. Ion thermal conductivity can change scaling as the tokamak minor radius increases with respect to the gyro-radius. Reprinted with permission from [33]. © 2002 American Physical Society.

are strongly unstable. The ETG mode is another plausible candidate responsible for the electron thermal transport. Besides zonal flows, another convective cell mode structure, referred to as a streamer (radial wavenumber $k_{\text{radial}} \cong 0$), can be generated in ETG turbulence. Such streamers give rise to transport in excess of simple mixing length estimates for ETG modes. Furthermore, the generation of zonal flows in ETG turbulence may be less important than in ITG turbulence, again leading to larger transport. Gyro-kinetic and gyro-fluid simulations are being used to identify conditions under which streamers may be a relevant factor in electron thermal transport (see section 2.2 for further discussion). Large transport may tend to drive the temperature profile to near marginal stability. Electron transport in recent experiments seems to exhibit a threshold depending on the electron temperature gradient, which may explain the so-called profile stiffness or profile resilience (see section 3.3). Further, the stabilization of the ETG mode [37] and the TEM mode [38] is sometimes consistent with the conditions required for the formation of internal transport barriers.

Intermittency in turbulent transport. Although the model given by equation (8) is simple and useful in dimensional arguments, it does not describe the underlying physics of the structure formation or bifurcations such as the L–H transition. This is because plasma turbulence can be highly intermittent, and the turbulent transport is then characterized by bursty behaviour. Theoretical descriptions of turbulence should then be based on a statistical approach rather than on a deterministic point of view [39, 40]. Intermittent transport often results from the dynamics associated with the self-organized-criticality [41] involving large-scale transport events such as avalanches and large-scale coherent structures such as zonal flows [42–44], streamers [45–47], low-frequency Kelvin–Helmholtz (KH) [48–50], generalized KH modes [51, 52], jets [53] or blobs in the tokamak scrape-off layer (SOL) [54, 55]. Research on the rare, large transport events that accompany the coherent structures has proceeded at several levels: (1) generation of large-scale coherent structures in turbulent plasmas, (2) interaction among different scale fluctuations including the coherent structures and (3) statistical approaches to turbulence theory.

Dynamics of zonal flows and multiple-scale interaction. Typical large-scale coherent structures in tokamak plasma turbulence are toroidally and poloidally symmetric zonal flows/fields and radially elongated streamers. The former can suppress the turbulent fluctuations and transport through the flow shear decorrelation of turbulence, while the latter may enhance plasma transport by increasing the radial correlation length. These structures are generally excited by a modulational instability in ITG or ETG turbulence [45, 46, 50, 56–66]. The underlying mechanism can be basically analysed using a simplified drift wave turbulence model, namely, the Hasegawa–Mima turbulence model. One important effect of zonal flows on drift wave turbulence is the shearing of turbulent eddies. Noting the complex temporal behaviour of zonal flows, it has been shown that fast time varying components of zonal flows are less effective in shearing turbulence eddies [67] than the mean $\vec{E} \times \vec{B}$ shear. This is the reason why the geodesic acoustic mode (GAM) [68] with $\omega_{\text{GAM}} \cong v_{T_i}/R$ does not reduce the ambient turbulence significantly for typical core parameters [69]. At the edge, sharp pressure gradients make the diamagnetic drift frequency at the relevant long wavelength closer to the GAM frequency. Therefore, the GAM could possibly affect the edge ambient turbulence [70, 71]. Since the GAM can take energy out of the lower frequency zonal flow component, due to geodesic coupling [71], GAMs can either enhance the shearing or reduce the shearing overall, depending on parameters. While the zonal flows are extensively studied especially in ITG turbulence, the dynamics of streamers, particularly in ETG turbulence, is still under investigation. Further, low-frequency fluid-like KH modes may be excited as one of the saturation mechanisms of zonal flows or streamers [45, 48, 49]. In addition, a poloidally non-symmetrical flow, the so-called generalized KH mode, in contrast to the zonal flow, may be non-linearly generated through the modulational instability of drift wave turbulence [52]. It may enhance the anomalous transport.

The complexity of plasma turbulence results from the properties of fluctuations, which are characterized by multiple spatio-temporal scales, as summarized schematically in figure 4. The interactions among these different spatio-temporal scales has been emphasized in recent years [3]. These processes are studied by including the interaction between the turbulent fluctuations with separate scales [40, 72, 73], between turbulent ITG/ETG fluctuations and flows with anisotropic spectra such as zonal flows/streamers and also among the mean shear flows, zonal flows and generalized KH modes in drift wave turbulence [52]. From the theoretical point of view, a new direction in studying the turbulence interaction and its role in transport aims to establish a theoretical framework that treats all fluctuations as an interacting dynamical system. On the other hand, a simplified minimal model that describes the coupled drift wave turbulence and zonal flows and/or streamers has been proposed [45]. This model has the characteristic form of a ‘predator–prey’ system in which the population of the drift wave quanta (prey) grows via linear ITG/ETG instability, generates zonal flows or streamers (and or generalized KH modes) (predator) via the modulational instability. Meanwhile, effort is being made to numerically simulate the direct or indirect interactions among the multiple-scale fluctuations and flows [44, 73–76]. More practically,

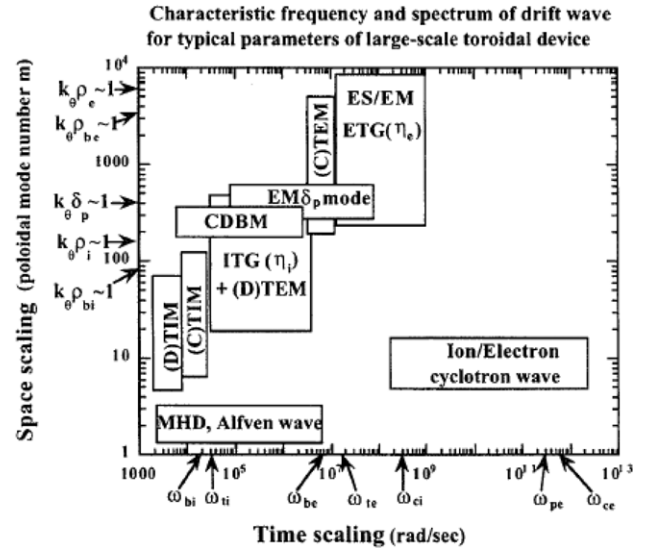


Figure 4. Typical spatio-temporal scales of micro-instabilities that cause anomalous transport: (D)TIM ((dissipative) trapped ion mode); (C)TIM ((collisionless) trapped ion mode); ITG (η_i) (ion temperature gradient mode); (D)TEM ((dissipative) trapped electron mode); CDBM (current diffusive ballooning mode); EM δ_p (electro-magnetic skin depth mode); (C)TEM ((collisionless) trapped electron mode); ES/EM ETG (η_e) (electrostatic/electromagnetic electron temperature gradient mode). Reprinted with permission from [747].

an electromagnetic two-fluid code, so-called CUTIE, has described quantitatively some processes occurring in some tokamak plasmas, which may involve the activity of meso-scale fluctuations [77–79].

Statistical description of turbulent transport. As a result of the progress made in the theory and the simulation of turbulent transport, a statistical approach describing the role of non-linearity in plasma turbulence has been advanced. The importance of developing a probabilistic theory of plasma transport, which focuses on calculating the probability distribution function (PDF) of the flux, rather than anomalous transport coefficients, has been considered in [52, 80]. The statistical nature of the turbulent fluctuations and their influence on transport are determined by the non-linear terms in the system of equations. These non-linear terms can be expressed as a sum of the drag, the drive and the noise with different scales in a renormalized Langevin equation [81]. The non-Gaussian PDF of the flux includes tails, which have a contribution from rare large events, such as the formation of some coherent structures. These large-scale structures could play a dominant role in determining the averaged transport. A calculation of the tail of the PDF of heat flux H due to toroidal ITG modes, based on a non-perturbative method (i.e. instanton method), is carried out by a given white noise and the tail is estimated as $P(H) \sim \exp(-cH^{3/2})$ (here c is a constant) [52]. The stretched exponential PDF tail implies that a coherent structure enhances heat transport over a Gaussian prediction. Non-linearity in the strong noise leads to more prominent non-Gaussian tails. A statistical theory of strong turbulence in inhomogeneous plasmas has been developed for the cases where fluctuations with different scale lengths co-exist [81]. In a dynamical interacting system, there may exist several states

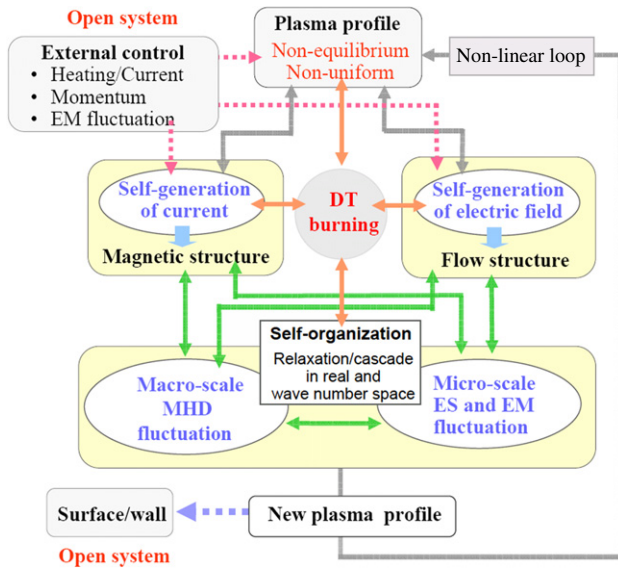


Figure 5. A schematic flowchart of multi-hierarchical high performance tokamak plasmas shows the interactions among different time and spatial scale fluctuations that play an essential role in structure formation.

of fluctuations due to the complex interactions among different scales. The suppressing (quenching) or enhancing (exciting) role of one mode on another mode in one state is determined by the relative magnitudes of the driving powers of different scale fluctuations by the global inhomogeneity. This statistical theory has also been applied to analysing the bifurcation of the radial electric field so as to describe the L–H transition in toroidal plasmas with multiple-scale fluctuations. The PDF of the radial electric field shows power-law tails, with the power index depending on the global inhomogeneity as well as the size of volume average. As the global gradient becomes larger, the tail becomes more prominent.

Concluding remarks. Stimulated by the growing interest in ITER burning plasma physics, the theory of plasma turbulence and transport has been advanced with the aid of significantly improved computer simulations. As we discussed in this section, high performance plasmas with high confinement and of a steady-state nature can be realized by having various prominent structures in the plasma. Therefore, understanding the underlying physical mechanisms and the selection rules for such structure formation and developing corresponding control methods are central subjects that will lead the fusion program to success. It is now widely recognized that such structure formation exhibits a complex nature when multiple physical processes are linked to one another. It is difficult to grasp such complex process based on the idea of a conventional one-to-one correspondence between ‘cause’ and ‘result’.

In order to grasp the global picture of self-organized plasmas that exhibit various structure formations, a non-linear loop system that shows the mutual linkage between different physical processes in tokamaks is illustrated in figure 5. The loop may be categorized into the following three primary dynamics. (1) Neoclassical dynamics: this leads to the self-generated bootstrap current and electric field (and thus to plasma flow and rotation) from the pressure gradient. A new

equilibrium magnetic field with plasma flows is established. (2) Fluctuation and self-organization dynamics: under the new equilibrium, various fluctuations from macro-scale MHD modes to micro/meso-scale electrostatic and electromagnetic modes (as shown in figure 4) are excited. These modes non-linearly interact in a wide frequency and wavenumber space, leading to self-organization in the fluctuation spectrum, including non-linearly generated global structures. These fluctuations change the plasma profile in various ways, such as diffusive transport, non-diffusive or intermittent transport and bursting blobs. It is also pointed out that zonal fields, which are the magnetic field version of zonal flows, may change the magnetic structures, specifically in high beta plasmas. (3) Global linkage as a non-linear complex loop system: each physical process with its own spatio-temporal scale is hierarchically linked to others through the evolving plasma profile and establishes a closed non-linear loop in a self-consistent manner as shown in figure 5. The closed loop is coupled to the external heating system, which is used to control the complex loop dynamics. Once a transport barrier is triggered, the loop reveals a strongly autonomous nature, so that external control becomes less effective. It is understood that steady-state transport barrier formation may correspond to one of the fixed solutions of the non-linear loop equations. In burning plasmas, the non-linear loop may be internally sustained via nuclear fusion, so that the level of the autonomous nature and/or complexity of the loop may be increased, depending on the operating Q (figure of merit) value.

Building on the knowledge of the more elementary processes, i.e. (1) and (2), that have been significantly advanced so far, fusion theory will need to step into the new regime, described by (3), in order to understand the complex autonomous dynamics of the non-linear loop and to develop control methods for burning plasmas.

2.2. Turbulence simulation

It should be noted that the assumption of adiabatic electron dynamics in the description of ITG-driven transport implies zero net particle transport, which is an unphysical simplification. Modern gyro-kinetic codes (GYRO, GS2, for example) are capable of treating ITG instabilities including complete kinetic electron dynamics, while the best theory-based drift wave models (GLF23 and MM95) also include kinetic electron physics. For serious physics studies, the GYRO and GS2 codes routinely include kinetic electron physics. Thus, the adiabatic electron model is largely irrelevant for modern gyro-kinetic transport studies, e.g. [82] gives detailed gyro-kinetic particle transport results (including ion, electron and ash transport) with full electron dynamics. In order to make the distinction between the simplified and the more complete models, we refer to the former as ‘ITG with adiabatic electrons.’ If the model including kinetic electrons has dominant linear instabilities which propagate in the ion direction, it is customary to call this ‘ITG-dominated transport,’ whereas if the linear modes propagate in the electron direction, one generally refers to them as ‘trapped electron mode (TEM) instabilities.’

Table 1. Overview of gyro-kinetic, toroidal turbulence codes presently in use.

Code	Main authors	Method	Simulation domain	Electron dynamics
SUMMIT	Parker <i>et al</i> [131]	PIC	Flux tube	Kinetic, electromagnetic
GTC	Lin [111]	PIC	Full torus	Adiabatic, electrostatic
GT3D	Idomura <i>et al</i> [92]	PIC	Full torus	Adiabatic, electrostatic
ORB	Villard <i>et al</i> [93]	PIC	Full torus	Adiabatic, electrostatic
GENE	Jenko and co-workers [122, 135]	Vlasov	Flux tube	Kinetic, electromagnetic
GS2	Dorland <i>et al</i> [46]	Vlasov	Flux tube	Kinetic, electromagnetic
GYRO	Waltz and co-workers [109, 748]	Vlasov	Full torus	Kinetic, electromagnetic

2.2.1. Models and codes. In the case of ordinary fluids, direct numerical simulation of turbulent flows is based on the Navier–Stokes equation. Here, most attention is usually paid to physics issues concerning the inertial range of spatial scales in which—due to the absence of energy sources and sinks—kinetic energy is merely passed on from one set of scales to the next. Unfortunately, the total computational effort that is required to address these issues scales approximately as the third power of the Reynolds number. Therefore, despite continuous growth in computer power, studies of high-Reynolds-number fluid turbulence will have to be based on approximation schemes in the foreseeable future.

In contrast to this, direct numerical simulation of plasma micro-turbulence is gradually reaching a level of maturity that allows for quantitative comparisons with experiments. This might, at first, sound amazing in light of the enormous complexity of the problem (multiple drive and saturation mechanisms, kinetic effects and cross-scale coupling, to name just a few). However, it is essential to note that in the case of magnetized fusion plasmas, the focus tends to be not on inertial range physics but on the turbulent transport. The latter is often dominated by a rather limited number of degrees of freedom that are embedded in a turbulent bath. Although resolution requirements may vary a lot with plasma parameters, one can generally say that quite comprehensive numerical simulations of plasma micro-turbulence under realistic conditions are becoming feasible with present-day supercomputers. Despite this good general prospect, it turns out that much effort needs to be put into the careful development and testing of turbulence models and codes.

Kinetic and fluid models. It is widely agreed upon that first-principles simulations of low-frequency (with respect to the ion cyclotron frequency) micro-turbulence in weakly collisional plasmas should be based on the gyro-phase-averaged Vlasov–Maxwell equations, which were first derived in the 1980s [18]. Here, the challenge is to compute the time history of each particle species’ distribution function in a five-dimensional phase space (the sixth dimension corresponds to the gyro-phase and is separated from the other five) along with that of the perturbed electromagnetic fields in real space. Noting that of the order of 100 (or more) velocity space quantities per grid point/cell are typically involved in gyro-kinetic computations, it has also been attempted to construct numerically less expensive models on the basis of non-standard fluid equations that capture all the relevant kinetic effects [83–85]. These ‘gyro-fluid’ models have been relatively successful in describing many qualitative features of plasma micro-turbulence and the associated transport. Over the last couple of years it has become clear, however, that

for reliable *quantitative* predictions, a gyro-kinetic treatment cannot be avoided [86–88]. Nevertheless, gyro-fluid codes contributed significantly to the progress in plasma micro-turbulence research in the 1990s, and they might continue to be helpful tools if used synergistically with gyro-kinetic codes. The most advanced non-linear gyro-fluid codes that are presently in use are described in [69, 89–91]. For the rest of this brief overview, we will focus mainly on gyro-kinetic and gyro-fluid simulation of tokamak core plasmas.

Computational gyro-kinetics. The employed algorithms for solving the gyro-kinetic Vlasov–Maxwell equations can be roughly divided into two groups according to the Lagrangian and the Eulerian description of phase space dynamics (besides this, there also exist so-called semi-Lagrangian methods which will not be discussed here).

- Particle-in-cell (PIC) codes follow the trajectories of an ensemble of N marker particles, at the same time using a real space grid to compute the interaction forces effectively. While they are relatively easy to implement and parallelize, one has to deal with the build-up of numerical noise which can affect long-time simulations as well as the dynamics of zonal flows or kinetic shear Alfvén waves [92–98]. This problem has been a subject of increasing interest in recent years, and significant progress has been achieved (see below).
- A complementary approach is to represent the gyro-centre distribution functions on a fixed grid in a five-dimensional phase space. The non-linear gyro-kinetic equations are then finite-differenced and solved according to techniques borrowed from computational fluid dynamics. Such schemes avoid noise problems and their consequences, but they tend to be more difficult to implement and somewhat less efficient. Moreover, one has to carefully remove grid-scale fluctuations in phase space, an issue well known from fluid turbulence studies.

At present, a number of non-linear gyro-kinetic codes for studying tokamak micro-turbulence are in use, with a few more under construction. An overview is given in table 1.

Noise reduction in gyro-kinetic PIC codes. As mentioned before, PIC simulations are based on sampling the phase space dynamics via superparticles. It can be shown [99, 100] that the statistical error of this method is given by $\sigma/N^{1/2}$ where σ is the variance of the estimator and N is the number of particles used in the computation. In principle, convergence can thus always be achieved by increasing N . But, in practice, this brute-force approach is often numerically prohibitive. One therefore aims

at reducing σ . Over the last decade or so, much progress has been made in this area.

The ‘ δf ’ method [101–104] utilizes a split of the total distribution function f into an equilibrium part f_0 and a fluctuating part $\tilde{f} = f - f_0$. Only the latter is represented by particles, while the former is treated analytically. Thus, a weight is assigned to each particle accounting for the fact that (in contrast to f) \tilde{f} is not constant along phase space trajectories. However, as has been demonstrated recently, collisionless systems can also do without weights if the exact equations of motion are solved [99]. In so-called ‘split-weight’ schemes [105], only the non-adiabatic part of f , i.e. $\tilde{h} = f - f_0(1 - q\phi/T)$, is kept. A modification of this method has been applied successfully in the electromagnetic regime [106].

More recently, an optimized particle loading technique has been proposed to further minimize the variance σ [107]. Here, the idea is to increase the particle density in regions of phase space where $|\delta f|$ is large. Through this adaptation, optimal sampling is achieved. The numerical noise is greatly reduced, along with the degree to which conservation laws are violated. Using optimized loading, gyro-kinetic PIC simulations could be extended well into the non-linear regime for the first time [93]. Nevertheless, dealing with particle noise may remain a challenge, as has been reemphasized recently in the context of electron-scale turbulence [108].

2.2.2. Some main physics issues.

Basic ITG turbulence. Over the past decade or so, much emphasis has been put on the study of fluctuations driven by ion temperature gradient (ITG) modes. A basic model for these micro-instabilities may be obtained by taking the electrons to be adiabatic (i.e. they are in the Boltzmann equilibrium at any time). This assumption removes complications associated with the time scale separation between electron and ion dynamics and with the co-existence of multiple micro-instabilities. It allows one to study a simplified but experimentally relevant system with reasonable computational effort. Several key features of basic ITG turbulence have been identified and investigated.

- ITG modes are linearly destabilized if and only if the inverse scale length of the ion temperature gradient exceeds a certain threshold, i.e. for $R/L_{T_i} \equiv |R\nabla T_i|/T_i > (R/L_{T_i})_{\text{crit}}$ where R is the major radius of the toroidal device. Increasing R/L_{T_i} beyond its critical value (which depends on the local plasma parameters), the induced ion thermal transport rapidly rises to values of the order of $\chi_i \sim \rho_i^2 v_{ti}/L_{T_i}$ and then stays at that level [109, 110]. Here, ρ_i is the ion gyro-radius and v_{ti} is the ion thermal velocity. From this one can predict that, under typical plasma conditions, moderate central ion heating is not expected to push the T_i profile much beyond its critical gradient. This kind of ‘stiffness’ in the ion temperature profiles has indeed been confirmed experimentally in various discharges and devices.
- As has been shown by many investigators (see, e.g. [21, 66, 111–116]), the dominant non-linear saturation mechanism for ITG modes—especially near the linear threshold—turns out to be the shearing of turbulent eddies

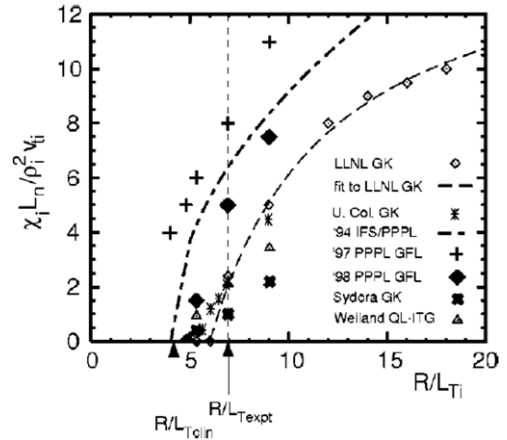


Figure 6. Ion heat diffusivity as a function of the normalized ion temperature gradient for various gyro-kinetic and gyro-fluid codes: the critical gradient exhibits a non-linear upshift. Reprinted with permission from [110]. © 2000 American Institute of Physics.

by self-generated zonal $\vec{E} \times \vec{B}$ flows. In some regimes, this may even result in turbulence suppression, associated with an effective upshift of $(R/L_{T_i})_{\text{crit}}$ [110]. This is shown in figure 6. On the other hand, linearly damped modes may be non-linearly excited in the course of ‘turbulence spreading’ (see [33] and references therein). For reasons like these, (quasi-) linear theory—although tremendously useful for transport modelling—cannot replace massively parallel non-linear computations.

- Although scalings of the ITG mode induced χ_i with collisionality [42, 117] and system size [32–34] may be found in the literature, these results must be viewed as preliminary. More comprehensive and realistic simulations, involving non-adiabatic electrons or core-to-edge coupling, are expected to give different answers.
- Beyond allowing us to gain basic insights into the behaviour of turbulent plasmas in toroidal magnetic devices, the adiabatic ITG model has also served as an environment for inter-code comparisons, involving both gyro-kinetic and gyro-fluid codes. The classic test case has become a set of parameters—called the cyclone base case—inspired by a particular DIII-D discharge. Many of the gyro-kinetic codes listed in table 1 have been able to reach convergence in this test case [110, 118, 119]. In this context, see figure 6.

Ion-scale turbulence involving non-adiabatic electrons. The adiabatic electron approximation automatically implies that both the particle and the electron thermal transport vanish identically. Furthermore, finite β effects cannot be incorporated since they are caused by parallel currents carried mainly by passing (i.e. non-adiabatic) electrons. Finite β effects (β denotes the ratio of the plasma pressure and the magnetic pressure) result from the inclusion of magnetic field fluctuations that can affect both the driving micro-instabilities and the non-linear saturation mechanisms; moreover, they allow for magnetic transport. Therefore, it is clear that this severe restriction must be transcended in order to proceed towards more realistic turbulence models. Fluid codes have

pioneered this area of plasma micro-turbulence simulation, but gyro-kinetic computations are also becoming available.

- *Trapped electron effects.* Gyro-fluid turbulence codes involving the dynamics of bounce-averaged trapped electrons were developed in the mid-1990's [120]. Here, passing electrons and finite β effects were neglected. Trapped electrons can contribute to the drive of ITG modes, but they may also be the source of trapped electron modes (TEMs). An attempt to predict thermal and particle diffusivities based on non-linear gyro-fluid computations in flux-tube geometry can be found in [121]. On the other hand, a systematic study of collisionless TEM turbulence in the framework of non-linear gyro-kinetics is presented in [119, 122]. Therein, it is shown that (1) even in the absence of a linear threshold, the non-linear system typically exhibits an effective threshold in the normalized electron temperature gradient, (2) zonal flows tend to be relatively weak away from the effective threshold and (3) a modified quasi-linear model is able to capture many features and parameter dependences of the TEM induced transport reasonably well. On the other hand, it was observed in the case of purely density-gradient driven TEM turbulence that there exists a non-linear upshift of the critical density gradient that is analogous to the Dimits shift in ITG turbulence with adiabatic electrons [123]. These results indicate that non-linear saturation of TEMs seems to be caused by zonal flows if and only if one approaches the linear stability thresholds. Further investigations of TEM saturation are thus called for.
- *Particle pinch effects.* A full torus fluid code involving both ions and trapped electrons has been used to study various aspects of turbulent transport [124]. It is found, e.g. that an anomalous particle pinch exists, driven by both a curvature effect and thermo-diffusion. The curvature contribution is exactly the same as the one predicted by 'turbulence equipartition' (TEP) theory [125, 126]. The amplitude of thermo-diffusion depends on the average phase velocity of fluctuations. In the regime dominated by ITG modes, it is directed inwards. When moving to high values of T_e/T_i , the trapped electron mode branch becomes dominant and the thermo-diffusion term ultimately reverses its sign. Moreover, it has been demonstrated that the turbulence can generate significant amounts of flows in the *parallel* direction when the $\vec{E} \times \vec{B}$ shearing rate becomes large (as in ITBs) [127]. Beyond these fluid results, recent gyro-kinetic work revealed that particle transport tends to be described surprisingly well by quasi-linear theory [82, 119]. This is largely due to the fact that the non-linear cross-phases tend to resemble the linear ones. As one surprising consequence, one finds that an anomalous particle pinch can also be carried by passing (not trapped) electrons [119, 128]. This kinetic effect had been overlooked in previous fluid studies. It must be stressed, however, that despite these interesting developments the direct applicability of turbulent pinch results to experiment is hampered by the fact that gyro-kinetic simulations generally predict that the pinch disappears for realistic values of collisionality [82, 129]. This discrepancy needs to be addressed in future work.

- *Electromagnetic effects.* Gyro-fluid models have also been extended to include passing electrons in a small mass ratio expansion (applicable to the plasma core, but not to the edge) [89, 130]. Here, trapped electrons were neglected. It was found that far below the ideal MHD ballooning limit, the scaling of ITG turbulence with β basically follows the (quasi-)linear expectations, which in this case predict a substantial drop in χ_i . However, as the critical β is reached from below, the (electrostatic) transport rises sharply. A likely explanation of this finding is that at the turning point, the dominant drive of the turbulence transitions from ITG modes to kinetic ballooning modes. Recent gyro-kinetic simulations have confirmed that for ITG/TEM systems well below the ideal MHD ballooning threshold, the transport tends to be mainly electrostatic, following the (quasi-)linear expectations [131, 132]. However, there are also indications that the electron heat flux might obtain a significant magnetic component as the kinetic ballooning regime is entered [132, 133]. Similar findings are expected for cases in which the dominant micro-instability becomes a micro-tearing mode. This situation might occur, for example, in spherical tokamaks such as MAST [134].

ETG turbulence and cross-scale coupling. Turbulence suppression in ITBs is generally attributed to the effect of equilibrium scale $\vec{E} \times \vec{B}$ shear flows, possibly aided by other mechanisms (such as low magnetic shear $\hat{s} \leq 0$ or high normalized pressure gradient $\alpha > 0$) which tend to weaken the drive of toroidal ITG modes and trapped electron modes. It is not clear, however, why the electron thermal transport is often not changed much while the ion channel can be reduced down to its neoclassical level. One plausible explanation of this experimental finding is the existence of turbulent fluctuations at space-time scales smaller than those of ITG turbulence. This is one of the reasons why ETG turbulence has been the centre of attention in recent years. Some of the key results in this area of research are the following.

- Toroidal ETG turbulence may exhibit streamers (radially elongated vortices illustrated in figure 7) that have been identified as residuals of linear modes [46, 135]. Due to their large saturation amplitude, the associated electron heat transport can exceed the small mixing length expectations by more than an order of magnitude, reaching experimentally relevant levels. The observed boost factor primarily depends on $R/L_{T_e} - (R/L_{T_e})_{\text{crit}}$ and magnetic shear [47, 135]. In contrast to ITG turbulence, zonal flows are found to be rather weak in toroidal simulations. (It is interesting to note that streamers have also been observed in fluid simulations of resistive ballooning turbulence [136] and in gyro-kinetic simulations of TEM turbulence [122]).
- This surprising result may be understood in the following way [47]. Depending on the relative importance of compression in the parallel and perpendicular dynamics, one of two Kelvin–Helmholtz-like secondary instabilities stop the exponential growth of linear ETG modes. Balancing the growth rates of primary and secondary modes (the latter is proportional to the amplitude of the former), one can estimate the saturation amplitude and the

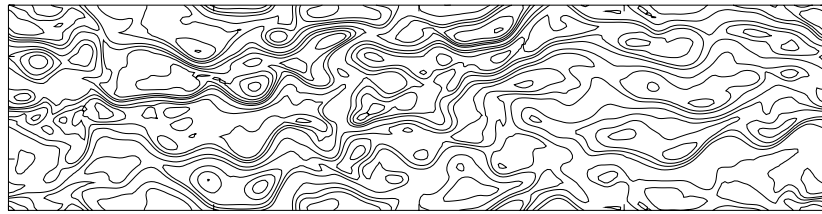


Figure 7. Characteristic contour lines of the electrostatic potential in the outboard x - y plane for toroidal ETG turbulence: formation of streamers (radially elongated structures). Reprinted with permission from [135]. © 2000 American Institute of Physics.

induced transport level. The observed agreement between this model and gyro-kinetic simulations is quite good [47].

- Recently, the above ETG work has been extended to include trapped electron effects. Based on results from non-local PIC simulations, Lin *et al* [137] argued that in this case, the ETG instability saturates via non-linear toroidal coupling. In such non-linear interactions, the wave energy at the unstable high toroidal mode number domain cascades towards the more stable lower toroidal mode number domain via scatterings off the driven low mode number quasi-modes. The transport level still exceeded the corresponding ITG level, but not by as much as in the simulations without trapping by Jenko and Dorland [47]. However, Nevins and co-workers showed that the transport at late times is very likely to be determined by numerical noise [108].
- To address the issues of ITB physics, ETG turbulence has also been studied by means of radially non-local gyro-kinetic simulations [138]. In this system, streamers are absent, and zonal flows—formed around (but not directly at) the q_{\min} (minimum safety factor) surface—tend to become more prominent as the magnetic shear goes to zero. Zonal flow saturation is found to be caused by a Kelvin–Helmholtz-like instability.
- Recently, this line of research triggered interest in the non-linear coupling of various kinds of plasma micro-turbulence. In [48], it was shown that linear ITG modes can be suppressed by strong, ETG-scale zonal flows. Using non-linear gyro-fluid simulations, it could be demonstrated that a complex interplay of ITG turbulence, ITG-scale zonal flows and (externally imposed) ETG-scale zonal flows can lead to a general reduction and a pronounced burstiness of the ion heat transport [44, 139]. The first self-consistent numerical simulations of cross-scale coupled turbulence have been presented in [140]. Therein it was demonstrated explicitly that, in general, transport on ion and electrons scales does not obey the superposition principle (see figure 8). In particular, it was shown that the residual level of electron heat transport in a transport barrier can be set by ETG turbulence.

2.2.3. Comparisons with experiments. Direct numerical simulation of plasma micro-turbulence is gradually reaching a level of maturity that allows quantitative comparisons with experiments. Supercomputers are becoming ever more powerful, and the codes are getting more comprehensive. Several codes now include non-adiabatic electrons (both trapped and passing) as well as electromagnetic effects. In addition, many of them may be run in general tokamak

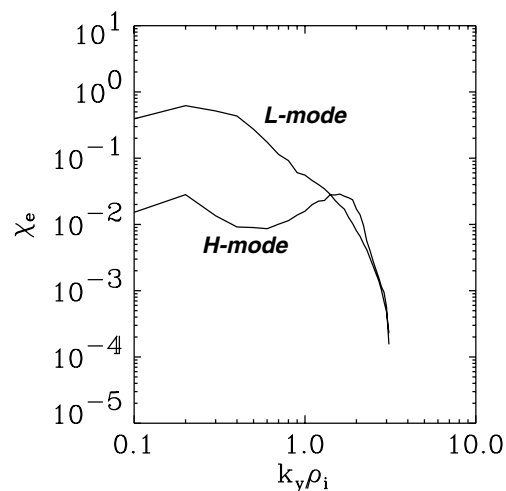


Figure 8. Gyro-kinetic simulations of tokamak edge turbulence without (‘L-mode’) and with (‘H-mode’) imposed $\vec{E} \times \vec{B}$ shear flows: the superposition principle for the electron heat diffusivity is violated, and ETG turbulence provides a floor in H-mode. Reprinted with permission from [140].

geometry, taking flux surface shaping into account. Instead of getting the required geometrical information from MHD equilibrium codes, one can also use a local solution of the Grad–Shafranov equation, which generalizes the well-known $\hat{s} - \alpha$ model to finite aspect ratio, elongation and triangularity [141]. Both PIC and Vlasov flux tube and full torus gyro-kinetic codes have been developed and complement one another very nicely (see table 1). To uncover systematic errors and numerical artefacts in models or codes, it will be vital to maintain a healthy variety of turbulence codes. This allows for cross-checking, which will help to reach a consensus on important issues and to build confidence in the results obtained.

There is much literature on comparisons between linear or quasi-linear theory and experiments. This approach, although limited, has proven to be very useful. For example, one can determine the expected presence or absence of certain micro-instabilities, critical gradients, linear growth rates (which can then be compared with measured $\vec{E} \times \vec{B}$ shearing rates), mixing length or quasi-linear estimates of transport coefficients and general trends as the plasma parameters are changed. However, there are many examples of situations in which (quasi-)linear theory is known to be misleading or even wrong. For example, it is well established that drift waves in a sheared slab geometry—although linearly stable—are non-linearly unstable [142]. Moreover, electron thermal transport induced by ETG modes can exceed quasi-linear estimates by more than an order of magnitude [47, 135]. And ITG

turbulence is often controlled or even completely suppressed by zonal flows, again an inherently non-linear effect [110,111]. To enhance our understanding of transport in fusion plasmas and to establish a more firm predictive capability, we must therefore continue to perform and analyse non-linear gyro-kinetic (and fluid) simulations.

First *quantitative* comparisons of turbulence simulations with experimental data have been published in the last few years. Gyro-fluid simulations [121] for plasma parameters from a particular L-mode discharge on the DIII-D tokamak yielded ion and electron thermal fluxes that were within a factor of two of the experimental results. On the other hand, the particle flux was too small, and the density fluctuation level was 4–5 times too large. Nevertheless, the wavenumber spectra of the density fluctuations showed good qualitative agreement. Only ions and trapped electrons were retained in these flux-tube simulations. Finite β and finite ρ_* effects were neglected, including equilibrium $\vec{E} \times \vec{B}$ shear, which was taken into account only as an *a posteriori* correction. Unfortunately, repeating these computations with a more comprehensive gyro-kinetic flux-tube code did not reconcile simulation and experiment [121]. The density fluctuation level and heat fluxes were still too large by about a factor of 3.

By means of Vlasov simulations including (1) gyro-kinetic ions and drift-kinetic electrons (keeping trapped and passing populations in both cases), (2) electron pitch-angle scattering, (3) finite β effects, (4) shaped equilibria and (5) finite ρ_* effects (in particular, equilibrium $\vec{E} \times \vec{B}$ shear), the measured thermal diffusivities in a DIII-D discharge could be matched by changing the nominal value of R/L_{T_i} within the experimental error bars [32]. The associated particle transport was not compared. Neither were fluctuation levels or wavenumber spectra. So although this is a very encouraging result, it will be crucial in future work to try to recover simultaneously as many turbulent features as possible. Such an approach will help to narrow the window of uncertainty even though the error bars on individual plasma parameters may be rather large. The long-term goal must be to reproduce all transport-relevant aspects in a variety of discharges, thus increasing our insight into the basic turbulent processes and enhancing our capability to predict the performance of future devices such as ITER.

2.2.4. Conclusions. As is shown in this brief survey, non-linear computations of plasma turbulence are becoming more and more comprehensive and mature, allowing for serious comparisons with experimental data (see figure 9). In the 1990s, the focus of most work in this area was on ITG turbulence with adiabatic electrons, leading to significant progress in our understanding of the anomalous ion heat flux observed in the experiments. Starting around the year 2000, the adiabaticity constraint was transcended in various ways, allowing for investigations of the origin of electron heat and particle fluxes, as well as the role of electromagnetic effects. Despite significant progress over the last few years, these topics will continue to challenge both theory and simulations for the foreseeable future. There is a host of unsolved questions—both fundamental and practical—which still need to be addressed, including the role of electron-scale turbulence and non-local phenomena in various regimes, the non-linear coupling of ion-scale turbulence to both larger and smaller scales, the physics

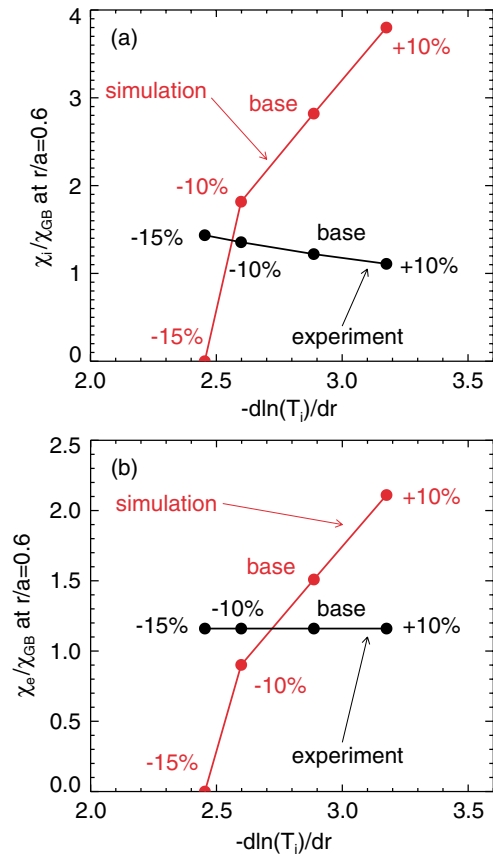


Figure 9. Ion and electron heat transport for a particular DIII-D discharge: the experimental values can be matched by the simulation if the normalized ion temperature gradient is varied within the error bars. Reprinted with permission from [32]. © 2003 American Physical Society.

of internal transport barriers, as well as many issues in the area of edge turbulence (not covered in this review). Some answers may hold surprises, possibly redirecting the way we think about turbulence and transport in fusion plasmas. Moreover, the complex issue of self-consistency between profile dynamics and turbulent transport will have to be tackled on the road to a predictive transport capability. This will force us to expand our view of turbulent dynamics, also taking into account processes traditionally treated in neighbouring sub-disciplines of fusion physics.

2.3. Turbulence measurements in tokamaks and comparison with theory/simulation

As often noted, the energy and particle confinement in tokamak experiments is generally not as good as predicted from transport calculations based on collisional processes alone, and the discrepancy is often attributed to transport arising from micro-instabilities driven unstable by various free energy sources. These micro-instabilities include ion temperature gradient driven modes (ITG: $k_{\perp}\rho_i \leq 0.5$), trapped electron modes (TEM: $k_{\perp}\rho_i \sim 0.2-1$) and electron temperature gradient driven modes (ETG: $k_{\perp}\rho_i \geq 2$) where k_{\perp} is the fluctuation wavenumber perpendicular to the magnetic field and ρ_i is the ion gyro-radius. In order to better understand the physics associated with these losses,

research at various tokamak facilities has been directed at detailed comparisons between turbulence measurements and turbulence theory/simulations. The goals of such comparisons are to improve the understanding of turbulence and transport, to test and provide feedback to theory and to obtain the ability to predict more confidently the operation of ITER. Such a predictive ability would potentially also allow us to extend the operating regimes of present-day machines, which would provide a stronger baseline for planning the ITER experimental program. Observations and simulations of low frequency, long wavelength fluctuations are consistent with the picture of these instabilities driving ion thermal and particle transport as well as some or all of the electron thermal transport [28, 143]. However, detailed validation of the simulations is still in progress. The physical complexity of a three-dimensional tokamak plasma, combined with many free energy sources and associated possible instabilities, has made the construction of complete simulation models difficult—the required computational times alone place restrictions on the work. These difficulties, combined with the complexities measuring relevant quantities measurements (e.g. we would like to measure turbulence-induced transport but often the best we can do is measure the fluctuating density \tilde{n}), make code validation a time and resource consuming effort.

In this sub-section the more recent comparisons between tokamak experimental measurements and theory/simulation are reviewed. The scope of this review is restricted to direct or nearly direct comparisons. Regrettably, this limitation eliminates a great deal of work—both experimental and theoretical—that does not include such direct comparisons. First are presented comparisons of general turbulence behaviour, followed by comparisons of high- k and magnetic turbulence and finally a section on experimental-theory comparisons in improved confinement regimes. Physics topics include measurement-simulation comparison relevant to low through high wavenumber turbulence (e.g. ion temperature gradient turbulence, trapped electron mode turbulence, etc), impurity enhanced confinement and core and edge transport barriers, including both density and temperature fluctuations and turbulence-induced fluxes. These fluxes and their dependence upon fluctuation level are generally inferred (except at the far edge where Langmuir probes can penetrate) from the correlation between power balance transport calculations and simultaneous turbulence measurements. Herein it is sought to convey a description of the measured quantities, the corresponding simulations or theory and the conclusions from the work.

2.3.1. General turbulence features. General features of plasma turbulence include fluctuation levels, fluctuation wavenumber and frequency spectra and correlation lengths—quantities that characterize the turbulent state of the plasma. Appropriate calculations for direct comparison with experimental measurements include the correct spatial, wavenumber and frequency ranges of the diagnostic. Additionally, similar or equivalent analysis techniques (e.g. Fourier transforms, time averages) must be used. While it is possible to obtain reasonable agreement of a single feature (e.g. spectral shape or correlation length), it is the total of such comparisons, e.g. agreement over a large radial region and

plasma parameter space of multiple turbulence features, that provide confidence in the validity of a given theory/simulation. The general comparisons in this section are generally the most advanced. Nevertheless, much work remains before a set of validated turbulence simulation codes is available. For example, note that Ohmic and L-mode plasmas have been the focus of many of the comparisons, while our ultimate goal is to understand turbulence well enough to exploit enhanced confinement regimes more effectively.

One of the most basic and straightforward measurements to compare is the magnitude and frequency distribution (i.e. frequency power spectra) of the density fluctuations. Measurements of the density fluctuation power spectra from reflectometry were compared with results from the DALFTI Landau-fluid model on ASDEX Upgrade [144]. The DALFTI model accounts for drift (Alfvén) wave, slab and toroidal ITG modes, as well as ideal and resistive interchange/ballooning modes [145]. The frequency spectra of the density fluctuations from several locations in the region $\rho = 0.85\text{--}0.95$ (where ρ is roughly equivalent to the radial location r/a) were found to compare favourably with the DALFTI results. The authors tentatively concluded that the DALFTI code with realistic flux-tube geometry appeared to reproduce the structure of the L-mode tokamak turbulence, although the fluctuation level might have been slightly underestimated.

A low frequency, low wavenumber density turbulence feature ($f < 400$ kHz, $k \sim 2$ cm⁻¹) was found to appear in the far infrared scattering signal on DIII-D as the line-averaged density was increased [146]. The appearance of this feature coincided with the saturation of the energy confinement time and was consistent with linear (GKS) [147] and non-linear (UCAN) [116] gyro-kinetic turbulence simulation codes. The GKS linear stability code predicted that at higher line-average density the ITG mode would emerge to be dominant over the TEM, which is consistent with both the appearance of the low frequency, low wavenumber feature and the change in the propagation direction of the density fluctuations from the electron diamagnetic to the ion diamagnetic direction (as measured in the lab frame). The radial variation and the magnitude of radial correlation lengths Δr from reflectometry were found to be similar to the trends predicted by ITG and electron drift wave estimates, as well as some meso-scale type correlation lengths [148]. In a study of dimensionally similar discharges, the radial variations of the heat diffusivities were found to scale between Bohm and gyro-Bohm consistent with GLF23 [20] transport simulations [149]. Experimental measurements of Δr in an L-mode plasma were compared with two UCAN simulations of the same plasma—one simulation with and a second simulation without zonal flows. The simulated values of Δr without zonal flows were very long, spanning much of the 65 cm minor radius, while the inclusion of zonal flows decreased the simulated Δr to near the measured values in both magnitude and radial behaviour.

More difficult to compare are the thermal transport levels. This is due to the fact that (with the exception of the far edge plasma which can be accessed by Langmuir probes) the transport must be inferred from a combination of measured temperature profiles, plasma species cross-coupling calculations and heating deposition estimates rather than from

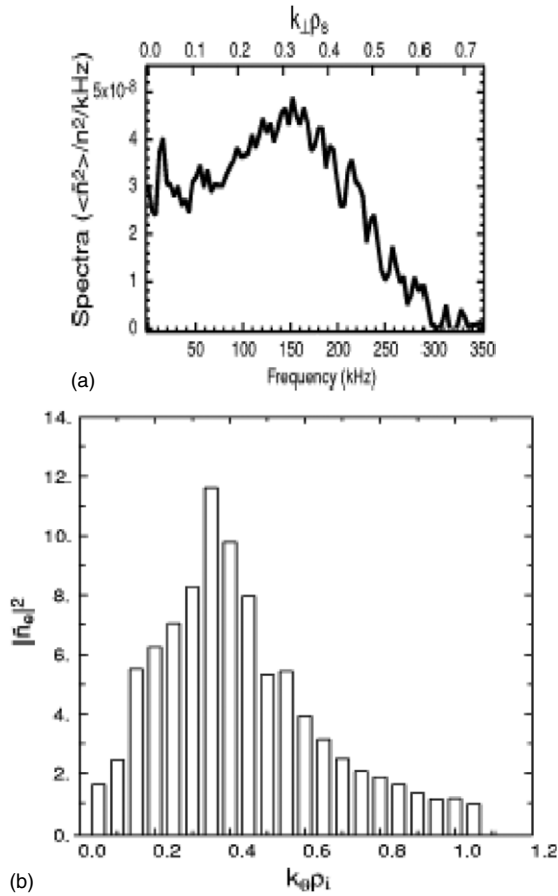


Figure 10. Wavenumber spectra from (a) BES measurements and (b) GRYFFIN simulation showing some similarity in shape. Reprinted with permission from [150]. © 2002 American Institute of Physics.

measurements of the turbulence-induced fluxes themselves. Thus, the comparison is at least one step removed from what one would ideally prefer. Such comparisons are nevertheless important and useful. For example, comparisons between DIII-D experiments and simulations by Ross *et al* [150] found that ion thermal transport simulated by the GRYFFIN code [21] was larger than the experimental value by a factor of 1.5–2.0, and the density fluctuation level was overestimated by a factor of ~ 4 with $(\tilde{n}/n)_{\text{exp}} \approx 0.4\%$, $(\tilde{n}/n)_{\text{Gryffin}} \approx 1.6\text{--}1.9\%$. Figure 10 [150] compares wavenumber spectra from the beam emission spectroscopy (BES) with the GRYFFIN simulation, showing similarity in the peak power location and the spread in wavenumber. A following study found that the energy fluxes obtained in GS2 [46] simulations were comparable to the GRYFFIN calculations and exceed the experiment by a factor of ~ 2 , while the simulated density fluctuation level (\tilde{n}/n) was closer to experiment, but still exceeded it by a factor of ~ 2 [150]. It should be noted that a recent re-evaluation of the BES data indicate an experimental (\tilde{n}/n) fluctuation level near 1% which brings the GS2 calculations of 1.3–1.5% into closer agreement [151].

As mentioned earlier, measurements of turbulence-induced fluxes are most easily achieved in the far edge plasma. These allow a direct comparison between the measured and the simulated flux value. Measurements of L-mode density fluctuation spectra and fluctuation induced particle flux from

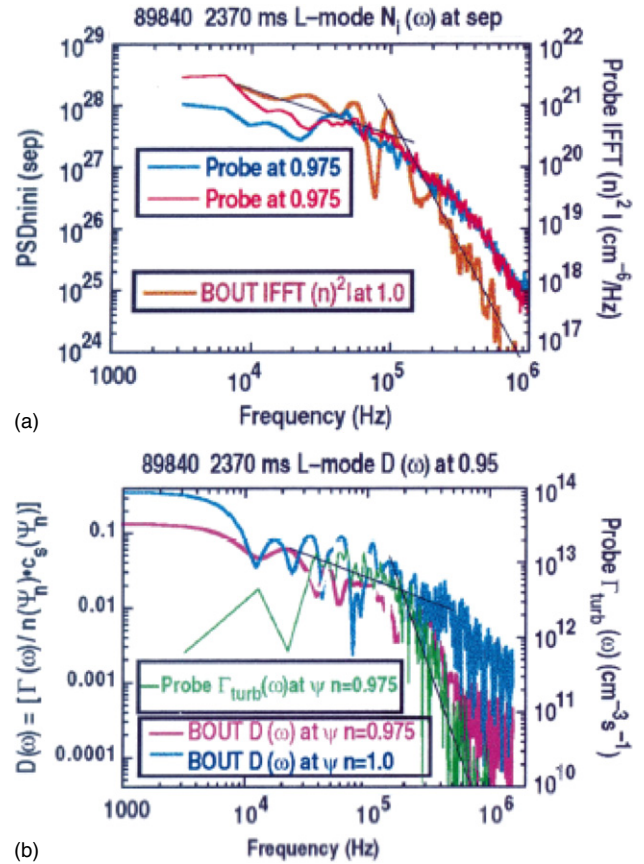


Figure 11. Comparison of power spectra of (a) density fluctuations and (b) particle flux from Langmuir probe data and BOUT L-mode simulations showing reasonable agreement between simulation and measurement. Reprinted with permission from [152].

Langmuir probes on DIII-D were compared with BOUT [19] simulations. Reasonable agreement in the shape and the spectral roll-off [152] was observed, as seen in figure 11. A two-scale falloff in the fluctuation spectrum was observed: f^{-1} scaling at low frequency and an f^{-4} scaling at higher frequency (≥ 200 kHz). The authors found that the spatial profile of the turbulence-generated diffusivity was in qualitative agreement with that required to produce pedestal profiles. Also, the turbulence-generated electric field profiles (as calculated by BOUT) across the separatrix were qualitatively consistent with those from H-mode experiments.

The density fluctuation behaviour as measured using reflectometry and Langmuir probes on T-10 was consistent with ITG and TEM in the core and with drift-resistive ballooning (DRB) mode instability in the edge [153]. Good agreement was found in the radial location where the core ITG and TEM growth rates dominate over the DRB as calculated using local turbulence models [154, 155] when compared with the spatial location where the experimental turbulence changed character. Density fluctuations measured by reflectometry were reported to possess long poloidal correlation lengths which were consistent with zonal flow activity. Finally, long radial correlation lengths with zero phase shift similar to ‘streamer’-like activity, were observed.

Comparison of different fluctuating fields (e.g. density and temperature) can also be used to test and validate theory and simulation. In this regard, high frequency charge-exchange

recombination spectroscopy (HF-CHERS) was utilized to measure simultaneously the carbon ion temperature and density fluctuations (\tilde{T}_i and \tilde{n}_C) on TFTR in order to provide a test of ITG theory [156]. Using BES measurements of the main ion density fluctuations \tilde{n}_i , it was found that the spectra of all three were similar across the radial range $r/a \sim 0.58$ – 0.99 . The ratio of relative fluctuation levels $(\tilde{T}_i/T_i)/(\tilde{n}_i/n_i)$ was ~ 2 , consistent with the general expectations of ITG theory, but it is also consistent with the effects of convective eddies on the fluctuations. Additionally, they found the results consistent with the ion temperature gradient being the free energy driving source in both the edge and core, while the damping terms might be different in the edge and core allowing different instabilities to dominate.

2.3.2. High wavenumber and magnetic turbulence.

The higher wavenumber range can be designated as the range $k_\perp \rho_i > 1$ and is typically thought to contain wavenumbers applicable to electron temperature gradient driven (ETG) modes, trapped electron (TEM) modes and high k ion temperature gradient driven (ITG) modes. Experimental measurements of high wavenumber turbulence and comparisons with theoretical predictions have been generally less common than lower wavenumber comparisons. Fortunately, this situation has recently begun to change with comparisons between measurements and theory in this wavenumber range becoming available. On the other hand, while measurement of internal magnetic fluctuations has undergone increased effort (e.g. see [157, 158]), to date there has been a lack of direct comparison with simulation. Nevertheless, this is an area of great importance as it directly addresses the knowledge and understanding of transport in regimes where transport due to other instabilities is thought to be low. Thus, there is a definite need to expand comparisons in this area. Below are presented comparisons between high k measurements and simulation, with some reference to magnetic turbulence from the Tore Supra results. The work from DIII-D reviewed below covers a range of wavenumbers, from high to low, but is included here (rather than in section 2.3.1) due to the high wavenumber results.

Density fluctuation measurements at higher wavenumbers (8.9 cm^{-1}) were performed on TFTR using micro-wave scattering and compared with local calculations of electron diffusivity and the current diffusive ballooning mode (CDBM) model [159]. The fluctuations were found to propagate in the ion diamagnetic drift direction in the plasma reference frame at about 8% of the ion diamagnetic drift frequency. The fluctuation amplitude (at 8.9 cm^{-1}) was seen to correlate well with local calculations of the electron diffusivity. The authors report that in these enhanced reversed shear plasmas (ERS) the global energy confinement time correlates with fluctuation amplitude, but only for fluctuations with wavenumbers greater than 5 cm^{-1} . The fluctuation frequency, wavelength and propagation direction of the 8.9 cm^{-1} data were found to agree qualitatively with CDBM theory [160]. The authors note that CDBM theory should be extended to the shorter wavelength regime before a quantitative comparison could be made.

A comparison between thermal transport in hot electron plasmas ($T_e > 2T_i$) and theoretical turbulence based transport predictions was carried out by Horton *et al* on Tore Supra [12].

They concluded that electromagnetic drift wave turbulence driven by electron temperature gradient modes provides an explanation of the measured confinement properties. They further found that this conclusion is consistent in broad terms with the measurement of internal magnetic fluctuations (measured using cross-polarization scattering) and their role in electron heat transport [157].

A new mm-wave backscatter technique was employed at DIII-D to probe wavenumbers in the range $k_\perp \rho_i \sim 2$ – 10 , which is applicable to ETG type modes [161]. The existence of short wavelength density turbulence was confirmed by utilizing several validity tests based on the physics of the scattering process. Additionally, multiple diagnostics were utilized to obtain density fluctuations measurements over a broad wavenumber range ($k \sim 1$ – 40 cm^{-1} or $k_\perp \rho_i \sim 0.2$ – 10). This diagnostic set included an FIR scattering system, the already mentioned mm-wave backscatter, beam emission spectroscopy system, fluctuation and correlation reflectometry and phase contrast imaging system. The data clearly indicated turbulence activity extending from low to high k with an observed trend of increasing frequency width with increasing wavenumber. Calculations using the GKS linear stability code showed that these discharges were unstable to a wide range of instabilities: ETG, ITG and TEM. It was found that the plasma was theoretically unstable over a broad range in wavenumber and spatial extent consistent with experimental observations. The predicted frequencies were smaller than those seen experimentally but were in qualitative agreement with the measured spectra.

2.3.3. Turbulence features in improved confinement regimes.

Here we consider improved confinement regimes as well as regimes leading to the L–H transition. In a multi-machine review paper, multiple tests of $\vec{E} \times \vec{B}$ velocity shear suppression of turbulence and turbulence-driven transport in both the edge and core of tokamak plasmas were summarized by Burrell [162]. Externally biased and naturally occurring H-modes, VH-modes, core negative and low magnetic shear plasmas from DIII-D, TEXTOR, CCT, TFTR, JT-60U, JFT-2M, TCV, TEXT were presented, but the review focused on tests of causality in DIII-D, TEXTOR and TFTR. The author concluded that the model of $\vec{E} \times \vec{B}$ velocity shear suppression of turbulence-induced transport has the universality needed to explain the observations for a wide range of plasma conditions in both the plasma edge and core. Furthermore, measured changes in the $\vec{E} \times \vec{B}$ shear coincident with measured changes in turbulence and turbulent transport were consistent with both qualitative and quantitative predictions of the model. Based upon the multiple causality tests covered in the paper, it was concluded that there was significant confidence that the basic model is correct.

Utilizing scanning Langmuir probes in the TEXTOR-94 tokamak, the variation of the plasma turbulence, the turbulence-induced particle flux and the density-potential cross-phase with externally induced $\vec{E} \times \vec{B}$ rotation was compared with several theoretical predictions [163]. Scaling of these quantities with local $\vec{E} \times \vec{B}$ shear flow was reported to be similar to theoretical predictions by [164, 165]. This similarity is shown in figure 12 [163], which shows reasonable agreement between measured values and the analytic predictions leading

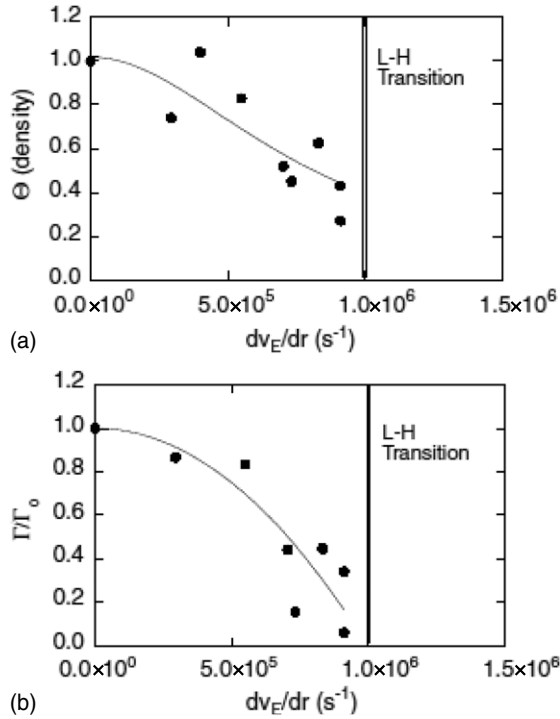


Figure 12. Scaling of (a) normalized density fluctuations comparing the Langmuir probe measurements and predictions of the Zhang–Mahajan theory [165] leading up to the L–H transition, and (b) normalized particle flux comparing the Langmuir probe measurements and predictions of the Ware–Terry theory [164] leading up to L–H transition. Reprinted with permission from [163].

to the L–H transition. Further, the authors found that the scaling of the cross-phase term with $\vec{E} \times \vec{B}$ shear was as strong as that found for the scaling of the turbulence, revealing that the cross-phase is an important component in the shear suppression of turbulent transport.

A study of micro-turbulence growth rates and flow shear induced turbulence suppression during JET high performance ITB plasmas was reported by Budny *et al* [166]. Comparison of linear growth rates from the GS2 code with $V_{E \times B}$ shearing rates found that the $V_{E \times B}$ shearing rate was comparable to the growth rate of the fastest growing toroidal mode number. This occurred where the ITB was formed and, importantly, tracked its subsequent outward movement. Measurements of density fluctuation levels—from a single reflectometry channel on the same discharge—showed a reduction in fluctuations outside the region where the ITB formed. Additionally, reflectometry data from a different discharge showed reduction in density fluctuations at wavelengths and frequencies in the ITG range in the region where the ITB was formed [167]. The authors of [166] conclude that the reduction of ion transport correlates with increases in the ratio of the $V_{E \times B}$ shearing rate relative to the ITG linear growth rate, $(\gamma_{E \times B}/\gamma_{ITG})$.

High performance ITB plasmas on DIII-D show a decrease in density turbulence, as measured by BES and FIR scattering, along with a decrease in thermal diffusivities consistent with the paradigm of $E \times B$ flow shear stabilization of turbulence [168]. Work on understanding the electron transport channel in ITB plasmas utilizing direct electron heating (either ECH or FW) resulted in increased ion and electron

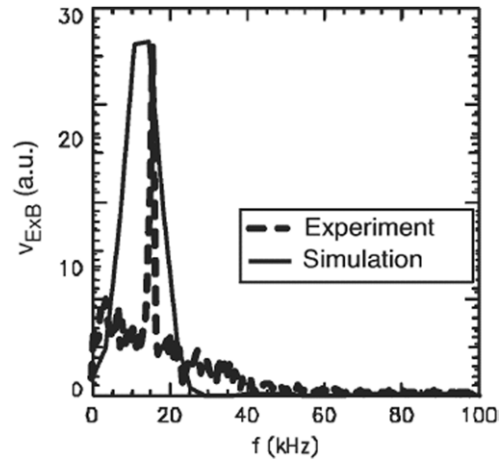


Figure 13. Comparison of a GAM $E \times B$ oscillation observed in a BOUT simulation of experimental discharge (109644) to the turbulence poloidal velocity spectrum derived from BES data. Reprinted with permission from [174]. © 2003 American Institute of Physics.

thermal diffusivities consistent with GKS calculations of destabilization of both long and short wavelength modes [169].

Impurity gas injection into negative central magnetic shear DIII-D discharges produced a reduction in density fluctuation levels (as measured by BES) as well as reduced transport levels [170]. This was in qualitative agreement with both linear GKS simulations that showed a reduction of linear growth rates as well as with non-linear UCAN simulation that showed a reduction of non-linear turbulence levels. GLF23 transport simulations indicated that while the growth rates of the low wavenumber fluctuations were reduced with neon injection, it was the $\vec{E} \times \vec{B}$ velocity shear suppression—resulting from improved angular momentum confinement and consequent higher rotation velocity—that was the dominant factor in the reduced turbulence and transport levels [171]. This suggests that a positive feedback mechanism exists between the fluctuations and momentum transport: increased rotation velocity increases the radial electric field and the $\vec{E} \times \vec{B}$ flow shear. Similar results were found when comparing impurity injection on DIII-D and JET [172].

Time-delay-estimation techniques applied to two-dimensional BES measurements of density fluctuations revealed a coherent oscillation in the poloidal flow field on DIII-D [173, 174] which was consistent with a high frequency branch of zonal flows identified as the geodesic acoustic mode (GAM) [70]. Turbulence simulations using the BOUT code [175] show an oscillation at the experimentally observed frequency consistent with the identification of the mode as a GAM. Figure 13 shows reasonable agreement between the experimental measurement and the BOUT code simulation.

The enhanced D_α H-mode (EDA H-mode) on Alcator C-Mod was found to be accompanied by a continuous, high frequency, quasi-coherent fluctuation (QC mode). This QC mode is believed to limit the impurity build-up during H-mode while allowing good energy confinement [176]. The authors report that measurements of this mode by various diagnostics (including phase contrast imaging) indicate reasonable agreement with BOUT simulations with respect to the mode structure, the fluctuation amplitude and the

frequency. Based upon this they have identified this quasi-coherent mode as the resistive X-point mode that is observed in the BOUT simulations. Measured poloidal correlation lengths and poloidal wavenumber spectra (from localized gas puff imaging techniques) and the time-averaged particle flux were found to agree within a factor of 2 with results from the NLET turbulence simulation code [177]. Similar agreement was found by the authors when comparing with the results of the BOUT turbulence simulation code. Based upon these observations and comparisons, the authors tentatively concluded that the turbulence in the edge of Alcator C-mod is due to the resistive ballooning instability.

2.3.4. Summary and conclusions. A range of experiment to theory/simulation comparisons has been conducted on various tokamaks. Far edge and scrape-off layer plasmas, as well as deep core plasmas, are being examined and compared with theory. Many different theories and simulations have been addressed using a variety of fluctuation diagnostics and techniques. The emerging picture is one of fairly good agreement between experiment and theory for various specific comparison points. These points include the predictions of ITG/TEM simulation and theory of turbulent correlation lengths, changes in confinement with impurity injection and gradient scale lengths and relative temperature/density fluctuation levels. The correlation (from a number of machines) of core turbulence reduction, confinement improvement and changes in the growth and damping rates of the various instabilities (ITG, TEM, ETG, etc) have improved confidence in these basic instability models. The identification of the unstable mode(s) in the edge of some machines, as well as zonal flow activity (GAMs), is encouraging. Finally, the evidence of $\vec{E} \times \vec{B}$ velocity shear suppression of turbulence and turbulent transport, and its detailed effect upon the fluctuation parameters, has provided confidence in the correctness of that model/paradigm. From the reviewed work it is apparent that these comparisons are only in their early stages. Considerable work remains before a set of validated turbulence simulation codes suitable for predictive purposes is available.

2.4. Neoclassical transport

The theoretical groundwork for neoclassical transport became well established in the 1970s for axisymmetric toroidal plasmas. Neoclassical theory describes the process by which particles, momentum and energy flow within and across the magnetic flux surfaces due to drifts and Coulomb collisions between plasma species. Two early reviews of the original work still serve today as primary references [178, 179]. Although the theoretical basis has been long established, many of the features of neoclassical theory and its limits are still undergoing validation. Advanced diagnostics, the attainment of experimental conditions with low collisionality and reduced turbulence and the incorporation of more rigorous models for the analysis of experimental data are facilitating this validation. In addition to reviewing the progress in evaluating neoclassical transport processes in the bulk plasma, we also address the extent to which neoclassical characteristics are observed in barriers (i.e. ion heat transport and bootstrap current), although barrier physics is discussed more extensively elsewhere in

this paper. Since the IPB [1] was published, (1) neoclassical ion thermal conductivity has been established as a firmer basis for transport when turbulence is suppressed, (2) initial measurements of the bootstrap current in the H-mode pedestal have, somewhat surprisingly, been found to agree with standard neoclassical expressions, (3) initial measurements of the relative toroidal rotation of different ion species appear to agree with neoclassical theory and (4) neoclassical ion temperature gradient screening of impurities has been observed, as discussed further in section 3.4. The issue of whether poloidal rotation is neoclassical is still open. The confirmation that neoclassical ion thermal conductivity is attainable under enhanced confinement conditions could have a very positive impact on ITER performance projections.

The transport of particles, energy, momentum and currents is all treated self-consistently in standard neoclassical theory—within the limitations of some ordering assumptions. One of the key assumptions is the ordering of scale lengths: drift orbit (banana) width is assumed small compared with the gradient scale lengths of density, the temperature and the radial electric field and small compared with the proximity to the magnetic axis or the plasma boundary. These and other assumptions (e.g. standard neoclassical theory does not include high plasma rotation or non-axisymmetric effects due to the presence of toroidal field ripple or magnetic islands) can be broken; they may have important implications for burning plasmas and therefore need to be evaluated. Neoclassical aspects of particle transport are described in section 3.4. Here we focus on other areas where significant new information on the validity of neoclassical transport has been obtained since the IPB report: ion thermal transport, bootstrap current, the relative toroidal rotation velocity of ion species for constructing the radial electric field and poloidal rotation. We also identify areas where theory is addressing limitations of the standard model, but because that literature is fairly extensive, we only cover the general issues here.

2.4.1. Ion thermal transport. Ion thermal transport appears to be governed by long wavelength turbulence under most plasma conditions as described in other sections of this chapter. However, the emphasis in recent years on attaining plasma conditions with suppressed turbulence has led to some conditions where the underlying neoclassical ion thermal transport might be tested.

The most notable reductions in long wavelength turbulence are in transport barrier regions—either at the plasma edge (ETBs) or internally (ITBs). In both ETBs and narrow ITBs, the ion banana width is comparable to the barrier width, which violates the ordering in standard neoclassical theory. Experimental evidence indicates that ion thermal conductivity is often comparable to the standard neoclassical value in ITBs [25]. Various theoretical extensions to standard neoclassical theory have been developed to examine the effects of large ion orbits in steep gradient regions and the effects of steep gradients on the orbits themselves. For example, ion orbit squeezing, which is the reduction of the banana width due to a gradient in the radial electric field [180], generally reduces the banana width to less than the gradient scale lengths and might explain a moderate reduction in ion thermal conduction

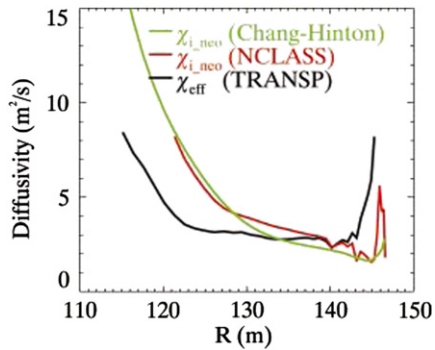


Figure 14. Single fluid thermal diffusivity in NSTX indicates a broad region in the core where the ion thermal conductivity may be less than the standard neoclassical value. The magnetic axis is located at ~ 103 cm, and the outer separatrix surface is at ~ 148 cm. Reprinted with permission from [182]. © 2003 American Institute of Physics.

in narrow ITBs. But incorporating the squeezing effect self-consistently with the profile of the radial electric field is only approximate because it requires incorporating non-local effects in the otherwise local assumptions of neoclassical theory. There have been several attempts to develop kinetic theories that relax or reverse the orbit size ordering, but usually in the extreme limit such that the gradient is much narrower than the orbit size. It is fair to conclude that neither the simplified orbit squeezing model nor other models have yet received sufficient experimental validation and acceptance to be used as reliable predictive models for the ion thermal transport in narrow ITBs. However, narrow ITBs generally are not considered attractive for high performance either in present plasmas or in future burning plasmas because of their limitations on MHD stability. Analysis of ion thermal transport in the edge pedestal is complicated by additional effects, such as the interaction with neutrals and ELM activity. Recent work on JT-60U has shown that the heat diffusivity between ELMs is reduced to the level of ion neoclassical transport in the ELMing pedestal region at low ν_* [181]. But increased ELM losses at low ν_* make it difficult to take advantage of the high confinement offered by the neoclassical transport. Nonetheless, this provides encouraging support for the use of standard neoclassical transport as a reasonable lower bound for the transport between ELMs in predictive simulations.

A greater interest lies in broad ITBs or other conditions where turbulence is reduced across most of the plasma. Such conditions have been observed in NSTX [182], where the low toroidal field and large trapped particle fraction also contribute to the expected dominance of neoclassical ion thermal conductivity. However, as shown in figure 14, transport analysis of some discharges indicates that the effective ion thermal conductivity is possibly even lower than neoclassical over the central half of the plasma. This has also been observed in conventional aspect ratio tokamaks over more limited regions. Uncertainties in the heating source and temperature measurements as well as modifications to standard neoclassical theory by the relatively large ion orbits, low aspect ratio and unbalanced neutral beam injection are still being investigated as possible sources of the difference.

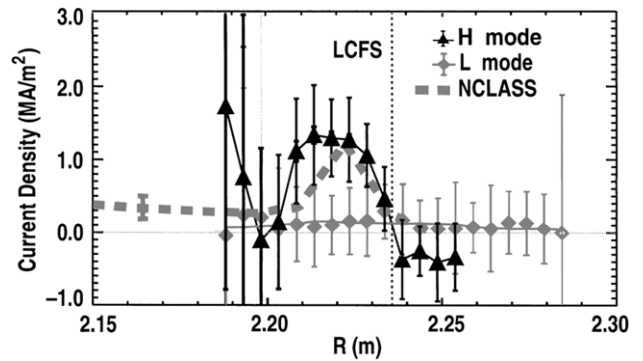


Figure 15. Calculation of edge current density from LIBEAM pitch-angle profile measurements for shot 115114 during the L-mode (grey) and late ELM-free H-mode (black) phase just before the collapse of the pedestal pressure, showing a large current peak in the pedestal region. Also shown for comparison is the toroidal current density calculated from a bootstrap constrained fit (dashed curve) for the H-mode phase. The last closed flux surface from EFIT on the LIBEAM trajectory is indicated by the dotted line. Reprinted with permission from [184]. © 2004 American Physical Society.

2.4.2. Bootstrap current in the edge pedestal and near the axis. The bootstrap current near the plasma boundary likely plays a crucial role in edge physics—through ELM dynamics, beta limits and access to second stability. Both dynamic [183] and static [184] analyses of the bootstrap current in the pedestal of DIII-D during a long ELM-free period following the L–H transition show agreement with standard neoclassical theory. Results of the static analysis by Thomas *et al* [184], which utilizes the high spatial resolution of the Li ion beam diagnostic, are shown in figure 15. It can be seen that the bootstrap current generates a local peak in the current density profile in the ETB region, while it is absent in the L-mode. The work of Wade *et al* [183] shows that the NCLASS [185] and Sauter *et al* [186, 187] models yield similar agreement in modelling the dynamic response, which exhibits a back-EMF in response to the sudden turn-on of the bootstrap current. (Although NCLASS and the Sauter models both incorporate full geometry effects, they have different additional strengths: NCLASS includes a more complete model for impurities, while the Sauter model has been fitted to kinetic calculations that use a more comprehensive model for the viscosity. Differences between them are generally less than $\sim 15\%$, which is comparable to the fundamental uncertainty in the basis theory.) The general agreement with standard neoclassical theory indicates that even though the ion orbit size is comparable to the barrier width, the standard neoclassical model produces reasonable bootstrap current results. This may be due to the fact that the electron banana orbit widths still satisfy neoclassical assumptions, while the corresponding assumption on ion orbits is only marginally broken and both contribute to the bootstrap current.

The bootstrap current vanishes at the magnetic axis in standard neoclassical theory because the trapped particle fraction vanishes under the usual ordering, but this may also be modified by finite orbits [188]. The presence of a finite bootstrap current and/or stability of a region near the axis with a very low current density (‘current hole’), as observed in some experiments [189, 190], could reduce the need for a seed current. The interesting phenomena of current holes are

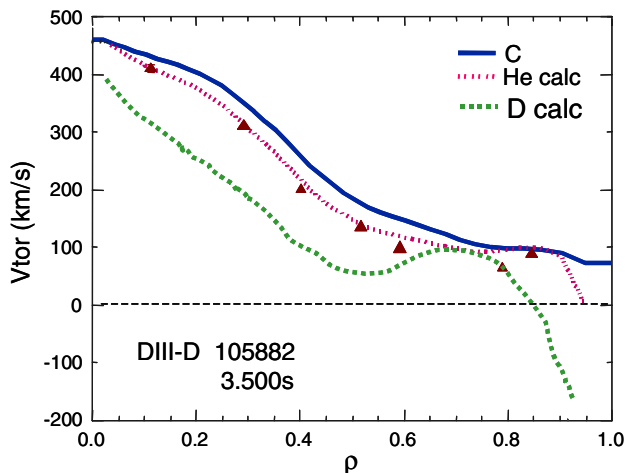


Figure 16. Profiles of the calculated helium (red dots) and deuterium (green dashes) toroidal rotation velocities compared with the measured helium (red triangles) and carbon (solid blue) toroidal rotation profiles. Errors in the measured C and He velocities are smaller than the difference between them. Reprinted with permission from [191]. © 2004 American Institute of Physics.

discussed further in section 3.7. But here again, self-consistent validated models for the current, equilibrium and stability do not yet exist for such extreme conditions.

2.4.3. Relative toroidal rotation of ion species. The relative toroidal rotation of ion species has long expected to be governed by the strong parallel friction of neoclassical theory. Recent simultaneous measurements of the toroidal rotation of two species on DIII-D [191] have confirmed the neoclassical model, as shown in figure 16. Although these observations were made under conditions where the neoclassical impurity poloidal rotation is negligible, they provide a firmer basis for reconstructing the radial electric field and the shear damping from impurity rotation measurements. Further refinements in the measurements and their interpretations are still needed, particularly in regard to the impact of poloidal rotation, which is discussed next. The bulk toroidal rotation, however, is not explained by standard neoclassical theory and can be significant even in Ohmic and RF discharges as discussed in section 3.5. However, extensions to neoclassical theory that incorporate the symmetry breaking around magnetic islands may contribute to the toroidal damping along with radial transport driven by turbulence.

2.4.4. Poloidal rotation. Poloidal rotation in the bulk plasma, under quasi-static conditions, is often assumed to be governed by neoclassical theory because of the strong poloidal damping provided by the neoclassical viscosity. This has been confirmed in collisional Ohmic plasmas [192]. Modelling of the collisional plasma edge (Pfirsch–Schlüter regime) in ASDEX Upgrade [193, 194] also indicates that the radial electric field is of the order of the neoclassical field, which implies that any anomalous poloidal rotation contribution is small. Furthermore, its dependence on the local ion temperature, the density, the poloidal and toroidal magnetic fields and the average toroidal rotation is similar to

the neoclassical electric field. The neoclassical model also explains the reduction in rotational shear for reversed magnetic fields, which leads to an increase in the L–H transition power threshold.

However, some measurements in the core of low collisionality plasmas appear to show much stronger impurity poloidal rotation than can be explained by standard neoclassical theory [195], but these measurements are still undergoing validation. Charge-exchange recombination spectroscopy is the primary method used to measure poloidal rotation in the core, and it is unfortunately restricted to species with $Z > 1$. This means that the poloidal rotation of main hydrogenic ions, which are expected to have much larger poloidal rotation because of their higher pressure gradients, cannot be measured directly. Experiments with helium plasmas may help resolve the poloidal rotation issue for main ions. In parallel with the improvements in diagnostics and analysis, theoretical models for the effects of strong auxiliary heating are being developed to evaluate their effect on poloidal rotation.

Spikes in the poloidal rotation velocity associated with bifurcations (not under quasi-static conditions, e.g. see [196]) are not explained by standard neoclassical theory, which is only applicable for time scales longer than the ion–ion collision timescale. The TFTR observations of a spike in the poloidal rotation during the formation of ITBs in TFTR [196] may be an illustration of ambipolarity breaking by loss of ripple-trapped fast ions from neutral beam injection followed by relaxation to a new state as the poloidal rotation is damped to the new state [197], which is analogous to the ion orbit loss model for ETB formation [198].

2.4.5. Conclusions. Significant progress has been made in validating several aspects of standard neoclassical transport: (1) neoclassical ion thermal transport is a reasonable lower limit when turbulence is suppressed, even in barriers, (2) the bootstrap current appears to be reasonably valid in the pedestal according to initial measurements and analysis, (3) the relative toroidal rotation of ion species obeys neoclassical theory and can be used to construct the radial electric field and (4) the poloidal rotation in the collisional regime appears to be neoclassical. All these observations strengthen our ability to model ITER performance. Unresolved issues, all of which are likely to have only a small impact on ITER projections, include (1) ion thermal transport near the axis of reversed shear plasmas where large ion orbits exist, (2) the bootstrap current near the axis of reversed shear plasmas and (3) poloidal rotation in low collisionality plasmas with strong auxiliary heating. However, if poloidal rotation can be generated which is much greater than expected from neoclassical theory in the absence of torques (e.g. from turbulence) it could affect the radial electric field, the $\vec{E} \times \vec{B}$ shear damping and the overall confinement. More accurate diagnostics for measuring the poloidal rotation are beginning operation and are expected to clarify the issue.

2.5. Summary of issues

With regard to understanding fundamental transport processes several important new trends and results can be identified since the publication of the IPB. (1) Ion thermal transport

is believed to be reasonably understood in terms of the dynamics of multiple-scale (wavenumber range and spatial distribution) turbulence, but predominantly long wavelength, ITG-type turbulence, interacting with self-driven zonal flows and driven $\vec{E} \times \vec{B}$ flows, and also depending on other factors such as magnetic shear and plasma shaping. However, electron thermal transport is not as well understood. A major open question for electron transport is whether short-scale-type, ETG or TEM, turbulence can generate sufficiently large transport to account for experimentally observed transport rates. In particular, whether the radially extended structures ('streamers') observed in some simulations exist and can account for observed electron transport rates is still unresolved. (2) Coupling between theory, numerical simulations, transport modelling and experiment has dramatically increased. Gyrokinetic turbulence simulation codes have been used to directly investigate transport properties of tokamak plasmas, as well as to benchmark the leading theory-based transport models. Both simulations (limited) and modelling (more extensively) make quantitative transport predictions and are now routinely used to compare and interpret experiments, while theories of turbulence regulation and suppression now inform all areas of work on improved confinement and transport. (3) Confidence that the current 'standard model' of turbulence (as already described) is generally correct has been substantially increased by direct, quantitative comparison of turbulence measurements with simulations, e.g. zonal flow/GAM features have now been directly observed in plasma turbulence measurements, etc. (4) There has been a resurgence of interest in neoclassical transport theory and in refining neoclassical predictions, based on the now widespread ability to obtain neoclassical levels of ion thermal transport. Overall, this progress in fundamental theory, non-linear simulations, and validation of turbulence models has substantially enhanced the ability to predict transport, particularly ion transport, on ITER and increased confidence in these predictions.

However, many issues still remain; other important issues not already mentioned include the extent to which recent areas of theoretical emphasis, such as turbulence spreading, intermittency and statistical descriptions, will prove necessary in describing tokamak transport processes. With regard to numerical simulations, the trade-offs between different numerical implementations with regard to computational efficiency, numerical noise and adherence to conservation laws are currently an area of active investigation. Most importantly, there is still no conclusion as to whether short wavelength modes (ETG, TEM) and cross-scale coupling can explain anomalous electron thermal (heat) and particle transport, especially in the presence of reduced or neoclassical ion transport. Also, while zonal flow and GAM turbulence features have now been observed on multiple devices, it has not yet been shown that these features have either the ubiquity or importance in controlling transport predicted by theory.

3. Core transport

The purpose of this section is to provide a description of both the current level of understanding and the outstanding issues with regard to core transport in tokamak plasmas. To this end, the section is structured into subsections as

follows: section 3.1 provides an introduction to the need for and benefits from reduced core transport in burning plasmas such as ITER, as well as an overview of the physical basis for obtaining such improved core confinement regimes. This is followed by four sections (3.2–3.5), detailing both experimental and modelling progress in understanding core ion and electron thermal, particle and impurity and momentum transport, respectively. Dimensionless parameter scaling experiments provide an important additional technique for transport understanding and projection—progress in this area is described in section 3.6. This is followed by section 3.7, which provides a summary of the transport properties of the improved core confinement regimes on current devices that are relevant to advanced operation on ITER, organized by differences in the q profile. Finally, section 3.8 provides a summary and a list of outstanding issues. The material in this section reflects the current focus of core transport research, which lies in understanding the physical processes governing the triggering and dynamics of regimes with reduced turbulent transport. Reduced transport has been achieved in all four transport channels (ion and electron thermal, particle and momentum transport channels), sometimes simultaneously. Rapid progress has also been made in improving the accuracy and physics capabilities of transport models, such that experimental and modelling results are integrated in the descriptions, rather than treated separately.

3.1. Enhanced core confinement regimes

Since the publication of the ITER Physics Basis (IPB) document [1], the focus of attention in transport studies has transitioned from conventional ELMy H-mode operation (the base or reference scenario in the IPB) to more 'advanced' modes of plasma operation with reduced core turbulent transport and enhanced confinement. As described in subsequent subsections, internal transport barriers and other forms of reduced core transport are now routinely obtained in all the leading tokamak devices [24, 25]. Rapid worldwide progress in the development of enhanced confinement modes of operation has contributed to an increased emphasis on developing both 'hybrid' and steady-state operation modes for ITER, as described in detail in chapter 6 of this issue [199]. Given this new focus on improved core transport, it is appropriate to begin this section with a consideration of the need for and benefits of, enhanced confinement, as well as an overview of the achieved improved transport regimes and the physical mechanisms responsible for the transport improvement.

3.1.1. Need for and benefits of improved confinement and transport control. Optimizing the tokamak as an energy producing system involves the simultaneous consideration of the following features: (1) high fusion power density, $\propto \beta^2$, (2) high fusion gain, $Q \propto \beta\tau$ and (3) high bootstrap fraction, $f_{BS} \propto q^2\beta$. From this, it can be seen that a simultaneous optimization of plasma confinement, a beta and current profile is required in order to optimize overall tokamak burning plasma performance. Commonly used figures of merit to evaluate success in this optimization include $\beta_N H_{L89}$, which combines the stability and confinement figures of merit, and a machine

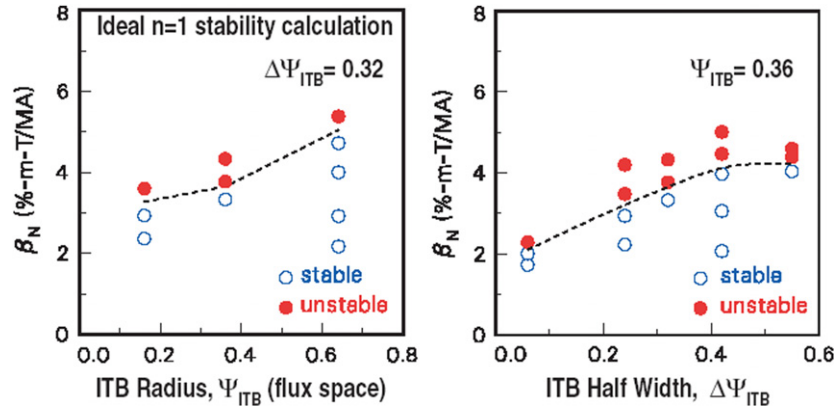


Figure 17. Ideal $n = 1$ stability calculations, using DIII-D parameters, indicate that the maximum achievable β_N (and hence plasma performance) increases with ITB radius, (a), and width, (b) [201].

size independent fusion gain parameter, $G \equiv (\beta_N H_{L89})/q_{95}^2$ (see section 6.2), where $H_{L89} \equiv \tau/\tau_{ITER-89P}$ and $\tau_{ITER-89P}$ is a confinement scaling expression for L-mode plasmas [1]. To provide some quantitative context, conventional ELMy H-mode discharges have $\beta_N H_{L89} \sim 4\text{--}5$ with $f_{BS} \sim 30\text{--}40\%$, hybrid scenario discharges have achieved $\beta_N H_{L89} \sim 7$ with $f_{BS} \sim 50\%$, while target conditions that would enable steady-state tokamak operation are $\beta_N H_{L89} \geq 10$, with $f_{BS} \geq 70\%$. Specific use of reduced transport/improved confinement include (1) for fixed Q , reduced machine size and/or maximum B_t , hence reduced machine cost, (2) for fixed machine size and plasma current, I_p , increased Q , and (3) for fixed machine size and Q , reduced I_p . This last option forms the basis of much of the hybrid and steady-state scenario development for ITER and is highly attractive as reduced current operation leads to both longer discharge pulse lengths and more reduced machine disruption loadings (see chapter 6 of this issue [199]).

It is important to realize that the desired goal is transport optimization and control, rather than confinement maximization per se. The benefits of an ability to modify and control core transport are multifold and include the following:

1. facilitation of ITB formation and of achieving enhanced confinement regimes,
2. optimization of confinement while avoiding stability limits,
3. generation of non-stiff core profiles breaks the link between core profiles and pedestal values that exists with stiff profiles; with stiff core profiles, performance is strongly governed by the achieved pedestal temperatures,
4. local transport control is the only possibility for controlling pressure and bootstrap current profiles in self-sustained magnetic plasma configurations and
5. transport control is required in order to vary the relative transport in different channels, e.g. in order to prevent preferential high- Z impurity accumulation.

These issues are now briefly introduced, using the same numbering as in the list above. (1) Core transport control tools such as $\vec{E} \times \vec{B}$ shear flow and magnetic shear modification (via current profile modification) are actively used to favour the creation of ITBs and reduced transport modes [24, 25]. Use of such techniques is envisaged to aid in obtaining the initial increase in Q in a reactor so as to enter a burning

plasma state. (2) Optimization of core profiles, e.g. ITB radius and strength, is required in order to maximize plasma confinement while avoiding stability limits. Too low a local transport coefficient, as can occur with some ITBs, leads to pressure gradients that are too steep, thereby lowering MHD stability margins. Modelling predicts that increased fusion performance, stability limits and well-aligned bootstrap current fraction are all simultaneously favoured by having moderate profile gradients (weak ITBs) at large plasma radius [200]. An example of such modelling, for DIII-D, is shown in figure 17, indicating that the maximum achievable β_N (and hence plasma performance) increases with the ITB radius and the width [201]. Experimental data support this picture; multi-machine data for high performance regimes show a clear correlation between maximum achievable β_N and pressure peaking [202, 203]. (3) In regimes, with ‘stiff’ plasma profiles, both core profiles and global confinement are determined by the edge pedestal values (see section 4 of this chapter for more details). Thus, in a burning plasma with stiff profiles, Q will be determined by edge pedestal temperature values (see section 5.5 of this chapter), high values of which are both difficult to achieve and are a challenge for divertor operation. In contrast, regimes with non-stiff core profiles, e.g. ITBs, allow global confinement to vary independently of pedestal temperatures, reducing the required pedestal values for a given Q . (4) As advanced tokamak research progresses and bootstrap current fractions increasingly dominate the total plasma current, the pressure profile, which is determined by plasma transport, will determine the current profile, which in turn couples back on the plasma transport and stability properties, i.e. advanced tokamak plasmas will be a highly coupled, self-organized non-linear system. A schematic illustration of multiple non-linear feedback mechanisms and couplings that can influence tokamak transport is given in figure 18 [204]. Local transport control is the only possibility for controlling pressure and bootstrap current profiles in such self-sustained magnetic plasma configurations. (5) Transport control is needed to vary the relative transport in different channels or of particular particle species. For example, highly peaked density profiles and transport barriers can combine to generate an undesirable central accumulation of high- Z impurities in JET [205], ASDEX Upgrade [206], DIII-D [207] and JT-60U [208]. As described in section 3.4, techniques

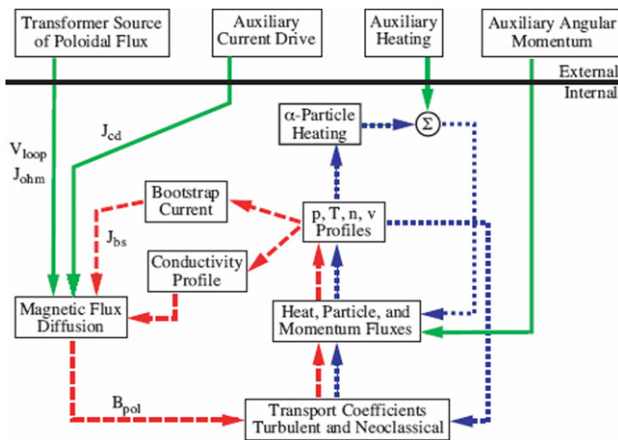


Figure 18. Illustration of the many non-linear feedback loops and couplings which govern tokamak transport. Reprinted with permission from [204].

such as central RF heating and real-time ITB control have been successfully used on several devices to preferentially flatten the density profile and reduce or eliminate such impurity accumulation [206–208].

3.1.2. Physics basis for improved core confinement regimes.

It was appreciated in the last decade that a physics basis for core transport should be able to account for the wide range of transport regimes that have been identified. Indeed, the dialogue in the community is shifting from one wherein plasma conditions are labelled as a separate regime to one in which a common physics basis is invoked to explain different plasma characteristics. A successful physics basis ultimately must have at its heart a description of a long wavelength turbulence set by the scale size of the ion gyro-radius and the means for moderating or eliminating it and quite possibly a shorter wavelength turbulence set by the scale size of the electron gyro-radius and any means for influencing this as well.

The richness of confinement characteristics observed in today’s tokamak experiments is quite remarkable and cannot be simply described as a linear function of global confinement quality. For example, all tokamak devices have access to L-mode confinement, which is typically characterized by ion-scale turbulence. Many have access to neoclassical transport in the ion channel and the means to achieve this vary. Reversal of the magnetic shear profile is found to facilitate entry to enhanced ion confinement regimes, but shear reversal is also found to be neither a necessary nor a sufficient condition for this entry.

The wide variety of dynamics observed helps fuel the strong desire to identify a unifying physics picture. Such variety includes the following. With reverse shear, the entry to enhanced confinement in the ion channel has been found to be continuous and slow compared with an energy confinement time, e.g. DIII-D negative central shear (NCS) plasmas and strongly co-rotating TFTR reverse shear (RS) plasmas [209]. This continuous character was also found on TFTR with monotonic q profiles, with reductions in ion thermal transport being found as the density profiles peaked in going from the L-mode to the supershot regimes [209]. Similar results have been obtained in power scans on JT-60U with

reversed and positive magnetic shear [210]. However, with reverse magnetic shear, some sudden transitions to enhanced confinement are observed that recall the dynamics of H-modes transitions, e.g. TFTR enhanced reverse shear (ERS) plasmas [196]. The analogue to the H-mode extends deeper than this bifurcating quality and extends to the observation of the formation of sheared flow layers preceding the bifurcation in some cases, as in TFTR [196], and for some H-modes in DIII-D [162]. While a consensus view regarding the physics underlying this shear layer formation is not in hand at this time, some speculation points to the possibility of transient turbulence-induced Reynolds stress-driven flows that decay after the bifurcation event.

As already mentioned, $\vec{E} \times \vec{B}$ flow shear is believed to be an element responsible for a wide range of plasma dynamics observed in many of these experiments. Indeed, driven flows and the accompanying variations in $\vec{E} \times \vec{B}$ flow shear have been found to have a profound impact on transport barrier dynamics and even their existence. For example, variations of the $\vec{E} \times \vec{B}$ flow shear with constant heating power on TFTR yielded reverse shear plasmas that spanned the confinement spectrum in a single discharge [211]. Such a discharge began with a bifurcation induced by poloidal flows to initiate the entry into the ERS state. Strong co-rotation yielded a reduction in the $\vec{E} \times \vec{B}$ flow shear that had been dominated by the plasma pressure, yielding a subsequent collapse of this confinement state to the L-mode state. This was followed by another increase in the $\vec{E} \times \vec{B}$ flow shear that was dominated by rotation and the (re)obtaining of neoclassical ion thermal transport rates. JT-60U has observed differing characteristics of the internal transport barrier characteristics, including variations between ‘box-type’ and ‘peaked’ temperature profiles that are correlated with the flow induced by various admixtures of co- and counter-injecting neutral beams [212].

In addition to magnetic shear and flow shear effects, impurity seeding in TEXTOR [213], DIII-D [171, 214] and JET [215] has been found to induce reduced ion thermal transport in some cases. Turbulence measurements have been compared with theory calculations for DIII-D and indicate that the impurity content can influence the linear stability of the long wavelength modes [170, 171, 214].

The range of electron thermal transport characteristics observed is even harder to characterize than ion thermal transport reductions. What is true is that reductions in electron thermal transport do not always accompany reductions in ion thermal transport. Also, strong electron heating has generally been found to be accompanied by electron thermal transport reductions in reverse shear plasmas (see references in [24, 25]), even in cases where the ion channel is unaffected. Understanding the cause of electron thermal transport and the variety of observations regarding its reduction remains an outstanding theoretical and experimental challenge. For a burning plasma the question is critical, as alpha heating will be predominantly in the electron thermal channel.

The leading picture that has the most promise for capturing the range of dynamics observed includes the following characteristics.

1. Turbulence suppression mechanisms are the key to obtaining reduced transport and transport control. Using linear theory, turbulence is expected to be suppressed

if the turbulence shearing rate $\omega_{E \times B}$ exceeds the maximum linear growth rate γ_{\max} of the dominant unstable mode [20, 27]. However, the various turbulence stabilization mechanisms differ with regard to the turbulence wavelength they affect, such that obtaining reduced transport is not equally possible with all suppression mechanisms (see section 2.1.2).

2. Shear in the $\vec{E} \times \vec{B}$ flow velocity likely plays a role in governing ion dynamics in many core enhanced confinement regimes. The multiplicity of feedback loops and accompanying dynamics, including variations in time scales, is qualitatively captured by this model [24, 25, 162, 216]. Sheared $E \times B$ flows affect mainly long wavelength (low- k) turbulence and as such can govern ITG-type fluctuations that are believed to control transport in the ion thermal and angular momentum channels. However, shorter wavelength (medium- and high- k) turbulence is not expected to respond to the $\vec{E} \times \vec{B}$ shear due to smaller spatial scales and larger growth rates. Quantitative modelling of profile evolution in the presence of $\vec{E} \times \vec{B}$ shear effects on turbulence is still in its early stages but has managed to replicate key experimental observations (see section 3.2). Today's plasmas, with their wide range of dynamics, provide the opportunity for developing such models and for assessing the value of flow shear control tools that may be used for controlling the turbulence and thus the pressure and bootstrap current profiles.
3. Magnetic shear reversal and/or α -stabilization/Shafraanov shift also often play a key role in facilitating entry into enhanced confinement. Theoretically, negative (reversed) or low magnetic shear, \hat{s} , and high α both act to reduce turbulence growth rates [20], thus facilitating turbulence reduction. In addition, reversed magnetic shear can also enable access to second stable core pressure gradients [217]. However, a key difference, when compared with the $\vec{E} \times \vec{B}$ shear, that affects only low- k turbulence, is that both these mechanisms can affect a wide range of turbulence wavenumbers, i.e. high- k as well as low- k . As such, these mechanisms can affect both electron and particle transports, which are thought to be governed by high- k ETG- and medium- k TEM-type turbulence. In accordance with this picture, these mechanisms appear to play a key role in the experimental generation of states of reduced electron transport [24, 25]. In general, the interplay between magnetic shear and flow shear effects has been identified as an essential component in ITB formation [216, 218].
4. Impurity seeding is now understood to reduce the linear instability of long wavelength turbulence in some circumstances, leading to the entry of radiation-improved confinement (RI) modes as seen on TEXTOR [213], DIII-D [171, 214] and JET [215].
5. Reduction of edge working gas influxes often improves the prospects for enhanced core confinement access by increasing density peaking. Leading models of enhanced core confinement point to the benefits of more centralized particle and heat deposition that may result from such reductions, yielding increases in pressure and velocity gradients and accompanying increases in $\vec{E} \times \vec{B}$ shear.

It should be emphasized that not all parts of the above picture are equally well understood or validated. In general, ion thermal transport is better understood than electron thermal, momentum or particle transport. In addition, there are experimental observations that are not well understood in the context of the picture outlined above. Most notable in this regard is that the onset of enhanced core confinement with reverse shear is often found to be correlated with the location and the timing of the appearance of low order rational values of q in the plasma, most notably $q = 2$ (ASDEX Upgrade, DIII-D, JET, JT-60U, TFTR, RTP and others, see references in [24, 25]). As the power threshold for ITB formation can be substantially reduced at such rational q values, this route to ITB formation is a standard method to access reduced core transport in machines with limited power density, such as JET, and is potentially ITER relevant [6]. Experiments and modelling aimed at further understanding this effect are actively underway. In this regard, spectroscopic observations from the LHD stellarator point to the existence of large sheared flows at the boundaries of magnetic islands, suggesting a possible mechanism for the development of transport bifurcations in tokamaks upon the appearance of low order rational surfaces [219]. In any case, these LHD observations suggest that a plasma flow induced by external means (e.g. ion Bernstein wave heating) may provide a means of initiating enhanced core confinement behaviour and for manipulating the pressure profile.

3.1.3. Conclusions. Confinement optimization is an essential component of tokamak performance optimization, and transport control is desirable for a wide variety of reasons. Tokamak transport is a highly coupled, self-organized non-linear system, and a common physics basis is essential to understand the multiple confinement regimes made possible by these non-linear interactions. Over the last decade such an understanding has begun to emerge, based on the interaction of turbulence suppression mechanisms, such as $\vec{E} \times \vec{B}$ sheared flows, negative or weak magnetic shear and Shafranov shift stabilization, interacting with multiple potential turbulence modes (ITG, TEM and ETG), spanning a broad wavenumber range. These non-linear coupled feedback mechanisms represent both an opportunity and a challenge for transport modification and control in burning plasmas. Indeed, it is only when burning plasmas are realized that possible additional feedback mechanisms, involving alpha heating effects, will be encountered for the first time. For this reason, a full understanding of the transport characteristics of burning plasma requires the ITER experiment.

3.2. Ion thermal confinement

Significant advances in our understanding of ion thermal confinement have been accomplished through close collaboration between theory and experiment. Progress has been made in our ability to carry out detailed experiments and in our ability to calculate the underlying processes governing confinement. Overall progress in our understanding of transport has been fostered by an increased emphasis on modelling being used both as an interpretive tool for current experiments and as a predictive tool. While physics questions remain, analysis and predictive approaches have culminated in drift wave turbulence being

commonly accepted as the standard model for cross-field turbulent transport in tokamak plasmas. This is, of course, neglecting the neoclassical and MHD effects that can also influence confinement. The mechanisms of drift wave transport include ion temperature gradient (ITG) modes, trapped electron modes (TEM) and electron temperature gradient (ETG) modes. The dominant mechanism for ion thermal transport is typically predicted to be the ITG mode. Numerous experiments on various tokamaks have been carefully performed to specifically isolate various dependences of the ion heat flux on quantities such as the normalized gyro-radius [220–224], plasma beta [224–226], collisionality [223, 227–230], safety factor [231], $\vec{E} \times \vec{B}$ shear [232] and ion to electron temperature ratio [233] in plasmas with L- and H-mode edges. Analyses of many these experiments have yielded results that are consistent with the predictions of drift wave theory.

Theoretically derived transport models have been developed and systematically tested using standardized profile data stored in the ITER profile database [234–236]. Three theory-based drift wave models that are now commonly used by the fusion community are the IFS/PPPL [237], MMM95 [238, 239] and GLF23 [20] models. While these models may not robustly yield accurate quantitative agreement with experimental data, the models typically predict many of the correct trends. Here, we will briefly discuss some recent successes as well as some outstanding physics issues in predicting the transport in L- and H-mode tokamak discharges including enhanced confinement regimes.

3.2.1. Effect of $E \times B$ shear stabilization. A commonly accepted paradigm associated with drift wave theory that has proven to be an essential ingredient in obtaining many core and edge transport barriers is $\vec{E} \times \vec{B}$ shear physics [114]. It has been widely predicted to be an important effect on long wavelength drift wave turbulence and has been validated experimentally on a wide variety of devices. A prime example of an experiment validating the $\vec{E} \times \vec{B}$ shear paradigm is a DIII-D experiment by Petty *et al* where co- and counter-NBI were applied to a plasma with an ELMing H-mode edge [220]. Here, the normalized ion gyro-radius was varied while other dimensionless parameters, except the Mach number, were held constant. Analyses of the experiment show that while the electron energy transport did not depend on the direction of the toroidally driven rotation, the ion transport was affected by the plasma rotation (see section 3.6). The ion thermal transport exhibited a Bohm-like behaviour for the counter-NBI pair of discharges, compared with gyro-Bohm-like behaviour for the co-NBI pair. The electron thermal transport followed a gyro-Bohm scaling for both pairs.

The differences in the observed thermal transport scaling were attributed to differences in the $\vec{E} \times \vec{B}$ shear between the co- and counter-rotating plasmas. While the Waltz $\vec{E} \times \vec{B}$ shear quench rule appears to work in many cases, it is worth noting that it assumes a reduction in transport that can be approximated by prescribing a net growth rate $\gamma_{\text{net}} = \gamma - \alpha_E \gamma_E$ that enters the quasi-linear mixing length rule [20]. Here, γ is the linear drift-ballooning mode growth rate in the absence of $\vec{E} \times \vec{B}$ shear, γ_E is the $\vec{E} \times \vec{B}$ shearing rate and α_E is the $\vec{E} \times \vec{B}$ shear coefficient. This prescription was derived based on non-linear ITG simulations with adiabatic electrons. The critical

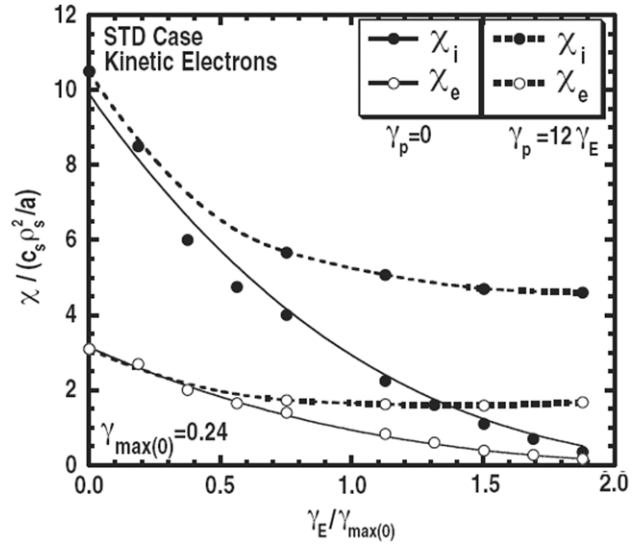


Figure 19. Ion heat (solid circles) and electron heat (hollow circles) diffusivities versus $\gamma_E/\gamma_{\text{max}(0)}$ with (dashed lines) and without (solid lines) the destabilizing effect of parallel velocity shear γ_p . The points are the GYRO results and the lines are curve fits. Reprinted with permission from [241]. © 2005 American Institute of Physics.

value of α_E needed to quench the turbulence in the absence of parallel velocity shear drive was believed to be in the range 0.6–0.75 [34, 240]. Recent ITG/TEM non-linear simulations (including kinetic electrons) using the GYRO code [32] show that α_E is robustly at 0.5 (see figure 19) including cases where all the modes in the spectrum are in the electron direction [241]. When parallel velocity shear is included, the transport may not be quenched by any level of $\vec{E} \times \vec{B}$ shear. This is especially important for higher q values and thus relevant to advanced tokamak (AT) scenarios.

3.2.2. Effects of magnetic shear on internal transport barrier formation. Internal transport barriers (ITBs), particularly in the ion channel, are now commonly observed in all major tokamaks [242–251]. ITBs are regions within the core plasma that can be characterized as having quenched or suppressed turbulent transport levels. ITBs provide improved performance and scenarios for breaking the profile stiffness. While the importance of the $\vec{E} \times \vec{B}$ shear in ITB plasmas has long been realized [162, 218], particularly for ion thermal confinement, the effects of negative central magnetic shear and Shafranov shift stabilization have recently been clarified [252–254]. Recent evidence from JET, ASDEX Upgrade, and JT-60U shows that the magnetic shear directly influences the ion heat transport when going from weakly positive to negative magnetic shear [210, 249]. Experiments on JET have shown that the target q profile influences the ITB triggering power [255, 256]. While negative magnetic shear does not appear to be necessary for ITB formation, data from several devices suggest that electron thermal ITBs require it [257–259]. Furthermore, strong negative shear allows ITBs to form where the turbulent transport is suppressed in all channels, as demonstrated on DIII-D [218, 260]. This is in contrast to purely $\vec{E} \times \vec{B}$ shear driven ITBs which typically only result in ion thermal barriers. ITB discharges with strongly reversed q profiles with little to no central poloidal field are now

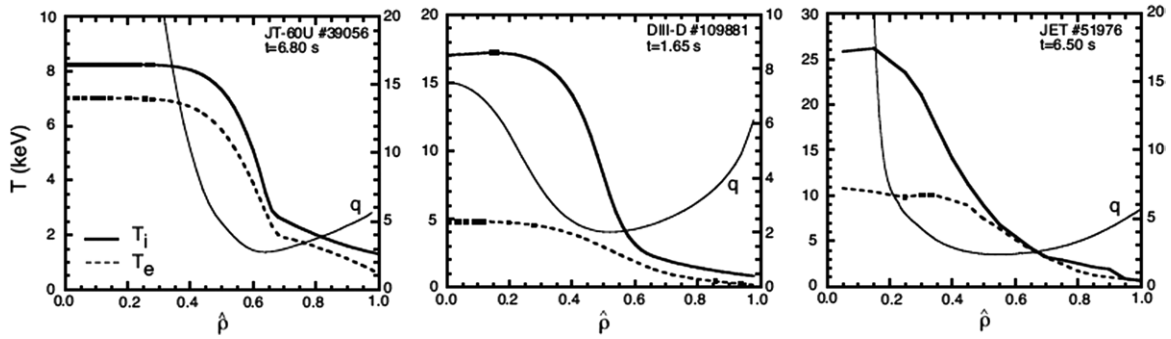


Figure 20. Temperature profiles for ions (solid lines) and electrons (dashed lines) along with the safety factor profile for ITB discharges from JT-60U, DIII-D and JET with strongly reversed magnetic shear [234].

routinely produced and very sharply defined ion temperature profiles have been produced. Figure 20 shows examples of ITB discharges from JT-60U, DIII-D and JET with strongly reversed q profiles from the ITPA profile database [234] (see also section 5.1).

In some strong negative shear discharges, the central ion temperature profiles are very flat within the reversed shear region (see figure 20(a)). An example of this is the box-type ITBs observed in JT-60U [259]. It remains unclear whether this central flattening is due to MHD activity, a breakdown of MHD equilibrium, enhanced neoclassical and/or turbulent transport or a combination of effects. The optimum reversal of the q profile for a given operating scenario has yet to be realized. In any case, negative central magnetic shear operation is now commonplace and understanding the relative roles of magnetic shear and Shafranov shift stabilization in core barrier formation is an active area of research. Furthermore, since toroidally driven $\vec{E} \times \vec{B}$ shear flows are likely to be small in a reactor such as ITER, negative magnetic shear and Shafranov shift stabilization are both more likely to be achievable and impact all channels of transport.

Emphasis on the so-called AT operational regime has aimed at achieving steady-state, long pulse, high performance H-mode discharges that utilize weak or slightly reversed central magnetic shear profiles at high beta with a central safety factor greater than unity [261]. While AT discharges tend to have larger amounts of Shafranov shift stabilization, parallel velocity shear [$\gamma_p = (Rq/r)\gamma_E$] destabilization can prevent $\vec{E} \times \vec{B}$ shear (γ_E)-quenching of the transport, which results in the $\vec{E} \times \vec{B}$ shear only suppressing the transport rather than eliminating it [262]. Another regime is also being developed that demonstrates high beta operation with $q(0) \sim 1$, a broad region of low magnetic shear and the absence of sawtooth activity. This regime has been labelled the ‘hybrid’ regime (see chapter 6 of this issue [199]) by working groups of the ITPA [263] and offers the potential of achieving many of the performance goals of ITER including high fusion gain [264]. At low q , the hybrid scenario tends to have less Shafranov shift stabilization than the higher q AT scenario, but non-linear simulations at low q suggest that $\vec{E} \times \vec{B}$ stabilization can win over γ_p destabilization and the transport can be quenched to neoclassical levels [241]. Unlike L-mode discharges with ITBs, high performance AT and hybrid H-mode discharges usually do not demonstrate sharp breaks in the profiles where the transport changes dramatically from

neoclassical to being strongly turbulent. DIII-D has been successful in demonstrating sustained H-mode discharges with reversed magnetic shear and weak or ‘leaky’ ITBs even in the presence of Type I ELMs [264, 265].

3.2.3. Temperature ratio effects. Another factor that can play a key role in suppressing ITG/TEM transport is the ion to electron temperature ratio. The T_i/T_e ratio is of particular interest when projecting the favourable transport from existing hot ion plasmas to proposed burning plasma experiments where T_i/T_e is expected to be less than or equal to unity. A recent DIII-D H-mode similarity experiment found that increasing T_i/T_e reduced the ion and electron energy transport and the helium particle transport for a 20% scan in T_i/T_e at fixed plasma β [233]. GLF23 modelling showed that the sensitivity of the energy transport to changes in T_i/T_e is likely explained by changes in the critical ion temperature gradient close to the threshold.

Temperature ratio effects can also impact the temporal response of turbulent transport. Recent DIII-D modulated ECH experiments, including ion measurements, have shown evidence of an ion heat pulse and its rapid propagation in response to an electron heat pulse which are consistent with ITG transport [266, 267]. Electron heating at $\rho \approx 0.45$ produced a phase shift resulting in a cooling of the ions at the plasma centre. Modelling showed that the drop in the ion temperature was the result of a decrease in T_i/T_e , which then caused an increase in the ion thermal diffusivity [267].

In perturbative experiments with cold edge pulses, the observed fast radial propagation of the pulses from the plasma edge to the core has been a challenge to be explained by local diffusive transport models. The ITG threshold has the unique signature that it increases when the T_i/T_e ratio increases and, therefore, offers a unique explanation of cold edge pulses propagating inwards and producing a core temperature rise as shown in TEXT [268], TFTR [269], ASDEX Upgrade [270] and RTP [271] experiments. At the plasma edge, a reduction in T_e raises T_i/T_e , which then increases the ITG threshold and produces a pulse of better confinement that appears as heating. Time-dependent transport modelling studies [267, 270] demonstrated that the IFS/PPPL, GLF23 and MMM95 models (which have an ITG threshold) have this phenomenon but single fluid models such as the CDBM model do not. While simulations using stiff critical gradient ITG models, such as the IFS/PPPL and GLF23, have produced the

same qualitative behaviour observed in cold pulse experiments, quantitative agreement is still lacking.

3.2.4. Improved confinement through impurity seeding. Another method of stabilizing drift wave turbulence that is potentially applicable to reactors is through impurity seeding, called the radiative improved RI-mode of operation. A deeper understanding of mechanisms that suppress ion temperature gradient (ITG) turbulence has been achieved by deliberate puffing of impurities, e.g. the RI-mode in TEXTOR and impurity seeded discharges in DIII-D and JET [171, 213, 215]. Such plasmas are characterized by an increased level of the effective ion charge, Z_{eff} , and electron density gradient. It has been demonstrated that both these factors are important in reducing the ITG transport via increases in the critical temperature gradient and the $\vec{E} \times \vec{B}$ shear suppression. An initial increase in Z_{eff} with impurity seeding leads to a reduction of ITG particle diffusivity, which scales as $Z_{\text{eff}}^{-1/2}$. As a result, a particle pinch generated mainly by trapped electrons leads to density peaking. This further reduces the growth rate of ITG modes and finally leads to a bifurcation of an RI-mode state with suppressed ITG transport. Gyro-kinetic analysis of a DIII-D L-mode experiment with neon injection showed that improvements in the ion thermal transport were attributable to an impurity driven enhancement of the $\vec{E} \times \vec{B}$ shearing rate along with a direct reduction of ITG turbulence [171]. Under H-mode conditions, impurity seeding can lead to a widening of the edge transport barrier where ITG is suppressed by both the density gradient and the radial electric field. Such a barrier broadening was observed by argon injection into JT-60 U [272].

3.2.5. Outstanding issues. While significant advances have been made in our predictive understanding of ion thermal transport, there remain important outstanding physics issues. While there are outstanding theoretical issues in neoclassical ion thermal transport, much of the focus is on turbulent transport issues. A prime example involves the degree of profile stiffness. Here, we define profile stiffness as the rate of increase in the ion heat flux in response to an increase in the ion temperature gradient above the threshold value. If the core temperature profiles are stiff, they are then unresponsive to changes in auxiliary power. A stiff core plasma is also sensitive to changes in the plasma edge conditions. There is ample experimental evidence of temperature profile stiffness from a variety of devices such as Alcator C-Mod [229], ASDEX Upgrade [273–275], DIII-D [276] and JT-60U [277]. For H-mode operation, the core performance is predicted to depend sensitively on the height of the pedestal. However, quantifying the level of stiffness in the plasma core has proven difficult. The MMM95 model [238, 239], which is based on the Weiland/Chalmers ITG/TEM drift wave model [278], can be categorized as weak to moderately stiff. Models based on gyro-fluid simulations, such as the IFS/PPPL [237] and GLF23 [20] models, are comparatively more stiff. For a given ion temperature gradient, the predicted ion heat fluxes from gyro-fluid simulations are significantly larger than those obtained from gyro-kinetic simulations [110]. Recently, the GLF23 model was renormalized to non-linear gyro-kinetic simulations making it less stiff and yielding fusion projections somewhat

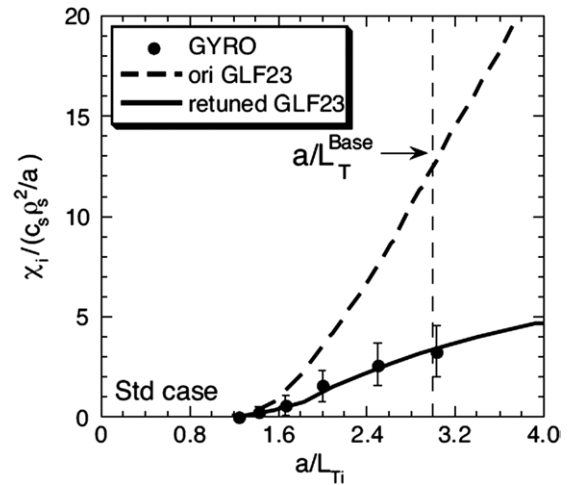


Figure 21. Ion thermal diffusivity versus normalized ion temperature gradient from GYRO non-linear simulations (points), original GLF23 model (dashed line), and returned GLF23 model (solid line). Reprinted with permission from [533]. © 2005 American Institute of Physics.

closer to that of the MMM95 model. Figure 21 shows the predicted ion thermal diffusivity from GLF23 plotted against the GYRO non-linear gyro-kinetic results for the standard case described in the 1996 GLF23 paper [20]. At the reference normalized ion temperature gradient of $a/L_{Ti} = 3.0$ (vertical dashed line), there is nearly a factor of three reduction in the transport as a result of renormalizing the model against the GYRO non-linear gyro-kinetic results.

Despite differing levels of stiffnesses, the gyro-fluid based (GLF23, IFS/PPPL) and fluid based (MMM95, Weiland) models have exhibited the same level of agreement when compared with the experimental profile data. In the standardized testing carried out by the ITER Modelling Working Group, it was found that it was difficult to distinguish statistically between various models based on how well they predict the temperature profiles in L- and H-mode discharges that do not display significant core transport barriers [234, 235]. However, the models lead to very different predictions in burning plasma performance when applied to future devices such as ITER [236, 279]. While the required pedestal temperatures T_{ped} from the MMM95, IFS/PPPL and GLF23 models needed to obtain a specific fusion gain can differ significantly, it is worth noting that they are all within the current range of possible T_{ped} projections.

Another example of an unresolved physics issue pertains to robust experimental observations in L-mode whereby the analysed ion thermal transport appears to follow a Bohm-like scaling. This result has been a challenge to explain the given intrinsic gyro-Bohm scaling of drift wave models. Transport modelling [239, 280] and turbulence simulations [32, 34, 281] of particular cases have been able to produce apparent Bohm-like scalings of the diffusivities. Figure 22 shows the results of GYRO non-linear simulations with various physical effects and their influence on the gyro-radius scaling in comparison with the experimental analysis of a recent DIII-D L-mode gyro-radius scan [32]. While the gyro-Bohm scaling can be broken close to the threshold temperature gradient, isolating a single piece of physics that robustly yields non-gyro-Bohm behaviour

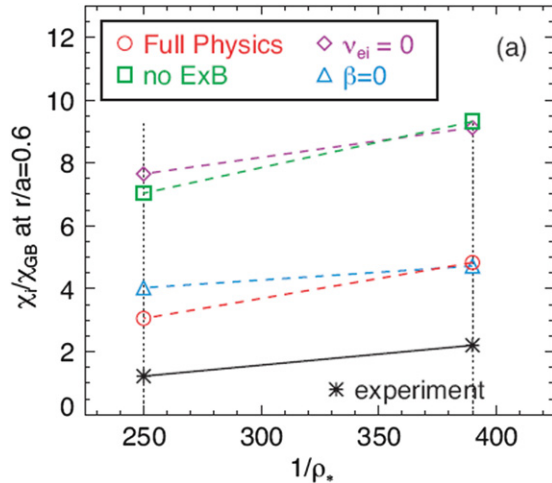


Figure 22. Impact of selected physical effects on the predicted ion energy transport using the GYRO code in comparison with experimental estimates. Reprinted with permission from [32]. © 2003 American Physical Society.

in the L-mode for the ion channel (but not the electron channel) remains elusive.

Transient transport phenomena have also posed a significant challenge to be explained by the theory and modelling community. DIII-D modulated ECH experiments have shown clear evidence that electron perturbations create changes in the ion heat response which are consistent with ITG transport [266]. Figure 23 shows the amplitude and phase of the electron and ion heat pulses for a DIII-D modulated ECH experiment accompanied by the predictions of the IFS/PPPL, GLF23, MMM95 and Itoh–Itoh–Fukuyama (IIF) models. This provides a clear example of an ion heat pulse and its rapid propagation in response to an electron heat pulse. Here, the IFS/PPPL and GLF23 models demonstrated the best level of agreement with the ion behaviour.

While the modulated ECH experiments provide an additional test for transport models, clear discrimination between the models in terms of their temporal response has proven difficult to achieve [266, 267, 282]. No single model has been able to consistently perform better than other models in reproducing the observed phase and amplitudes of both the electron and the ion temperature perturbations as well as the equilibrium profiles. One can, however, discriminate against single fluid models based on these results. In other perturbative experiments with cold edge pulses, the observed fast radial propagation of the pulses from the edge into the plasma core has been difficult to explain by local diffusive (i.e. drift wave) transport models. Simulations using stiff critical gradient ITG models, such as the IFS/PPPL and GLF23, have produced the same qualitative behaviour observed in cold pulse experiments, but quantitative agreement is still lacking and, like the modulated ECH experiments, no single model has been able to satisfactorily reproduce all of the observed temporal behaviour [267, 283].

One final example of an outstanding physics issue pertains to understanding turbulent transport in low aspect ratio tokamaks. Unlike standard higher aspect ratio tokamaks, low aspect ratio devices such as NSTX [284] and MAST appear to be dominated by high- k rather than low- k turbulence. They

also typically operate at a much higher β . Recent analyses of NBI-heated NSTX discharges indicate that within the spatial region from $r/a = 0.2$ – 0.65 , where the heat transport is confidently known, the electrons dominate the heat loss with $\chi_i \ll \chi_e$. This is seen in figure 24, where the ion thermal diffusivities at $r/a = 0.4$ for a collection of both L- and H-mode neutral beam heated discharges are up to an order of magnitude, on average, less than the electron thermal diffusivity. Furthermore, χ_i is at or above the level predicted by neoclassical theory (as determined from the NCLASS model [185]).

3.3. Electron thermal transport

For more than two decades the electron temperature profiles in conventional tokamak plasmas, L- or H-modes without ITBs, are observed to react weakly to changes in the auxiliary heating power deposition profile, as described in [285–291] and more recently in [11, 274, 292–295]. This property has been named ‘profile consistency’ [296], ‘profile resilience’ or more recently ‘profile stiffness’. In experiments with central heating the normalized electron temperature gradient, $R/L_{T_e} = R\nabla T_e/T_e$, exhibits in all tokamaks a rather constant value around 10 [297]. With off-axis heating the electron temperature profile generally remains peaked and R/L_{T_e} keeps a finite value well above zero. Electron heat transport has been extensively investigated, in particular supported by the installation of electron cyclotron heating systems in several devices. This heating method provides narrow on-axis or off-axis power deposition profiles with pure electron heating. These studies yield experimental results strongly suggestive of electron heat transport that is governed by turbulence increasing above a threshold in normalized gradient, $R/L_{T_{e,crit}}$. This means that the heat flux is low below the threshold and increases above it. The rate of increase above the threshold can be characterized by the ‘stiffness factor’. Some of the results addressing this hypothesis are summarized in [297] and discussed for individual devices in [298–304]. It will be shown later that in general the value of R/L_{T_e} deduced from the experimental temperature profiles is significantly larger than $R/L_{T_{e,crit}}$: the electron temperature profiles in present-day tokamaks are not infinitely stiff.

The theory of heat transport presented in section 2 indicates that electron heat transport may be driven by turbulence excited by TEM and/or ITG modes [20, 278, 305] and/or by ETG modes [306, 307]. It must be stressed that, in general in conventional scenarios, due to its very small scale ETG driven turbulence can only cause a relevant electron heat flux if larger cells, so-called streamers, develop [47, 307]. These three different instabilities have respective thresholds in ion or electron normalized temperature gradients, above which turbulence and the corresponding transport increase. Formulae have been derived for the threshold of TEM [308] and ETG [47], which can be easily compared with the experiment. Several plasma parameters play a role, in particular T_e/T_i , the density gradient, the magnetic shear and the safety factor. In addition TEM are predicted to be stabilized by collisionality due to detrapping of electrons. Note that, as already indicated in section 3.2 of this chapter, the ion temperature profiles also exhibit profile resilience which can be

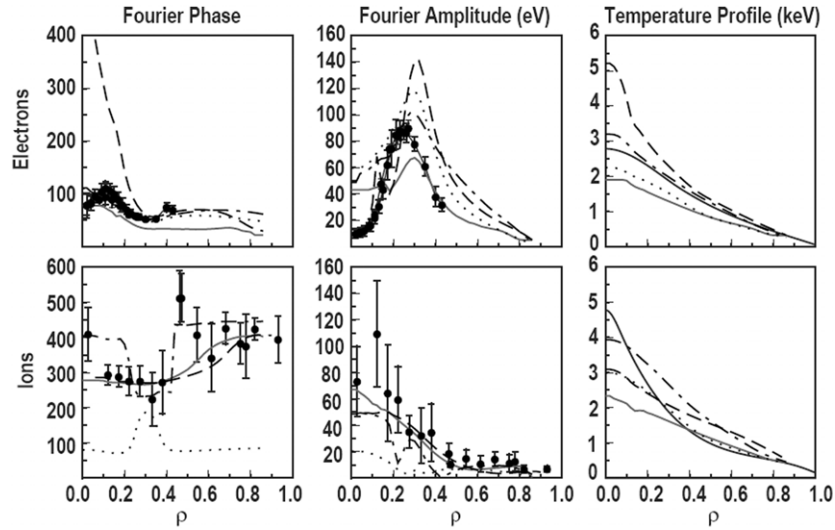


Figure 23. Fourier analysis of the phase and amplitude for δT_e and δT_i for measured data (solid circles), the IFS/PPPL model (dashed lines), the IIF model (dotted lines), the MMM95 model (chained lines) and the original GLF23 model (solid grey lines) for the case of $\rho_{ECH} = 0.3$. Reprinted with permission from [266].

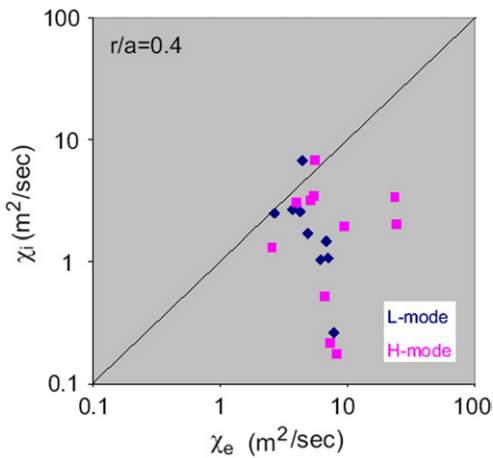


Figure 24. Ion thermal diffusivity plotted against the electron thermal diffusivity for L-mode (blue) and H-mode (red) NSTX plasmas.

attributed to the same reasons applying to ion heat transport by ITG [275, 309].

A simple empirical model based on the existence of a threshold $R/L_{T_{e,crit}}$ has been successfully tested on ASDEX Upgrade ECRH heated plasmas [310]. It includes the increase in transport above the threshold and the $T^{3/2}$ gyro-Bohm dependence. Based on this initial study, this transport model has been extended with a $q^{3/2}$ dependence, which yields the required radial dependence of transport as well as its dependence with plasma current [23]. The q dependence takes into account the shift of the k spectrum of the modes to lower values with q [20, 122].

The relative contributions of these three different instabilities to electron heat transport vary depending on the plasma conditions. In the cases with dominant electron heating and $T_e > T_i$, for instance with ECRH, the electron heat flux is large compared with the ion heat flux and transport is dominated by the TEM. The ITG contribution is small because of the low ion heat flux. The ETG modes are stable:

due to $T_e > T_i$ the calculated threshold is clearly higher than the measured R/L_{T_e} . This simple and clear situation where the TEM contribution dominates can be investigated experimentally under good conditions as described below. In contrast, comparable electron and ion heat fluxes lead to similar T_e and T_i values and all the three modes can be expected to contribute to electron heat transport. This is a complicated experimental situation that will be discussed later in this section. Finally, if the turbulence can be stabilized in a region of the plasma, an electron ITB can be created as discussed at the end of this section. In this work we report the essential recent results on electron heat transport in tokamaks and do not intend to provide a complete overview of this topic.

It must be underlined that electron heat transport can also be driven by global MHD instabilities. This topic is out of the scope of this section and we concentrate on cases where their effects are negligible.

3.3.1. Electron heat transport with dominant electron heating. In the cases with dominant electron heating, with low heat flux in the ion channel and high heat flux in the electron channel, $T_e > T_i$ and $R/L_{T_e} > R/L_{T_i}$, the electron heat flux can be considered in general as mainly driven by the TEM instability [308]. Such a situation can be achieved in plasmas with strong electron heating only, for instance ECRH or ICRF, and at moderate and low collisionality. Collisionality plays an important role in two ways. Firstly, low collisionality allows the separation of the ion and electron temperature profiles and heat fluxes. Secondly, increasing collisionality gradually stabilizes the TEM modes as discussed later. In the cases where electrons and ions remain separated, the study is simplified and electron heat transport can be studied in practice independently of the ions. The experimental investigations and the comparison with theory are clearer, providing an unambiguous check for the TEM theory of electron heat transport. Even if such situations are not relevant of the

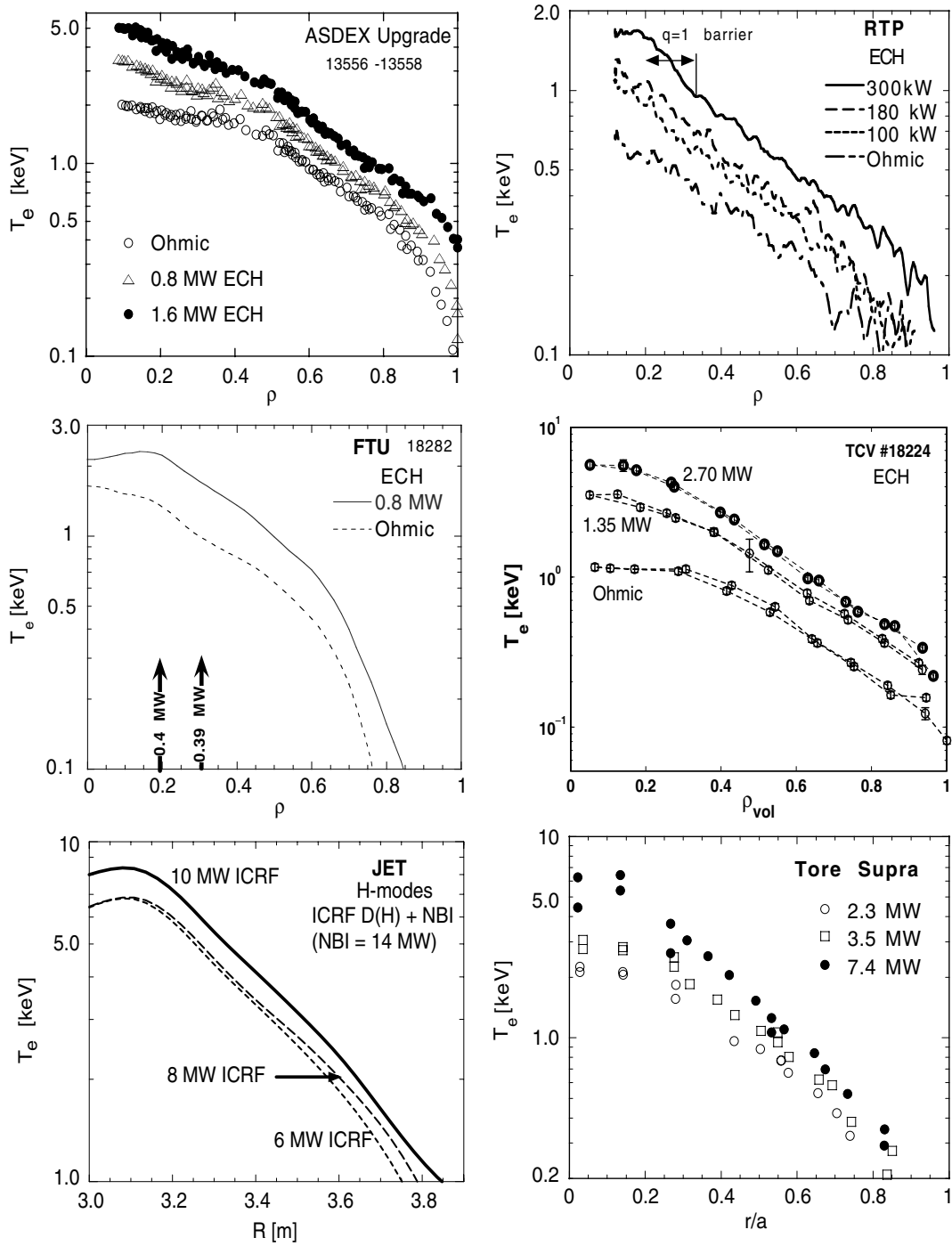


Figure 25. Electron temperature profiles from different tokamaks on logarithmic scale showing the region with constant normalized temperature gradient. Reprinted with permission from [297]. © 2001 Institute of Physics.

conditions which will be found in burning plasmas, they are essential to assess our understanding of the underlying physics.

In the following we summarize the experimental results obtained in plasmas with dominant electron heating. These are L-modes with rather low coupling between ion and electron and with a low heat flux in the ion channel compared with that transported by the electrons.

With central heating, the electron temperature profiles plotted on a logarithmic scale have a very similar shape [297]. Examples are shown in figure 25. The profiles exhibit the same slope and are shifted with respect to each other depending

on the edge or pedestal temperature. The same slope means that R/L_{T_e} is the same, or equivalently, the core temperature is proportional to the edge temperature [275]. Only a large variation of the electron heating power (up to 7 MW) deposited centrally, as done in Tore Supra, could produce a measurable variation of R/L_{T_e} [300]. In such cases only, the extrapolation to zero power may yield the actual threshold $R/L_{T_{e,crit}}$. Under this assumption the Tore Supra results suggest a threshold with a dependence on s/q , the ratio of magnetic shear to safety factor. In the cases with a smaller range in heating power, the measured R/L_{T_e} remains about constant independently of

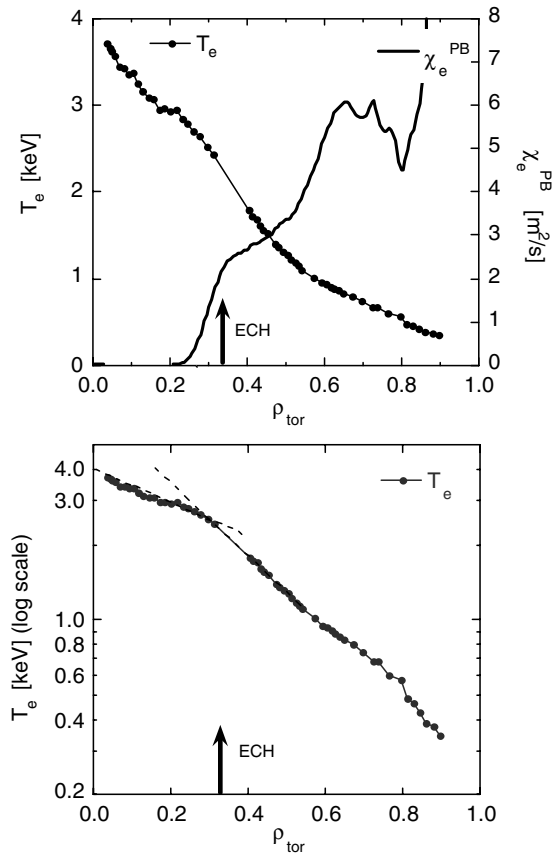


Figure 26. Top: Temperature profile (linear scale) and power balance heat diffusivity for moderately off-axis ECRH. Bottom: Electron temperature profile on log scale which indicates the change in slope ($\nabla T_e/T_e$) at the ECRH deposition, indicated by the dashed lines. Reprinted with permission from [311].

heating power, but this value is believed to be significantly above the threshold, as discussed below.

Localized electron heating deposited off-axis is a powerful tool to investigate properties of electron heat transport and the possible existence of a threshold. In fact, when off-axis heating is applied the temperature profile, plotted on linear scale, remains peaked and seems to react weakly to the large difference in heat flux on each side of the deposition [290, 298, 303]. However, plotted on a logarithmic scale, the T_e profile indicates indeed a low value of R/L_{T_e} inside of the power deposition compared with the outer part [311]. An example with off-axis ECRH is illustrated in figure 26 showing that the T_e profile appears quite peaked on a linear scale, but less peaked in the core in term of normalized gradient. It is believed that in the plasma region inside of the off-axis power deposition R/L_{T_e} is just above but close to the threshold [312].

Experiments were made in ASDEX Upgrade in which R/L_{T_e} has been varied gradually by using ECRH at two different radial positions, keeping the edge temperature constant. The results strongly support the existence of a threshold: the electron heat diffusivity goes to zero for a clearly finite value of ∇T_e corresponding to R/L_{T_e} [312]. Similar experiments carried out more recently in DIII-D [313] and TCv [314] yield very comparable results.

The analysis of turbulence stability for these three experiments indicates that the TEMs are the most unstable

modes. In particular, in ASDEX Upgrade linear calculations of turbulence stability were carried out with the gyro-kinetic code GS2 for these discharges and compared in detail with the experimental results [308]. They indicate that TEM indeed dominate electron heat transport in these conditions. Due to the large T_e/T_i ratio, the ETG turbulence is not excited in these cases. The threshold in R/L_{T_e} provided by GS2 analyses agrees with the experimental value $R/L_{T_e, \text{crit}} = 4$ and the increase of heat flux with R/L_{T_e} above the threshold also has the same dependence as in the experiment.

These similar results from ASDEX Upgrade, DIII-D and TCv underline the important point that in general, in the region of the plasma where the electron heat flux is large, the value of R/L_{T_e} is clearly above the threshold by a factor up to 2 or 3. To some extent this is also visible in experiments with a very large variation in central heating power [300]. Hence the T_e profiles are intrinsically not very stiff: a change in heat flux can in principle cause a significant variation in R/L_{T_e} . The fact that varying the central heating power in general does not cause a large change in R/L_{T_e} is due to the three effects. Firstly, the T_e profiles cannot easily drop below the R/L_{T_e} threshold: even with Ohmic heating only they remain above the threshold. Secondly, the edge temperature increases with heating power, which allows the core electron temperature to increase without changing R/L_{T_e} significantly. Thirdly, due to the $T_e^{3/2}$ gyro-Bohm dependence of heat transport driven by micro-turbulence, the actual profile stiffness increases with temperature: at high temperature the profiles tend to be closer to the threshold, preventing any strong change of gradient with heat flux. The empirical transport model reproduces well the general behaviour of the temperature profiles and is in rough agreement with the results from global confinement scaling laws [23]. This study describes in detail the effect of the edge temperature, stiffness characteristics and power deposition on the properties of the electron temperature profiles.

Power modulation and the analysis of the resulting temperature oscillations yield the so-called heat pulse diffusivity χ_e^{HP} [315]. This quantity is the derivative of the electron heat flux versus electron temperature gradient at the time-averaged working point. It yields precious information on the stiffness properties of the electron heat transport. In particular, if a threshold exists the change of slope in q_e , from flat to steep, induces a jump in χ_e^{HP} as pointed out in [310]. This provides a direct experimental indicator of a threshold. Power modulation and transients have been studied for a long time as reported for instance in the review papers [315–317] and references therein. However, at that time, the experimental information could not be ordered to a consistent physics picture of electron heat transport.

Recent studies using modulation techniques have been guided by the possible existence of a threshold in R/L_{T_e} and could indeed support this hypothesis in ASDEX Upgrade [298, 304, 312]; DIII-D [313] and FTU [303, 318]. In these devices the propagation of the heat pulses reacts strongly to the off-axis heating. In the ASDEX Upgrade and DIII-D common experiments described above [312, 313], where R/L_{T_e} has been varied keeping the edge temperature constant, power modulation was also applied. The results from the two devices for χ_e^{HP} are shown in figure 27 and support the possible existence of a threshold. Indeed, as shown in [312],

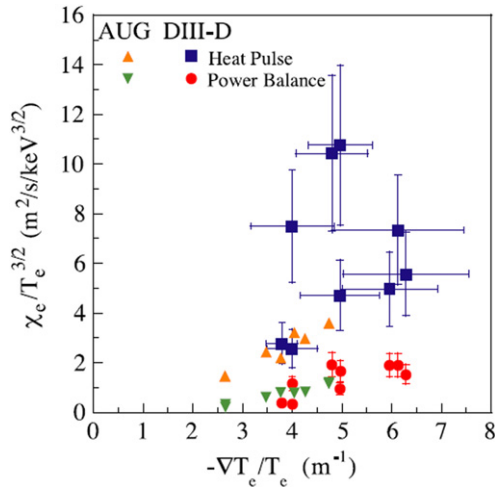


Figure 27. Data from ASDEX Upgrade and DIII-D from common experiments where $\nabla T_e / T_e$ has been varied. This shows rather good agreement for the power balance, including an offset in $\nabla T_e / T_e$. The values for χ_e^{HP} are not inconsistent. Reprinted with permission from [313].

the empirical model with critical R/L_{T_e} agrees with both the χ_e^{PB} (heat diffusivity defined from the static power balance) and χ_e^{HP} data for a threshold value just below the range covered by the data in R/L_{T_e} . However, in these experiments the values of R/L_{T_e} could not be reduced enough to drop below $R/L_{T_{e,\text{crit}}}$. Therefore these studies have been extended very recently in ASDEX Upgrade experiments in a new variation of R/L_{T_e} at low current to reduce the residual Ohmic power in the off-axis case. This allowed R/L_{T_e} to be indeed scanned across the threshold which was clearly revealed by the expected jump in χ_e^{HP} [304].

Collisions are expected to stabilize the TEM. This property can explain experimental observation made in TCV [314] and ASDEX Upgrade [129, 304]. Indeed a transition from TEM to ITG-driven electron heat transport has been observed. In such case the ETG can also be unstable according to theory, but no experimental evidence has been found so far [129]. It must be stressed again that ETG turbulence drives significant transport if the cells are large enough, streamers are required. The stability criterion is not a sufficient condition for heat to be driven by ETG. In FTU experiments using pellet injection have carried out leading to quite high collisionality with large gradients. The stability analyses show that the TEM modes are expected to be stable and that electron transport may be driven by ITG and ETG [319]. They also indicate that the increase in the density gradient caused by the pellets leads to a stabilization of these modes which explains the observed improvement of confinement.

Summarizing, several experiments and analyses under quite different conditions and devices strongly support the hypothesis that in plasmas with dominant electron heating a threshold in R/L_{T_e} exists and leads to the observed stiffness. In the majority of the cases, the most unstable modes are found to be the TEM which are believed to be the main cause for electron heat transport in plasmas with dominant electron heating. The threshold of the ETG modes decreases with decreasing values of T_e / T_i and this turbulence might dominate electron heat transport in some cases described in [300] and [318] and at high

collisionality when in addition TEM modes are stabilized. So far no evidence for ETG driven heat transport has been found in present machines. However, this is a crucial issue for ITER because ETG can be expected to be unstable in its core region.

3.3.2. Electron heat transport with comparable electron and ion heating. In the cases with comparable ion and electron heating (e.g. with NBI heating) the T_e profiles also exhibit profile stiffness described above. They have about the same value of R/L_{T_e} as indicated above and it is also widely observed that this value does not vary in power or density scans, [274, 275, 292–294]. In plasmas heated by NBI the ion heat flux may be larger than the electron heat flux. However, the latter is never negligible and reaches at least 20% of the total heat flux, in general more. Consequently, even in experiments using in addition off-axis ECRH, the electron heat flux inside of the ECRH deposition cannot be very small and it is significantly above the residual Ohmic heat flux. This strongly limits the experimental possibilities. In contrast to the plasmas described in the previous section, the temperature profiles exhibit R/L_{T_i} larger or close to R/L_{T_e} . The TEM and ITG modes are both contributing to electron heat flux and the resulting electron heat transport depends on both the ion and electron temperature profiles. The investigation of these cases is complicated by the coupling between channels. In addition, due to the different profiles of R/L_{T_e} and R/L_{T_i} the dominant modes might depend on the radial position [309]. Moreover, in such situations T_e / T_i is generally close to or below unity and the threshold formula for ETG given in [47] indicates that these may be unstable. Nevertheless, dedicated experiments provide important elements to be compared with theory.

The specific aspect of electron transport in the frame of ITG/TEM physics has been addressed in two dedicated series of experiments in DIII-D [233, 266]. The ratio T_e / T_i is predicted by theory to be essential for the stability of these modes. The first set of experiments presents steady-state investigations in which the ratio T_e / T_i has been varied keeping either T_e or T_i constant. They indicate a strong dependence of electron heat transport which suggests $\chi_e \propto T_i^3$. This is in agreement with the sensitivity of the ITG/TEM stability to T_e / T_i . The second set of experiments [266] uses ECRH power modulation in NBI-heated L-modes. A modulation in both the electron and ion temperatures is observed. As the energy exchange time is long compared with the modulation period, this indicates a dependence of χ_e upon T_i or T_e / T_i . The transport models based on ITG/TEM physics indeed produce a modulation in both T_e and T_i . The quantitative agreement, which was rather poor in reference [266], could be improved recently by increasing the stiffness of electron transport [320]. In ASDEX Upgrade, experiments using steady-state and modulated ECRH were performed in low density H-modes to ensure strong ion heat flux and low coupling with the electron [321]. These results also show that ion transport is strongly affected by changes in the electron temperature when ECRH is applied. The analysis of modulation data also suggests the existence of a threshold $R/L_{T_e} = 6$ outside the very central part of the plasma ($\rho > 0.25$). This is in agreement with the expected values within the experimental uncertainties. The results also indicate an increase in stiffness towards the edge as experimental results from DIII-D [322]. Turbulence stability

analyses indicate that in these discharges all the three modes ITG, TEM and ETG may be unstable but a clear statement on their respective contributions to electron heat transport cannot be made so far due to the experimental uncertainties.

The scaling experiments made in DIII-D and mentioned in section 3.2 for the ions also yield important information on electron heat transport in NBI-heated L- and H-modes [225, 227, 231–233]. There are three main conclusions. Firstly, the ρ_* scaling experiments indicate that electron transport is always gyro-Bohm whereas ions do not show an unambiguous behaviour. Secondly, the beta dependence is very weak for the electrons, which probably rules out magnetic flutter as a main contributor. Thirdly, electron heat transport seems to be weakly sensitive to $E \times B$ shear stabilization.

In summary, the understanding of electron heat transport in experiments with comparable ion and electron heating is more complicated and more difficult to assess than in the cases with dominant electron heating. It is highly probable that ITG/TEM turbulence is the main contributor to electron heat transport, as ITG modes are the main players for ion heat transport (section 3.2). However, the quantitative comparison is not precise and the ETG modes might also play an important role, not quantified at all yet.

In burning plasma experiments one expects a strong centrally peaked electron heating and a weaker ion heating. The weak ion-electron coupling is compensated by the large size of the machine and by the long energy confinement time, such that electrons and ions are weakly coupled in the very core but increasingly coupled towards the plasma edge. Therefore, electron heat transport in the very core could be dominated by TEM modes, similar to the description given at the beginning of this section. Due to the very low collisionality these modes will be highly unstable and will probably dominate electron heat transport. Further outside, the ITG contribution will increase and electron heat transport is expected to be close to what was addressed in the above paragraphs, with the difference being that collisionality will be lower and ρ_* as well. The effect of this latter point is an important issue for extrapolations. In a fusion reactor the temperatures will be higher than in present tokamaks and due to the $T_e^{3/2}$ dependence of transport the temperature profiles will be kept closer to their respective thresholds. It is therefore essential to assess the sensitivity of the ITG/TEM stability to T_e/T_i and more experimental results on this topic would be very useful. Finally, the ETG may well contribute to electron heat transport but and experimental results on this issue are highly desirable.

3.3.3. Electron internal transport barriers. Internal transport barriers characterized by large temperature gradients are able to yield simultaneously a large fraction of non-inductive bootstrap current and high performance due to the high temperature which can be reached. Scenarios exploiting the dominant ion heating by NBI have been extensively investigated, as described in the previous sections. They produce strong ITBs in the ion channels but generally weak or no ITBs in the electron channels. Strong electron ITBs have been created with dominant electron heating, generally in conjunction with current drive, using RF scenarios such as LH, ECRH and to a lesser extent ICRF. The main experimental studies and results on this subject have been reviewed in

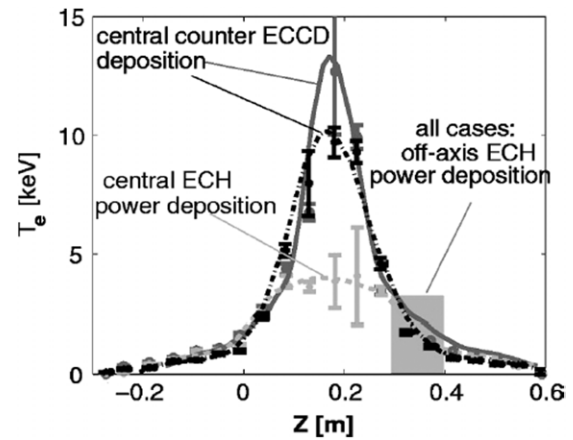


Figure 28. Electron temperature profiles in TCV showing that central counter-ECCD (solid line $P_{\text{tot}} = 2.25$ MW; dashed-dotted line $P_{\text{tot}} = 1.8$ MW) creates a strong electron ITB whereas ECRH (dashed line $P_{\text{tot}} = 2.25$ MW) does not. Reprinted with permission from [337]. © 2001 American Institute of Physics.

[25, 323] and can be found for the different tokamaks as follows: ASDEX Upgrade [324–326]; FTU [327]; JET [328–330]; JT-60U [331–333]; Tore Supra [334, 335]; TCV [336–339] and T-10 [340].

Electrons ITBs, generally obtained at very low densities, lead to central electron temperatures that can reach up to 20 keV [326] and steep gradients with R/L_{T_e} up to 20 [323]. This latter value is 2–3 times larger than generally measured in conventional plasmas and indicates a clear barrier. The radial position of the barrier foot is related to the position of the minimum q value; however, due to the uncertainties of that quantity it is not possible to specify if it is right at this position or slightly inside. The change in gradient which determines the foot of the barrier is generally very clear on the temperature profile, see for instance [328, 332, 337]. An example of electron ITB created with central counter-ECCD is shown in figure 28. In all the studies the creation and sustainment of electron ITBs are found to be related to magnetic shear. In T-10 flat or even slightly positive shear seems to be sufficient to create an electron ITB [340]. In the other tokamaks electron ITBs with dominant electron heating require negative magnetic shear [325]. Experiments in which the depth of the reversed q profile could be varied indicate that the strength of the barrier increases with the reversed character of the q profile [326, 333, 339, 341]. In JET, turbulence calculations indicate that the formation of an electron ITB is related to the stabilization of the TEM for a reversed shear such that $s \leq -0.5$ [330]. As the ITB develops in time after it has started, the velocity shearing rate can further contribute to turbulence reduction. An additional contribution to stabilization can be provided by the gradient of β [254]. These mechanisms provide a positive feedback loop as higher pressure and steeper gradients can further stabilize. In a reactor such a loop may be supported by the increase in fusion power with increasing pressure. As discussed above, one may expect that TEM driven turbulence is responsible for electron heat transport in most of the low density plasmas heated with pure electron heating. This is particularly true for these plasmas before the ITB formation. Therefore, one may assume that the stabilization of these modes causes the ITB formation, as

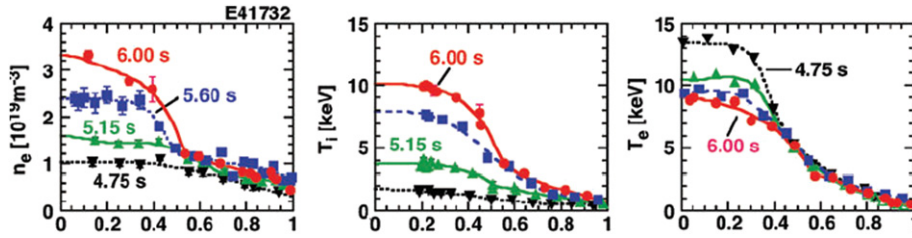


Figure 29. Results from JT-60U showing that the electron ITB decreases with time which corresponds to an increase of NBI power and ion temperature. Reprinted with permission from [333]. © 2004 Institute of Physics.

indicated by the JET analysis. This is supported by turbulence measurement as shown in [334, 340, 342]. It is however not excluded that in fully developed electron ITBs the large value of R/L_{T_e} either destabilizes them again or destabilizes the ETG modes, which therefore may limit the maximum gradient. This has been analysed for electron ITBs obtained in Tore Supra [343]. This latter possibility is supported by simulations suggesting that ETG driven turbulence is required to keep the gradient close to the experimental value [20]. Transport studies indicate that the electron heat diffusivity χ_e drops by almost an order of magnitude across an electron ITB. Typical values for χ_e are $1\text{--}4\text{ m}^2\text{ s}^{-1}$ outside of the barrier and $0.5\text{--}0.1\text{ m}^2\text{ s}^{-1}$ inside of the barrier [327, 328, 334–336]. This value is low but remains at least one order of magnitude higher than the electron neoclassical value. Therefore turbulent transport is not fully suppressed, in contrast to what is observed in ion ITBs.

In electron ITBs with dominant electron heating the ion temperature remains much lower than the electron values and T_e/T_i can be as high as 30. The T_i profiles do not exhibit signs of an ITB. Attempts to increase T_i adding NBI heating to plasmas with an established electron ITB lead to the decrease in the strength of the electron ITB [333], as illustrated in figure 29. With sufficient ion heating an ion ITB is formed whereas the electron ITB seems to disappear. In one single case, clear electron and ion ITBs could be produced simultaneously [324]. In general, plasma density also leads to a decrease in the electron temperature and eventually the electron ITB disappears. These effects are not well documented and incompletely understood so far.

Electron ITBs can be sustained in steady-state with an adequate shaping of the current profile as demonstrated on one hand, with LHCD in JET [328], JT-60U [344] and Tore Supra [335], and on the other hand, with fully non-inductive current drive based on a combination of off-axis co-ECCD and central co-ECCD or counter-ECCD in TCV [338, 339].

The plasmas with electron ITBs do not yield performances particularly relevant for future burning plasmas, but they demonstrate the possibility for steady-state and control of barriers. In addition, they yield physics understanding which will be useful to assess theory. They show that strong rotation is not required and that current shaping is essential. Further useful issues deal with investigations on the cause of a barrier (change in threshold or real turbulence stabilization), cause of the residual transport in the barrier and effect of T_e/T_i on achievement of electron ITBs. Understanding the physics reasons may be useful in obtaining ion and electron ITBs simultaneously, which is a key issue for advanced tokamak scenarios, particularly in burning plasma with strong electron heating and no momentum source.

3.4. Particle and impurity transport

Density control is essential for burn control in a fusion reactor, where understanding of particle confinement and transport is indispensable. Studies of particle confinement and transport have been performed from the earliest investigations of confinement in fusion relevant plasmas. However, this understanding is still limited compared with that of energy confinement and transport due to conditions peculiar to particle confinement and transport, such as the existence of two kinds of dominant particle source (central and edge sources), and the important role of a convection in addition to diffusion. Recently, understanding of particle confinement and transport has been strongly enhanced by establishing experimental and analytical methods in conjunction with theory-based modelling (see also sections 2.1 and 2.2). An anomalous particle pinch at low collisionality has been observed in a number of devices and explained in the framework of the ITG/TEM transport theory. In improved confinement plasmas with internal transport barriers (ITBs), impurity accumulation due to reduced turbulent transport and a strong neoclassical inward pinch driven by the large density gradient is recognized as one of the largest concerns for applying ITB plasmas to a fusion reactor. Suppression of impurity accumulation has been developed using central electron heating, and it is understood in terms of the combined effects of neoclassical impurity transport and turbulence-driven transport.

3.4.1. Particle confinement times with consideration of central and edge particle sources. As noted above, the understanding of particle confinement has lagged behind the understanding of energy confinement chiefly due to existence of two dominant particle sources, i.e. central fuelling by NBI and edge fuelling by gas puffing and recycling. In order to improve this situation, a scaling law for the total number of ions in the main plasma of JT-60U ELMy H-mode plasmas was proposed that uses separately defined confinement times for central fuelling and edge fuelling [345]. The confinement time increases with density for core fuelling and decreases with density for edge fuelling. However, the particle confinement exhibited a different dependence in reversed magnetic shear plasmas with an internal transport barrier. The scaling also enabled the discussion of density controllability by considering the different effects on the particle balance of fuelling and divertor pumping. The same method was applied to DIII-D ELMy H-mode plasmas, where a stronger density dependence was obtained compared with the JT-60U plasmas [346]. For a more systematic understanding of particle confinement, a database should be accumulated that includes many machines.

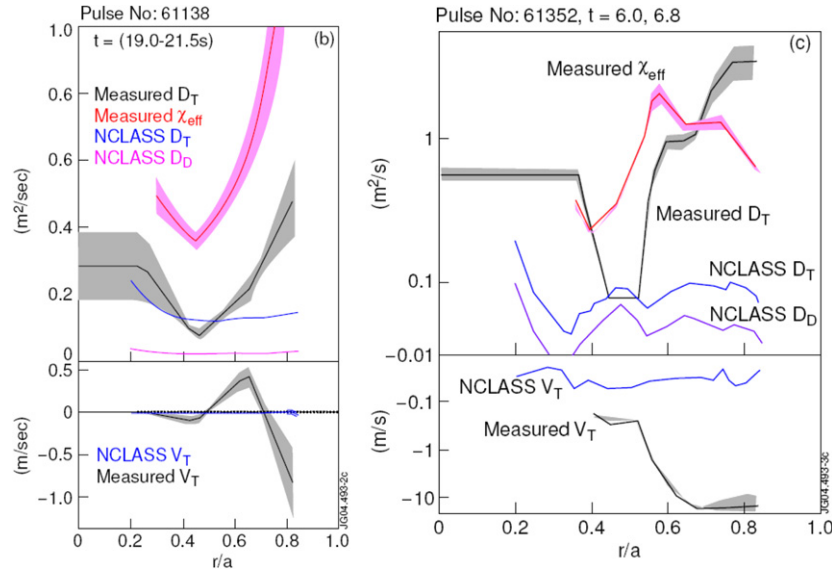


Figure 30. Tritium diffusion and convection coefficients measured in the JET trace tritium experiments in comparison with the neoclassical predictions for the high-density ELMy H-mode (left column) and for a discharge with strong internal transport barrier (right column). Shaded areas indicate the confidence limits for the fitted quantities. Reprinted with permission from [350].

3.4.2. Estimation of local particle transport coefficients.

Local particle transport has been analysed to understand the physical mechanisms responsible for the shape of the density profile. In the analysis of many cases, an inward pinch is introduced to explain a peaked density profile in the absence of a central particle source. The particle flux is expressed as $\Gamma = -D\nabla n + nV$, where D is the particle diffusivity and V is the convection velocity. A negative value of V indicates an inward particle pinch. The existence of the convection term makes estimation of the particle diffusivity difficult, because perturbative techniques, such as modulated gas puffing and density profile evolution, are then necessary to estimate separately the D and V . In DIII-D, particle transport coefficients were estimated for different operating modes by analysing the temporal evolution of the electron density profile with modulated gas puffing and immediately after the L–H transition [347]. The value of D increased with radius in the L-mode and ELMy H-mode plasmas and D at the edge for the L-mode plasma was about twice that for the ELMy H-mode plasmas. In the ELM-free H-mode plasmas, D decreased rapidly outside a normalized radius of about 0.8 and an inward pinch velocity was observed. The trace tritium transport experiments performed in TFTR [348] and JET [349] also provided valuable data for estimating D and V . In these machines, an inward pinch velocity was also observed. In TFTR, the tritium diffusivity in the central region of enhanced reversed shear plasma was smaller than that in the central region of reversed shear plasmas. However, the inward pinch velocity was almost the same for both plasmas.

Recent JET trace tritium experiments provided thermal tritium particle transport coefficients (D_T , V_T) and their dependence on dimensionless parameters in the wide variety of plasma operating regimes [350–352]. The values of D_T and V_T were found to substantially exceed neoclassical values in all regimes except in ELMy H-modes at high density, and in the region of ITBs in RS plasmas as shown in figure 30. In hybrid scenarios ($q_{\min} \sim 1$, low positive

shear, no sawteeth), increasing triangularity and plasma current increased particle confinement time, which can be explained in terms of a reduction in D_T , but transport remained in excess of neoclassical values. Comparing different regimes (ELMy H-mode, ITB plasma, and hybrid scenarios) outside the central plasma region ($0.65 < r/a < 0.80$), the tritium diffusion coefficient (D_T/B_t) scaled in a manner closer to gyro-Bohm ($\sim(\rho_{\theta*})^3$, where $\rho_{\theta*} = q\rho_*$), but with an added inverse β dependence. In contrast, for ELMy H-mode discharge pairs with all dimensionless parameters except ρ_* kept constant, gyro-Bohm behaviour was confined to the inner part of the plasma ($r/a < 0.4$), and the outer plasma behaved more like Bohm ($\sim\rho_*^2$). Similar dimensionless parameter scans established contrasting trends for particle confinement (increases with v_* and β) and energy confinement (decreases with v_* and independent of β) resulting in strong variation of the D_T/χ_{eff} ratio, i.e. between 0.3 (at high density and low q_{95}) and 2.0 (at low density and high q_{95}). This result seems contrary to results obtained in ASDEX Upgrade [206,353] and DIII-D [354]. In ASDEX Upgrade, strong linkage between particle and energy transport as $D \propto \chi$ (typically $D/\chi = 0.15\text{--}0.25$) was observed. In DIII-D, it was experimentally observed that the particle diffusivity and the thermal diffusivity do not differ greatly and have roughly the same radial dependence. In JT-60U weak positive shear and reversed shear plasmas, the electron effective diffusivity, defined only considering the diffusion term, was well correlated with the ion thermal diffusivity in the ITB region [208].

3.4.3. Mechanisms of inward pinch.

Neoclassical transport predicts a particle pinch driven by the toroidal electric field (i.e. Ware pinch). In ASDEX Upgrade high-density plasmas, the behaviour of the density profiles was described well with the assumption of $D \propto \chi$ (typically $D/\chi_{\text{eff}}^{\text{turb}} = 0.15\text{--}0.25$, where $\chi_{\text{eff}}^{\text{turb}} = \chi_e^{\text{exp}} + \chi_i^{\text{exp}} - \chi_i^{\text{neo}}$) and an inward pinch of the order of the Ware pinch [206,353]. In JET, a long timescale density peaking was observed, leading to plasmas with densities

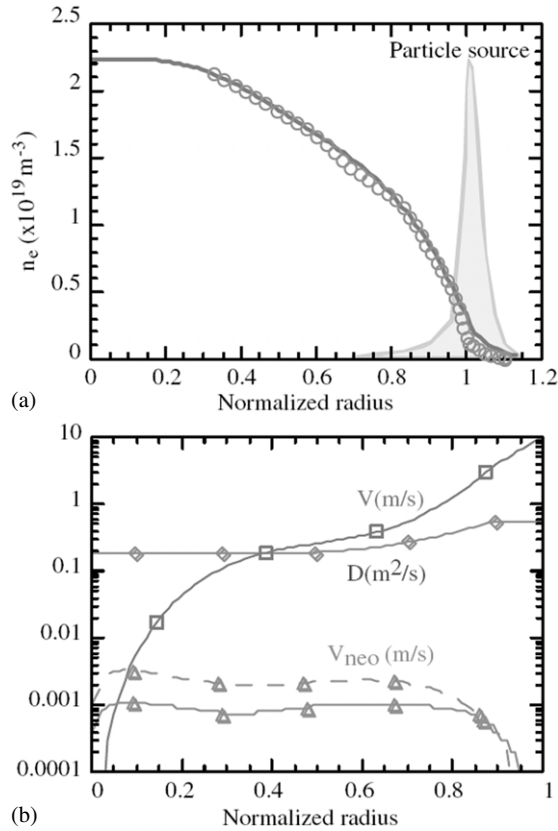


Figure 31. 1D simulation of discharge No 30428 with LHCD in Tore Supra, at $t = 30$ s: (a) density profile (line: simulation; circles: reflectometry measurements) and particle source profile; (b) pinch velocity (squares) and diffusion coefficient (diamonds) used to reproduce measured density profile, V_{neo} given by NCLASS (triangles), V_{neo} when assuming $Z_{\text{eff}} = 6$ instead of 2 and iron impurity only (dashed line/triangles). Reprinted with permission from [357]. © 2003 American Physical Society.

exceeding the Greenwald density, $n_G(10^{20} \text{ m}^{-3}) = I_p/\pi a^2$ (MA,m). The value of $D \cong 0.25\chi_{\text{eff}}$ and the Ware pinch gave an acceptable fit to the measured density profile [355]. While other analyses from JET indicated that an anomalous pinch seems to be necessary, at least for L-mode plasmas [356]. Clear experimental evidence for the existence of an anomalous inward pinch was shown in Tore Supra [357] and TCV [358], where peaked density profiles without central fuelling were observed with zero loop voltage. Figure 31 shows a density profile in a stationary, fully relaxed discharge in Tore Supra with current fully driven by the LH waves. To explain the shape of the experimental density profile, a particle pinch velocity of 2 orders of magnitude above the neoclassical value is required [357].

One of the candidate explanations to the puzzle of what conditions lead to the anomalous pinch was proposed in analysis of ASDEX Upgrade: collisionality plays a relevant role in determining the density peaking [359,360]. The density peaking measured in ASDEX Upgrade H-mode plasmas was shown to decrease with increasing collisionality as shown in figure 32. Analysis of an extensive database of JET H-mode plasma density profiles showed that the density peaking factor increases as the plasma collisionality decreases [361], which confirms the observation in ASDEX Upgrade. However, the transport analysis in ASDEX Upgrade indicated that the

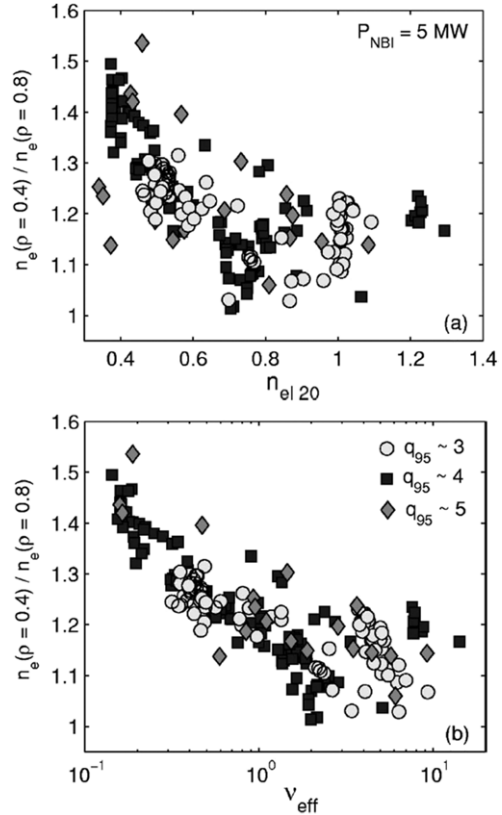


Figure 32. Density peaking, defined as $n_e(\rho = 0.4)/n_e(\rho = 0.8)$ versus the line-average density (in 10^{20} m^{-3}), panel (a), and versus v_{eff} , panel (b), for the subset of stationary plasmas in the ASDEX Upgrade H-mode database, with total NBI heating power of 5 MW. The effective collisionality, v_{eff} , is defined as $v_{\text{eff}} \equiv v_{\text{ei}}/\omega_{\text{De}}$ where v_{ei} is the electron-ion collision frequency and ω_{De} is the curvature drift frequency, $\omega_{\text{De}} \equiv 2k_{\perp}\rho_s c_s/R$. Reprinted with permission from [360]. © 2003 American Institute of Physics.

ratio of V/D is independent of collisionality [362]. The transport analysis in JET also indicated that the anomalous pinch was of the order of the Ware pinch, and the discharge with lower collisionality showed flatter density profiles in H-mode plasmas, while the effect of the anomalous pinch tended to increase at low collisionality in L-mode plasmas [356]. The dependence of the anomalous inward pinch on dimensionless parameters should be understood systematically as discussed above for the particle diffusivity in the future work.

3.4.4. Model of anomalous particle transport. Theory-based transport models have been developed to explain the experimental observations (also see sections 2.1 and 2.2). The experimental observation that the density peaking factor increases with decreasing collisionality was explained with a theory-based fluid transport model for ion temperature gradient and trapped electron modes, GLF23 [20]. It was shown that the anomalous particle inward pinch decreases with collisionality and the relative role of the Ware pinch becomes important at high collisionality. Other models have also been proposed to explain the anomalous particle inward pinch. Numerical simulations have confirmed that a turbulent particle pinch exists, which is mainly driven by magnetic field curvature and thermodiffusion [124]. In TCV, the best overall agreement

with a database was obtained with models combining an anomalous pinch mechanism, such as the curvature pinch, which is proportional to the gradient of the safety factor, with the Ware pinch [358]. The multi-mode model, in which the ion temperature gradient modes, trapped electron modes and drift-resistive ballooning modes as well as smaller contributions from kinetic ballooning modes are included, provided a good match to density profiles in TFTR plasmas [238]. A canonical profile depending on the ratio of the diffusion coefficients for passing and trapped particles was compared favourably with the experiments in DIII-D [363]. When the sources can be neglected, a crucial parameter determining the shape of the density profile was the relative transport between the passing and trapped particles. In Alcator C-Mod plasmas without a central particle source, the outflow was driven by the TEM turbulence in the internal transport barrier and it was balanced by the inward Ware pinch, leading to steady-state [123]. Many models have been proposed as described above, but a clear answer is still missing for mechanisms driving the anomalous transport.

3.4.5. Effects of density peaking on confinement. One of the main physics issues for ITER standard operation is sustaining good H-mode confinement in high density close to Greenwald density. Several methods have been discovered as described in section 2.7 of chapter 4 of this issue [364]. Related to particle transport, good H-mode confinement has been obtained with peaked density profiles in the high-density region. Figure 33 shows a DIII-D discharge with a good H-mode confinement, $H_{L89} \approx 2$ (i.e. defined relative L-mode scaling), where a continuous rise in the line-averaged density up to $\bar{n}_e \approx 1.4n_G$ was obtained at low constant gas puff rate [365]. The pedestal density in this discharge quickly saturated at $n_{ped} \approx 0.8n_G$, and further \bar{n}_e increase was entirely due to density peaking. Similar discharges have been obtained in ASDEX Upgrade [353] and JET [355]. The slow density peaking considered as a main contributor to improved confinement at high density seems to be a result of the neoclassical particle pinch described above. In JT-60U weak and reversed shear plasmas, high confinement was achieved at density above the Greenwald density by tailoring the density ITB [366]. Stable H-mode operation beyond the Greenwald density was obtained with high field side pellet injection in ASDEX Upgrade [367]. Deeper fuel penetration was achieved with high field side injection due to a rapid movement of the ablatant towards the outer major radius attributed to a vertical curvature and ∇B drift current induced inside the ionized ablated material. The deep pellet fuelling allows higher central densities to be achieved compared with those with strong gas puffing and similar edge densities. See section 2.7.3 for more discussion of pellet fuelling and its impact on divertor operation.

Density peaking is effective for achieving high average density with relatively low edge density. However, its direct effects on confinement improvement are not clear in the above discharges. The clearest effects were found in impurity seeded plasmas. Enhanced confinement regimes with impurity seeding such as the RI-mode in TEXTOR [368] have been demonstrated more recently in high-density discharges in DIII-D [369] and JET [370]. The effect of impurity seeding on plasma confinement is explained by reduction

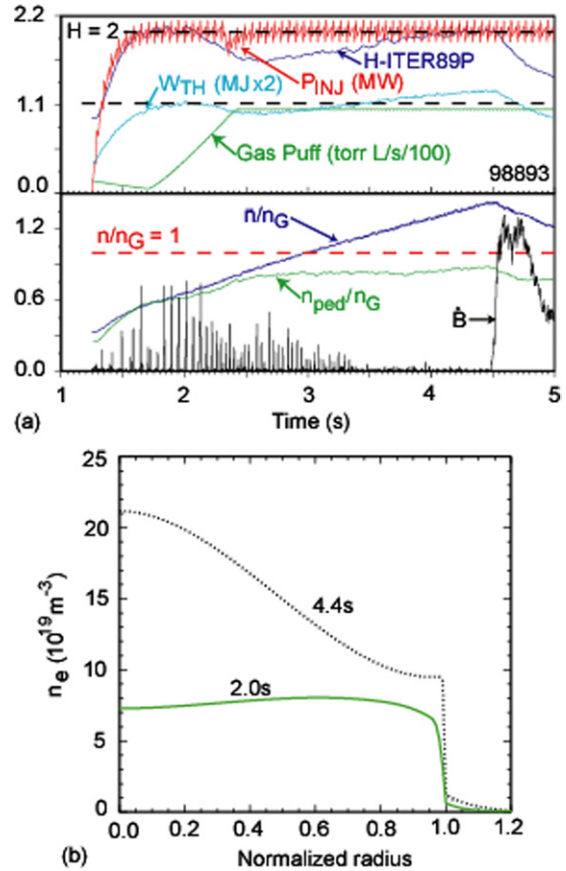


Figure 33. (a) Time behaviour of the plasma stored energy W , normalized energy confinement time relative to ITERL-89P scaling, gas puff rate, line-averaged and pedestal density normalized to the Greenwald density, and amplitude of a $3/2$ MHD mode, as measured by Mirnov coils, in high-density DIII-D discharge. (b) Density profiles at $t = 2$ s (just after the onset of gas puffing) and at $t = 4.5$ s (near the end of discharge). Reprinted with permission from [365].

of the ITG mode growth rate due to a Z_{eff} increase and a peaking of the density profile caused by an anomalous particle pinch driven by the dissipative trapped electron (DTE) mode in combination with the effect of the $\vec{E} \times \vec{B}$ shearing rate [213, 371].

3.4.6. Prediction of ITER density profile. The importance of the inward pinch increases in a fusion reactor due to low central particle fuelling. In the present ITER design, a flat density profile is usually assumed [372]. However, as shown in figure 34 [373], moderately peaked density profiles due to the anomalous inward pinch can be expected in ITER according to predictions of the GLF23 transport model and the theory of turbulent equipartition (TEP) [374, 375]. If a peaked density profile is obtained in ITER due to an inward pinch even with edge particle fuelling, higher fusion gain will be achieved. However, strongly peaked density profiles in ITER should be avoided since they may provoke an early onset of the neoclassical tearing modes (NTMs) or undesirable central accumulation of high Z impurities.

3.4.7. Density profile control. Density profile control is important not only for burn control but also for suppression

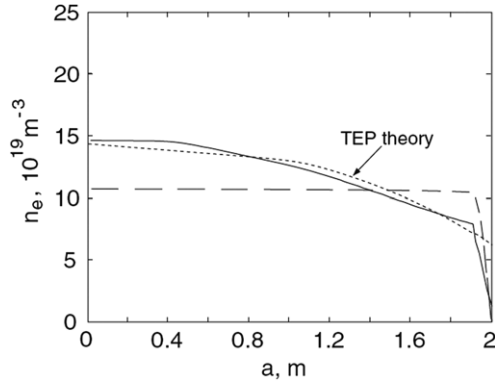


Figure 34. Steady-state distributions of the plasma density, n_e as a function of the minor radius in the reference ITER inductive scenario (15 MA, $Q = 10$). Full curve shows the results of the GLF23 model with the boundary conditions $n_{e,\text{ped}} = 0.79 \times 10^{20} \text{ m}^{-3}$ and $T_{e,\text{ped}} = 5 \text{ keV}$ at the pedestal top. Results of the scaling-based model are shown as the broken line. The dotted line shows the prediction of the turbulent equipartition (TEP) theory, where the shear profile is defined by the GLF23 modelling. Reprinted with permission from [373].

of impurity accumulation as will be described later. In ASDEX Upgrade [206], a strong linkage between D and χ was observed in the work described above. The variations in the heat flux profile have a strong effect on the χ -profile as well as on the D -profile due to the generally observed self-similarity of the temperature profile. Consequently, on- and off-axis heating led to flat and peaked density profiles, respectively. Particle depletion from the plasma core was observed with centrally deposited ECH and ECCD in TCV [376]. The correlation of density pumpout with the loss of axisymmetry suggested that neoclassical transport processes involving locally trapped particles near the helically displaced magnetic axis might account for the phenomenon. The flattening of the density profile by ECH is commonly observed not only in tokamaks but also in helical devices, so studies that develop a common physics basis for transport in toroidal plasmas might help improve the understanding of mechanisms responsible for the density profile flattening by ECH. A similar particle depletion was observed in DIII-D quiescent double-barrier (QDB) plasmas [377] and JT-60U weak positive shear plasmas with Ar accumulation [208] by applying central ECH, and in Alcator C-Mod [378] by applying central ICRF, which were accompanied by impurity exhaust from the inside of the ITB as discussed below. In T-10, a peaked density profile was obtained after pellet injection even with ECH [379].

3.4.8. Impurity transport in ELMy H-mode and enhanced confinement regimes. Impurity transport in standard ELMy H-mode plasmas exhibits a variety of behaviours, which is strongly influenced by the main ion density and temperature profiles and sometimes a function of the impurity charge, plasma rotation and other parameters as well. Intrinsic carbon and neon in JET ELMy H-mode plasmas [380] were found to have similar transport properties and both had hollow profiles. Strong outward convective velocities in the core were consistent with neoclassical temperature gradient screening in these plasmas where the electron density was relatively flat. In the edge region, $r/a > 0.8$, an (anomalous) impurity pinch

along with strong ELM mixing was needed to simulate the impurity profiles. He, C, Ar and Ne in DIII-D H-mode plasmas also showed no tendency to accumulate in any local region when the electron density is relatively flat [381].

In more detailed studies, the temporal evolution of impurity transport has been used to separately determine the diffusivity and pinch contributions to the impurity fluxes as a function of the charge. In ASDEX Upgrade [382] the temporal evolution of impurity profiles between sawtooth crashes showed radially increasing particle diffusivities for Ne, Ar, Kr and Xe. The diffusivities and convective velocities were close to neoclassical for the lower Z species (Ne and Ar), while both the diffusivities and inward drift velocities were much stronger than neoclassical for the higher Z species. High toroidal rotation was not taken into account in the neoclassical calculations and may have influenced the behaviour. In DIII-D [183], the transition from H-mode to VH-mode led to a transient response from peaked to hollow impurity profiles where the diffusivities and convective velocities of various impurities could be determined [383]. The flat electron density and strongly peaked ion temperature profiles in the low turbulence VH-mode plasmas allowed a confirmation of the neoclassical ion temperature gradient screening contribution (including its increasing strength with charge) to the outward convective velocity, even though the diffusivity was strongly governed by turbulence. The temperature gradient screening effect should have a favourable effect on higher Z impurity profiles in low collisionality plasmas such as ITER even when turbulent diffusivity dominates over neoclassical [384].

The transport of impurities in enhanced confinement regimes, especially those with internal transport barriers (ITBs), is a critical issue in burning plasma regimes due to the possibility of excessive fuel dilution caused by accumulation of impurities, including helium ash. Because the turbulence-driven transport in these regimes is relatively small, the effect of collision-driven transport (i.e. neoclassical transport) becomes increasingly important and in some cases may dominate the transport properties. The effect of neoclassical transport is particularly acute in regimes that have peaked density profiles due to the strong dependence of the impurity convection on the background density gradient. To first order, neoclassical theory predicts that $V_Z^{\text{neo}}/D_Z^{\text{neo}}$ to be strongly dependent on the ion density gradient and weakly dependent on the ion temperature gradient: $V_Z^{\text{neo}}/D_Z^{\text{neo}} \approx g_{n_{D \rightarrow Z}} \nabla n_D / n_D + g_{T_i} \nabla T_i / T_i$ where $g_{n_{D \rightarrow Z}}$ and g_{T_i} are complex functions of the impurity charge Z , plasma collisionality ν_* , and magnetic geometry. Generally, $g_{n_{D \rightarrow Z}} > 1$ and $g_{T_i} < 1$ in the banana regime of transport (i.e. $\nu_* < 1$) and $|g_{n_{D \rightarrow Z}}| \gg |g_{T_i}|$, with both increasing in magnitude strongly with Z . There are several ramifications apparent from this formula. First, in the cases with strongly peaked density profiles (and low levels of turbulence-driven transport), preferential accumulation of impurities in the core region would be expected regardless of the magnitude of the ion temperature gradient. Second, the degree of accumulation would be strongly Z dependent with the higher Z impurities showing stronger preferential accumulation. Third, in the cases with flat density profiles but a strong ion temperature gradient, hollow impurity density profiles would result due to the outward transport associated with ∇T_i . Finally, preferential accumulation of helium ash

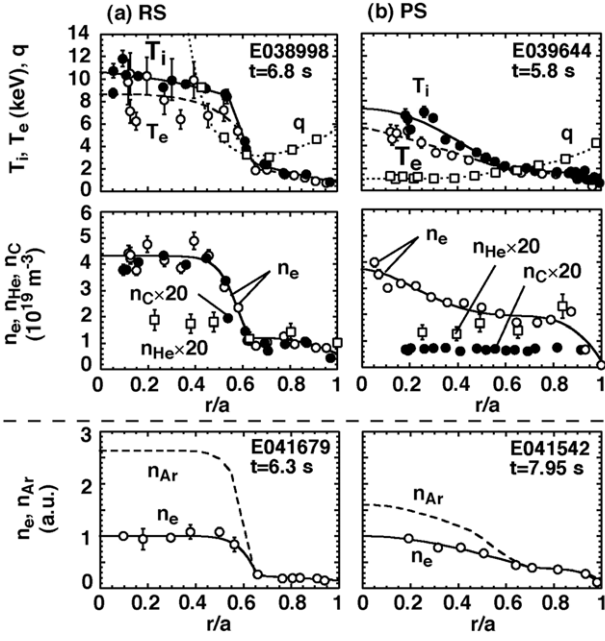


Figure 35. (Upper figures) profiles of T_i , T_e and q , (middle figures) profiles of n_i , n_e , n_{He} and n_{C} , (bottom figures) profiles of n_e and n_{Ar} in (a) reversed shear plasma ($I_p = 1.3$ MA, $B_T = 3.7$ T, $q_{95} = 4.9$ – 5.2 and $HH_{y2} \sim 1.6$) and (b) weak positive shear plasma ($I_p = 1.0$ MA, $B_T = 2.0$ – 3.8 T, $q_{95} = 3.7$ – 6.3 and $HH_{y2} \sim 1.0$). In the bottom figures, n_e is normalized at $r/a = 0$ and n_{Ar} is adjusted to n_e outside the ITB. Reprinted with permission from [208].

due to neoclassical transport is expected to be weak (but still present) due to its low Z . Note that this does not preclude accumulation of helium ash due to differences in the sources of helium and the fuel mix.

Experiments tend to support the predictions of neoclassical impurity transport in regimes with enhanced confinement. However, there are few instances in which both the measured particle diffusivity and convective velocity are found to be consistent with neoclassical predictions. The earliest of the studies on ITB plasmas was done on TFTR using perturbative gas injection to measure D_Z and V_Z simultaneously [348, 385]. The inferred diffusivities for deuterium, helium and carbon were found to be consistent with neoclassical predictions, within the uncertainties of the measurement and theoretical prediction. Subsequent studies in JT-60U RS plasmas [386], JET strong ITB plasmas [205, 387] and DIII-D QDB plasmas [388] showed the strong Z dependence of V_Z predicted by neoclassical theory even at relatively low Z (helium to neon). In the JT-60U (He) and JET cases, the measured D_Z is found to be consistent with neoclassical predictions in the ITB region while in the DIII-D and JT-60U (C and Ar) cases the measured D_Z is significantly higher than the neoclassical prediction. In all the cases, either strong accumulation or long confinement times of higher Z impurities (argon in JT-60U, nickel in JET and nickel and calcium in DIII-D) are observed. Typical profiles of electron and ion temperatures, safety factor and densities of electron, helium, carbon and argon in JT-60U are shown in figure 35 for (a) reversed shear and (b) weak positive shear plasmas with ITB. Note that all of these regimes have strongly peaked electron (and, hence, deuterium ion) density profiles, which according to neoclassical theory should result

in an even more strongly peaked impurity density profile. The helium density has not been observed to be strongly peaked in any of the experiments, because it is a low Z impurity. The helium diffusivity and convection velocity estimated in JT-60U indicated the possibility of sufficient helium exhaust even in ITB plasmas [386]. For more discussion of He exhaust see section 2.3 of chapter 4 of this issue [364].

3.4.9. Impurity control. The application of ECH inside the ITB region has been shown to be effective in reducing the level of impurity accumulation in experiments on JT-60U [208] and ASDEX Upgrade [206]. The application of on-axis ICRF heating is also shown to be effective in reducing the density and impurity peaking in Alcator C-Mod [378]. In both cases, the reduced impurity accumulation is attributed to a reduction in the background density gradient, leading to a marked decrease in the inward convection of impurities. Figure 36 shows JT-60U case [389], where both electron and argon density profiles become flatter during ECH injection. The flattening of the argon density profile is consistent with the reduction of the neoclassical inward convection velocity due to the reduction of background plasma density gradient. In contrast, observations in enhanced confinement regimes with flat density profiles indicate that neoclassical transport can play a beneficial role in screening impurities from the core. In particular, experiments in DIII-D VH-mode plasmas [383, 390] confirmed the existence of the ‘temperature screening’ effect of neoclassical impurity transport as shown in figure 37, including the predicted Z dependence. The observed outward convection led to extremely hollow carbon and neon density profiles in these plasmas. In the enhanced confinement regime in JET impurity seeding plasmas [370] with high triangularity configuration and continuous D_2 puffing, an outward impurity convection velocity was also observed, which features flat or slightly hollow impurity profiles and high radiation from a narrow region at the edge [391]. In DIII-D argon seeded plasmas, a hollow Z_{eff} profile was observed [369].

3.4.10. Impurity transport in burning plasmas. Observations to date are consistent with a transport model that combines turbulence-driven and collisional transport in a linear fashion:

$$\Gamma_Z = -(D_Z^{\text{turb}} + D_Z^{\text{neo}})\nabla n_Z + n_Z(V_Z^{\text{turb}} + V_Z^{\text{neo}}). \quad (9)$$

Theoretically, this is valid since the particle transport due to fluctuations results from collective mechanisms that have structures much larger than the characteristic scale length for collisional momentum exchange between particles, allowing one to treat the processes separately. Because of the extremely low value of D_Z^{neo} in most cases, D_Z^{turb} is expected to dominate the total diffusivity. However, the strong Z dependence of V_Z^{neo} can make it such that collisional effects dominate impurity convection in certain situations. Hence, it is possible to observe effects of neoclassical transport even in plasmas in which $D_Z^{\text{turb}} > D_Z^{\text{neo}}$ and also to have impurity density profiles that are significantly different from the profile expected purely from either turbulence-driven or neoclassical transport. This has been shown to be the case in analysis of experiments on DIII-D [383] and JET [205]. Applying this type of model to burning

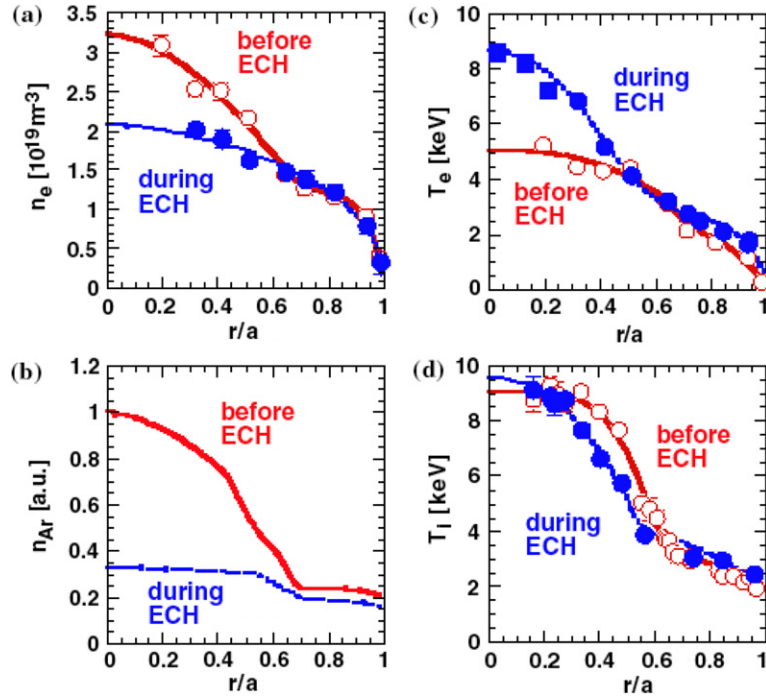


Figure 36. Argon exhaust with EC heating in a high β_p mode plasma. Profiles of (a) electron density n_e , (b) argon density n_{Ar} , (c) electron temperature T_e and (d) ion temperature T_i before and during EC heating. Profiles before EC heating are denoted by solid lines (with open symbols), while those during EC heating are denoted by dotted lines (with closed symbols). Reprinted with permission from [389].

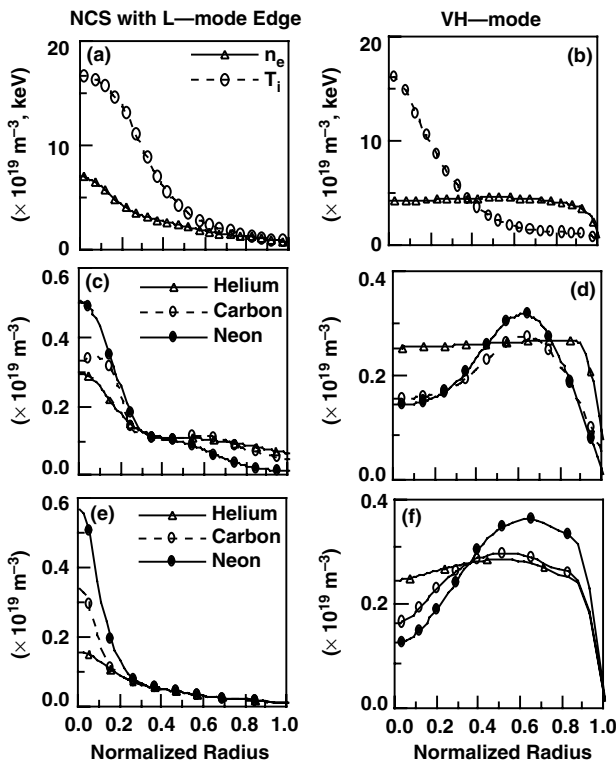


Figure 37. (a)–(b) Measured electron density and ion temperature profiles, (c)–(d) measured helium, carbon and neon density profiles (normalized) and (e)–(f) computed helium, carbon and neon density profiles using the transport model in an NCS and VH-mode discharge in DIII-D. Reprinted with permission from [390].

plasma conditions, it has been shown that the combination of reduced turbulence-driven transport and peaked density profiles (typical of ITB plasmas) lead to stringent constraints on the allowable level of low Z impurities for ignition [390]. In contrast, flat density profiles are found to be beneficial, allowing a significantly higher impurity level than their ITB counterparts.

3.4.11. Summary. Significant progress has been achieved in experimental studies and theory-based modelling of particle and impurity transport. Since density profile has a large impact on the plasma performance in a fusion reactor, further systematic understanding of particle confinement and transport is required. The dependence of particle transport coefficients on dimensionless parameters should be investigated for systematically understanding collisionality dependence of the density peaking. Recent studies indicate that the density profile could be peaked even with low central fuelling for ITER standard operation due to the turbulent driven inward pinch. On the other hand, in ITER steady-state operation with reduced turbulent transport, it is important to investigate whether a peaked density profile and a density ITB can be obtained under the reactor-relevant conditions of low central fuelling. Furthermore, the optimum density profile for achieving high fusion gain without strong impurity accumulation should be investigated together with the establishment of control methods for the density profile and impurity accumulation in the future work.

3.5. Toroidal momentum transport and spontaneous rotation

Experiments and simulations of toroidal momentum transport in tokamaks have demonstrated that transport of toroidal

rotation is determined by mechanisms similar to those driving particle and energy transport [392, 393]. Toroidal momentum transport is generally found to be anomalous, with χ_ϕ much larger than neoclassical values. Moreover, the viscosity coefficient, which is responsible for the radial transport of toroidal rotation, is reduced inside ITB similar to the diffusion and thermal heat conductivity coefficients. This was demonstrated by many simulations using various transport models for DIII-D [394, 395], JET [396, 397], Alcator C-Mod [398], MAST [393, 399] and other tokamaks. We briefly discuss the response to an applied torque, and then address the issue of rotation in the absence of a strong torque in more detail because of its greater relevance to burning plasmas like ITER. The behaviour of toroidal rotation in the vicinity of an ITB is of particular interest because of its influence on triggering and/or sustaining the barrier.

3.5.1. Transport in the presence of strong applied torque.

The toroidal rotation induced by NBI in machines such as JET, DIII-D, JT-60U and ASDEX Upgrade to a large extent determines the radial electric field in the core, see e.g [333, 397]. The toroidal rotation profile hence is an important element in ITB formation. It may influence transport coefficients through creation of shear in the $\vec{E} \times \vec{B}$ drift and suppression of turbulence levels. This is similar to the situation that one might expect for burning plasma conditions. Indeed, even without NBI heating one might obtain strong enough toroidal rotation in the core to increase the radial electric field.

3.5.2. Spontaneous rotation.

Toroidal rotation in the absence of NBI (in Ohmic or ICRF heated plasmas) has been observed in Alcator C-Mod [398, 400–402], MAST [403, 404], JET [405, 406], Tore Supra [407, 408] and other machines. It is especially large in the H-mode. The toroidal rotation is co-current directed, and according to [398] the change of toroidal rotation after the L–H transition is $\Delta V_\phi = k\Delta W/I_p$, where $k \sim 0.1$, V_ϕ is in km s^{-1} , the stored energy ΔW is in kJ, plasma current I_p is in MA. For Tore Supra [407] the coefficient k is a factor of 2 less, possibly related to the relative machine size. On MAST the direction of the toroidal rotation changed from the co-current to the counter-current direction when switching from inboard to outboard gas puffing. Strong counter-current rotation has been observed in DIII-D plasmas with ECH [409], which further demonstrates the possibilities of rotation drive in the absence of external momentum input. The rotation is counter-current in the centre and co-current near the plasma edge, and depending upon the ECH resonance location, the velocity shear profile can be controlled.

Several mechanisms might be responsible for the generation of the toroidal rotation in the absence of external NBI torque, and several theoretical models have been put forward. In [410, 411] the neoclassical torque in the Pfirsch–Schlüter regime has been calculated. The role of neutral viscosity in the framework of neoclassical theory has been considered in [412, 413]. However, since from many experiments it is known that the toroidal momentum is transported in the radial direction with transport coefficients similar to those for particles and energy, the pure neoclassical approach might be not sufficient.

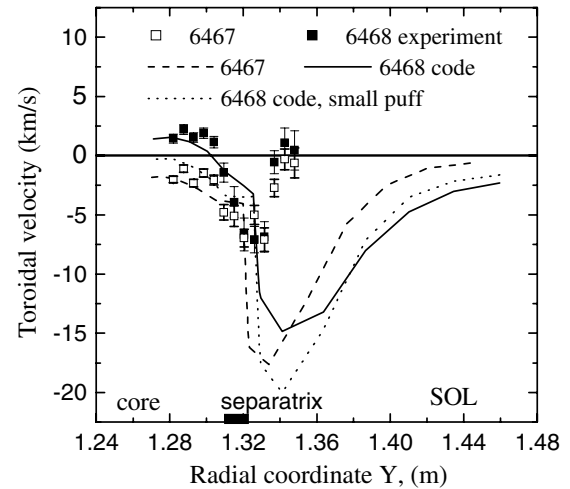


Figure 38. Toroidal velocity in MAST at the outer midplane for shot Nos 6467 (outboard puff) and Nos 6468 (inboard puff). Simulations were performed with the B2SOLPS5.0 transport code. Reprinted with permission from [414].

In [414] a mechanism for toroidal rotation generation in the edge plasma by inboard/outboard gas puff was suggested. The inboard gas puff leads to more counter-current directed toroidal rotation at the outer midplane. It is demonstrated that counter-current toroidal torque can be generated by inboard gas puff by creating inboard/outboard parallel fluxes associated with the ionization source on the closed field lines. These fluxes are transported by the vertical ∇B ion drift providing counter-current acceleration. Simulations performed for MAST by B2SOLPS5.0 transport code are consistent with experimental observations, as shown in figure 38. The positive direction here corresponds to the counter-current direction, so indeed for the case of inboard gas puff the toroidal rotation is more positive than for the case of outboard gas puff.

In [415] the effect of ITG modes on the generation of toroidal rotation has been considered. It was shown that a specific feature of the ITG modes, i.e. the dependence of the frequency on the radial toroidal velocity gradient, causes inward transport of toroidal momentum at the edge plasma. It is not, however, quite clear whether the ITG modes are excited in the edge region, since it is possible that the parameter $\eta_i = d \ln T_i / d \ln n$ is not large enough within the edge transport barrier. An inward pinch of the toroidal momentum was also predicted in [416]. The convective term was calculated using a combination of the quasi-linear and neoclassical approaches for the banana regime. This convective term exists independently of the type of the electrostatic turbulence. Since both models [415] and [416] predict an inward pinch of the toroidal momentum, the resulting steady-state profile of the toroidal velocity should depend on the steady-state density and temperature profiles, i.e. on the edge values of the density, temperatures and toroidal rotation.

Another attempt to explain the co-current rotation observed in ICRF heated H-mode discharges is through the toroidal torque provided by the radial electric field arising due to orbit shifts of high energy ions generated by ICRF waves [417–420]. A particular prediction of some of these theories [418, 420] is that the rotation should switch direction to counter-current with the ICRF resonance located on the

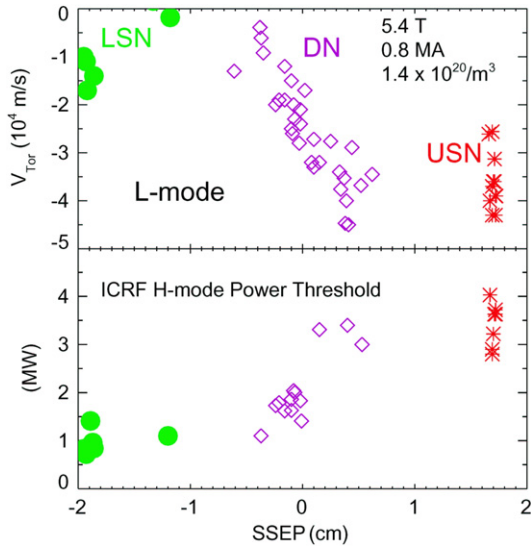


Figure 39. The central toroidal rotation velocity in Alcator C-Mod during the L-mode portion of LSN (green dots), DN (purple diamonds) and USN (red asterisks) 0.8 MA, 5.4 T discharges with $n_c = 1.4 \times 10^{20} \text{ m}^{-3}$ as a function of distance between the separatrices SSEP is shown in the top frame. In the bottom is the minimum ICRF power required to induce L–H transition as a function of SSEP. Reprinted with permission from [424].

high magnetic field side, which was not observed in the experiments [398].

Modelling of the toroidal rotation profile in ICRF and Ohmic H-mode discharges was performed for Alcator C-Mod without momentum input in [421, 422]. A simple model was used

$$\frac{\partial n m_i V_\phi}{\partial t} + \frac{1}{r} \frac{\partial}{\partial r} r \left[-D_\phi \frac{\partial}{\partial r} (n m_i V_\phi) - \frac{V_c r}{a} n m_i V_\phi \right] = 0. \quad (10)$$

The toroidal momentum diffusivity D_ϕ was $\sim 0.2 \text{ m}^2 \text{ s}^{-1}$ in the L-mode and $\sim 0.07 \text{ m}^2 \text{ s}^{-1}$ in the H-mode. In ELM-free H-mode the profiles were consistent with an inward convection velocity of the order of 10 m s^{-1} . The values of the transport coefficients were significantly larger than the neoclassical predictions.

In the Alcator C-Mod experiments [421, 423, 424] the role of the edge plasma in the formation of the central toroidal rotation in the absence of the toroidal momentum torque has been emphasized. When switching from lower single null to the upper single null divertor configuration (with the ion $\vec{B} \times \vec{\nabla} B$ drift downward), the edge toroidal rotation changed sign from co-current to the counter-current direction [424]. This is illustrated by figure 39, where the central toroidal rotation in the L-mode of Alcator C-Mod is plotted versus the distance between two separatrices. This seems to play a role in the higher H-mode power threshold for upper single null discharges. Similar indications were observed on MAST [403, 404].

3.5.3. Toroidal rotation in the vicinity of an ITB. In the presence of an ITB a drop in toroidal rotation is usually observed [396, 425]. An example of the toroidal rotation profile with an ITB in the presence of NBI is shown in figure 40 for

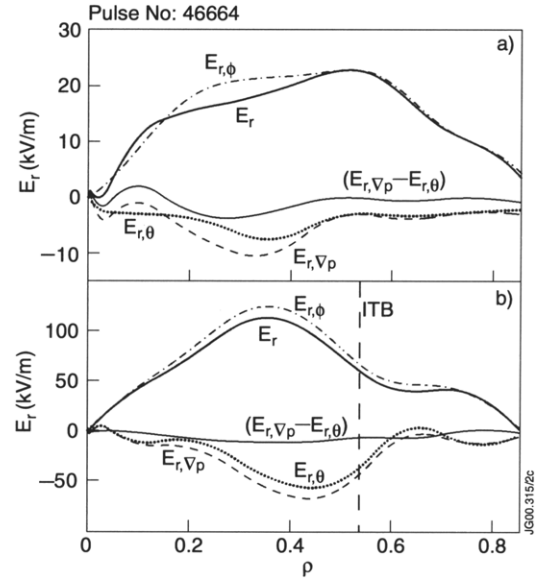


Figure 40. E_r and its components 0.6 s before (a) and 0.6 s after (b) the ITB formation. The main component $E_{r,\phi}$ is proportional to the toroidal rotation velocity. The footpoint of the ITB is shown by the vertical dashed line in (b). Reprinted with permission from [397]. © 2001 Institute of Physics.

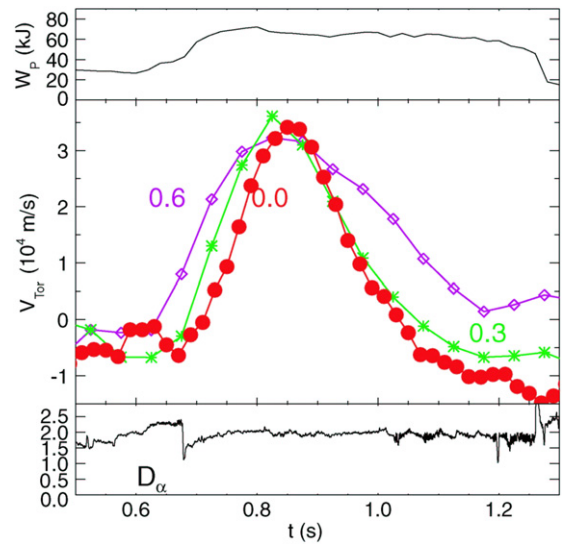


Figure 41. The plasma stored energy, impurity toroidal rotation velocity at three radii and the edge D_α brightness for an off-axis ICRF heated ITB discharge. Reprinted with permission from [421].

JET [397]. One can see the rise of the $\vec{E} \times \vec{B}$ shear in the barrier vicinity. Without NBI the toroidal rotation profile was measured on Alcator C-Mod, figure 41 [421]. The hollow profile in the centre indicates the presence of a negative electric field in the vicinity of the barrier.

There is concern for ITER that the possibility of no external torque from neutral beam injection will preclude any of the beneficial effects desired from rotation and velocity shear: ITB formation and resistive wall mode suppression. While the mechanism responsible for the generation of spontaneous rotation observed on many devices is not well understood, it is promising that ICRH and ECH may provide

control knobs for rotation and velocity shear production, and allow ITB formation without NBI.

3.5.4. Conclusions. As presented above there are many effects in plasma rotation generation and transport that cannot be explained with existing theoretical models. Therefore we can conclude that our present understanding of the transport of toroidal momentum is incomplete and the mechanisms of generation of toroidal rotation in the absence of NBI are not completely understood. Further investigations are necessary, but there is promise for velocity (and shear) generation in future devices without external momentum input. Scaling and parameter studies of spontaneous rotation are ongoing on a variety of devices with the goal of extrapolation to ITER.

3.6. Dimensionless parameter scaling experiments

Most experimental investigations of transport seek to isolate the dependence of the transport on one or more of the control (or ‘engineering’) variables that can be set by the experimenter, such as the toroidal field or the plasma current. However, the underlying equations believed to govern the plasma behaviour are sensitive only to algebraic combinations of these engineering variables that can be cast in dimensionless form [426]. Therefore, posing experiments where these dimensionless parameters are varied individually may have significant benefits in both understanding and projection to future devices. For example, different models for plasma turbulence yield significantly different scalings with respect to dimensionless parameters [426]. Therefore, measurement of these scalings may eliminate large classes of potential candidates to explain anomalous plasma transport. Another advantage of this approach is that the projection to burning plasma experiments from present-day transport experiments can be reduced to a one-parameter extrapolation, compared with the standard engineering variable approach with five or more variables [427]. In this section, recent experimental results and interpretation will be discussed. The use of the dimensionless scaling approach to prediction of transport in future devices will be discussed in section 5.4. Comparison of statistical analysis of the international global energy confinement database with the experimental determinations of confinement scaling using dimensionless parameters will be discussed in section 5.3.

The choice of dimensionless parameters is clearly a crucial step in this approach to understanding transport. The formal theory of dimensional analysis [428] tells how many parameters are required and sets the algebraic form they must take. However, any linearly independent combination is also suitable. The approach adopted in most experiments is to choose variables that have physical significance [426]. The standard set of variables includes the particle gyro-radius normalized to the minor radius of the plasma (ρ_*), the ratio of the kinetic energy density to the magnetic energy density (β), the collision time normalized to the particle transit time (ν_*), the plasma flow velocity normalized to the ion sound wave velocity (M) and the number of particles in the Debye sphere (N_D). These parameters uniquely specify the plasma conditions. The device geometry also may be important for transport, but the parameters defining the geometry are written

in terms of ratios of like-dimensional quantities such as aspect ratio or elongation. The plasma safety factor also belongs to this latter category. Finally, since the plasma is composed of multiple species of particles, the ratios of the quantities among the species such as mass and charge can appear, as can ratios of the various moments of the distribution between species, such as the ratio of the electron temperature to the ion temperature.

It is not possible to obtain plasmas in two different tokamaks in which all of these dimensionless parameters are fixed. However, the parameter N_D is typically 10^9 larger than the other dimensionless parameters. Therefore, it is assumed that mismatches in this variable are ignorable for transport physics, which is equivalent to ignoring very fast or very small scale effects. To validate this assumption, so-called ‘identity’ discharges have been made between pairs of tokamaks. These discharges match the remaining dimensionless parameters (other than N_D) and then test whether the measured transport scales in a manner predicted by the dimensional analysis, given the choice of dimensionless parameters.

The approach outlined above has now been validated in both L-mode and H-mode experiments [429]. An example for H-mode plasmas in DIII-D and JET is shown in figure 42. Over the region where the dimensionless parameters are well matched, $0.35 < \rho < 0.85$, the measured energy transport scales as predicted by the dimensional analysis. The same type of match was obtained in L-mode plasmas between Alcator C-Mod and DIII-D [429]. It must be emphasized that all the engineering parameters are different in these experiments, yet the dimensionless parameters which describe the intrinsic properties of the plasmas are held fixed. The mere fact that the profiles can be made to agree, with control only over global quantities, is a substantial confirmation that the variables chosen are an appropriate set to describe the plasma. The match of the properly normalized diffusivities indicates that plasma energy transport can be described by means of algebraic combinations of these variables. Furthermore, any quantities of importance that were not considered are either matched fortuitously or the dependence of the transport on these quantities is sufficiently weak that the mismatch can be ignored. For example, the mismatches in toroidal rotation and Z_{eff} , shown in figure 42, are either insignificant or lead to coincidental offsetting errors.

A case in which the chosen variables do not describe the plasma behaviour has been published recently [430]. Many authors have quoted confinement quality degradation as a function of the proximity to the empirical density limit ($n_G \equiv I_p/\pi a^2$), where n_G is the line-averaged density in units of 10^{20} m^{-3} , I_p is the total plasma current in MA and a is the midplane minor radius in m. It has been proposed that n/n_G , along with ρ_* and β , might be a better dimensionless set than the one described above with ν_* . In order to test this hypothesis, identity discharges between JET and DIII-D were found. The first observation was that it was not possible to match the profiles of the normalized plasma parameters with this choice of variables (see figure 43) [430]. Given this mismatch, it is not surprising that the global energy confinement did not match the identity constraints. Because the proposed variable n/n_G contains integral quantities rather than purely local quantities, this failure to realize a match may not be too surprising. It seems inappropriate, however, to reverse the argument in order to refute that the density limit is related to transport [431].

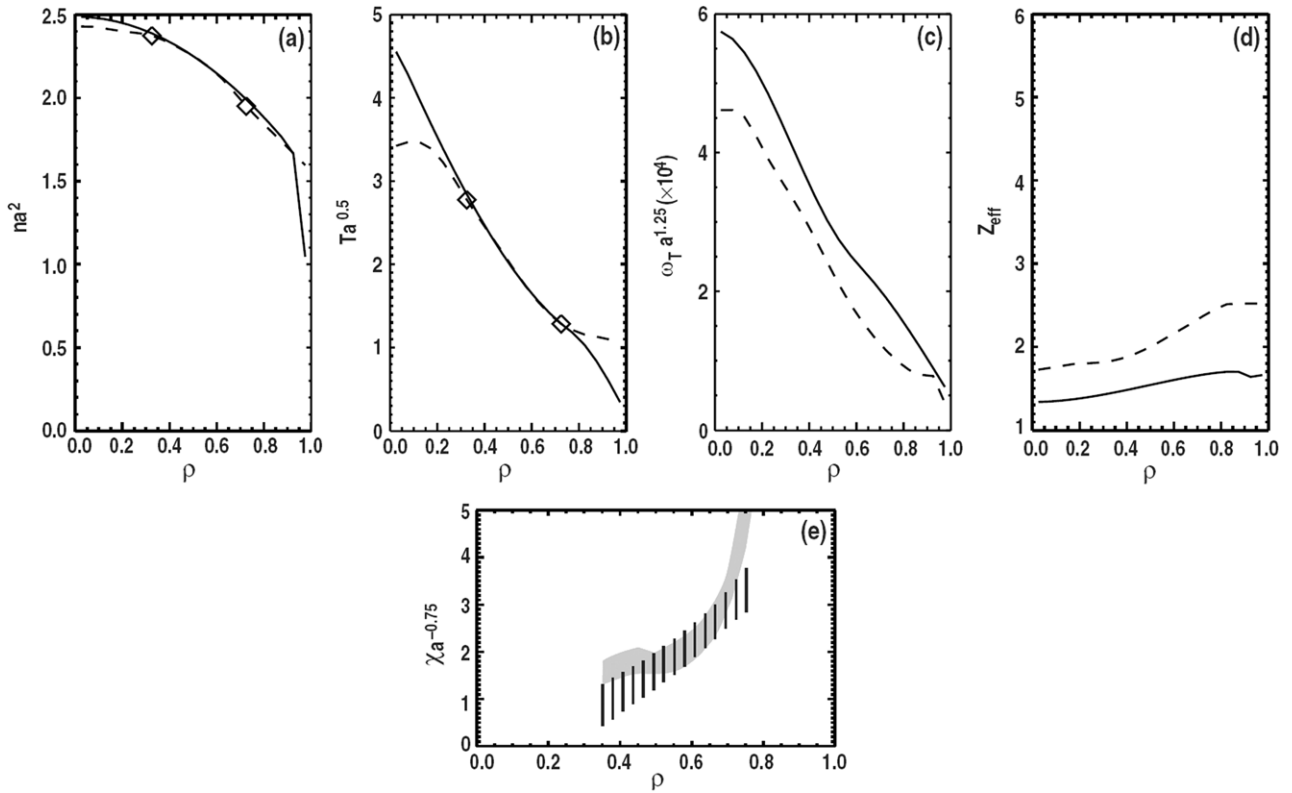


Figure 42. Comparison of the fitted or inferred scaled parameters for identical ELMing H-mode discharges in DIII-D (solid lines) and JET (dashed or shaded lines) as a function of normalized radius: (a) scaled density (b) scaled temperature, (c) scaled toroidal rotation, (d) Z_{eff} and (e) scaled one-fluid diffusivity (with uncertainties). Reprinted with permission from [429].

Significant new work on the scaling of energy transport with β has been published. Earlier work on DIII-D [225] and JET [228] indicated that energy confinement was practically independent of β in both L-mode and H-mode plasmas. Analysis of the international database of global energy confinement in L-mode and H-mode plasmas consistently yielded a strong degradation of energy confinement with β . The β scaling does not affect the projection to ITER using the dimensionless scaling method, since β in the two cases should be the same. However, the β scaling has a significant impact on the optimization of tokamak fusion performance [432]. This is discussed further in section 5.4. In order to resolve the discrepancy between the database analysis and the experiments, confinement scaling scans in H-mode have been extended to a larger range in β . The independence of transport from β over the range from just above the L–H threshold up to 90% of the ideal ballooning limit has been verified with multiple point scans [432, 433]. The experimental database is summarized in figure 44, along with the β scaling implicit in the IPB98y, 2 confinement scaling [2]. Recent work on the method of analysis of the global database [434] has improved the agreement of the database result with the experimental data (see section 5.3).

The complete independence of confinement on β is somewhat surprising from theoretical considerations. Increasing β increases the coupling between drift waves and Alfvén waves. For β well below the ideal ballooning limit, this increased coupling should be stabilizing to drift modes, since the electromagnetic wave is robustly stable. As β approaches

the ideal limit, a sharp increase in transport would be expected due to the onset of resistive instabilities below the ideal limit. In addition, the increasing magnetic well with increasing β (due to the Shafranov shift) would also be stabilizing. Therefore, one might expect a favourable β dependence on transport up to a significant fraction of the ideal well limit, followed by a sharp increase in transport close to the ideal limit. Clearly, a more complete understanding of these effects on the plasma turbulence causing the energy transport is needed.

Recent experiments have also shed light on the role of shear in the bulk $\vec{E} \times \vec{B}$ rotation. As mentioned above, the toroidal Mach number of the ion flow, M , is one of the dimensionless parameters used to characterize the plasma. Experiments in TFTR showed that M does not have a significant effect on transport [435]. However, experiments and theory have indicated that the shear in the bulk $\vec{E} \times \vec{B}$ rotation can have a significant effect on the transport [34, 245]. From radial force balance, the $\vec{E} \times \vec{B}$ velocity has a pressure gradient term, which scales as $1/\rho_*$, and a rotation term which scales like M [220]. In DIII-D, two ρ_* scans were performed—one with counter-NBI and the other with co-NBI. The ρ_* scaling obtained is different in the two cases, with the main difference in the measured profiles being the quality of the match of M in each case (figure 45). Using the GLF23 model including $\vec{E} \times \vec{B}$ velocity shear by a linear, no-threshold model, the difference in scaling is shown to be consistent with the lack of match in M . Furthermore, the effect of $\vec{E} \times \vec{B}$ velocity shear only affects the ion transport scaling and not the electron scaling. This has serious implications for theoretical

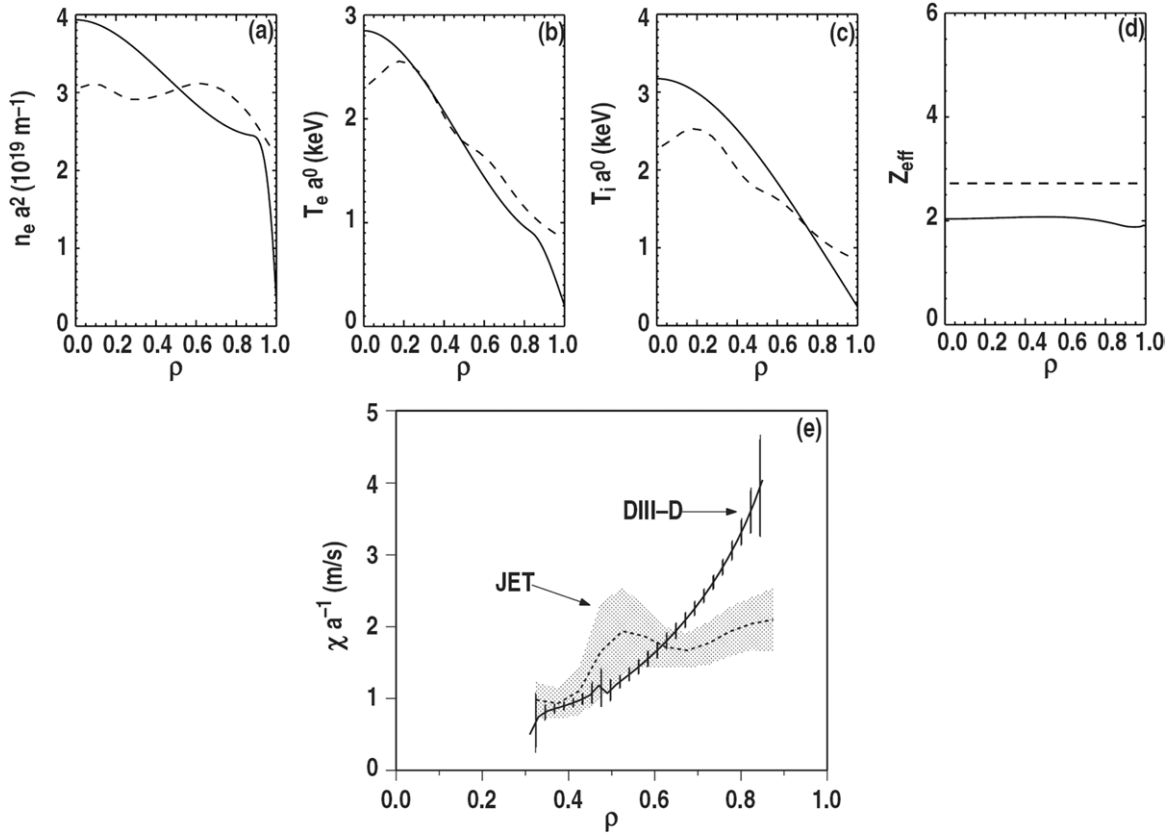


Figure 43. Comparison of the fitted or inferred scaled parameters for identical ELMing H-mode discharges in DIII-D (solid lines) and JET (dashed or shaded lines) as a function of normalized radius. The collisionality has been replaced with the proximity to the empirical density limit in the dimensionless parameter set: (a) scaled density (b) scaled electron temperature, (c) scaled ion temperature, (d) Z_{eff} and (e) scaled one-fluid diffusivity (with uncertainties). Reprinted with permission from [430]. © 2004 Institute of Physics.

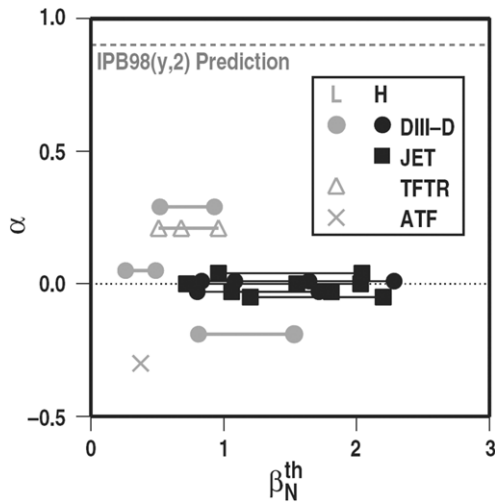


Figure 44. Scaling of thermal confinement time with β (defined by $B\tau_{\text{th}} \sim \beta^{-\alpha}$) versus the normalized thermal β (β_N^{th}) to indicate the proximity to the β limit. The effective β scaling of the IPB98y,2 scaling is also shown. Reprinted with permission from [432]. © 2004 American Institute of Physics.

models. It is normally assumed that the turbulence governing ion transport also dominates the electron transport. Evidently, this is not the case, or at a minimum, if the electron transport is dominated by turbulence with the same linear dispersion

relation as that governing the ion transport, the turbulence dominating the electron transport must be at wavelengths that are not affected by the $\vec{E} \times \vec{B}$ velocity shear. In this DIII-D experiment (and most others in present-day tokamaks), the $\vec{E} \times \vec{B}$ velocity shear is dominated by the terms proportional to M . However, in ITER, it is expected that the pressure gradient term will become important. This change does not affect the applicability of dimensionless scaling results from present-day experiments as long as care is taken to match M or the scaling results are obtained in regimes where the effects of $\vec{E} \times \vec{B}$ shearing are not significant.

Previous experiments from DIII-D, JET, and ASDEX Upgrade indicated that the ρ_* scaling of energy transport in low- q , ELMy H-mode plasmas (like the ITER baseline scenario) is locally gyro-Bohm [2]. More recent experiments in JET with Type I and Type III ELMs find gyro-Bohm scaling in both cases [351]. Experiments in JT-60U [230] find the ρ_* scaling in H-mode plasmas is weaker than gyro-Bohm; however, there is a systematic mismatch in β in the scans that may move the scaling closer to gyro-Bohm.

Three other dimensionless scaling studies warrant discussion here. First, experiments on DIII-D have shown that both the electron and the ion energy transport have strong dependences on the temperature ratio (T_i/T_e) [233]. This implies that simple 0D extrapolations to burning plasmas from discharges with $T_i > T_e$ in present-day machines may be optimistic in plasmas where $T_i \cong T_e$. Modelling indicated that

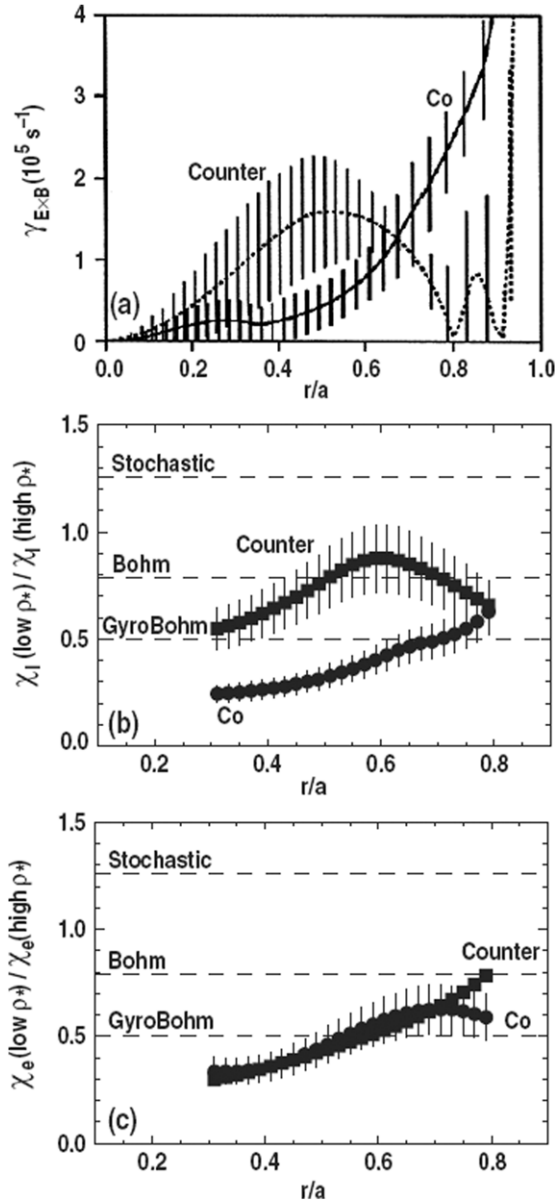


Figure 45. (a) Comparison of the shear in the bulk $\vec{E} \times \vec{B}$ rotation velocity for co-NBI and counter-NBI discharges with otherwise similar parameters in DIII-D. (b) Ratio of ion diffusivities for co-NBI and counter-NBI ρ_* scans. (c) Ratio of electron diffusivities for co-NBI and counter-NBI ρ_* scans. Reprinted with permission from [220]. © 2002 American Institute of Physics.

this strong dependence may arise from the dependence of the ITG threshold on the temperature ratio. Scaling on transport with hydrogenic ion mass has been evaluated in H-mode discharges in JET [436]. There is an apparent favourable dependence of global confinement on the ion mass that cancels out the unfavourable mass scaling from the increase in ρ_* . However, the local transport analysis does not clearly show this. A detailed discussion is beyond the scope of this review. Finally, the dependence of energy transport on cross-sectional shape has been studied in DIII-D discharges in both L-mode and H-mode [437]. In H-mode, there appears to be a strong favourable dependence with increased elongation. If the shape change is done at fixed plasma current, this favourable

dependence is offset by an unfavourable q dependence, i.e. the shape and q dependences largely cancel. However, at fixed q , the shape dependence shows itself quite strongly. Significant modelling is still required to understand how q , magnetic shear, and cross-section shape affect the turbulence that drives the transport.

In the ITER Physics Basis [1] there was extensive discussion of potential systematic errors that could affect the dimensionless parameter scaling technique, such as the mismatch of $E \times B$ rotational shear addressed above. The effect of ‘stiff’ transport or threshold behaviour of the turbulence has been invoked from the beginning of dimensionless scaling experiments [305] as a potential problem. In order to analyse such a situation, a specific model for such a dependence will be used [310].

$$\chi = \chi_0 + CT^\alpha \left(\frac{|\nabla T|}{T} - k \right)^\beta H \left(\frac{|\nabla T|}{T} - k \right). \quad (11)$$

Here, the threshold behaviour occurs when the temperature scale length decreases below $1/k$. In a perfect ρ_* scan, the temperature scale length is fixed, so all the discharges in the ρ_* scan are equally near to the threshold, unless k is dependent on ρ_* . Both full numerical simulations and parameterized models such as the IFS/PPPL model exhibit gyro-Bohm scaling, which indicates these theoretical models have k independent of ρ_* . Therefore, threshold-type phenomena do not necessarily invalidate the dimensionless parameter scaling approach.

In general, there are no direct limitations to the dimensionless scaling technique. However, there are potential systematic errors, in addition to the obvious problem of choosing the correct set of dimensionless parameters, discussed above. If the plasma behaviour had a strong non-linear dependence on a physical parameter, then slight mismatches in that parameter in scans where it should be held fixed would affect the inferred scaling. Measuring individually the scaling of transport with each of the dimensionless parameters allows one to identify which parameters could be so sensitive. The strongest dependence found is the ρ_* scaling, which is the one of most interest. This would indicate that mismatches in the other parameters have only a slight effect on the ρ_* scaling. Quantities such as the fusion cross-section and atomic transition rates do not depend only on the dimensionless parameters from plasma physics, and therefore, these are not scalable using only these parameters. However, for burning plasma applications, the effects of the fusion reactions and radiation on the transport of energy in the core can be added separately. The goal of the dimensionless scaling is to determine the loss power required to support the scaled profiles against turbulent transport, and the contribution of self-heating and radiation to this loss power can be estimated directly without resort to scaling. A difficulty arises if the scaling on the boundary layer at the edge is set by atomic physics, for example, through fuelling and radiation. Because H-mode plasmas have a significant fraction of the total stored energy confined by the edge transport barrier, divergence of the scaling of the pedestal from the core scaling could result in a global scaling different from that measured in the core. The experimental data gathered thus far indicate that the ρ_* scaling of plasmas most like the ITER baseline scenario (low- q , H-mode) have the same scaling for global and local transport. This points to the necessity for machines at a variety of ρ_*

values to gain confidence in this scaling method. Another potential systematic error that can occur is that the relative proximity to the L–H threshold condition can change during a scan. Previous experiments on JET clearly showed that the power required to obtain fixed β can be dominated by the power requirement to stay in H mode, rather than the loss power to transport. In general, the dimensionless scaling method assumes that the system does not undergo a qualitative ‘change of state’ during the scan. (The specific case of threshold phenomena was addressed above.) It should be noted that it is a new extensive review of dimensionless scaling experiments and techniques where these issues are addressed [438].

3.7. Improved core confinement regimes for advanced operation scenarios

The advanced operation scenarios for next step devices such as ITER should have a larger fraction of self-generated bootstrap current than the standard ELMy H-mode operation to extend the pulse length. These include ‘steady-state operation’ and ‘hybrid operation’ as discussed in chapter 6 of this issue [199]; the former means the operation where the whole of the plasma current is non-inductively driven, while in the latter a substantial fraction of the plasma current is non-inductively driven to enable extended operation under the available flux swing of the transformer. These operations require a high poloidal beta with a reduced plasma current to enhance the bootstrap current fraction f_{BS} . To achieve a high fusion power density and a high fusion gain with reduced plasma current, a high normalized beta (β_N) and high confinement enhancement (H-factor) are also needed. The latter is achieved by transport reduction and enhanced confinement in the plasma core including formation of an ITB. In the ITER Physics Basis [2], the pellet enhanced performance (PEP) mode and optimized shear (OS) mode in JET, supershot in TFTR, high β_p mode and reversed shear plasmas in JT-60U and negative central shear (NCS) mode in DIII-D are described as examples of this regime. In recent years, development of this regime using weak or negative shear plasmas has been pursued as a major objective in many devices. Here, results in leading tokamaks with NBI heating, namely JET, JT-60U, DIII-D and ASDEX Upgrade will be mainly shown. Experiments in other devices are found in recent review papers [24, 25]. Because avoidance of large sawtooth crashes is believed to be necessary to achieve this regime, operation with $q(r) \geq 1$ is employed. In the following, discharges will be classified in order of their values of magnetic shear (q profiles) and their $q(0)$ values. As shown below, tailoring and controlling the q profile is closely related to the improved core confinement and stability, and therefore is a key to developing these scenarios. A schematic graph of a desired q profile can be seen in figure 1 in chapter 6 of this issue [199].

3.7.1. Strong reversed shear regime. In the strong reversed shear regime, namely $s_{\min} < -1$ (s_{\min} denotes the minimum value of magnetic shear s) or $q(0)/q_{\min} \geq 1.5$, strong ITBs with a clear change in the slope in ion temperature (T_i), electron temperature (T_e) and electron density (n_e) profiles are observed in many machines, and high bootstrap current fractions (f_{BS}) are expected. The strong ITBs can result in very high confinement, though the beta limit tends to be

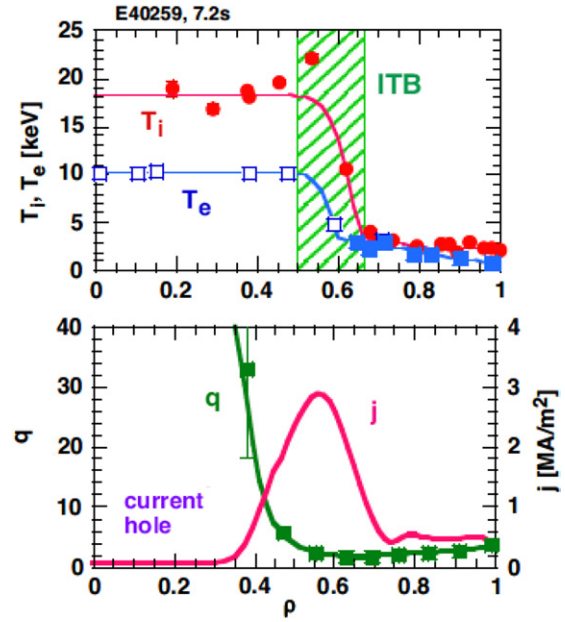


Figure 46. Radial profiles of ion temperature T_i , electron temperature T_e , safety factor q and current density j , in a JT-60U current hole discharge in which $Q_{DT}^{eq} = 1.2$ has been achieved. $I_p = 2.6$ MA, $B_T = 4.3$ T, $q_{95} = 3.3$, $n_e(0) = 9.9 \times 10^{19} \text{ m}^{-3}$. Reprinted with permission from [389].

low due to a localized large pressure gradient. One of the mechanisms for strong ITB formation seems to be an enhanced effect of the Shafranov shift (α stabilization) in a high q regime [439], though parallel velocity shear destabilization can prevent $\vec{E} \times \vec{B}$ shear quenching of the turbulent transport [262]. Since the ITB foot is usually located near the q_{\min} radius, expanding the negative shear region by off-axis current drive is useful to enlarge the volume enclosed by the ITB and improve the performance [440]. The ITB foot, however, can expand into the positive shear region for weaker ITBs with reduced temperature gradient [212], and the formation of ITBs in both positive and negative shear regions (double ITBs) is also observed [441].

In this regime, ITBs were obtained in ASDEX Upgrade with NBI (+EC) heating during the current ramp [324, 442, 443], in addition to DIII-D, JET and JT-60U. In JT-60U, optimization of reversed shear plasmas with an L-mode edge was continued in the modified W-shaped divertor, resulting in the record of DT-equivalent fusion gain $Q_{DT}^{eq} = 1.25$ [444]. In JET, improved coupling of LH waves resulted in stronger reversed shear than previous OS plasmas, and it was found that lower power was required to form ITBs and to achieve enhanced confinement [256]. The ITB emergence occurred preferentially when the minimum q reached an integer value, and two ITBs developed and followed two integer surfaces on each side of q_{\min} [6, 441]. A rarefaction of the rational surfaces around the low-order ones may be related to the ITB formation [13, 330].

Existence of a central region with nearly zero toroidal current, a ‘current hole’, was observed in an extreme case in this regime on JET [190] and JT-60U [189]. Though the temperature gradient was nearly flat in the current hole, high temperature plasmas exceeding 10 keV were confined with ITBs around the current hole as shown in figure 46, which

resulted in high $Q_{DT}^{eq} = 1.2$ in JT-60U [389]. The current hole formation is attributed to generation of off-axis non-inductive current; the toroidal electric field at the centre and hence the central toroidal current density decreases with rising off-axis non-inductive current, and the current hole in the central region is finally formed. The decrease of central current density stops ('current clamp') when it drops to nearly zero and the current hole structure is maintained by some mechanism. Though some simulation studies indicate that a resistive kink instability works to maintain the current hole [445,446], no corresponding signals have been observed in experiments so far [447] and the mechanism is not fully understood yet. Flat temperature and density profiles inside a steep gradient ITB layer, 'box-type ITBs', are often observed in strong reversed shear plasmas even without a current hole [37, 447, 448]. This suggests that some mechanism, other than high q values, causes flat profiles.

Collapses were observed with a relatively low beta in this regime, and extending the duration of the ITB was one of the major issues. This was accomplished by off-axis current drive (by LHCD, bootstrap current and ECCD) to maintain the inverted q profile as described in section 3.3 of chapter 6 of this issue [199] and pressure profile control (decrease in the pressure gradient in the ITB layer) with an H-mode edge [444]. It was found that the box-type ITB with strong negative shear can be sustained, resulting in high confinement, $H_{H98(y,2)} = 2.2$, and a large bootstrap current fraction, $f_{BS} > 80\%$, with $\beta_N = 1.9\text{--}2.2$ in JT-60U [449] without collapses if the q profile was maintained and the pressure gradient was not so large. It should be noted that q_{95} was high (> 8) and the toroidal beta was low in these discharges to enhance f_{BS} . Lower q_{95} is possible with strong off-axis current drive that replaces the bootstrap current [440]. In DIII-D, strong negative shear was established by off-axis ECCD during the high beta phase, which increased the T_i gradient and sustained the high beta conditions; $\beta_N \sim 2.8$, $\beta_t \sim 2.9\%$ and $H_{L89} \sim 2.3$ were maintained with $q_{min} > 2$ for nearly 2 s [450]. It was noted that the T_e gradient was weak in these discharges in spite of strong negative shear, which is in contrast to results in JT-60U and JET. The extended duration made it easier to investigate the transport properties in these discharges, including impurity accumulation discussed in section 3.4.

3.7.2. Weak shear regime with $q(0) > 1$. The weak negative or positive shear regime, namely with $-1 < s \leq 1$ in the core region or with $1 < q(0) \leq 1.5q_{min}$, is believed the most promising candidate for steady-state operation in ITER since enhance core confinement, high bootstrap current fraction, high MHD stability and good confinement of high energy particles are expected. In JET, OS plasmas belong to this regime. It was found that the ITBs were formed in the vicinity of low-order rational q surfaces with $q = 2$ or $q = 3$ [246, 451]. It is considered that the destabilization of the MHD mode at $q = 2$ or $q = 3$ by the coupling to the surface mode could provide a locally enhanced shear in the plasma flow and act as a trigger for ITB formation [6, 451]. The highest D-D neutron emission rate of $5.6 \times 10^{16} \text{ n s}^{-1}$, which was equal to the records in TFTR and JT-60U, was achieved in a discharge with an L-mode edge [452]. In 1998, D-T operation was performed in the OS plasmas. ITBs

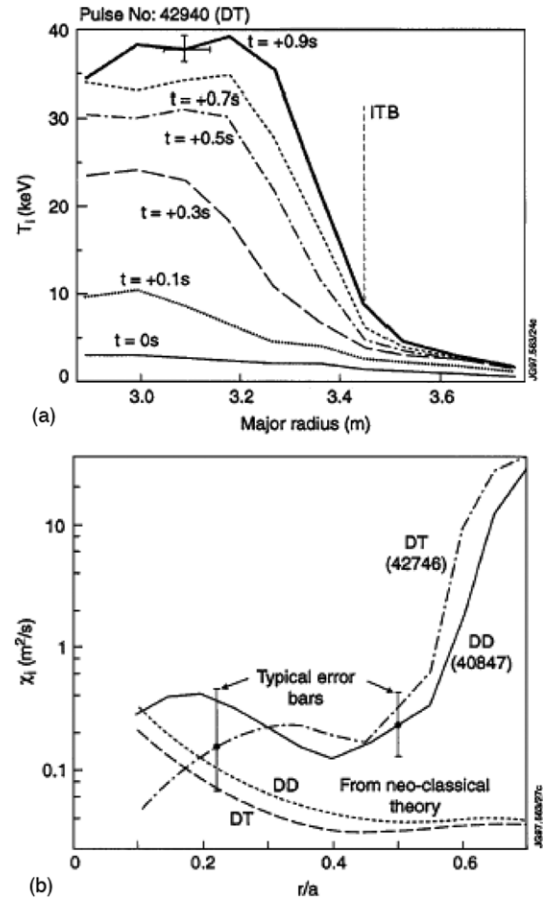


Figure 47. (a) Ion temperature profile along a major radius in a JET optimized shear D-T discharge. I_p was continuously increased up to 3.4 MA and $B_T = 3.8$ T. (b) Radial profile of ion thermal diffusivity in D-T and D-D JET optimized shear discharges. Reprinted with permission from [247]. © 1998 American Physical Society.

were produced in D-T plasmas with similar additional heating power levels and similar current profiles to those in D-D. Central ion temperatures of approaching 40 keV as shown in figure 47(a) and a triple product of $1.1 \times 10^{21} \text{ m}^{-3} \text{ keV s}$ were achieved, leading to 8.2 MW of fusion power [247, 453]. The values of χ_i were similar to those in D-D discharges as shown in figure 47(b). Improvement in the coupling of the LHRF system made it possible to employ off-axis LHCD during the high heating power phase to sustain the inverted q profile, and the ITB was maintained up to 11 s using feedback control of pressure profiles [454]. Steeper temperature gradients were observed in these discharges with LHCD and weak negative shear than those without LHCD and with weak positive shear [455].

The high β_p mode in JT-60U also belongs to this regime. Though beta collapses were observed in L-mode edge discharges, quasi-steady sustainment was obtained in ELMy H-mode edge discharges (high β_p ELMy H-mode), in particular with high plasma triangularity, δ [456]. A clear T_e ITB, in addition to the T_i and n_e ITBs, was observed, which was not seen in previous high β_p mode with an L-mode edge and low δ . Erosion of the ITB by Type I ELMs was not observed. The sustainable value of $\beta_N H_{L89}$ increased with δ , which seems to be caused by higher edge stability for high δ . High performance with $\beta_N \sim 2.5$, $H_{H98(y,2)} \sim 1.4$, $f_{BS} \sim 50\%$ and

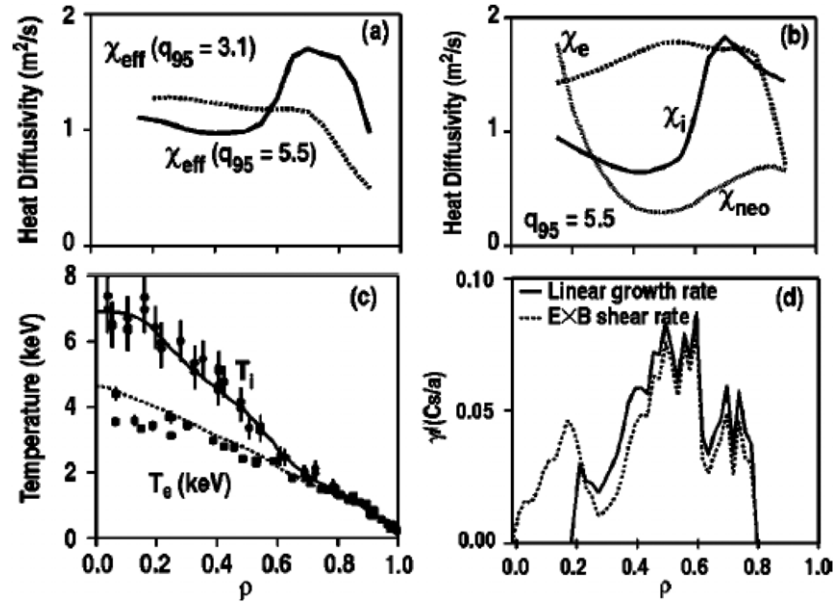


Figure 48. Transport properties of a DIII-D weak negative shear discharge. $I_p = 1.2$ MA, $B_T = 1.6$ T, $q_{95} = 5.5$, $q_{\min} \sim 1.5$ and $q(0) \sim 2$. The q_{\min} surface is located at $\rho \sim 0.35$. (a) χ_{eff} compared with χ_{eff} for a low q_{95} discharge with the same shape, size and toroidal field, (b) χ_i , χ_e and χ_i^{neo} ; (c) measured electron (squares) and ion (circles) temperature profiles and drift wave model predictions for ion (solid line) and electron (dashed line) temperatures and (d) a comparison of the normalized linear growth rate and the normalized $E \times B$ shearing rate for the drift wave calculation. Reprinted with permission from [459]. © 2001 American Institute of Physics.

full non-inductive current drive was achieved with negative neutral beam (N-NB) injection into high δ , high β_p H-mode discharge [457]. Weak, parabolic-type ITBs were obtained with a monotonically increasing q profile with $q(0) \sim 1$ and $q_{95} = 4.7$.

In DIII-D weak negative shear (WNS) plasmas belong to this regime. In this kind of discharge, early NBI heating is employed during the current ramp as in NCS plasmas. The formation of strong ITBs was avoided by triggering the H-mode transition during the current ramp [458]. $\beta_N \sim 2.9$ and $H_{H98(y,2)} \sim 1.4$ were obtained with weak ITBs whose foot was located at $\rho \sim 0.5$ – 0.6 . The normalized radius of the q_{\min} surface was less than 0.4 and the ITB foot was located in the positive shear region. The sustainable beta was limited by neoclassical tearing modes (NTMs). $\beta_N H_{L89} \sim 10$ ($\beta_N \sim 3.8$) was maintained for 0.8 s and $\beta_N H_{L89} \sim 9$ for 2.0 s ($16\tau_E$) [459, 460]. In the first case, β_N exceeded the ideal no-wall limit. The results of transport analysis are shown in figure 48 together with results for a lower q_{95} , sawtoothed ELM discharge. The effective one-fluid heat diffusivity, χ_{eff} , is compared for two discharges in figure 48(a). The two discharges have similar χ_{eff} in the core, while the high q discharge has significantly higher χ_{eff} in the outer 40% of the plasma. The ratio of χ_{eff} is smaller than the q^2 scaling observed in dimensionless scaling experiments in DIII-D [231]. In the high q discharge, χ_i in the central region is significantly smaller than χ_e and within a factor two of neoclassical prediction (figure 48(b)); however, there does not appear to be the formation of a clear ion ITB since only modest gradients are observed in the measured T_i profile as shown in figure 48(c). This figure also shows that the observed T_i and T_e profiles are well matched by GLF23 transport model simulation. The GLF23 model is a gyro-fluid representation of the transport due to ion temperature gradient (ITG) modes, trapped electron

modes (TEM) and electron temperature gradient modes (ETG), including the effect of $\vec{E} \times \vec{B}$ shear on the mode spectrum [461]. The q profile continues to evolve and reaches $q_{\min} \sim q(0) \sim 1$. Hence this kind of discharge is connected to the following class of regime (‘hybrid scenario’) continuously in DIII-D. Full non-inductive operation was recently achieved with strong off-axis ECCD [462, 463], in which $\beta_N \sim 3.5$, $\beta \sim 3.6\%$ and $q_{\min} > 1.5$ were maintained for 1 s. The profiles of the toroidal rotation, in addition to T_i and T_e , were well reproduced in a discharge in this regime with the transport modelling code GLF23 [463].

In JET and DIII-D, the ITB can be degraded or destroyed by giant ELMs, though it is maintained in plasmas with giant ELMs on JT-60U. In JET, introducing high Z impurities (e.g. krypton) was employed to enhance the edge radiation and to reduce the edge pedestal pressure and the ELM amplitudes, and the ITB was maintained in H-mode edge plasmas [464, 465]. In DIII-D, a sustainable combination of ITB and edge pedestal was achieved with counter-NBI and was called the QDB mode [242, 466]. The q profile with weak negative shear continued to evolve, but slowly possibly thanks to the effect of counter NBCD. The χ_i is close to the neoclassical theory prediction in the negative shear region [200]. In the double-null configuration with higher triangularity ($\delta_x \sim 0.8$), the plasma pressure has been increased throughout the discharge volume due to the improvement in the edge stability [467].

3.7.3. Regime with central flat q profile with $q(0) \sim 1$. The last class of regime can be defined as plasmas with $q(0) \sim 1$ without large sawteeth and with a relatively large region of flat q around the axis. This regime was developed in DIII-D [265, 458, 459] and ASDEX Upgrade [442, 468] intensively. The key point is that $q(0)$ does not fall below unity by some mechanism, like small fishbone (ASDEX Upgrade) or

NTM (DIII-D), though the classical diffusion of poloidal flux predicts that $q(0)$ should fall below unity. Higher β_N and higher confinement are expected than the standard H-mode because of absence of a large sawtooth that triggers NTMs. This class of discharge is believed to be the best candidate for the so-called hybrid scenario in ITER, in which extended pulse length than the standard operation is required to gain the neutron fluence. The development of this class of regime is discussed in chapter 6 of this issue [199] in detail. In both DIII-D and ASDEX Upgrade, early NBI heating during the current ramp was employed to enter this regime.

In DIII-D, high performance with $\beta_N \sim 3.8$ and $H_{98(y,2)} \sim 2$ was obtained with infrequent ELMs, but was terminated by the appearance of a 2/1 NTM [458]. In these discharges, large $\vec{E} \times \vec{B}$ shear was obtained and χ_i was reduced over most of the discharge to within 2–3 times the neoclassical prediction, though the temperature profile was smoothly peaked and no strong ITB structure was seen. Using feedback control for the density and beta, $\beta_N \sim 2.7$, $H_{L89} \geq 2.5$ and $\beta_N H_{L89} \sim 7$ were maintained for 6.3 s or $\sim 34\tau_E$ or $>3\tau_R$, where τ_R denotes the current relaxation time [459, 460]. The reference value for β_N was chosen just below (95% of) the beta limit for $m/n = 2/1$ tearing modes. A small $m/n = 3/2$ mode appeared and remained throughout the discharge with little impact on confinement; the effect on τ_E is estimated to be less than 10%. The q profile reached a stationary state after less than 2 s at high β_N and $q(0)$ was kept just above unity without sawteeth or fishbones. The $m/n = 3/2$ tearing mode seems to have a role in maintaining this q profile. Predictive transport calculations utilizing the GLF23 code demonstrate that the predicted T_e and T_i profiles agree well with the experimental results. The GLF23 results indicate that the reduction in transport is due to a combination of $T_i/T_e > 1$ and sufficient $\vec{E} \times \vec{B}$ shear, although χ_i is significantly larger than the neoclassical value [265]. In discharges where higher rotation was obtained with proper error field correction applied, higher confinement was observed [469].

The extent of the existence domain of operating regime was investigated by scanning q_{95} and the density [469, 470]. The q_{95} was scanned from 4.9 to 3.2. For discharges with $q_{95} < 4$, sawteeth were observed, which reduced the operational β_N limit slightly. The presence of sawteeth did not affect strongly the confinement and H_{89} remained almost constant. $\beta_N = 2.7$ and $H_{L89} = 2.3$ were maintained for 9.5 s in a discharge with $q_{95} = 3.2$. The density range was 30–70% of n_G , and they found that β_N increases while H_{L89} decreases with the density. At the highest density, $\beta_N = 3.2$, $H_{98(y,2)} = 1.2$, $T_i/T_e = 1.3$ were obtained [469].

In ASDEX Upgrade, the stationarity of q profiles is explained by magnetic reconnection driven by strong $m/n = 1/1$ fishbones, which, in the absence of sawteeth, also expel energy and impurities [442, 471]. The highest fusion triple product in ASDEX Upgrade, 0.9×10^{20} keV s m⁻³ ($\beta_N = 2.4$, $H_{L89} = 3.0$) was obtained in this regime. Though this regime, called the ‘improved H-mode’, was originally considered with ITBs, it was found that the temperature profiles were also ‘stiff’ in this regime hence no ITBs were formed. The behaviour of the T_i , T_e and n_e profiles of selected discharges with the same plasma current, NBI heating power and plasma shape

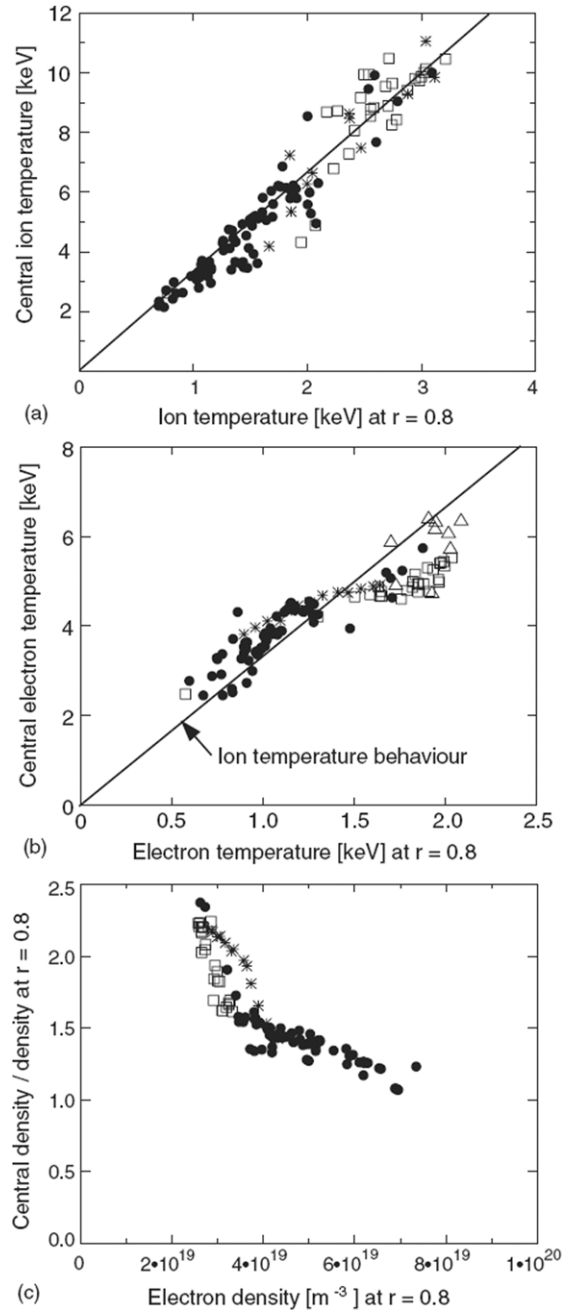


Figure 49. The behaviour of the ion temperature, the electron temperature and the density of the selected discharges in ASDEX Upgrade. (a) $T_i(0)$ as a function of $T_i(0.8)$, (b) $T_e(0)$ as a function of $T_e(0.8)$ and (c) $n_e(0)/n_e(0.8)$ as a function of $n_e(0.8)$. The data from the improved H-mode and the data from the standard H-mode are shown by open squares and closed circles, respectively. Stars denote discharges with pre-heating and gas puff for higher density. Triangles denote discharges with additional EC heating. Reprinted with permission from [472].

are shown in figure 49 [472]. The data from the improved H-mode is shown by open squares, whereas the data from the standard H-mode, in which no NBI heating during I_p ramp was employed, is shown by closed circles. The density was scanned for $0.3 < \bar{n}_e/n_G < 0.6$. The T_i profiles of the dataset are observed to be stiff, as shown in figure 49(a), i.e. one can use a single multiplication factor to normalize the

profiles after which they have a unique shape. The standard H-mode discharges and improved H-mode discharges follow the same scaling, though the improved H-mode has higher edge and core temperatures. On the other hand, the central T_e falls below the linear scaling in the high edge temperature regime, as shown in figure 49(b). This may be explained by the fact that NBI predominantly heats ions at these high electron temperatures. Indeed, when EC heating is applied at the centre, $T_e(0)$ increases and reaches values which are close to the linear scaling, as shown by open triangles in figure 49(b). The n_e profiles are more peaked at lower densities even in standard H-modes as shown in figure 49(c). In the improved H-mode, a stronger increase in the density peaking is observed inside $\rho = 0.4$. The density profile peaking seems to be a key to improving the energy confinement with stiff temperature profiles. In a double-null configuration with higher triangularity, $\delta = 0.43$, in a modified divertor geometry, higher $\beta_N = 3.5$ was maintained over a range of $q_{95} = 3.0\text{--}4.5$ in steady-state [468,473]. The pedestal density was raised with increasing triangularity and reached $1 \times 10^{20} \text{ m}^{-3}$. $H_{H98(y,2)} = 1.1\text{--}1.2$ with Type II ELMs was obtained at the high density $\bar{n}_e/n_G = 0.85$. Higher confinement up to $H_{H98(y,2)} = 1.5$ was obtained in a lower density regime. The simulation of the temperature profiles with the Weiland model are in agreement with experimental observations within the error bars of the measurements [474]. The existence domain was documented for $3.2 < q_{95} < 4.5$ [475].

In JET, similar discharges to those hybrid scenario discharges in DIII-D and ASDEX Upgrade were obtained with NBI heating or LHCD during current ramp. The fishbone instabilities were observed, and $q(0) \sim 1$ was maintained without sawtooth instabilities. At $I_p = 2.8 \text{ MA}$, $B_t = 2.6 \text{ T}$ and $q_{95} = 3.2$, $\beta_N = 1.4$ and $H_{L89} = 2.0$ were obtained. A weak T_i ITB was observed though the confinement was moderate [476]. Experiments matching the plasma shape q profile and ρ_* of ASDEX Upgrade was attempted, and $\beta_N = 2.8$ and $H_{H98(y,2)} = 1.4$ were achieved without ITBs at $I_p = 1.4 \text{ MA}$ and $B_t = 1.7 \text{ T}$ [477,478]. Stationary conditions were obtained with small NTM and fishbone activity in the core.

In JT-60U, $\beta_N = 2.7$ was sustained for 7.4 s in a high β_p ELMy H-mode discharge with $I_p = 1.0 \text{ MA}$, $B_t = 1.8 \text{ T}$, $q_{95} = 3.3$ and $\delta \sim 0.45$ [479]. The $m/n = 3/2$ NTM was observed continuously in this discharge and $q(0)$ was maintained above unity. No strong ITBs were observed. These features are similar to those of hybrid scenario discharges in DIII-D and ASDEX Upgrade, though the confinement was moderate ($H_{L89} \leq 1.8$, $H_{H98(y,2)} \leq 0.9$). After the modification of NBI systems for extended pulse length, longer sustainment of high β_N was achieved; $\beta_N = 2.5$, $H_{L89} \sim 2.0$ at $q_{95} = 3.4$ for 16.5 s and $\beta_N = 2.3$ for 22.3 s [480, 481]. It should be noted that no sawteeth were observed even in a discharge without $3/2$ NTMs. No fishbone instabilities were observed either. Analysis remains to be performed to determine if the current diffusion in this kind of discharge is classical. In a low- q regime with $q_{95} = 2.2\text{--}2.7$, $\beta_N = 3.0$ was maintained for 6.2 s without large sawteeth or NTMs [482]. The absence of sawteeth in a low- q regime seem to be related to broad temperature profiles due to off-axis NBI heating.

The core transport in hybrid regime is not fully understood yet. No ITB structures are recognized, and the temperature profiles are reported to remain stiff in some devices. The confinement is, however, better (typically 20% and up to 50%) than the prediction by the ELMy H-mode scaling and the $\vec{E} \times \vec{B}$ shear seems to play a role in the transport reduction. The experimental temperature profiles are reproduced only when the $\vec{E} \times \vec{B}$ shearing stabilization is included in the GLF23 simulation [262]. This suggests that the turbulent transport is somewhat regulated, though not fully suppressed, in this regime. This process, however, may also exist in the standard ELMy H-mode, and the higher confinement observed for the hybrid regime could be related to the negative β dependence of the IPB98y2 scaling [478]. The improved performance on sustainable beta and confinement in this regime is attributed to stabilization of NTMs by eliminating large sawtooth activities. Since NTM can be triggered without sawteeth and the threshold beta of NTM onset depends on ρ_* or v_* , extrapolation of the operational domain to lower ρ_* and v_* is required, and is actually in progress, to address the feasibility of this mode to ITER.

3.7.4. Prospect towards reactor-relevant conditions. Most of the experimental results so far were obtained with dominant NBI heating with energies $< 120 \text{ keV}$, which implies dominant ion heating, $T_e < T_i$, as well as substantial input of toroidal momentum and particles into the plasma core. In ITER and future fusion reactors, the heating will be dominated by high energy α particles, MeV-range NBI and RF, all of which heat electrons dominantly and input minimal toroidal momentum or particles. Therefore, it is of great concern if improved core confinement regimes can also be maintained in such conditions.

The high values in T_e/T_i are predicted to enhance the ITG instability [483] that is believed to dominate the ion heat transport, and therefore it is a concern whether the improved ion confinement is maintained even with $T_e > T_i$. In fact, a tendency was found that the H factor increased with T_i/T_e in the database of advanced tokamak discharges as show in figure 50 [203], suggesting a role of T_i/T_e in confinement improvement. In strong reversed shear plasmas, it was observed that the ion ITB was maintained with $T_e > T_i$ [324, 332, 344]. In JT-60U, it was also observed that the formation of ion ITB was possible with the existence of the electron ITB, namely with $T_e > T_i$ conditions. On the other hand, ITBs in positive shear plasmas were found to degrade with electron heating using ECRF in DIII-D and JT-60U [169, 332]. In JT-60U experiments (figure 51), the ion ITB degradation took place 0.5 s after the start of ECH, and T_e/T_i was saturated while the gradient of E_r continued to decrease. This suggests that the degradation of ion ITB may not be caused by a change in T_e/T_i but decrease in the E_r gradient caused by ECH. The mechanism of E_r gradient reduction by ECH is not well understood yet. In the hybrid regime, $T_e \sim T_i$ was achieved with ICRF heating in ASDEX Upgrade and no change in confinement was observed [475].

The large $\vec{E} \times \vec{B}$ shear is believed to suppress the ITG mode [114, 218] and is effective to establish and maintain the ion ITB. A significant fraction of $\vec{E} \times \vec{B}$ shear is generated through the toroidal momentum input from tangential NBI,

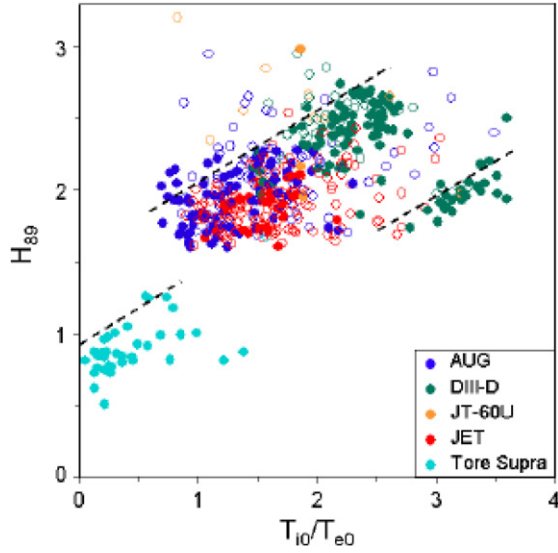


Figure 50. Confinement enhancement factor H_{89} versus the ratio of the central ion (T_{i0}) and electron (T_{e0}) temperatures in the ITPA database for advanced tokamak plasmas. Transient (open symbols) and stationary (closed symbols) results are given. Reprinted with permission from [203].

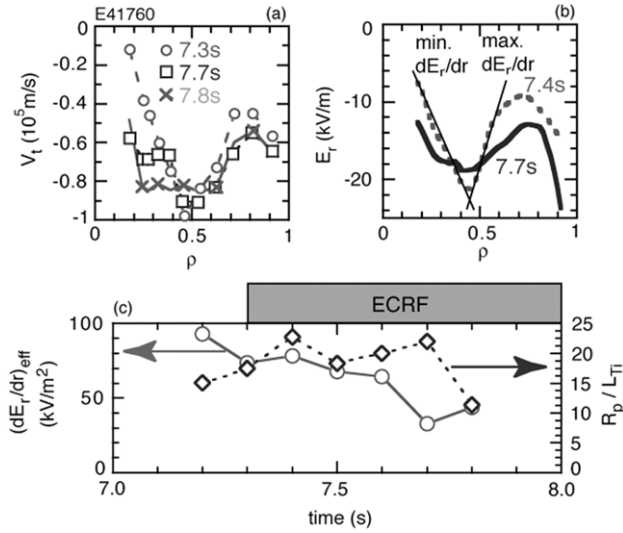


Figure 51. Degradation of an ion ITB with ECRF heating observed in a JT-60U weak positive shear plasma. (a) Profiles of toroidal rotation of carbon ions. (b) Profiles of radial electric field E_r . (c) Temporal changes in the effective E_r gradient $(dE_r/dr)_{\text{eff}}$ and the maximum in the normalized ion temperature gradient, R_p/L_{T_i} profile. Here $(dE_r/dr)_{\text{eff}} \equiv (|dE_r/dr|_{\text{max}} + |dE_r/dr|_{\text{min}})/2$, which is closely related to transport reduction in the ITB in JT-60U. Reprinted with permission from [332].

and the ITB control was demonstrated by changing the NBI directions [200, 212]. Though strong ITBs are observed with balanced injection of NBI in JT-60U [212], a difference in orbits of co-injected and counter-injected beam ions may produce local toroidal rotation shear. In strong reversed shear plasmas, effects of negative magnetic shear and of the Shafranov shift, the latter is enhanced due to larger q values, seem to suppress anomalous transport even without the $\vec{E} \times \vec{B}$ shear. In fact, strong T_e ITBs are observed in many devices

without NBI heating. Limited experiments have been made for ion heating without NBI. In JET, ICRF heating in a ^3He minority scheme was employed to heat the bulk ions without any external momentum input in a reversed shear plasma produced and maintained by LHCD [484]. As a result, an ion ITB was formed in a nearly zero shear region, though its radius was small. The toroidal rotation and the $\vec{E} \times \vec{B}$ shear were about one order magnitude smaller than those in typical JET ITB plasmas. In hybrid regime, the $\vec{E} \times \vec{B}$ shearing rate seems to have a role in reducing the transport though no clear ITB structure is recognized and hence the small momentum input experiment is important as well as in ITB plasmas. Strong ICRF heating, comparable to NBI heating power has been attempted in JET and ASDEX Upgrade [475, 484, 485]. In ASDEX Upgrade, no confinement degradation was observed. In JET, $H_{L89} = 2$ was achieved at $T_i(0)/T_e(0) \sim 0.8$ though β_N was moderate, up to 1.55, and the pedestal height was low compared with the NBI-dominated hybrid discharges with similar heating power. Transport properties in these discharges are not analysed yet.

Some discharges for advanced operation scenarios have lower densities in terms of the density normalized by the Greenwald density (n_G) required for ITER and future reactors. This is partly because the ITB formation seems to be easy in a low density regime [486], where the intense central heating with NBI is possible and a larger $\vec{E} \times \vec{B}$ shear tends to be obtained through larger toroidal rotation with the same injected torque. In strong ITB plasmas with reversed shear, high central densities were obtained with NBI fuelling and pellet fuelling inside the ITB layer [366, 440, 487], and we will have no problems in viewpoint of core transport for high densities. However, the edge or pedestal densities were relatively low in previous experiments. In ITER and fusion reactors, central NBI fuelling should be small and fuelling with pellet inside the ITB will be difficult. The strong density ITB should be avoided to suppress impurity accumulation as discussed in section 3.4. Hence a moderately peaked density profile is expected and high pedestal density is required. A reduced density gradient may result in enhanced transport since a steep density gradient or a small value in $\eta_i = L_{n_e}/L_{T_i}$, where L_{n_e} and L_{T_i} are scale lengths for n_e and T_i profiles, respectively, is believed to work to suppress the ITG mode. In a JT-60U reversed shear plasma, about half of NBI heating power was replaced by ICRF, and a strong T_i ITB was maintained with a reduced density gradient and an enhanced T_e ITB [488]. This indicates that a steep density gradient is not necessary for T_i ITB sustainment. On the other hand, a high pedestal density will enhance the power for off-axis current drive to maintain the reversed shear profile. In ITB plasmas with weak magnetic shear, few attempts were made to raise the density near n_G . In JT-60U high β_p H-mode, the achievable density was limited to 70% of n_G with gas puffing and pellet injection. Injection of Ar was required to reach 92% of n_G with $H_{H98(y,2)} = 0.96$ [366]. The temperature ITBs seems to get weaker, though the density ITB remained, in these high-density regime, but the reasons are not well understood. In hybrid regime, density scan was intensively performed in DIII-D and ASDEX Upgrade as described in section 3.7.3. Though in both devices, it was found that the confinement was slightly degraded with the density, the ASDEX Upgrade results, $H_{H98(y,2)} > 1.1$ at 85% of the Greenwald density [468, 473], is promising.

3.8. Summary and outstanding issues

Remarkable progress has been made in developing and understanding regimes of improved core confinement since the publication of the IPB. Internal transport barriers and other forms of reduced core transport are now routinely obtained in all the leading tokamak devices worldwide. Reduced transport has been achieved in all four transport channels (ion and electron thermal, particle, and momentum transport channels), sometimes simultaneously. This rapid worldwide progress in the development of enhanced confinement modes of operation has contributed to an increased emphasis on developing both hybrid and steady-state operation modes for ITER.

Ion thermal transport (section 3.2) is now relatively well understood and is believed to be regulated by ITG-type turbulence. Theory-based modelling can qualitatively replicate ion transport across a wide range of operating regimes (RI-mode, ITB discharges with varying levels of magnetic shear, hybrid, non-ITB AT discharges, etc), with quantitative agreement in many cases. The predictive ability of these ion transport models has progressed to the point that modelling is now regularly used in experimental design. These successes have increased confidence in projections to ITER, as discussed further in section 5. Important outstanding issues include: quantifying the level of profile stiffness in the plasma core; identifying the physical mechanism for the robust observation of Bohm-like ion transport scaling in L-mode (drift wave models are intrinsically gyro-Bohm); replicating both the amplitude and phase response of modulated transport experiments in a single transport model, and understanding the fast radial propagation of heat pulse experiments, which is difficult to explain using local diffusive models.

Electron thermal transport (section 3.3) is relatively less understood than ion thermal transport. A larger number of turbulent modes, covering a broader wavenumber range, can contribute to electron transport, namely ITG, TEM, as well as ETG type turbulence (the latter short wavelength ETG modes only being capable of causing significant transport if larger-cells, so-called ‘streamers,’ can be formed). This larger range of turbulence activity and interactions is perhaps responsible for the more diverse range of experimental results and theoretical interpretation seen in this area, as compared with ion transport. A feature of electron transport are ‘profile stiffness’, with extensive evidence for the existence of a threshold in the normalized gradient above which turbulent transport increases dramatically, potentially explaining the observed stiffness. Electron transport barriers can be achieved, usually in association with reversed magnetic shear profiles. Current evidence is that TEM and ITG turbulence usually dominate electron transport, but that ETG modes may play a limiting role when electron ITBs are formed. Scaling experiments indicate that electron transport is gyro-Bohm, in accord with theoretical expectations for drift wave-like turbulence. Outstanding issues in this area include: providing an unambiguous resolution of whether a threshold exists in the normalized temperature gradient; resolving the existence and relative role of TEM and ETG turbulence, and including their behaviour accurately in transport models; and more extensive experimental studies of transport behaviour with dominant electron heating, especially in enhanced core confinement regimes.

Particle transport (section 3.4) is also relatively less well understood than ion thermal transport, due to the existence of both edge and core particle sources, and the importance of both convective and diffusive transport. However, substantial progress has been made since the publication of the IPB. High confinement has been obtained with peaked density at high density (at and above the Greenwald density). An inward particle pinch has been observed on multiple devices, and may be explained in the framework of ITG/TEM turbulent transport. Evidence for neoclassical inward particle transport driven by the density gradient has also been found in ITB discharges on multiple devices. However, this inward neoclassical particle transport is also consistent with the observation of high-Z impurity accumulation in many ITB discharges. To counter this latter effect, control of the density peaking has been developed for such ITB discharges, utilizing on-/off-axis RF heating. Remaining issues in this area include: determining the optimum level of density peaking in ITER, as there is competition between improved confinement with central density peaking, and confinement reduction due to high-Z impurity accumulation, which also increases with density peaking; determination of what density profile can be obtained in ITER with low central fuelling; and establishing whether current density profile control techniques are consistent with reactor conditions.

For a number of reasons, momentum transport and plasma rotation are less well understood than the other plasma transport channels (section 3.5). These include an incomplete knowledge of momentum sources (e.g. the source of ‘spontaneous’ plasma toroidal rotation), and sinks (e.g. resonant and non-resonant interaction with error fields). The applicability of neoclassical theory in determining poloidal rotation is also currently an open question. Thus, while scaling studies and similarity experiments have been initiated, an ability to predict momentum transport and rotation for ITER is currently lacking.

With regard to the dimensionless parameter scaling techniques (section 3.6), considerable progress has been made since the IPB, and several of the issues outstanding at that time have been addressed. This approach has now been successfully applied to transport scaling in both L- and H-mode plasmas, and the matching of plasma parameters in the identity experiments have been expanded to include $\vec{E} \times \vec{B}$ shear effects. Significant new work on the scaling of energy transport with β has been performed, showing a weak or null dependence of the transport on beta, in contrast to both theoretical expectations and global database scalings (see section 5.4). Other issues are that dimension scaling studies indicate that both electron and ion energy transport have strong dependences on the ion/electron temperature ratio, implying that 0-D extrapolation to reactor conditions ($T_i \sim T_e$) from hot ion plasmas may be optimistic. Such dependences are, however, in agreement with theoretical and modelling expectations for ITG dominated transport.

Finally, the transport properties of improved confinement regimes relevant to advanced operation on ITER (steady-state and hybrid scenarios) were presented in section 3.7. A major feature of the results is that improved confinement regimes can be routinely obtained on all major devices with a broad range of q profiles (with strongly reversed through weak shear, and with

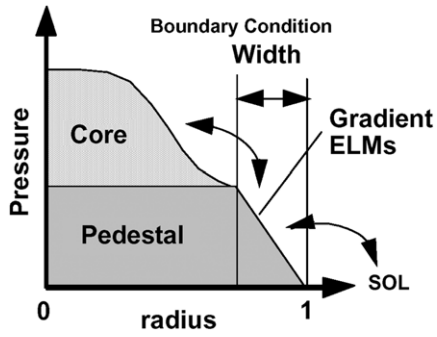


Figure 52. Schematic radial profile of plasma pressure.

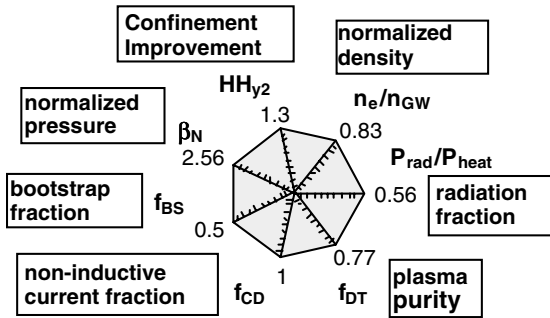


Figure 53. Integrated plasma performance required for a steady-state operation in ITER.

a range of q_{\min} values). With regard to extrapolation to reactor conditions, progress has been made with regard to obtaining reduced core transport with $T_i \sim T_e$, low momentum input and at high density, though in all the cases further investigation and experimental demonstration of robust high confinement operation are desirable.

4. Pedestal transport and dynamics

This section reviews recent progress in the research on the H-mode edge and pedestal physics. The edge pedestal parameters are essentially important for burning plasma performance because they determine the boundary conditions for the core plasma as well as the source of heat and particle flows into the SOL and divertor plasmas (figure 52). For example, projections for ITER show that its fusion gain depends strongly on the pedestal ion temperature. Furthermore, the H-mode pedestal plays a central role in achieving integrated plasma performance: in order to sustain burning plasmas in tokamak power plants, we need to sustain high values of the energy confinement improvement factor (the H-factor), normalized beta (β_N), bootstrap and non-inductively driven current fractions, plasma density, fuel purity and radiation power simultaneously (figure 53) [489]. The roles of the pedestal in each of these are as follows. Because of the stiffness in the temperature profile, the energy confinement and the fusion gain are strongly affected by the pedestal temperature. The pedestal temperature decreases with increasing pedestal density, because the pedestal pressure is limited by ELMs to be a nearly constant value. Therefore, in order to achieve high confinement enhancement at a high density, improved pedestal pressure is essentially important.

For MHD stability at high β_N , we need to increase the pedestal pressure so as to achieve a broad pressure profile, since a moderate pressure gradient in the core region is needed to stabilize global ideal low n modes and neoclassical tearing modes. In order to sustain the current profile with an optimum shape for high confinement and stability, distribution of the edge bootstrap current has to be controlled at an optimum level. The pedestal temperature, density and ELMs determine the shielding and pumping of impurities, thus the pedestal characteristics are a key to particle control. In addition, the ELM heat load on the divertor plates should be reduced to a tolerable level. The data show that the energy loss in a Type I ELM crash tends to increase with increasing pedestal pressure (or both the energy loss and the pedestal pressure increase with decreasing collisionality). We have to develop techniques for Type I ELM mitigation, or access to small/no-ELM regimes, by keeping a favourable pedestal pressure at an ITER-relevant low collisionality.

From the physics point of view, the H-mode pedestal is a complex system. The pedestal structure and its dynamics are determined by both the plasma physics (transport, MHD stability) and the atomic physics. The scale length of the pedestal parameters is of the same order as the ion orbits and the penetration depth of the neutrals. Furthermore, the spatial distribution of the pedestal parameters and their temporal behaviour show two or three-dimensional structures. The time scales of the leading phenomena span from the growth time of ideal MHD/turbulence to the wall saturation time, with the parallel and perpendicular transport times and the edge current growth time in between.

The main research issues were raised and categorized in the excellent review reports [490–493]. Since then, by revealing the above mentioned physics through experimental, theoretical and numerical approaches, recent pedestal research has shown significant progress, particularly in achieving high confinement at high density, Type I ELM mitigation and development of small/no-ELM regimes, and predictive capability for burning plasmas. In the following subsections, we will review recent progress and remaining issues for pedestal research: enhanced confinement at high density, the pedestal structure, turbulence suppression and the L–H transition, pedestal transport theories, integrated modelling, Type I ELMs and their mitigation, small/no-ELM regimes, pedestal MHD stability theories and pedestal control schemes.

4.1. Regimes of improved H-mode confinement at high density and operational limits

One of the main physics issues identified in the ITER Physics Basis document [1] was an observation that it is difficult to maintain H-mode confinement in tokamak experiments at high plasma density with gas puff fuelling. While regression analysis of the Type I ELMy H-mode confinement database was indicative of τ_E increasing with plasma density, $\tau_E \propto \bar{n}_c^{0.41}$ [1], the density scans with gas puff fuelling in individual devices revealed a saturation or even decrease of τ_E , as initially shown in JET [494] and later reproduced in other devices. Figure 54(a) shows that the $H_{H98(y,2)}$ factor decreases with increasing density as reported from JT-60U [294]. In the Type I ELMy H-mode, the pedestal pressure is limited by ELMs.

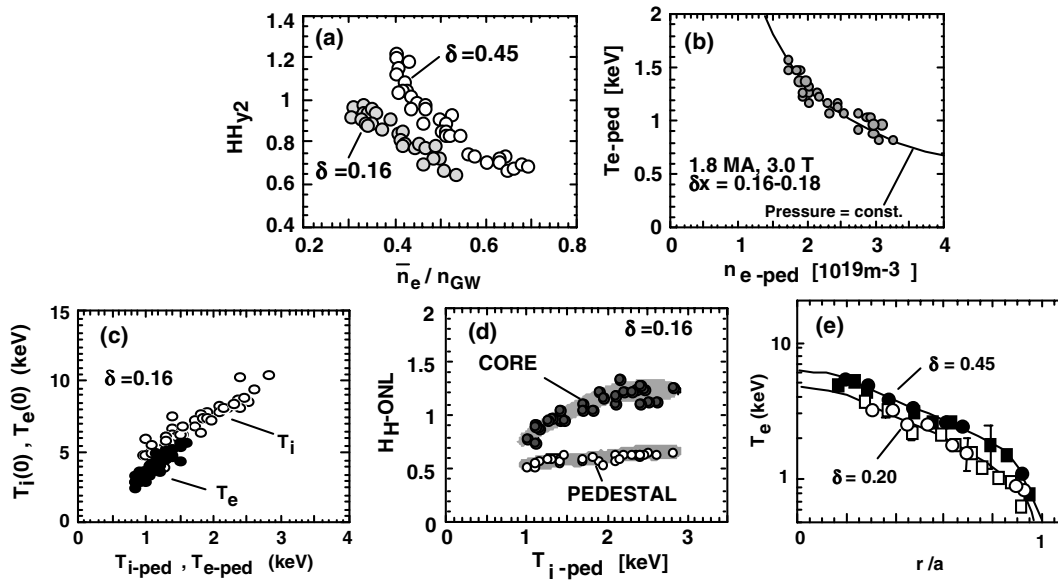


Figure 54. Type I ELMy H-mode in JT-60U [294]. (a) Density dependence of the HH_{y2} -factor for the Type I ELMy H-mode discharges (low- δ (= 0.16), high- δ (= 0.45)). (b) Pedestal electron temperature as a function of pedestal electron density ($\delta = 0.16$). (c) Relationship between pedestal and central values of T_e and T_i . (d) Pedestal ion temperature dependence of confinement enhancement factors based on the offset non-linear scaling. (e) Comparison of the electron temperature profile for high and low δ cases with the same pedestal density.

Under this limitation, when the pedestal density increases, the pedestal temperature decreases (figure 54(b)) and the core temperature also decreases due to the profile stiffness effect, i.e. $T_{core} \propto T_{ped}$ as seen in figure 54(c) (see also section 3.3). As a result of this linkage, the stored energy does not increase with increasing density and the confinement enhancement factor decreases because the scaling has a positive dependence of the confinement time on density. Figure 54(d) shows that the core confinement enhancement factor relative to the offset non-linear scaling [495] decreases with decreasing pedestal ion temperature. Therefore, the basic factors determining the confinement degradation at high density is the limitation of the pedestal pressure by ELMs and the profile stiffness.

Based on this knowledge, in recent years several methods have been discovered that allow H-mode operation with a good confinement at densities close to and even higher than so-called the Greenwald density. These methods include the increase of triangularity in the plasma cross-section [494], deep pellet fuelling, strong gas puff at plasma midplane combined with intense pumping from the divertor [365], low steady gas puff allowing density peaking [355] and controlled impurity injection [370].

4.1.1. Effects of plasma shape on global and pedestal confinement. At high triangularity, δ , a good confinement enhancement factor can be kept at higher density [496, 497] because of the improved stability against ELMs [498] (see section 4.8). At high triangularity, the edge pressure is higher than that in low δ discharges and thus the pedestal and core temperatures are higher at a given pedestal density (figure 54(e)), and the confinement enhancement factor becomes higher as shown in figure 54(a) [499]. Figure 55 illustrates the behaviour observed in JET [370] and ASDEX Upgrade [248] at different, fixed values of the plasma triangularity δ . The confinement improvement factors relative

to the H-mode confinement scalings [1] decrease with \bar{n}_e/n_G at constant δ and increase with δ at fixed \bar{n}_e/n_G . In highly shaped plasmas ($\delta = 0.35-0.45$), the $H_{H98(y,2)}$ factors reach ≥ 1 at $\bar{n}_e/n_G \approx 1.1$ in both devices. In JET at high triangularity ($\delta > 0.4$), a good confinement ($H_{H98(y,2)} = 0.9-1.0$) at high density ($\bar{n}_e/n_G \geq 1$) is linked with access to the mixed Type I/II ELMy regime characterized by higher pedestal pressure at high density than with Type I ELMs (figure 56) [500].

Another favourable effect of high triangularity was reported from JT-60U [501]. Figure 57(a) ($\delta = 0.44-0.48$) shows that the pedestal pressure ($\sim n_{e,ped} T_{e,ped}$) remains roughly constant for the standard ELMy H-mode with Type I ELMs (open circles). While in the high β_p ELMy H-mode (small closed circles), the pedestal pressure can be higher than that of the standard H-mode. This enhanced pedestal pressure is due to improved edge stability enhanced by high β_p values: figure 57(b) shows the pedestal β_p ($\beta_{p,ped}$) increases with increasing total β_p at high $\delta = 0.44-0.48$ (circles). This relationship between $\beta_{p,ped}$ and the total β_p seems independent of existence of the ITBs (open symbols: without ITB, closed symbols: with ITB), which means that this relation does not come from the profile stiffness. On the other hand, $\beta_{p,ped}$ is almost constant at low δ (squares). One candidate explanation for this improvement is that a larger Shafranov shift improves the pedestal stability at high triangularity.

A range of plasma parameters ($\delta \geq 0.4$, $\beta_N \sim 3$, $q_{95} \geq 3.6$ and $q(0) \sim 1$ at a near double-null configuration) has been found in ASDEX Upgrade, where the ‘improved’ H-mode with $H_{H98(y,2)} = 1.2-1.3$ and small (Type II) ELMs is observed at densities up to $\bar{n}_e/n_G \approx (0.8-0.9)$ [468]. Similar regimes with somewhat different characteristics have been obtained in DIII-D [469, 470], JT-60U [366, 479] and JET [478, 485]. The physics of these favourable regimes and prospects for an ‘improved hybrid’ scenario in ITER based on such regimes are discussed in section 3.8 of this chapter and section 3.3 of chapter 6 of this issue [199].

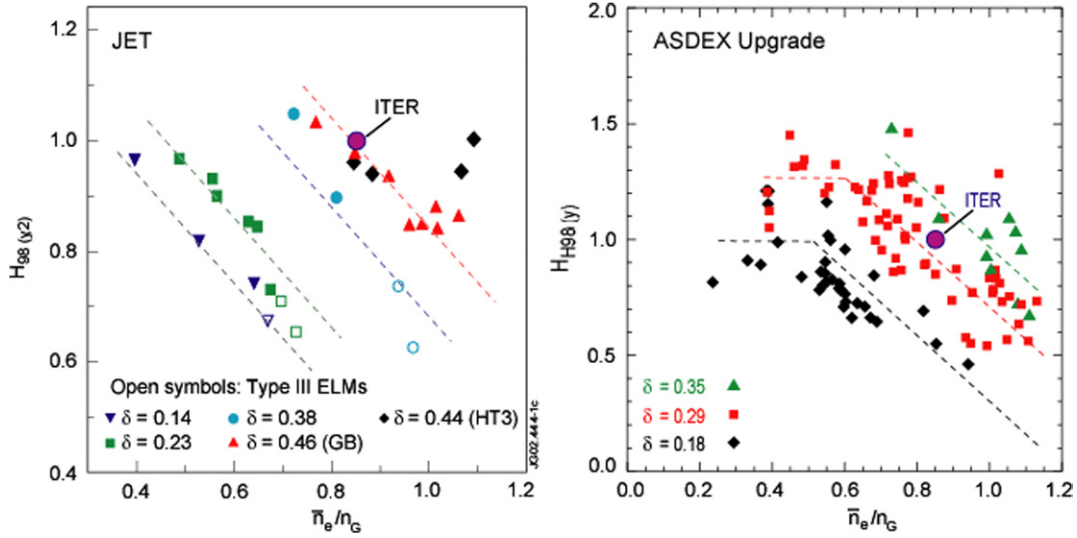


Figure 55. Confinement enhancement factors relative to the empirical H-mode confinement scalings as a function of \bar{n}_e/n_G at different triangularities δ . (Left) JET. Reprinted with permission from [370]. (Right) ASDEX Upgrade. Reprinted with permission from [248].

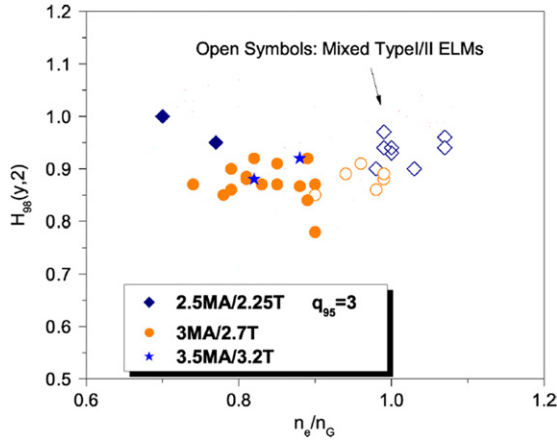


Figure 56. Confinement enhancement factors for the density scans in JET at $q_{95} = 3$, with I_p/B_t of 2.5 MA/2.25 T, 3 MA/2.7 T and 3.5 MA/3.2 T. Reprinted with permission from [500].

4.1.2. High density discharges with pellet fuelling. Figure 58 (left column) shows a JET discharge demonstrating the potential of high field side (HFS) pellet injection for fuelling the plasma to high density with simultaneous high confinement in a large tokamak [502]. In this discharge with a tailored injection rate, a density above the Greenwald density has been achieved with a large peaking factor, $n_e(0)/n_{ped} \approx 2$, $H_{98(y,2)} \approx 0.82$ and $\beta_N \approx 1.8$, although further work is needed to optimize the stationarity. The right column in figure 58 shows a flat density profile in ASDEX Upgrade near the H-mode density limit with strong gas puffing, and strongly peaked density profiles with high field side pellet injection [367]. One can see that pellet fuelling achieves higher central densities compared with strong gas puffing at similar edge densities. Evolution of the density profile after injection of a single pellet is also shown.

HFS pellet injection is presently considered as a main fuelling technique compatible with reactor conditions. However, this technique is not yet sufficiently developed to be accepted as a convenient tool in current experiments. Further

work is required. High density discharges with good H-mode confinement sustained for long times with density peaking and with impurity seeding are discussed in section 3.4.5.

4.1.3. Understanding of density-limiting processes. There are several density limits in tokamaks [1, 431]. Two of them, i.e. the H-mode density limit associated with a back transition from H- to L-mode and the ultimate L-mode density limit related to plasma disruption are the most important for reactor like devices. The figure of merit for the L-mode density limit is the Greenwald density [1, 431],

$$n_G = \frac{I_p}{\pi a^2} \equiv 1.59g \frac{B_t}{q_{95}R} \quad (10^{20} \text{ m}^{-3}, \text{ MA}, \text{ T}, \text{ m}), \quad (12)$$

where $g = q_{95}/q_{cyl}$ is the plasma shaping factor with $q_{cyl} = 5a^2 B_t / (RI_p)$. Typically, at operation in the Type I ELMy H-mode with gas puff fuelling, an increase in density above some limit leads to a transition from Type I to Type III ELMs accompanied with reduction of the stored plasma energy by 15–40% [503]. A further increase in the gas fuelling rate leads to a back transition to the L-mode, correlated with complete divertor detachment and/or divertor/X-point MARFE formation [1]. At even higher fuelling rates, the L-mode density limit disruption occurs, terminating the discharge.

Models for the H-mode density limit. A number of semi-empirical and theoretical models for the H-mode density limit have been suggested. The Borrass model identifies the density limit with a complete divertor detachment. The limit on the separatrix density that follows from the ‘two-point’ SOL model has been obtained in the form [504] $n_{sep} \propto q_{\perp}^x B_t^{5/16} / (q_{95}R)^{11/16-x}$, where $x = (10 - \xi) / [16(1 + \xi)]$, ξ is an arbitrary constant, $q_{\perp} = (P_{heat} - P_{rad}^{tot}) / S_{sep}$, $P_{rad}^{tot} = P_{rad}^{core} + P_{rad}^{div}$ and S_{sep} is the separatrix surface area. This relation, in combination with an empirical scaling for n_{ped}/n_{sep} , normalized to a typical JET discharge with a strong gas fuelling and flat density profile gave the Borrass

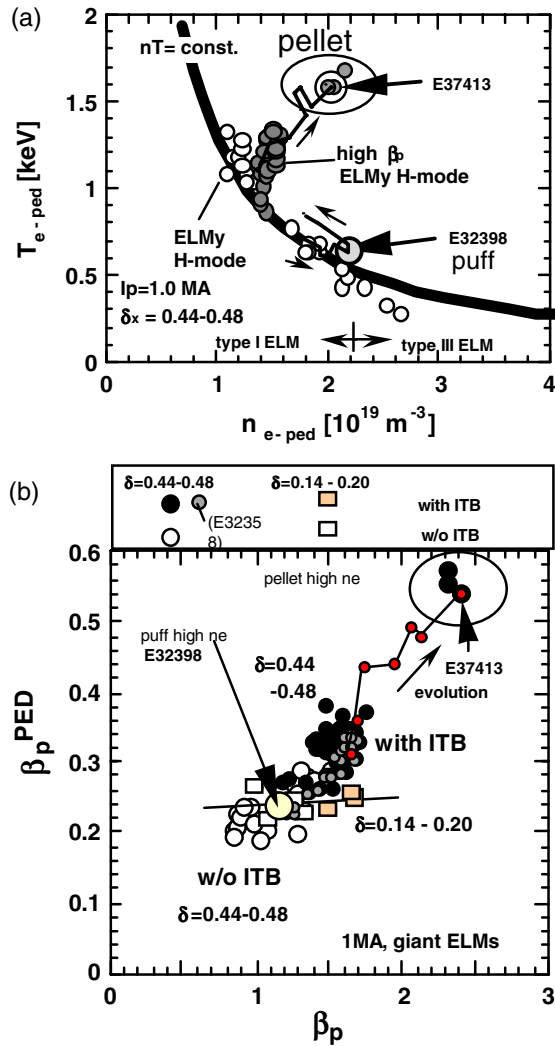


Figure 57. JT-60U pedestal conditions. (a) $n_{e,\text{ped}}$ versus $T_{e,\text{ped}}$ for ELMy discharges at 1 MA and $\delta = 0.44\text{--}0.48$ (open circles: standard ELMy H-mode, small closed circles: Type I ELMy high β_p H-mode including pellet injected discharges). (b) Dependence of the pedestal poloidal beta, $\beta_{p,\text{ped}}$, for the Type I ELMy discharges at 1 MA (circles: high $\delta = 0.44\text{--}0.48$, squares: low $\delta = 0.14\text{--}0.2$, open: without ITB, closed: with ITB). Reprinted with permission from [501].

scaling [505],

$$n_{\text{BLS}} = 4.14 \frac{q_{\perp}^{0.094} B_t^{0.53}}{(q_{95} R)^{0.88}} (10^{20} \text{ m}^{-3}, \text{ MW m}^{-2}, \text{ T}, \text{ m}), \quad (13)$$

where $n_{\text{BLS}} = n_{\text{ped}} \approx \bar{n}_e$. This scaling with the same normalization constant fits also the ASDEX Upgrade data [506]. Simulations of SOL and divertor plasma in JET with the B2-EIRENE code [507, 508] have revealed a divertor detachment and a saturation of the upstream separatrix density at plasma parameters similar to those at the H-mode density limit in experiments [504]. The H-mode density limits observed in JET and ASDEX Upgrade with gas fuelling agree well with the Borrrass scaling (figure 59(a)) and are, in average, $\sim 20\%$ below the Greenwald scaling although some points are close to n_G (figure 59(b)) [509]. A log-linear regression analysis of the JET database using B_t , R , q_{\perp} , q_{95} and δ as variables yields an empirical scaling for the H-mode density

limit similar to equation (13) [510]. There are data, however, which contradict to assumption that the divertor detachment is a main reason for the H–L transition. Results of studies of high-density discharges in JT-60U [511] suggest that the ultimate cause of the H-mode density limit is deterioration of confinement. It was observed that density increase under low radiation conditions was limited by either H–L transition or transition from a Type I to a Type III ELMy regime without any sign of divertor detachment, although the latter always occurred at densities approaching the density limit under high radiating conditions. Also, in deriving the Borrrass scaling, a Bohm-like radial transport in the SOL was assumed, although much higher absolute values of D_{\perp} (a factor of 50–100 in DIII-D case [431, 512]) are needed in model calculations for quantitative agreement with experimental data. Therefore, the relation (13) should be treated as empirical rather than theory-based scaling.

The scaling (13) predicts a relatively low H-mode density limit for ITER, $n_{\text{BLS}}(\text{ITER}) \approx 0.45n_G$, suggesting that it could be difficult to obtain the required plasma density, $\bar{n}_e \geq 0.85n_G$, in this device with gas puff alone. On the other hand, Mahdavi *et al* [513] using a model for divertor power balance combined with an analytical gas fuelling model, have shown that the maximum achievable pedestal density in ITER could be close to or exceed n_G with gas fuelling alone, if a DIII-D type open divertor configuration with pumping from the divertor is utilized. Although the basic ideas of this approach are reasonable, the model itself is over-simplified and can hardly be expected to be relevant for extrapolation to ITER. In particular, the model for power balance in the SOL neglects the impurity radiation and the volumetric recombination of the divertor plasma.

Modelling of the edge plasma in ITER using the B2-EIRENE code revealed a saturation of the separatrix density at the level of $(3\text{--}4) \times 10^{19} \text{ m}^{-3}$ under gas fuelled conditions, in good agreement with the Borrrass predictions [514]. To ensure a broad operational space in ITER with a closed divertor, substantial core fuelling, e.g. injection of pellets penetrating beyond the H-mode pedestal has been adopted [515].

Integrated core–pedestal–SOL (ICPS) modelling with the multi-mode transport model (MMM) applied for the plasma core with boundary conditions on the separatrix obtained from B2-EIRENE calculations shows that a reasonable operation space with $\bar{n}_e = (0.7\text{--}1.3)n_G$ and $Q = 6\text{--}30$ would exist in ITER at a strong core fuelling rate $15\text{--}60 \text{ Pa m}^3 \text{ s}^{-1}$ combined with an edge gas puff fuelling rate $0\text{--}70 \text{ Pa m}^3 \text{ s}^{-1}$, which satisfies acceptable steady-state power loads ($\leq 10 \text{ MW m}^{-2}$) on the divertor target [516]. In these simulations, a modified MMM transport model is applied at the plasma edge to produce an edge pedestal. The ICPS model has been calibrated against an H-mode discharge in JET and fitted well the edge parameters in ASDEX Upgrade density scan experiments.

Models for the L-mode density limit. In most experiments with gas puff fuelling and flat density profiles, the H–L transition occurs rather close to the L-mode disruptive limit (DL), $n_{H-L}/n_{\text{DL}} = 0.7\text{--}0.9$ [431, 509]. Therefore, both the H- and L-mode density limits in present machines can be reasonably well characterized by the Borrrass and Greenwald

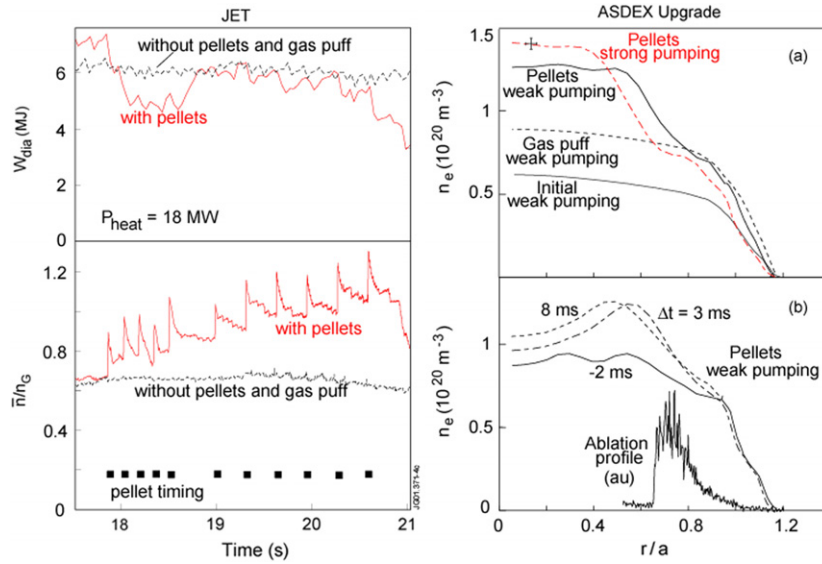


Figure 58. (Left) Time evolution of the normalized electron density n_e/n_G and total plasma energy content W_{dia} in JET discharge #53212 with high field side pellet injection at $I_p = 2.5$ MA, $B = 2.4$ T, $\delta_U/\delta_L = 0.34/0.3$ and $\kappa = 1.67$. Dashed lines correspond to a reference discharge without pellet injection and gas puff. Reprinted with permission from [502]. © 2002 Institute of Physics. (Right): (a) density profiles in ASDEX Upgrade when ramping up from the initial profiles to the H-mode density limit by strong gas puff (dashed curve) or to stable H-mode operation beyond the Greenwald density by pellet refuelling with turbomolecular pumps only (solid curve) or with cryopumping (chain curve). (b) Density profiles before and after single pellet injection and the pellet emission profile. Reprinted with permission from [367].

scalings. However, due to stronger B_t dependence (at constant q_{95}) in the Greenwald scaling, it predicts a significantly higher (by a factor of 2) density limit for ITER compared with the Borrass scaling. In this regard, an accurate comparison of the density limits predicted by the two scalings with the disruption limit in Alcator C-Mod at high B_t , close to that in ITER, would be of interest.

It is generally accepted that the disruptive density limit is associated with cooling of the plasma edge that causes the current profile to contract, destabilizing the $m/n = 2/1$ MHD mode [1]. Two cause of edge cooling, i.e. increase in radiative power loss and transport enhancement, are considered [431].

Radiation models describe satisfactorily a number of aspects of the L-mode density limit, such as radiation collapse at $P_{\text{rad}} \approx P_{\text{heat}}$, MARFE formation and divertor detachment [1]. However, they predict a strong dependence of the limit on heating power and impurity content that are not seen in some experiments [431].

Recent experiments support earlier indications of a possible link between the cross-field particle transport in the edge plasma and the density limit [431]. General trends observed in Alcator C-Mod [517] and DIII-D [518,519] are as follows. As \bar{n}_e/n_G is increased from low values to values approaching ~ 1 , a benign cross-field heat convection increases to a level that impacts the SOL power loss channels and reduces the separatrix electron temperature. And finally, non-diffusive, intermittent transport phenomena known as ‘blobs’ (normally associated with a far SOL) invade the closed flux surface region and carry a convective power loss that impacts the power balance of the discharge. Shortly before a disruption, the radiation power loss also increases.

Strong enhancement of turbulent transport in the SOL with increasing density has been found in theory-based modelling.

Three-dimensional non-linear gyro-fluid simulations of the Braginskii equations in a simple geometry have revealed very high turbulent transport ($\sim 50 \text{ m}^2 \text{ s}^{-1}$) driven by the resistive ballooning instability at plasma parameters typical for the SOL at the density limit in present experiments [520]. Simulations of the edge plasma turbulence using the BOUT code in a realistic divertor geometry [177,521] have shown that turbulent transport at the plasma edge increases strongly with density (by factors 10–100) near the Greenwald density and can lead to an X-point MARFE formation when impurity radiation is included. Tokar [522] has demonstrated the importance of the synergy between anomalous transport and impurity radiation for density limit phenomena using an analytic model for the drift-resistive ballooning instability in a plasma with a circular cross-section.

The ratio \bar{n}_e/n_G is not dimensionally correct. Experiments on DIII-D and JET have shown that, when the ratio \bar{n}_e/n_G was kept fixed with other dimensionless parameters kept constant, the normalized energy confinement time on DIII-D was 20% smaller than on JET, while at fixed v_* the normalized energy confinement times on JET and DIII-D agreed within $\sim 5\%$. These results suggest that scaling transport properties from present devices to ITER at fixed \bar{n}_e/n_G would result in incorrect predictions [430].

Using the standard non-dimensional scaling approach, i.e. taking β_N and v_* the same as those in JET shot #53212 ($B_t = 2.4$ T, $I = 2.5$ MA, $a = 0.96$ m, $\beta_N = 1.8$, $\bar{n}_e/n_G = 1$, and pellet fuelling, as shown in figure 56) [370] one obtains

$$\left(\frac{\bar{n}_e}{n_G}\right)_{\text{ITER}} = \left(\frac{B_{t,\text{ITER}}}{B_{t,\text{JET}}}\right)^{1/3} \left(\frac{a_{\text{ITER}}}{a_{\text{JET}}}\right)^{2/3} \left(\frac{\bar{n}_e}{n_G}\right)_{\text{JET}} \approx 2 \quad (14)$$

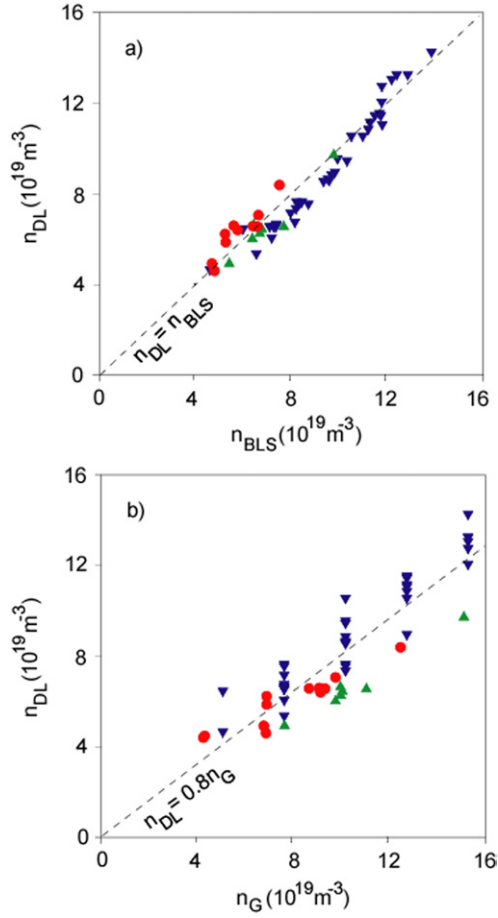


Figure 59. Experimental H-mode density limits, n_{DL} , versus Borraass (a) and Greenwald (b) scaling predictions for a set of data from JET and ASDEX Upgrade discharges with gas puff fuelling. Experimental data are from JET Mark-I and Mark-II (upward triangles), the gas box divertor configuration (bullets) and from the ASDEX Upgrade Divertor II configuration (downward triangles). Reprinted with permission from [509].

and

$$\langle T \rangle_{ITER} = \left(\frac{B_{t,ITER}}{B_{t,JET}} \right)^{2/3} \left(\frac{a_{ITER}}{a_{JET}} \right)^{1/3} \langle T \rangle_{JET} \approx 2 \langle T \rangle_{JET} \quad (15)$$

for the ITER non-dimensionally similar discharge. At $\bar{n}_e/n_G \sim 1$ in ITER, the plasma temperature should be four times higher and $\langle v_* \rangle$ eight times lower than those in the JET discharge. For coupled core and edge temperatures (e.g. ‘stiff’ profiles) this suggests that radiative instabilities (MARFES) and resistive ballooning mode instabilities would be less pronounced in ITER than in the JET discharge. This means that the Greenwald density may be exceeded in ITER.

4.1.4. Summary. Experiments on major tokamaks demonstrate that increasing the triangularity of the plasma cross-section permits the attainment of high energy confinement in Type I ELMy H-mode at high plasma densities, close to the Greenwald density where ITER is planned to operate. However, these favourable results cannot be extrapolated directly to ITER using the dimensionless scaling techniques since plasma in these discharges has

significantly higher collisionality ν_* than ITER at the same β_N and $\bar{n}_e/n_G \sim 1$. Recent experimental and theoretical studies confirm the hypothesis that increase in anomalous particle transport at the plasma edge plays a role in the L-mode density limitation. Due to higher temperature and lower ν_* expected at $\bar{n}_e/n_G \sim 1$ in ITER, the resistive ballooning modes near the separatrix could be stable and an X-point MARFE may not penetrate inside the separatrix, making density limitations less severe compared with present experiments. Definitive experimental tests of this statement can only be made in reactor-scale devices.

The H-mode density limits in present experiments with gas puff fuelling and flat density profiles are described reasonably well by the Borraass scaling. The density limit predicted by this scaling for ITER is about 2 times below the Greenwald density. Experiments show that achievable averaged plasma density in the H-mode increases with density profile peaking. Some theoretical models for turbulent transport, supported by limited experimental data, predict moderate density peaking in ITER in the absence of core plasma fuelling. However, to ensure achieving high core density in ITER, substantial core fuelling, e.g. via pellet injection in addition to gas puff, would be needed.

To predict achievable densities in ITER with a good accuracy, first principle theories for the density limit are required. Such theories should include detailed SOL and pedestal physics taking into account transport, atomic and MHD processes. For testing the theories, accurate measurements of transport coefficients and radiation in the SOL and H-mode pedestal with a good temporal and space resolution are necessary.

4.2. Pedestal characteristics and structure

4.2.1. The importance of H-mode pedestal characteristics. Successful ITER operation will require both high pressure at the inner edge of the H-mode transport barrier and small ELMs. ITER will operate near the density limit in order to achieve the highest fusion power output, $P_{fus} \propto n^2$, and to maintain the power above the value required for transition to H-mode, $P_{fus}/P_{LH} \propto n^x$, where $1 < x < 1.4$. The relatively flat density profile expected in ITER H-mode discharges implies a pedestal density also near the density limit. To achieve high efficiency, $Q = P_{fus}/P_{aux}$, requires good energy confinement, $P_{fus}/P_{loss} \propto n^x H_{L89}^y$, where $-1 < x < 1$ and $2 < y < 3$ [2], where H_{L89} is the ratio of H-mode to L-mode energy confinement time. H_{L89} is expected to improve with pedestal temperature at a given pedestal density as seen experimentally, for example in figure 54, and expected theoretically from turbulent transport models [523, 524] that predict core temperatures to be highly dependent on the value of the temperature at the top of the H-mode pedestal. Estimates of the pedestal temperature required for $Q = 10$ at $P_{fus} = 400$ MW with $n_{ped} \sim 0.7 \times 10^{20} \text{ m}^{-3}$ vary from $T_{ped} \sim 4$ keV for GLF23 [236] to $T_{ped} \sim 2.5$ keV with the less stiff multi-mode model [236, 525]. Thus high pedestal pressure is needed to simultaneously meet the goals of high fusion power output and high efficiency. The largest allowable energy loss across the separatrix during an ELM is set by the maximum acceptable peak heat flux to the divertor plates as described in chapter 4 of

this issue [364] and section 4.6 of this chapter. Unfortunately, the ELM energy loss generally increases with the pedestal pressure. Although several factors, including the duration of the ELM energy loss, can influence the divertor peak heat flux from ELMs (chapter 4, this issue [364]), the acceptable ELM energy loss for the T_{ped} range above is roughly 5–10% of the energy in the pedestal, $W_{\text{ped}} = (3/2)p_{\text{ped}}V$. Since this ELM energy loss as a fraction of pedestal energy is typical for Type I ELMs in present-day tokamaks, ELM mitigation techniques (section 4.6.3) or alternatives to the Type I ELM regime which maintain high pedestal pressure (section 4.7) may be required for ITER.

4.2.2. Requirements and projections for H-mode transport barrier width. As described in section 4.8, the peeling–ballooning mode model for the onset of the ELM instability is well supported by experiments. Since the peeling–ballooning mode limits the pressure gradient in the H-mode pedestal region, the pedestal pressure is set by a combination of this limit and the radial extent of the steep gradient region that corresponds to the edge transport barrier. Using the predictions from peeling–ballooning theory for ITER shown in figure 88, a ratio of transport barrier width to minor radius of $1 < \Delta/a < 2.5\%$ would be needed to reach pedestal temperatures in the required 2–4 keV. Transport barrier widths in this range are typical in present-day tokamaks [526–528], however a well-validated means of predicting the H-mode transport barrier width in ITER is still lacking and remains a major topic of research. Attempts to project a barrier width for ITER through physics based or empirical scaling from multi-tokamak databases are described below [529]. This approach has not yielded a result that is consistent with the experience on all tokamaks, perhaps due to the wide variation of parameters in such databases and the difficulty of separating the edge stability constraint. A more controlled set of inter-machine comparison experiments has been, or will be, carried out which use the dimensionless parameter approach to derive a scaling for the transport barrier width [530–532]. These experiments, some of which are described below, have so far not provided a complete scaling relation for the barrier width but do provide some insight into the important parameters. Also, work is underway to extend turbulent transport models through the pedestal region [533]. This approach may ultimately provide a firm basis for understanding the pedestal transport barrier structure.

Below we describe three physics-based arguments as to what might set the transport barrier width and examine how well they fit the available data and what they would predict for ITER. Scaling laws derived for the H-mode transport barrier width are compared with experimental results in databases available to the international community through the ITPA. PDB3V2 [534] includes pedestal information for Alcator C-Mod, ASDEX Upgrade, DIII-D, JET and JT-60U, including both electron and ion pedestal parameters; however, the data is mostly averaged over ELMs. D3DPED [529] is comprised entirely of DIII-D data with the Thomson scattering measurements of the electron pedestal parameters taken roughly every 10 ms in 173 discharges. At present there are transport barrier width measurements available for JT-60U, DIII-D and Alcator C-Mod.

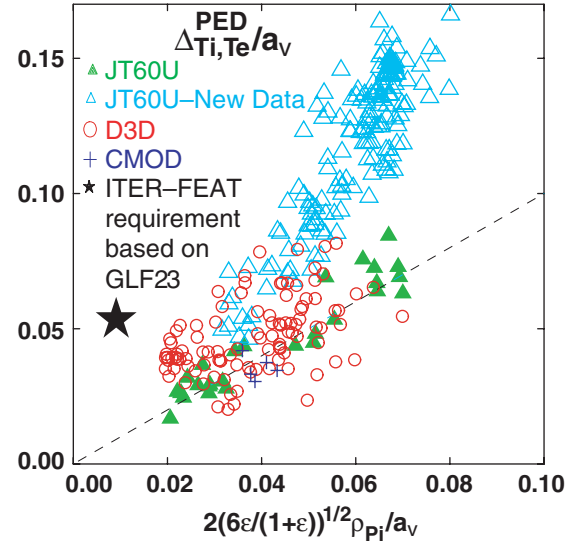


Figure 60. Normalized transport barrier width is correlated with ion poloidal gyro-radius, ρ_{pi} . Older JT-60U data at low triangularity is in agreement with scaling based on turbulence suppression from an edge radial electric field generated by loss of ions on banana orbits crossing the separatrix, as described in section 4.2.2. Reprinted with permission from [529].

Some authors have suggested a scaling for the transport barrier width based on a process that might create the velocity shear. Shaing [535] and others have argued that the velocity shear that suppresses turbulence in the H-mode pedestal is driven by the $\vec{J} \times \vec{B}$ force associated with currents that must flow in response to the loss of ions on orbits that cross the separatrix. The range of this force is then roughly the width of the banana orbit for a barely trapped ion

$$\Delta \approx 2 \frac{f_i v_{\text{ti}}}{\Omega_{\text{pi}}} \approx 2 \frac{\sqrt{2\varepsilon/(1+\varepsilon)} \sqrt{3kT_i/m_i}}{eB_p/m_i} = 2\sqrt{6\varepsilon/(1+\varepsilon)} \rho_{\text{pi}}, \quad (16)$$

where $\Omega_{\text{pi}} = B_p/m_i$ is the ion gyro-frequency in the poloidal field, B_p , and $\rho_{\text{pi}} = \sqrt{kT_i/m_i}/\Omega_{\text{pi}}$ is the ion poloidal gyro-radius. The radial electric field acts to squeeze the orbits giving [198] $\Delta \propto \rho_{\text{pi}}/\sqrt{Q}$, where $Q = |1 - E'_r/B_p\Omega_{\text{pi}}|$. Since the ∇p term typically dominates the E_r determined from radial force balance, we obtain $Q = 1 + (\rho_{\text{pi}}/\Delta)^2$. Itoh [536] noted that viscosity, μ , would drive the shear flow region inward from the region where the force was present giving a scaling for the transport barrier width, $\Delta \propto \sqrt{\rho_{\text{pi}}^2 + \mu/v_i}$, where v_i is the ion collisionality. The measured barrier width for the three machines is compared with equation (16) in figure 60 using poloidally averaged values for the poloidal field, minor radius and width: $B_p = \mu_0 I_p / \Gamma$, where Γ is the plasma circumference, and $a_v = \sqrt{V/2\pi^2 R}$, where V and R are the plasma volume and major radius. Previous work on JT-60U [526] gave $\Delta_{\text{Ti}} \cong 2.3\rho_{\text{pi}}$ for ELM-free discharges, where this relation held well over a range of safety factors, $2 < q < 7$, and to some extent was independent of plasma shape over a range of triangularity, $0.05 < \delta < 0.4$, and elongation, $1.4 < \kappa < 1.7$. This is close to the value predicted by equation (16) for JT-60U, $\Delta = 2.2\rho_{\text{pi}}$ or $\Delta = 2.0\rho_{\text{pi}}$, with orbit squeezing. More recent JT-60U data for ELMing

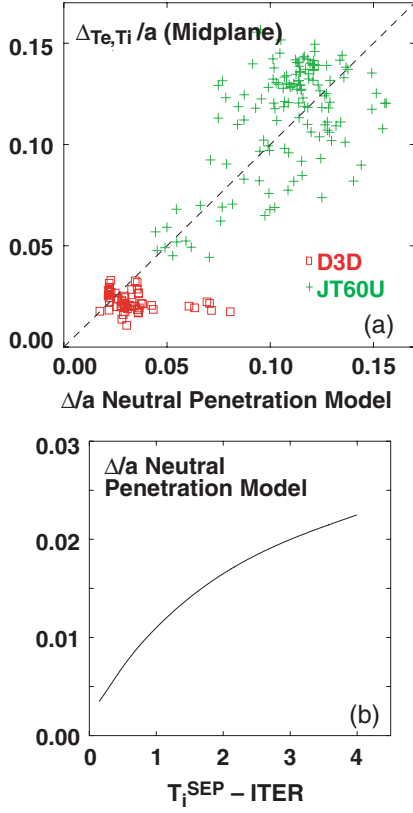


Figure 61. (a) Comparison between the transport barrier width at the midplane and the width of the steep density-gradient region inside the separatrix from neutral penetration. (b) Transport barrier width prediction for ITER as a function of the separatrix ion temperature; the 3% width required by stability is reached only at very high T_i^{ped} . Reprinted with permission from [529].

discharges, most of which is at higher triangularity, departs from this scaling but a strong correlation with ρ_p is still clear. The DIII-D data lie near the predicted value, however, there is no clear trend with ρ_{pi} . The Alcator C-Mod data is also near the predicted value, but other data from Alcator C-Mod show no correlation with ρ_{pi} [527]. This scaling would give a pedestal width in ITER of $\Delta/a = 0.004$ ($\Delta_v/a_v = 0.01$), which would give an expected pedestal temperature of only 1 keV for ITER based on the stability calculations of figure 88. (Note that the required value for ITER based on GLF23 from figure 88 is mapped from the midplane value to a_v in figure 60.) Experiments on DIII-D, however, in which divertor pumping and gas puffing were used to vary the pedestal temperature over a wide range indicated that a simple function of temperature could not account for both the variation of the width between ELMs and the overall behaviour as the density was varied [528]. The JT-60U discharges are in a low collisionality regime where the viscosity term may be expected to play a role and result in a different scaling. In addition, DIII-D discharges where the $\vec{v}B$ drift direction was reversed did not show a significant change in transport barrier width although a significant change in orbit loss would be expected. These results suggest that a more detailed study of the possibility that the ion orbit loss region sets the transport barrier width is needed before it can be applied with confidence to a prediction for ITER.

In another approach to H-mode transport barrier width scaling, the process which creates E_r is not directly considered, rather it is assumed that any E_r profile consistent with the radial force balance can be obtained by adjusting the particle and power fluxes. Taking transport coefficients that were reduced continuously with increasing $\vec{E} \times \vec{B}$ velocity shear, Hinton and Staebler [537] demonstrated a transport bifurcation and derived a barrier width scaling set primarily by the edge localized neutral particle source

$$\Delta \approx [2\lambda L_n^{sep} \ell n(c\Gamma_{sep} Q_{sep})]^{1/2}, \quad (17)$$

where $\lambda = v_n/n_e(\sigma v)$ is the neutral mean free path, L_n^{sep} is the density-gradient scale length at the separatrix, and Γ_{sep} , Q_{sep} are the particle and heat fluxes at the separatrix on which the width depends only logarithmically. Work on DIII-D [513, 538] has shown that the shape of the density profile in the transport barrier is consistent with what would be expected for neutral penetration. In this model, when the density is sufficiently high, neutrals cannot cross the SOL to reach the main plasma without undergoing charge exchange or ionization (in which case they are recycled to the divertor). Thus, at high density, neutrals crossing the separatrix have acquired the velocity of the ions in this region, $v_n \approx \sqrt{2T_i^{sep}/\pi m_i}$. This type of process generally characterizes the DIII-D discharges. At low density, neutrals at the Frank–Condon velocity can cross the separatrix and reach regions of higher ion temperature. Since the charge-exchange rate is somewhat larger than the ionization rate, a large fraction of the Frank–Condon neutrals can acquire velocities more characteristic of the H-mode pedestal temperature. This effect is further enhanced by the fact that above 300 eV the ionization rate decreases while the charge-exchange rate continues to increase. The JT-60U discharges in the ITPA database with large widths are generally in the Frank–Condon dominated regime. Figure 61 shows a comparison between this neutral penetration model [538] and transport barrier widths. The Alcator C-Mod results are not included in the figure since almost all the density profile is predicted to be outside the separatrix making it difficult to relate the density profile to the particle source inside the separatrix. In this analysis the separatrix ion temperature for DIII-D is taken to be the temperature at 95% of the poloidal flux, which may account for some of the large predicted values. Because of the high densities required in ITER for a high level of fusion power, the ITER case is similar to DIII-D. A prediction of the ITER pedestal width based on this model as a function of separatrix ion temperature is shown in figure 61(b). This model suggests that, at least in the case of gas puff fuelling, it would be difficult to obtain a large enough width based on stability considerations (figure 88) unless the separatrix temperature was so high that it would be in conflict with the ITER divertor requirements. However, specific inter-machine comparison experiments [530–532] were carried out to address the question of whether the neutral penetration depth is setting the H-mode transport barrier width. No change in Δ/a was observed in comparison with the Alcator C-Mod, DIII-D and JET tokamaks with v_* , ρ_* , β , q and the plasma shape fixed at the top pedestal under conditions where the neutral penetration would be expected to vary significantly.

Another approach to determining the barrier width is based on the idea that the inner edge of the barrier is defined by the point at which the velocity shear is sufficient to quench the turbulence [523]. There is computational and theoretical support for the principle that the turbulence is quenched when the velocity shearing rate in the absence of turbulence exceeds the linear growth rate of the instabilities [523]. ITG modes still may dominate the region near the inner boundary of the transport barrier and we take as a guide the results from core transport simulations [20,523]. Typically the pressure gradient term dominates the radial electric field derived from ion radial force balance so that

$$\omega_{E \times B} \sim \frac{c_s^2}{\Delta^2 \Omega_{ci}} > \gamma_L \sim \frac{(c_s a)(a/\Delta)^{\zeta_1} (T_e/T_i)^{\zeta_2}}{f(s, \alpha) g(Z_{\text{eff}}) h(v_{*s})}. \quad (18)$$

The destabilizing effect of the temperature gradient is given by a/Δ taking the temperature gradient scale length as the transport barrier width. The exponent ζ_1 is a function of the type of instability, e.g. slab versus toroidal ITG; for shifted circles GLF23 simulations give $\zeta_1 \approx 3/2$ [20]. The T_e/T_i term is the stabilizing effect of high ion relative to electron temperature, for shifted circles $\zeta_2 \approx 3/2$ [20]. $f(s, \alpha)$ is a function that has a similar form to the s - α diagram of the ideal MHD ballooning mode, reflecting the similar effects of curvature and shear on ITG modes [20]. As with ideal MHD, at high magnetic shear increasing shear is stabilizing and increasing pressure gradient is destabilizing, while the opposite is true at low shear where something like a second stable regime occurs. We would expect $f(s, \alpha)$ also to be a function of plasma shape as is the case for ideal MHD. $g(Z_{\text{eff}})$ represents the stabilizing effect at high Z_{eff} . $h(v_{*s})$ represents the stabilizing effect of collisionality where the collision frequency in this case is normalized to the sound transit time characteristic of the eddy turnover time; for DIII-D, JT-60U and ITER, $v_{*s} \ll 1$. Recent work [253] has shown that the effectiveness of the velocity shear is expected to be reduced at high elongation through essentially replacing the field in Ω_{ci} by $B_{\text{eff}} \approx \kappa B_t$. Solving equation (18) for $\Delta^* = \Delta/a$ gives

$$\Delta_*^{1/2} = \rho_{*s} \left(\frac{T_e}{T_i} \right)^{1/2} f(s, \alpha) g(Z_{\text{eff}}) h(v_{*s}). \quad (19)$$

The normalized width, Δ^* , is plotted against $\rho_{*s} = c_s/\Omega_{ci}$ for data from JT-60U, DIII-D and Alcator C-Mod in figure 62, where all the values are measured at the top of the pedestal. It is clear that this quantity does not organize the data well; the small trend between DIII-D and JT-60U comes mostly from the κ term in the effective field. Adding the temperature ratio term only further increases the scatter in such a plot. It should be noted that the scale length for the variation of the shear, and also possibly of the temperature ratio and Z_{eff} , may be comparable to the transport barrier width that introduces an implicit dependence of the terms on the right-hand side of equation (19) on Δ^* . For example, strong shear dependence could make the width more a function of the shear profile and only weakly dependent on ρ_{*s} . The strong dependence of the barrier width on ρ_{*s} given in equation (19) is also inconsistent with experiments on DIII-D in which ρ_{*s} at the top of the pedestal was varied while keeping other dimensionless parameters fixed. These experiments showed no change in

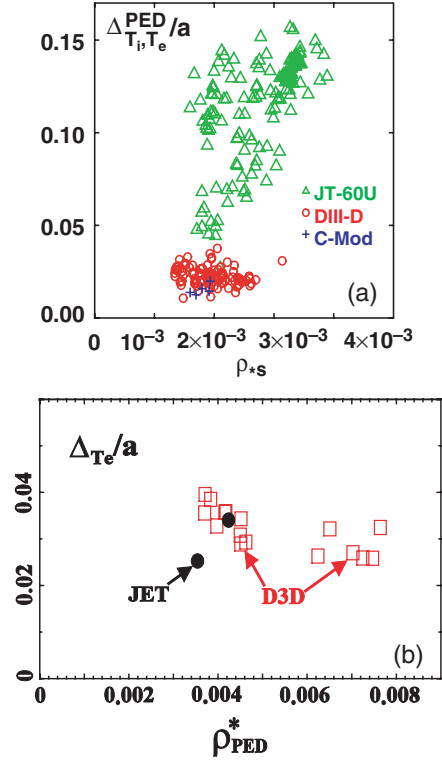


Figure 62. (a) The normalized transport barrier width on the outer midplane is not well correlated with normalized gyro-radius, suggesting that the more complex terms in equation (19) may be important. Reprinted with permission from [529]. (b) The DIII-D/JET pedestal comparison experiments show no strong dependence of the pedestal width on ρ_{*s}^{ped} when v_{*s}^{ped} , β^{ped} , q and plasma shape were held fixed [532].

barrier width for about a factor of 2 change in ρ_{*s} as shown in figure 62(b) [532]. These considerations indicate that a more complete theoretical understanding of the behaviour of the ITG growth rates in the pedestal region in real geometry is required before this type of argument can be applied to a prediction of the barrier width.

Finally we consider an empirical scaling approach guided to some extent by the discussion above [529]. The rather clear dependence of the JT-60U data on ρ_p suggest this type of term should be included. The DIII-D data however suggest a mixture of density and temperature dependence. Previous empirical scaling work on DIII-D gave $\Delta_{\text{pe}} \propto (\beta_p^{\text{ped}})^{0.4}$. Following Hatae [539], separate temperature and density dependences are allowed for through ρ_* and a dimensionally correct form for the density normalized to the Greenwald density, $n_{*G} = 0.1n(10^{20}/\text{m}^3)a^{1.75}/I_p(\text{MA})$. Terms reflecting the effect of the plasma cross-sectional shape on the velocity shear and ITG growth rates are also included. Fits were done to both a dimensionless form and a form that allows for explicit size dependence. For the DIII-D data the larger D3PED data were included. The size dependent fit gives

$$\Delta_* = 0.12 \rho_{*s}^{0.39} (B_t/B_p^{\text{ave}})^{0.31} n_{*G}^{0.19} \kappa^{-0.5} (1 + \delta)^{0.57} R^{1.6} a^{-0.5}. \quad (20)$$

This form predicts a pedestal width for ITER well above the value required by stability. Fitting to a dimensionless

expression gives

$$\Delta_* = 0.044 \rho_{*s}^{0.38} (B_t/B_p^{\text{ave}})^{0.27} n_{*G}^{0.19} \kappa^{-0.98} (1+\delta)^{0.52} R^{1.6} \varepsilon^{-2.3}. \quad (21)$$

This form does not organize the different machines as well as equation (20), but it also predicts that the required pedestal width for ITER is met.

4.2.3. H-mode pedestal pressure scaling. A scaling law can be derived directly for the pedestal pressure from the PDB3V2 database that was described above [540]. For this scaling the pedestal pressure gradient is taken as the ideal infinite n ballooning mode stability criteria,

$$\left(\frac{dp}{dr}\right)_0 = \frac{1}{2\mu_0 R} \left(\frac{RB_p}{a}\right)^2 \left(\frac{2}{1+\kappa^2}\right) \quad (22)$$

modified by a factor to take into account a Shafranov shift dependence and the stronger shape dependence of lower n peeling–ballooning modes,

$$\left(\frac{dp}{dr}\right)_{\text{crit}} = \left(\frac{dp}{dr}\right)_0 F(\text{shape}, \beta_p), \quad (23)$$

$$F(\text{shape}, \beta_p) \propto \kappa^{C_1} (1+\delta)^{C_2} A^{C_3} (P_{\text{tot}}/P_{\text{LH}})^{C_4}, \quad (24)$$

where $P_{\text{LH}} = 2.84 M^{-1} B^{0.82} \bar{n}_e^{0.58} R a^{0.81}$ is the L- to H-mode transition critical power, A is the aspect ratio and M is the atomic mass number. Expressing the β_p dependence in terms of power also allows for an explicit variation of the pressure with power. The H-mode transport barrier width is taken as $\Delta_* \propto \sqrt{\rho_p/a}$ [541]; this form is suggested by equation (19) where the strong variation of the magnetic shear, s , over the barrier introduces a Δ_* term to the right-hand side. The resulting scaling,

$$p_{\text{ped}} = 2.41 \times 10^3 \left(\frac{M}{n_{\text{ped},20}}\right)^{1/3} \frac{R^{4/3}}{a^4} \frac{I_{\text{p,MA}}^2}{\left(\frac{1+\kappa^2}{2}\right)^{7/3}} \times (1+\delta)^{3.2} \kappa^{3.62} A^{-2.94} \left(\frac{P_{\text{tot}}}{P_{\text{LH}}}\right)^{0.06} \quad (25)$$

is shown in figure 63. This scaling predicts a $T_{\text{ped}} = 5.3$ keV at $n_{\text{ped}} = 0.7 \times 10^{20} \text{ m}^{-3}$, which exceeds the requirement for ITER to achieve $Q = 10$ even for the stiff GLF23 model.

4.2.4. Conclusions. There remains large uncertainty in the prediction of the ITER pedestal parameters. The peeling–ballooning model fits the variation of the edge pressure gradient with shape and other parameters well (section 4.8), but understanding of the H-mode transport barrier width scaling is still lacking. The transport barrier width relative to the minor radius required for ITER is at least not larger than is common in existing tokamaks. Furthermore, although arguments like those leading to equation (19) would suggest that the transport barrier width would be reduced at the small ρ_* values expected in ITER, no such strong dependence has been observed. Scaling of the pedestal pressure, although not strongly based in physics, also indicates that the ITER pedestal temperature should more than meet the required value. The main concern for the ITER pedestal may then be whether

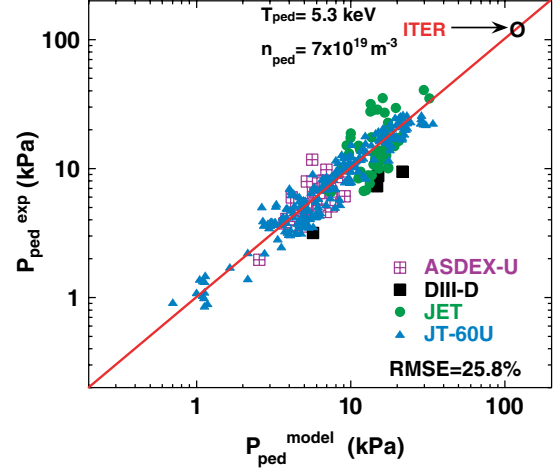


Figure 63. Comparison of pedestal pressure values in the PDB3V2 database with the model given in equation (25). This model predicts $T_{\text{ped}} = 5.3$ keV for ITER at $n_{\text{ped}} = 0.7 \times 10^{20} \text{ m}^{-3}$. Reprinted with permission from [540].

the large ELMs associated with the large pedestal energy can be mitigated or replaced by a more benign form of H-mode pedestal transport as discussed in sections 4.6 and 4.7 of this chapter, as well as in chapter 4 of this issue [364].

4.3. L–H transitions

The transition from the L-mode to the H-mode (L–H transition) is a subject that has been under constant investigation for a long time because of its complexity. This section presents new experimental results, while theoretical developments are presented in the following section. Joint experimental and theoretical studies have led to the implementation of a number of models that capture the experimentally observed dependence of the threshold power on plasma density, magnetic field and ion ∇B drift direction at the L–H transition. Experiments have also been performed expressly to validate the theoretical models. For example, a recent analytic model for the finite beta stabilization of drift-resistive ballooning modes involving zonal flow generation [542] has shown good agreement with data on DIII-D and Alcator C-Mod [543, 544]. Also, new edge diagnostics or diagnostics with better temporal or spatial resolution at the plasma edge have been developed and have contributed to advances on the experimental side of L–H transition studies.

In COMPASS-D, the H-mode is initiated when all turbulence mechanisms are stabilized [545]. The stabilization of one of these mechanisms cannot be considered as a criterion to reach the H-mode. The plasma edge potential, and therefore the radial electric field, in JFT-2M changes rapidly at the L–H transition [546, 547]. This synchronization is clearly evidenced in discharges with the injected power slightly above the threshold power. For a given plasma configuration and global parameters, the transport coefficients in Alcator C-Mod show a bifurcation when the temperature or temperature gradient at the plasma edge rises above a threshold value [548, 549]. The analysis of JET H-mode discharges shows that the electron edge temperature or the dimensionless parameter ρ_* must exceed a threshold value to obtain an L–H transition [550].

The same behaviour was also shown with the ion temperature [551]. However, the comparison between experimental data and models in JET only shows partial agreement. Therefore, in general, further model development is still required to cover more precisely all situations encountered in all devices.

The search for critical parameters in L–H transition experiments also continues in order to shed light on the underlying processes. In most cases, the variation in the threshold power constitutes the measure of the influence of the different parameters. For instance, the ion $\vec{\nabla}B$ drift direction relative to the X-point position changes the threshold power in DIII-D by a factor of two [552]. The potential underlying process responsible for the L–H transition must have: (a) different values at the same power for the two $\vec{\nabla}B$ drift directions and (b) equal values at the L–H transition. The shear in the poloidal group velocity of density fluctuations at the plasma edge fits these conditions. This is in contrast with JET plasmas where the ion $\vec{\nabla}B$ drift direction has less influence on the threshold power, but induces a significant difference in the ion temperature at the plasma edge [551].

The plasma shape and divertor configuration have significant influence on the threshold power. In JET, the threshold power decreases with decreasing X-point height above the divertor floor [553]. The removal of the divertor septum, however, had a reduced effect on the threshold power. Increasing the lower plasma triangularity decreases the threshold power when the edge density exceeds $1.7 \times 10^{19} \text{ m}^{-3}$. The H-mode accessibility in TCV Ohmic plasmas strongly depends on the plasma configuration. The minimum threshold power is obtained when L–H transitions occur during the formation of the diverted configuration [554]. The plasma configuration has an even stronger influence on the H-mode access in the new large spherical tokamaks (STs). In MAST, the threshold power is substantially reduced when the plasma is in double-null configuration [555], while in NSTX, the single-null configuration has a lower threshold [556].

The underlying effect of the plasma or divertor configuration on the threshold power is often related to the influence of the neutral density at the plasma boundary. This is confirmed by the reduction of the threshold power when the gas is injected from the high field side instead of the low field side as observed in NSTX [556], MAST [555] and COMPASS-D [555]. In all the devices, the L–H transitions are synchronized with the sawteeth [547, 557], indicating that the energy conveyed to the plasma edge following a sawtooth crash can also play a role in the L–H transition process.

All these effects contribute to the observed variation in the threshold power around the value estimated from the simple scaling that takes into account the plasma density, magnetic field and plasma size. For example, the repetition of an identical ASDEX Upgrade discharge on a day-to-day basis leads to a residual scattering of about 10%. This variation cannot be attributed to the vessel conditioning after an opening since these transitory phases were removed from the analysis [558].

The reduction in the scattering in the international threshold database (13 tokamaks, approximately 700 selected time slices) is one of the major goals of the ITPA Confinement Database and Modelling Topical Group. Several contributions from different tokamaks were revised and L–H transitions

known as occurring at an excessive threshold power, such as transitions obtained below $q_{95} = 2.5$, were deselected [559]. This operation alone reduced the RMSE value of the fits in the plasma density n_e , magnetic field B_t and plasma outer surface area S from 27.9% to 27.1%. The RMSE value decreased to 21.4% when a reduced set of data was used. This reduced set consists of more homogeneous data regarding future devices and normalization, device per device, was applied with known influencing parameters. The resulting scaling has the following form:

$$P_{\text{LH}} = 0.042 n_{20}^{0.73} B_t^{0.74} S^{0.98} \text{ (MW)}. \quad (26)$$

In ITER, it is planned to operate the L–H transition at $n_e = 0.5 \times 10^{20} \text{ m}^{-3}$. With $B_t = 5.3 \text{ T}$ and $S = 680 \text{ m}^2$, the threshold power in ITER will be 52 MW.

Recently, the roles of aspect ratio ($A = R/a$), absolute magnetic field at the outer equatorial mid plane ($B_{t,\text{out}}$) and effective ion charge (Z_{eff}) in the threshold power estimation were studied [560]. The contribution from MAST and NSTX allows the incorporation of the aspect ratio in the scaling. The influence of Z_{eff} is extracted from a subset of a data since the value is missing for many time slices. The threshold power can then be expressed as

$$P_{\text{LH}} = 0.072 n_{20}^{0.7} B_t^{0.7} S^{0.9} (Z_{\text{eff}}/2)^{0.7} F(A)^\gamma, \quad (27)$$

where $F(A) = 0.1A/f(A)$, $f(A) = 1 - [2/(1+A)]^{0.5}$ and $\gamma = 0.5$. Using this expression, for $Z_{\text{eff}} = 2.0$ the prediction for ITER is $P_{\text{LH}} = 40\text{--}50 \text{ MW}$, which should be reliable.

Recent progress in the analysis of the threshold database has not led to significant changes in the scaling coefficients. Therefore, these scalings can be used for predicting the threshold power for access to the H-mode regime in future devices.

4.4. Pedestal transport theory and modelling

Among all theories excellently reviewed by Connor and Wilson [561], most experimental evidence supported those that involved the paradigm of sheared electric field suppression of turbulence. However, the underlying mechanism that generates the radial electric field (E_r) and the corresponding ‘trigger’ (the Reynolds stress, ion orbit loss, the Stringer spin-up, effect of neutrals) is still open: the variety of observations cannot be encompassed by any single theory. This may imply that in different experiments different triggers can be involved. The most elaborated family of theories can be categorized as phase-transition models. First of all, these models have a simple structure that allows additional effects to be included, and secondly these models can be readily incorporated into transport codes. Recently, a minimal model of the L–H transition was formulated by Kim and Diamond [52], which recognizes that in addition to the mean flows turbulence suppression may be due to zonal flows that are self-generated by turbulence via the Reynolds stress. Zonal flows are very effective in suppressing turbulence because their radial scale is the same as the radial scale of turbulence, and their energy source comes from the non-linear coupling with turbulence. Zonal flows and turbulence together conserve total energy. Thus, suppression of turbulence by zonal flow means non-linear energy transfer from fluctuations to axisymmetric modes

that do not contribute to heat transport. Suppression of turbulence leads to a weakening of zonal flow generation that can result in bursty temporal behaviour (as in predator-prey models). Zonal flows may trigger the L–H transition by damping turbulence until the shearing of the mean flows becomes strong enough to damp both turbulence and zonal flows. Taking into account zonal flows reduces the L–H transition power threshold.

For predictive modelling a ‘flow-turbulence’ relationship must be incorporated into a transport code. To approximate the theory, a detailed model of the temporal evolution through the L–H transition (rather than only stationary profiles in the L- and H-modes) of the T_e , T_i , n , E_r profiles and turbulent fluxes should be included. This demands that T_e , T_i and n must all be included in the ‘minimal model’ mentioned above. This was done in [562], where the four-field edge turbulent layer model (ETL-model) was formulated to describe the non-linear dynamics of zonal flows and convective cells driven by the drift-resistive interchange instability at the plasma periphery. It was shown that the Braginskii hydrodynamic equations for four fluctuating fields—electron and ion temperatures, density and the electrostatic potential—can be reduced to the three Lorenz-like equations coupled through the equation for the kinetic energy of the fluctuations. It was shown that the control parameter for the L–H transition is the edge pressure gradient and that its critical value is much lower in the four-field (T_e , T_i , n , φ) model than in a two-field (T , φ) model. The ETL-model was then used as a boundary condition of the third kind (matching of fluxes) for the ASTRA transport code [155]. The ETL-model simulations pointed out that the L–H transition power threshold depends on the values of the temperature and density of plasma and neutrals at the separatrix, which can be ‘hidden’ parameters influencing scalings for the power threshold and width of the edge transport barrier (ETB). For example, the U-shape dependence of the L–H transition power threshold, P_{th} , on averaged density in DIII-D,

$$P_{\text{th}} \approx 1.7\langle n_{19} \rangle + 15.4/\langle n_{19} \rangle - 7.9, \quad (28)$$

where P_{th} is in MW and $\langle n_{19} \rangle$ is the density in units of 10^{19} m^{-3} , can be simulated by a change in the neutral density at the separatrix, which mainly influences the transition through the charge-exchange friction term in the shear velocity equation (see figure 5 of [155]). Recent pedestal studies on DIII-D confirmed a strong correlation between the width of the H-mode density barrier and the neutral penetration length [563]. These results are obtained by comparing experimental n_e profiles with the predictions of an analytic model based on the coupled continuity equations for the electrons and neutrals. So the pedestal width depends on both the fuelling source and plasma transport.

Theory based simulations of zonal flow generation by finite β drift waves have been carried out by Guzdar *et al* [543]. It was shown that the growth rate of zonal flows, which are $\vec{E} \times \vec{B}$ flows at zero frequency driven by a modulational instability of finite β drift waves, is determined by the dimensionless parameter $b = \beta(qR/L_n)^2$ and has a minimum at $b = b_c$. b_c is a threshold for the onset of the L–H transition because when $b > b_c$ positive feedback takes place: zonal flow growth suppresses fluctuations and decreases turbulent transport, then the density profile becomes

steeper and b increases and thereby increases the growth rate of zonal flow. Maximizing the growth rate over the radial mode numbers gives the threshold condition. In terms of measurable plasma parameters the threshold condition is $\Theta > \Theta_c$, where $\Theta = T_e/L_n^{1/2}$, T_e is the electron temperature, L_n is the density scale length at the steepest part of the density gradient and $\Theta_c = 0.45 B_t^{2/3} Z_{\text{eff}}^{2/3} / (RA_i)^{1/6}$. This threshold shows very good agreement with edge data from discharges undergoing the L–H transition in DIII-D [543]. The critical parameter is the same for the L–H transition in discharges with oppositely directed ∇B drifts. The difference in power thresholds (edge temperature) is due to a difference in density scale length for the two cases. Pellet-induced H-modes, which have a reduced power threshold, occur at the same value of the critical parameter. This is an impressive example of how seemingly different L–H transition mechanisms can be unified by identifying the appropriate trigger parameter.

So what should we expect from the comprehensive theory-based model of the L–H transition?

1. Instead of comparing models with stationary experimental profiles in the L- and H-modes, the temporal evolution of T_e , T_i , n , E_r profiles and turbulent fluxes through the L–H transition should be reproduced. The causal relationship between the sheared $\vec{E} \times \vec{B}$ flow generation, the corresponding turbulent transport suppression and the steep temperature and density-gradient formation in a narrow layer inside the separatrix should be explained. Note that the time scale of ETB formation is much faster than the energy confinement time.
2. The critical parameter for the onset of ETB formation should be identified, which seems to be related somehow to the edge temperature. The critical temperature scales positively with B_t and negatively with density.
3. The simulations must give the correct parametric dependences for the power threshold: P_{th} increases with density, magnetic field and major radius, and P_{th} can show hysteresis.
4. The model must include neutral physics, because in DIII-D a good correlation between the width of the density ETB and the neutral penetration length was found, although the ETB width does not show any clear dependence on plasma parameters.
5. A challenging test for an L–H transition model is simulation of the core-edge interaction: ETB formation influences global confinement on a time scale much faster than the energy confinement time.
6. The underlying physical mechanism of an L–H transition model must be robust because the H-mode is universal with respect to heating methods and devices.

Existing models are able to reproduce key features of ETB formation, and the relevant physical mechanisms appear to have been identified, i.e. the ‘bricks’ are ready to construct the castle of a unified L–H transition model. A good example of implementing theory-based models in a boundary turbulence code is BOUT (for BOUNDary Turbulence), which extends the simpler models by including the full divertor geometry with a magnetic separatrix, an X-point and scrape-off layer (SOL) physics [564]. L–H transition simulations were performed using a three-dimensional (3D) nonlocal

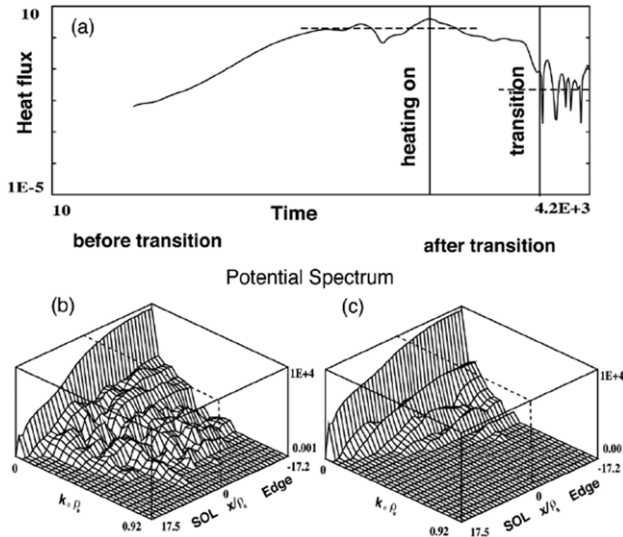


Figure 64. (a) Time history of electron heat flux with sources, (b) potential k spectrum before the transition and (c) potential k spectrum after the transition. Reprinted with permission from [564].

electromagnetic turbulence code, which models the boundary plasma using fluid equations for plasma vorticity, density, electron and ion temperatures and parallel momenta. With sources added in the core-edge region and sinks in the SOL, the code follows the self-consistent profile evolution together with turbulence. Under DIII-D tokamak L-mode conditions, the dominant source of turbulence is pressure-gradient-driven resistive X-point modes. These modes are electromagnetic and curvature-driven at the outside midplane region but become electrostatic near X-points due to magnetic shear and collisionality. Classical resistive ballooning modes at high toroidal mode number, n , co-exist with these modes but are subdominant. Results indicate that, as the power is increased, these modes are stabilized by increased turbulence-generated velocity shear, resulting in an abrupt suppression of high- n turbulence and the formation of a pedestal in density and temperature, as is characteristic of the L–H transition. The time history of the radial electron heat flux at the separatrix is shown in figure 64(a). At $\omega_{ci}t = 3200$, the electron and ion heating power (each of 1 MW) are turned on near the inner boundary and plasma background profiles are allowed to evolve. After a period of adjustment, the electron heat flux and fluctuating electron temperature are suppressed by more than one order of magnitude. Radial profiles of the poloidal fluctuation spectrum before (figure 64(b)) and after (figure 64(c)) the transition indicate the suppression of high- n modes, which yields the reduction of the related transport. These simulations indicate the following scenario for the bifurcation transition as shown in figure 65: as the plasma is heated in the core, the ion and electron temperature at the core-edge boundary increase and their gradient scale lengths get smaller, especially at the edge due to edge-SOL boundary conditions. The steep pressure profiles drive strong instabilities and turbulence, which provides large cross-field transport. The strong turbulence also drives strong $\vec{E} \times \vec{B}$ shear flow due to Reynolds stress. Before the transition, this flow dominates over the diamagnetic flow. However, as the pressure profiles steepen, the $\vec{E} \times \vec{B}$ shear flow reaches a sufficient level

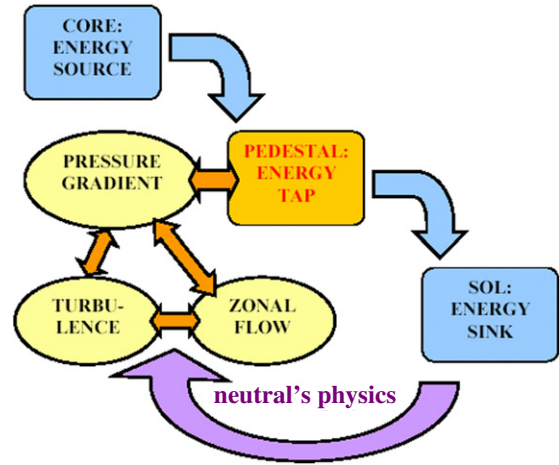


Figure 65. Sketch of the L–H transition physics: the pedestal zone plays the role of a tap for the energy flow from the core to the SOL plasma. So the core energy content is determined by edge pedestal physics, which includes the self-consistent turbulence-flow generation driven by the pressure gradient and is strongly influenced by neutral physics and SOL transport.

to suppress the turbulence. After the transition, large E_r shear flow is sustained by the steep pressure gradients and the plasma stays in the H-mode.

Although these results are very suggestive and encouraging, for a detailed quantitative comparison of simulations with experiment, some additional physics must be incorporated. For example, it was shown analytically that the influence of an X-point on the L–H transition power threshold appears to be important [565]. This conclusion was drawn in the context of the Alfvén-drift paradigm for the L–H transition. It took into account that difference in the up–down temperature due to curvature drift in tokamaks with a separatrix can be of order unity depending on the ion drift direction. A numerical test of the L–H transition power threshold dependence on the change in local beta near the X-point, as noted in [565], would be valuable.

4.5. Modelling the pedestal structure

The major purpose of modelling the pedestal structure is to understand and predict the temporal variation of the pedestal width and height for the plasma density and temperatures. Several codes have been developed for this purpose [516, 533, 566–570]. This modelling could be thought of as providing the boundary conditions for the core plasma and SOL/divertor plasma. On the other hand, the pedestal structure is affected by the core plasma (e.g. α -stabilization due to large Shafranov shift), and divertor conditions also affect the separatrix conditions for the pedestal. Furthermore, there is little separation of spatial scales in this region, since the ion poloidal gyro-radius is comparable to the plasma gradient scale lengths. Therefore, the modelling of pedestal structure inevitably requires the full integration with the core and SOL/divertor plasmas. Such a full integration is the final target of the model development, while at present most codes use the separatrix surface as an interfacing surface with other sophisticated SOL/divertor code results. One of the difficulties in modelling the pedestal structure

is that there exist various physics mechanisms with very different time scales. The global pedestal structure evolves on a transport time scale, but during this evolution, MHD phenomena with very short time scales occur, as from Type I ELMs. Thus, most of the modelling codes are based on a transport code with some description of the enhanced transport from microturbulence and MHD events. MHD events are often modelled only by evaluating analytic stability criteria calibrated with an MHD code (e.g. MISHKA) [567, 568] or the pedestal is treated in a time-averaged way with the critical pressure gradient determined by a simple analytic formula for ballooning modes [516, 566]. The occurrence of an MHD event (ELM) is characterized by an increase in the turbulent cross-field transport or an average value of the enhanced transport. Modelling of the transport barrier width is not yet well developed. Some codes employ an ad hoc model of the transport barrier width by introducing an appropriate transport suppression factor due to $\vec{E} \times \vec{B}$ shearing rate together with the reduction of turbulence growth rate by magnetic shear [516, 566, 568]. More fundamental treatment of the turbulence and its suppression is another interesting approach when integrated with a transport code [569, 570]. Detailed treatment of neutrals penetrating from the SOL is another important ingredient for the modelling of pedestal structure, since the density pedestal may be dominated by the localization of ion source from neutrals [569, 570]. Table 2 summarizes the existing codes and their employed physics models for the modelling of pedestal structure. Somewhat more detailed descriptions and calculation results with some of the codes as examples are provided below.

The integrated ICPS model presently consists of two parts: the core, from the centre of the plasma to the separatrix and including the pedestal, is modelled with the 1-1/2 D code ASTRA, and the scrape-off layer and divertor plasma are modelled using a parametrization of separatrix plasma conditions obtained from the coupled plasma fluid–neutral Monte Carlo code B2-EIRENE for ITER conditions. A variant of the model, which uses a simpler two-point model for the scrape-off and divertor plasma, is used to fit results from present-day experiments [516, 566]. B2-EIRENE simulations revealed the existence of two regimes, one at moderate divertor pressure and a second at higher (saturated) divertor pressure [571]. Scaling relations were developed in each regime [571, 572], and these were then used as boundary conditions for the core plasma modelling [516, 566, 573–575]. The transport model for the core–pedestal part is neoclassical plus a modified multi-mode model (MMM95) for plasma turbulence. The particle transport coefficient is taken as $0.1(\chi_e + \chi_i)$, where the χ 's are electron and ion thermal diffusivities, and the Ware pinch is also included. Sawteeth are approximated by increasing the transport coefficients by a factor of four inside the $q = 1$ surface. The effect of ELMs is represented in a time-averaged sense by limiting the pressure gradient to the ballooning limit. The turbulent transport is assumed to be reduced by the radial electric field shear and magnetic shear, according to

$$\chi = \chi_{\text{MMM}} \{ (1 + (\omega_{E \times B} / (G\gamma_0))^2) \cdot \max(1, (s - t)^2) \}, \quad (29)$$

where $\gamma_0 = \langle \gamma_{\text{ITG}} \rangle$ is the volume averaged growth rate for ITG mode turbulence for the normalized radius $\rho \leq 0.9$ and is an

estimate for the growth rate in the absence of stabilization; $\omega_{E \times B}$ is the $\vec{E} \times \vec{B}$ shearing rate; and s is the magnetic shear with threshold parameter t .

Figure 66 shows the application of the model to JET. The electric field shear term (first term) alone produces a pedestal appreciably lower than that experimentally obtained in JET (figure 66 left, upward triangles). The additional magnetic shear term (second ‘ s ’ term above) is therefore included, and a threshold formulation is used because the major part of the profile (low shear) is well represented by MMM transport. Smaller numerical values for G and t give stronger stabilization. The profiles obtained for two combinations of these parameters ($t = 0.5, G = 0.5$ and $t = 0.5, G = 1.0$) are shown in figure 66. The former combination gives a better fit to the temperature profile; and the density profile is well fitted for both combinations. This best fit ($t = 0.5, G = 0.5$) also agrees well with the ASDEX Upgrade (AUG) database shown in figure 67.

Another code example is the dynamic evolution of electron temperature, density and current density after an ELM crash calculated by the JETTO code [567], which is shown in figure 68. In this calculation, the pedestal width is prescribed and all transport coefficients within the pedestal are reduced to the level of ion neoclassical thermal conductivity. When the ELM stability criterion for either ballooning or kink modes is violated, transport within the barrier is temporally increased. The critical pressure gradient and edge current are variable numerical parameters, which are checked against the results of the MHD stability codes IDBALL and MISHKA and adjusted accordingly. Both the pressure gradient and the edge current drop as a result, so the plasma returns to the pre-ELM state and the cycle repeats [576].

4.6. Type I ELM structure, effects on the pedestal profiles and mitigation techniques

Type I ELMs are spontaneous periodic relaxations of the pedestal of H-mode plasmas, occurring in a repetitive manner once the applied power exceeds ~ 1.5 – 2 times the L–H threshold power [577, 578]. Type I ELMs have similar characteristics in all devices, and their crash dynamics, MHD signature and stability are known better than for any other ELM type. Type I ELMs are replaced, at low input power (compared with the L–H threshold power) or at high density, by Type III ELMs. This section deals mainly with Type I ELMs but reference is made to Type III ELMs when significant differences are observed or specific experimental information is available. This section first describes the ELM cycle and the effect of ELMs on the pedestal profiles. Then, the influence of plasma parameters, such as q_{95} and plasma shape on ELMs, is discussed. And last, recent progress in Type I ELM mitigation techniques is briefly reviewed.

4.6.1. The ELM cycle—build-up and collapse of the pedestal.

Figure 69 shows the time evolution of the D_α emission from the divertor, plasma stored energy and pedestal temperature and density in a JET Type I ELMy H-mode [497]. After the fast collapse of the pedestal, both n_e and T_e start to build up again, until the next ELM occurs. The ELM crash occurs on very fast timescales, of the order of 100–300 μs [579–582], with very

Table 2. Comparison of physics models incorporated in existing codes for modelling of pedestal structure.

Model	Code				
	ICPS [516, 566]	JETTO [567] EDGE2D NIMBUS	LEHIGH [568] (BALDUR, JETTO, ASTRA together with HELENA and MISHKA)	BOUT-UEDGE [569]	XPTOR [533]
1. Transport models for turbulent plasma	Originally; modified IFSPPL model for ions and modified RLW transport for electrons Updated to modified multi-mode model (MMM95 [236, 238, 239])	Bohm/gyro-Bohm Weiland MMM95	MMM95 [236, 238, 239] GLF23 [20] Mixed-Bohm /gyro-Bohm	Self-consistent turbulent fluxes from 3D resistive ballooning modes, including X-point and EM effects	GLF23 [20] has been used to model the ion particle, electron and ion thermal, and momentum transport within the pedestal region
2. Mechanisms of turbulence suppression in pedestal region	$E \times B$ + magnetic shear for growth rate	$E \times B$ + magnetic shear or simply magnetic shear	$E \times B$ shear	$E \times B$ and magnetic shear included in turbulence	$E \times B$ shear + magnetic shear + shafranov shift stabilization NCLASS
3. Transport model in the pedestal region after suppression of turbulent transport	Neoclassical	Local neoclassical (NCLASS) + fraction of anomalous or non-local neoclassical on the top of barrier	NCLASS + residual anomalous transport used in ASTRA code Ion thermal neoclassical transport at top of pedestal used throughout pedestal in JETTO	Residual turbulence + estimate from simple neoclassical expression	
4. Model for pedestal width	Self-consistently determined with transport suppression model	Fixed or given by formulae	Self-consistently (ASTRA) Fixed or given by formulae (JETTO) Models for pedestal width in [721] (BALDUR)	Edge profile evolved self-consistently from fluid neutral model source and residual turbulence	Self-consistently determined with transport suppression model
5. Model for critical pressure gradient and ELM trigger	Analytical formula for ideal ballooning mode	Ballooning criteria for α_{crit} or analytical peeling criteria for current MISHKA is used routinely to check the validity of analytical criteria	Ballooning criteria for α_{crit} or analytical peeling criteria for current (JETTO, ASTRA) Whichever mode becomes unstable first causes the ELM crash	Pressure and current terms (ballooning/peeling) that drive ELMs are in the simulation equations, similar to ELITE	MHD constraints not presently employed Transport is assumed to be electrostatic within GLF23
6. Model for transport during ELM cycle	Not explicitly treated Time averaged pedestal structure is calculated	Gaussian shape for χ_i with width from MISHKA Amplitude and duration can be prescribed or taken from a solution of corresponding time evolving equation	Dynamic model for ELMs (JETTO, ASTRA) Each ELM crash produces a rapid change in the edge profiles for T , n , and j , followed by a rebuilding of the pedestal	ELM crash and full ELM cycle under development	Presently not being treated
7. Model for MHD 'equilibrium' during ELM	Not solved			ELM crash and full ELM cycle under development	Presently not treated
8. Model for particle transport	$0.1(\chi_i + \chi_e)$ and Ware pinch	Bohm/gyro-Bohm Weiland and MMM (including off-diagonal elements) Ware pinch NCLASS pinches		Self-consistent from fluid turbulence	GLF23 + NCLASS for ions Electron density from quasi-neutrality using predicted main ion profile along with experimental impurity and fast ion density profiles Particle source taken from experimental analysis (TRANSP or ONETWO)
9. Model for neutrals	Astra routine based on Dnestrovski and Kostomarov For ITER, direct core fuelling with profile calculated from simple NBI model (without energy input); results insensitive to penetration depth for penetration inside pedestal radius	Diffusive equation for neutrals in JETTO (FRANTIC) Monte Carlo for EDGE2D (NIMBUS)	Monte Carlo (JETTO, BALDUR)	Various models including fluid, analytic or Monte Carlo (seldom used and not yet with turbulence -transport coupling)	
10. Boundary condition for separatrix values	Scaling relations calculated by B2-EIRENE	Density and temperature at the separatrix are usually prescribed, sometimes taken from EDGE2D	Prescribed (JETTO, ASTRA) Boundary taken at top of pedestal from pedestal model (BALDUR)	Extends from pedestal to wall, thus including separatrix	Boundary conditions enforced inside separatrix location using experimental values

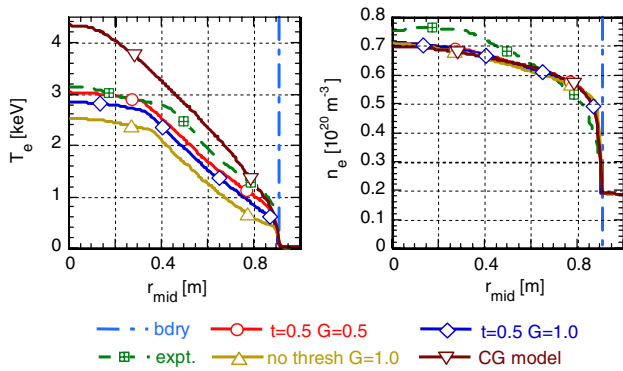


Figure 66. Profiles for JET: experimental, MMM model results for the two parameter sets and without shear stabilization and CG (critical gradient) model results. Left—electron temperature. Right—electron density. Reprinted with permission from [516].

little variation observed as function of plasma parameters and machine size. After the crash, the recovery of the pedestal top values occurs on a much longer timescale, accompanied by the rebuilding of the pedestal profiles. The ELM crash causes a widening of the pedestal profiles, which then progressively narrow down and become steeper until the next ELM occurs (see for instance [583] for a detailed study of the dynamics of the density profiles in ASDEX Upgrade and [580] for the behaviour of T_e pedestal profiles on the ELM timescale in JET). The comparison of the ELM density collapse at low and high field sides [583–585] indicates that the ELM crash occurs first in the low field side of the tokamak, with the density perturbation propagating to the inboard side at approximately the speed of ion sound. This observation is consistent with the MHD interpretation of ELM events as ballooning-type instabilities.

ELM MHD precursors have been studied in most tokamaks (a comprehensive review is found in [586]). Clear precursors correlated to the onset of the ELM have been identified in ASDEX Upgrade for both Type I and III ELMs [587] and in JT-60U for Type I ELMs [581, 582]. This is not the case for JET and DIII-D, where a cause–effect between MHD precursors and the Type I ELM crash has not been clearly established [588, 589].

As also shown in the example of figure 69, it is commonly observed that dT_e/dt between ELMs is not constant and that T_e may reach saturation well before the ELM crash. A possible correlation between the inter-ELM transport (or the rate at which the pedestal profiles recover after an ELM and ultimately the ELM frequency) and MHD activity is investigated in [590] in JET ELMy H-mode plasmas. A correlation is found between the intensity of washboard modes (band(s) of fluctuating magnetic activity rotating in the electron diamagnetic drift direction) and the rate of rise of the pedestal temperature between ELMs, which slows down or even saturates for the increasing intensity of the WB mode activity. The correlation between these MHD modes (possibly of resistive origin) and the build-up of the electron temperature give strong indications that WB may be responsible for an enhanced transport of energy across the separatrix, although this enhanced transport is not sufficient to saturate the density increase between ELMs.

4.6.2. Effect of ELM crash on n and T profiles. The success of the peeling–ballooning model for the prediction of Type I ELM onset (see section 4.8 and references therein) has brought about a hypothesis linking the change in mode number and spatial extent of the most unstable mode to the ELM size. The correlation between the plasma volume affected by the ELM crash and ELM size has been analysed in detail using fast electron temperature profile measurements in JET [580, 591]. An example of such a study is shown in figure 70, for a density scan at fixed plasma parameters: the plasma depth affected by an ELM is determined by subtracting the post-ELM T_e profile from the pre-ELM T_e profile (the two profiles are separated in time by $\sim 300 \mu\text{s}$, and the time resolution of the measurement is $\sim 10 \mu\text{s}$), and the perturbed profiles are then normalized to their maximum. While the energy loss per ELM (ΔW_{ELM}) decreases by a factor 2 to 3 as the density increases, the plasma depth affected by the ELM does not change, as long as Type I ELMs are present. Similar results are found for giant ELMs in JT-60U [592], as well as in DIII-D (figure 9 in [593]). Further analysis of the T_e and n_e profile perturbations at the ELM crash reveals that the change in ELM size with density is due to a strong reduction in the amplitude of the temperature drop at the ELM, while the magnitude of the density crash stays approximately constant with density [579, 593]. At high pedestal density, Type I ELMs can occur without any change in the pedestal temperature, i.e. with the ELM loss channel being purely convective [580, 593]. In the case of MAST [594], all ELMs appear to be purely convective, although in that case the ELM classification (Type I or Type III) is not clear. Data from NSTX [595] also indicate that ELMs are prevalently convective, in this case for Type I ELMs.

The beneficial effect of triangularity δ in achieving a high density at high confinement [494, 497] has stimulated intensive studies of the pedestal and ELMs at the high δ , near that foreseen for ITER. In general, increasing δ corresponds to an increase in the pedestal pressure and the absolute ELM size, although in most cases [579, 580], the relative ELM losses (i.e. the energy loss per ELM normalized to the pedestal energy content) depend weakly on the triangularity (see chapter 4 of this issue [364]). JET [580] and DIII-D [596] data indicate that the plasma depth affected by the ELM decreases with increasing δ , although the absolute size of the ELM increases. In contrast, [597] reports a triangularity dependence of the relative ELM losses and ELM-affected depth in ASDEX Upgrade. The role of plasma shape (in particular of triangularity and squareness) in the MHD stability of the pedestal and ELMs has been clearly demonstrated by the analysis of DIII-D shape scans [598, 599], where shape variations, pedestal pressure and access to second stability have been convincingly linked. In NSTX [595], both the frequency and size of Type I ELM vary considerably between SN and DN plasmas, although a link between ELM characteristics and the distance between the first and second separatrix has not been identified so far.

Recent JET experiments have found a dependence of the pedestal pressure [600] and ELM size [592] on the safety factor. In particular, it appears that increasing q_{95} from ~ 3.6 to 4.6 causes a reduction in relative ELM losses of more than a factor of 2, due to a decrease in the amplitude of the temperature drop

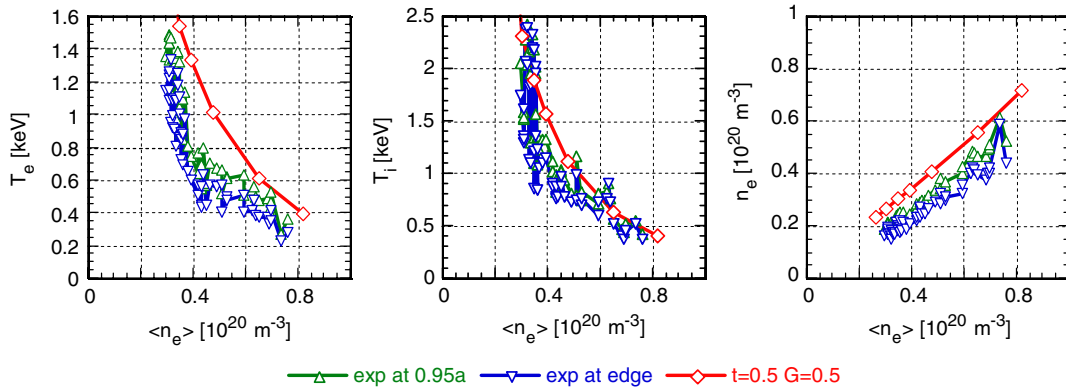


Figure 67. Simulated and experimental edge parameters for a density scan for ASDEX Upgrade ($t = 0.5, G = 0.5$). Reprinted with permission from [516].

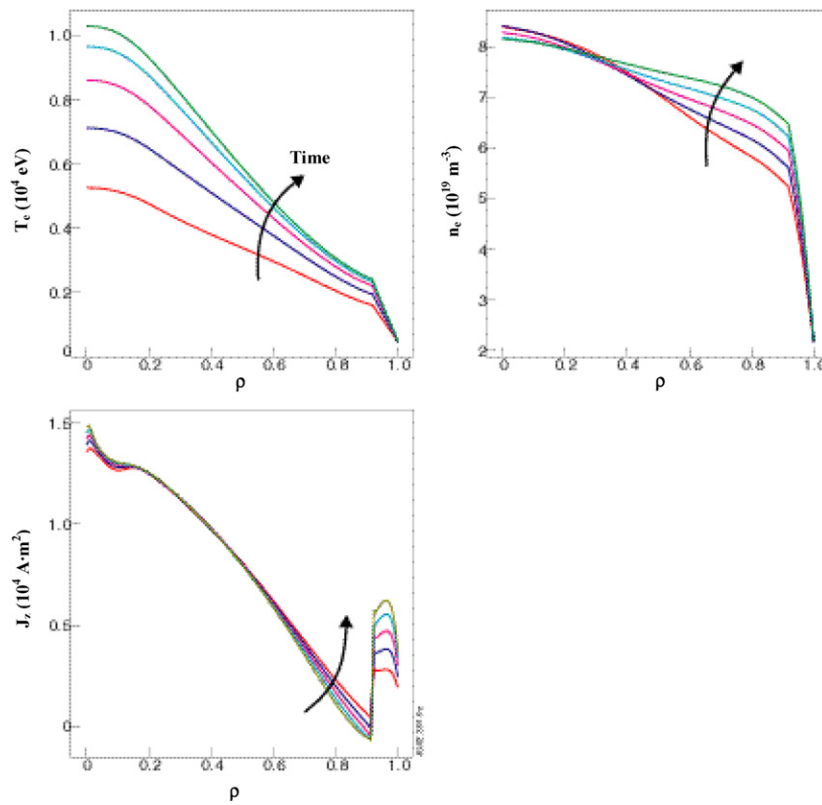


Figure 68. Evolution of electron temperature, density and current density after ELM crash from the JETTO code.

at the ELM, at a constant perturbation radius. Comparison of these findings with data from other devices is a matter of high priority for future work.

4.6.3. Type I ELM mitigation techniques. The concern about the lifetime of the divertor target plates in ITER, due to erosion and/or sublimation under the high transient power loads associated with Type I ELMs [601], has stimulated research of control techniques and plasma regimes that couple the required global plasma confinement properties to tolerable ELM loads of plasma facing components. This section reviews ELM control techniques relying on external actuators, namely control of edge current, edge magnetic field ergodization in H-mode plasmas and pellet-induced ELMs, while plasma regimes

without Type I ELMs are described in section 4.7. These techniques are of interest for ELM studies because of the insight they can provide on the physics of ELMs, as well as for their possible applications to ITER. The extrapolation of these ELM control techniques will require a detailed assessment to quantify how much of the decrease in ELM energy loss comes from the method itself and how much comes from reducing the pedestal pressure, and therefore the plasma’s global performance.

Experiments where the plasma edge current is changed by external means were carried out in COMPASS-D [602] and JET [603]. In both the cases, an increase in the edge current density J_{edge} was associated with a modification of the ELM behaviour: in COMPASS-D this increase is associated

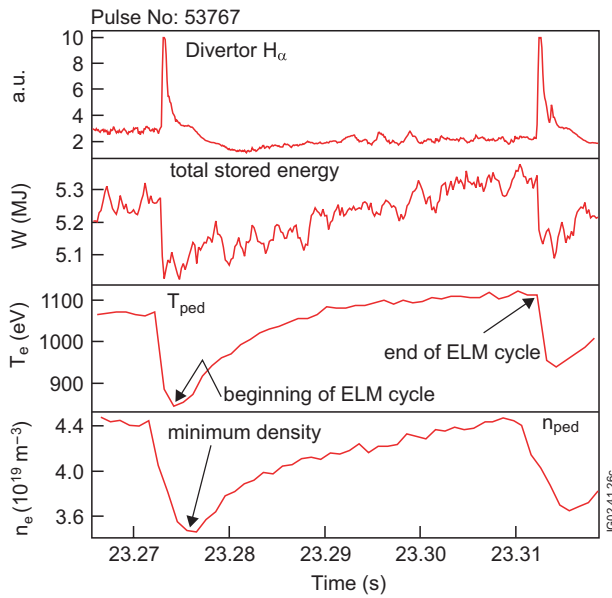


Figure 69. Example of a typical ELM cycle (Type I, JET). The time evolution of the D_α emission from the divertor, the plasma stored energy W , pedestal electron temperature T_e and density n_e are shown in boxes 1 to 4. The fast collapse of D_α , T_e and n_e at the ELM crash are highlighted by the arrow. Reprinted with permission from [497].

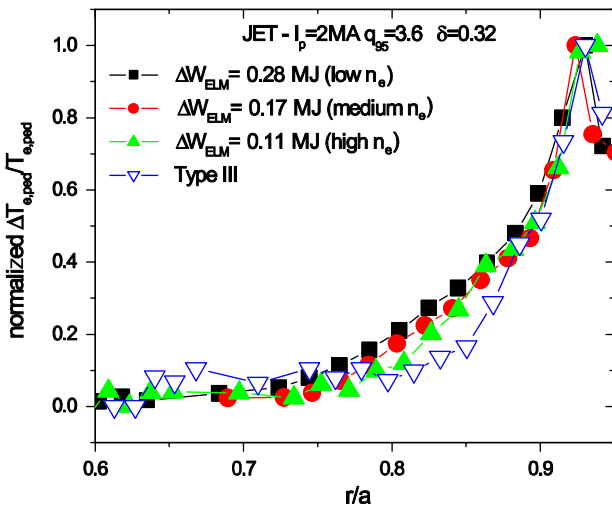


Figure 70. Perturbation of the electron temperature profile caused by ELMs (normalized to its maximum) versus normalized major radius, for a density scan at fixed plasma parameters in JET. With Type I ELMs, the ELM-affected volume is constant for a variation of $\Delta W_{\text{ELM}} \sim 2-3$, while it decreases with Type III ELMs. Reprinted with permission from [591].

with bursts of ELM activity (Type III ELMs), while in JET an increase in J_{edge} is invoked to explain the suppression of Type I ELMs (in favour of Type III ELMs) in plasmas with a non-monotonic q profile. In both the cases, the effects are claimed to be consistent with the destabilization of edge peeling modes. A possible control scheme, exploiting the effect of edge currents on the MHD stability of the pedestal and on ELM frequency (and size), has been investigated in TCV [604]. In these experiments, square voltage perturbations are applied to the poloidal field coils, on single null, Type III

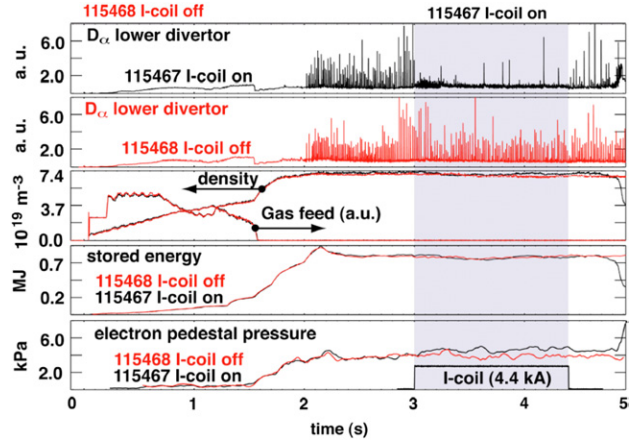


Figure 71. Example of Type I ELM suppression by application of an edge resonant magnetic perturbation by the ‘I coils’ in the DIII-D: comparison of discharge 115468 (I coils off, black) and 115467 (I coils on, red). In order from top to bottom: D_α recycling at lower divertor for I coils off (first box) and on (second box); plasma density and gas fuelling (box 3); plasma total stored energy (box 4) and electron pressure at the top of the pedestal (last box). The shaded region indicates the time when the ‘I coils’ are pulsed on in discharge 115467 [749].

ELMy H-modes, with the frequency of the perturbation ~ 2 times the natural ELM frequency of the plasma under study. The resulting up/down movement of the plasma in an up/down asymmetric field results in periodic variations of J_{edge} with good correlation between the perturbation induced by the coil (when in the direction of increasing J_{edge}) and the generation of an ELM, with the average ELM frequency increasing by upto a factor of two, compared with a control case. Further work is required, for assessing the technical viability of this technique for ITER, to quantify the achievable reduction in the ELM size as well as the impact of such a control method on plasma confinement. This technique has been applied in the ASDEX Upgrade tokamak, and ELMs have indeed been generated by plasma ‘jolts’, as described in [605].

The application of a magnetic perturbation resonant at the edge of the plasma is another method that has been studied for ELM control. Experiments in COMPASS-D [602] showed that the application of a resonant field could increase the frequency of Type III ELMs, as well as induce ELMs in ELM-free H-modes. The same conceptual method has been recently used in DIII-D [606], where the suppression of Type I ELMs at constant plasma confinement has been demonstrated using in-vessel magnetic field coils (figure 71). Further experimental work is required to extend these promising results to ITER. In particular, Type I moderation or suppression should be extended to a range of relevant plasma parameters (and possibly different devices), as well as to demonstrate the compatibility of this control scheme with the overall plasma MHD stability.

The possibility to control ELM frequency and size by pellet injection was put forward in [607], observing that pellets trigger ELMs and that those pellet-triggered ELMs may be associated with a reduced power load onto the divertor plates. More recently, ELM control by a repetitive pellet injection was demonstrated in ASDEX Upgrade [608] (see figure 89 in section 4.9). Pellet size and velocity were adjusted

(within the technical capability of the system) to trigger ELMs without contributing significantly to core plasma fuelling. It is observed that ELM triggering occurs only $\sim 200 \mu\text{s}$ after the injection, suggesting that only a fraction of the pellet mass is sufficient to destabilize locally the pedestal and cause an ELM. It is found that MHD signature and divertor power loads of pellet-triggered ELMs are similar to those of ‘natural’ Type I ELMs of the same frequency (the frequency is adjusted by means of an external gas fuelling in a control discharge with all parameters as in the pellet case). Although, to establish a basis for extrapolation, this technique has to be extended to a wider range of plasma parameters, in particular towards high T_e pedestals, as well as a rigorous assessment of the impact on confinement, code simulations [609] indicate that shallow pellet injection has the potential for Type I ELM mitigation in ITER.

Other techniques, such as the direct current drive in the plasma periphery for edge current control (and ELM suppression), are being investigated at the moment in several devices, and first results should be available in the near future.

4.7. Alternatives to Type I ELMy H-mode regime

H-modes with Type I ELMs are by far the most common high confinement regimes in today’s tokamaks, and their global performance and pedestal parameters have been studied extensively. Accordingly, this regime has been chosen as the reference operating scenario for ITER and other divertor burning plasma experiments. There is good confidence that the regime can be accessed and that plasma confinement will be sufficient to meet the fusion performance targets. The periodic energy losses due to ELM crashes are included in these projections and they do not have a major impact on this performance. There is a concern, however, as discussed in section 4.6 of this chapter as well as in chapter 4 of this issue [364], about the impact of these losses on the surfaces of the divertor and the first wall. If too large, repeated heat pulses could cause surface erosion and/or melting, leading to a reduced divertor lifetime and increased impurity influxes. Another issue, mainly arising in advanced scenarios as discussed in section 3.7, is many experiments find that large ELMs can disrupt or terminate internal transport barriers, through coupling to core MHD and/or transient modification of profiles [377, 603, 610–613]. It is recognized that some mechanism is needed to increase particle transport at the edge of an H-mode plasma, since otherwise particles and impurities tend to accumulate. To avoid these potentially serious drawbacks, it would obviously be preferable to have a regime which gave similar plasma performance to the Type I ELMy regime, which has controlled density and impurities but in which heat loss is more continuous and evenly distributed, either with smaller periodic ELMs or a continuous edge fluctuation. This has motivated increasing attention to alternative regimes in the years since the ITER Physics Basis [1]. Several candidate regimes have been identified and there are active research programs on all the world’s divertor tokamaks. The key experimental results on each regime are summarized below. It must be recognized that, since most of these regimes are comparatively new, there is a less complete physics picture of their accessibility, pedestal parameters and

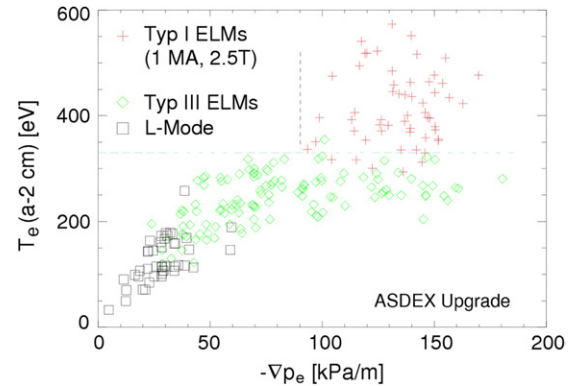


Figure 72. Electron temperature versus electron average pressure gradient. Type III ELMs occurs only below a certain edge temperature limit. Reprinted with permission from [274].

performance projections than is now available for Type I ELMs. Inter-machine comparisons have proven particularly useful in regard to understanding the conditions for transferring and extrapolating the regimes. Issues requiring further study are discussed in section 4.7.6.

4.7.1. Type III ELMs. Type III ELMy H-modes are commonly observed in all divertor tokamaks [274, 614–616]. Compared with the Type I ELMy regime, H-modes with Type III ELMs have higher ELM frequency, smaller energy loss per ELM, ΔW_{ELM} , but reduced energy confinement (by 10–30%). In terms of reproducibility and robustness of the regime, Type III ELMy H-modes are comparable to H-modes with Type I ELMs. The Type III ELMy regime limits the operational space for Type I ELMs. In fact, Type III ELMs are observed at low power above the L–H threshold power, so the transition to Type I ELMs requires a minimum power. Moreover, the transition to Type III ELMs limits the density achievable in the Type I ELMy H-mode regime (i.e. the density achievable with good confinement). In contrast to Type I ELMs, Type III ELMs are commonly observed also in plasmas with an internal transport barrier, where the benefit of a Type III ELMy edge can be combined with the reduced core transport [611]. The study of the physics mechanisms driving Type III ELMs, and of the scaling of the operational space of Type III ELMs with machine size and plasma parameters, is therefore important to be able to control or avoid this regime in ITER.

Type III ELMs are observed below a critical pedestal temperature, T_{crit} , and at pedestal pressures at or below that of Type I ELMs, as shown in figure 72 [274]. T_{crit} increases with decreasing density ($T_{\text{crit}} \propto 1/n$) at low density [614, 616]. Type III ELMs of standard ELMy H-modes and of plasma with an ITB belong to this low collisionality branch of the pedestal n_e – T_e diagram. In this region of n_e – T_e , consistent with the decrease in T_{crit} with density, it is found that increasing density decreases the power required for the transition from Type III to Type I ELMs. At high density, in contrast, T_{crit} is low and almost independent of density. This high collisionality branch of n_e – T_e includes the high-density ELMy H-mode with or without impurity seeding. ASDEX Upgrade [293] and Alcator C-Mod [615] have only observed Type III ELMs at high collisionality, while in DIII-D [614] and JET [616] they

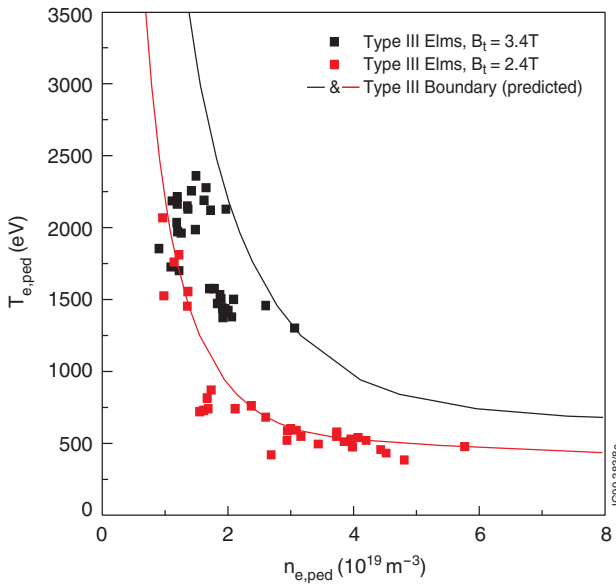


Figure 73. Pedestal n_e – T_e diagram for Type III ELMs in JET and comparison with the model. Reprinted with permission from [616].

are found also at low collisionality [616, 617]. T_{crit} tends to increase with toroidal field in both high and low n_e branches [615, 616].

A model for the Type III ELM instability [618] that considers the resistive interchange instability with magnetic flutter (RIF) reproduces the density dependence of T_{crit} for Alcator C-Mod, ASDEX Upgrade, DIII-D and JET. In JET, this model also describes the toroidal field dependence of T_{crit} , as shown in figure 73. Nevertheless, the JET results also show that this model does not predict correctly the experimental variation of T_{crit} with isotopic mass and q_{95} [616].

Whether Type III ELMs at low and high collisionality are due to the same physics mechanism is however still an open question, since there are results that point to a different instability for the two collisionality branches. The result that a plasma current ramp down can stabilize low collisionality Type III ELMs suggests current driven peeling modes as the driving instability for those ELMs [612, 616]. At high collisionality, a model based on the resistive ballooning instability [619] reproduces correctly the JET data of the critical density for the transition from Type I to Type III as $n_{e,\text{crit}} = B_t/q^{5/4}$.

The energy confinement enhancement factor, $H_{98(y,2)}$, for Type III ELMs decreases with density and increases with triangularity in a similar manner as for Type I ELMs, indicating that those trends are not specifically related to the ELM type. Although the transition from Type I to Type III ELMs results in a quantitatively similar loss of confinement both at low and high collisionality, the observed decrease in pedestal pressure at the transition is due to cooling of the pedestal at high collisionality, while it is due to loss of pedestal density (at constant or increased temperature) at low collisionality [616].

The increase in confinement at high density for Type III ELMy H-modes at high triangularity has been exploited in JET to demonstrate a radiating Type III ELMy H-mode scenario (radiative power fraction > 70%) where low inter-ELM heat flux to the divertor and low ELM energy losses are combined

[620]. Although the uncertainties in the extrapolation are large, at low q_{95} ($= 2.7$) and with $H_{98(y,2)} = 0.75$ – 0.8 at $n = n_G$, this scenario has a combination of plasma parameters that just falls within the predicted operation domain for the $Q = 10$ ITER inductive operation at 17 MA.

Although fewer data exist for Type III than for Type I ELMy H-modes, they indicate that the fraction of pedestal energy loss at the ELM, $\Delta W_{\text{ELM}}/W_{\text{ped}}$, decreases with increasing pedestal collisionality [620], similar to the trend found with Type I ELMs. At the same collisionality, there is no difference between the $\Delta W_{\text{ELM}}/W_{\text{ped}}$ of impurity seeded and non-seeded Type III ELMy H-modes, and this appears to be lower than for Type I ELMs. This result is consistent with the fraction of plasma volume affected by the ELM temperature crash being smaller for Type III ELMs than for Type I ELMs [591].

4.7.2. Enhanced D-alpha and similar regimes. The ‘Enhanced D_α ’ (EDA) H-mode regime was the first regime observed to provide control of particles and impurities without any periodic ELMs. It was first observed on Alcator C-Mod in 1996 [621–623]. Global confinement can be as good as in Type I ELMy regimes, with H_{ITER89P} up to 2, while density and radiated power are steady in contrast to usual ELM-free H-modes. The regime is favoured by higher q_{95} and triangularity and, for deuterium plasmas, is obtained most reliably at $q_{95} > 3.5$ and $\delta > 0.35$ [624]; some examples at lower q and q have since been observed and the q_{95} limit in hydrogen plasmas is 2.5 or lower [625]. ELM-free and EDA discharges are best separated in edge operational space by the collisionality and normalized pressure gradient, with $\nu^*_{95} \geq 1.5$ at the highest α_{ped} [527].

The salient feature of this regime is a continuous, localized fluctuation referred to as a quasi-coherent (QC) mode. Detailed multi-diagnostic measurements have been done in recent years of fluctuations in density, electrostatic potential and magnetic field [176, 625–629]. The mode is localized to a region of a few mm near the bottom of the density pedestal, has a peak frequency in the range 50–120 kHz and is of fairly short wavelength (i.e. high m, n), with $k_\perp \sim 1.2$ – 4 cm^{-1} . Accordingly, the magnetic perturbation falls rapidly with distance from the mode surface. Figure 74 shows magnetic and density signatures on Alcator C-Mod. The mode amplitude is variable and correlates well with the effective particle transport; with a weak amplitude n_e radiation can still rise, while a very strong mode can start to increase energy as well as particle transport. Target density and neutral pressure have been shown to correlate with the existence and strength of the mode. The observed scalings of the fluctuation characteristics and their regime of occurrence suggest that the QC mode may be some type of resistive drift-ballooning mode. Features similar to the QC mode have been observed in electromagnetic edge turbulence simulations [627, 630]. Simulations of an Alcator C-Mod experiment with the boundary-plasma turbulence code BOUT show a resistive X-point mode in good agreement with observations [176].

Studies of pedestal profiles and stability have shown that there is not a marked difference in the width of n_e and T_e pedestals between ELM-free and EDA plasmas [631]. Widths vary from 2 to 8 mm [527, 625, 632] and show little systematic

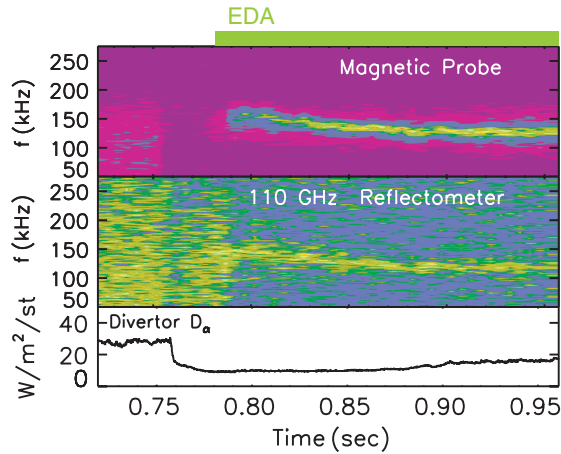


Figure 74. Measurements of the quasi-coherent mode in an enhanced D_α H-mode on Alcator C-Mod, made by a magnetic probe close to the LCFS (top) and a reflectometer channel probing the density pedestal (middle). Reprinted with permission from [629].

variation with $\rho_{i,\text{pol}}$ or other plasma parameters. Widths of the soft x-ray emission do vary and are narrower and shifted to smaller midplane radii in ELM-free plasmas. This reflects the differences in the impurity pinch and diffusivity [633]. Discharges with a QC mode, but no ELMs, are found to be ideal MHD stable despite steep gradients of up to $dp/d\psi \sim 1.2 \times 10^7 \text{ Pa Wb}^{-1}$ when edge bootstrap currents are consistently included. As discussed further below and in section 4.8, at higher T_{ped} (typically for $T_{\text{ped}} > 400 \text{ eV}$) and/or ∇p , the QC mode broadens and small ELMs, tentatively identified as Type II can appear on top of a generally enhanced D_α level [634]; the two regimes appear closely linked in their operational space.

Experiments aimed at reproducing the EDA H-mode have been carried out on DIII-D, JET and ASDEX Upgrade [530, 617, 635]. On DIII-D and ASDEX Upgrade, when edge dimensionless parameters β , ν^* and ρ^* were matched to values on Alcator C-Mod, an edge fluctuation similar to the QC mode appeared, indicating that the access regime is well described by such variables. Figure 75 shows an example of such an experiment on Alcator C-Mod and DIII-D, in both an ‘EDA’ (left) and ‘small ELM’ (right) regime. The operating window varies between machines, partly due to differences in L–H thresholds. It has proven difficult, however, to produce a steady-state ELM-free regime on these experiments; edge densities tend to rise and periodic ELMs are observed, indicating that the mode strength is insufficient to control particle transport. A regime similar to EDA was recently seen on JET in an experiment which matched the shape of Type II ELMy discharges on ASDEX Upgrade [600].

A regime very similar to the EDA has been achieved on the JFT-2M tokamak and named the ‘high recycling steady’ (HRS) H-mode [636]. It is also characterized by steady conditions without large ELMs (figure 76(c)). The regime is again favoured by higher q_{95} , higher density and neutral pressure. Recent experiments in the JFT-2M tokamak have concentrated on the studies of the access conditions for the HRS H-mode regime in terms of the pedestal parameters [637]. The HRS regime is more likely at higher edge density and lower edge temperature, while the ELMy H-mode having large ELMs

appears at lower edge density and higher edge temperature. It is found that the ELMy/HRS operational boundary occurs at the normalized electron collisionality of $\nu_{e*} \sim 1$ in the plasma edge region, depending slightly on q_{95} (figure 76(d)).

A key feature of the HRS H-mode is the presence of coherent magnetic fluctuations in the frequency range of the order of 10–100 kHz. It is suggested that the edge MHD activity may keep the edge pressure below a certain level needed to induce a large ELM. Detailed fluctuation measurements with magnetics, reflectometry and probes [638, 639] show that there are both a high frequency mode of $f \geq 200 \text{ kHz}$ with $n \sim 7$ and a lower frequency mode of $f \sim 50\text{--}120 \text{ kHz}$ with $n = 1$.

Recent inter-machine comparisons between Alcator C-Mod and JFT-2M, at matched plasma shape, show very similar access conditions, suggesting that the EDA and HRS H-modes are in fact the same regime though there are differences in fluctuation details [640]. Both the EDA and HRS regimes have been successfully combined with internal transport barriers for long durations [378, 398, 636, 641–643], giving steady double-barrier regimes.

4.7.3. ‘Quiescent’ H-mode. The ‘quiescent H-mode’ (QH regime) was first observed on DIII-D in 1999 [644] and has been reproduced most robustly on ASDEX Upgrade [645, 646]. Like the EDA regime, it offers good confinement, similar to that of the Type I ELMy regime, and has particle transport sufficient to stop the accumulation of n_e and impurities. However, the details of the responsible mode, and its regime of accessibility, are quite different [466]. An edge fluctuation termed the ‘edge-harmonic mode’ is observed which has a much longer wavelength than the quasi-coherent mode. It is typically seen by magnetics diagnostics and on n_e and T_e diagnostics and is localized at the foot of the pedestal. The oscillation is coherent and periodic, with a base frequency of $\sim 6\text{--}10 \text{ kHz}$, but not sinusoidal, giving a variable mix of toroidal wavenumbers, e.g. $n = 1, 2, 3$, and/or 4, etc and has a poloidal wavelength of $\sim 1 \text{ m}$. An example is shown in figure 77. Up to 11 harmonics have been seen on ASDEX Upgrade [646]. On ASDEX Upgrade, in addition to the low- f EHO, a much higher frequency magnetic mode (named the HFO) is also observed. This has $f \sim 350\text{--}500 \text{ kHz}$ and its modulation envelope corresponds closely to the waveform of the EHO, as shown in figure 78. This raises the possibility that the EHO is a manifestation of the higher frequency instability. Due to diagnostic resolution it is not certain whether the HFO also exists on DIII-D.

The ELM-free QH regime has only been observed on DIII-D with counter-NBI, though the EHO is sometimes seen on ELMy H-modes with co-NBI [647]. Rotation is always in the direction of neutral beams. A large plasma–wall distance at the LFS of the tokamak is also required, suggesting the role of fast ions. On ASDEX Upgrade, the QH regime has also been obtained with near-radial NBI and is facilitated by the additional application of ICRH, which would increase the fast particle population, though RF is not required [645]. On JT-60U, ELM frequency and size both clearly decrease as beams are shifted from co to counter-injection [648]. A quiescent, ELM-free regime occurs with full counter-injection. ELM-free phases and fluctuations similar to the EHO have

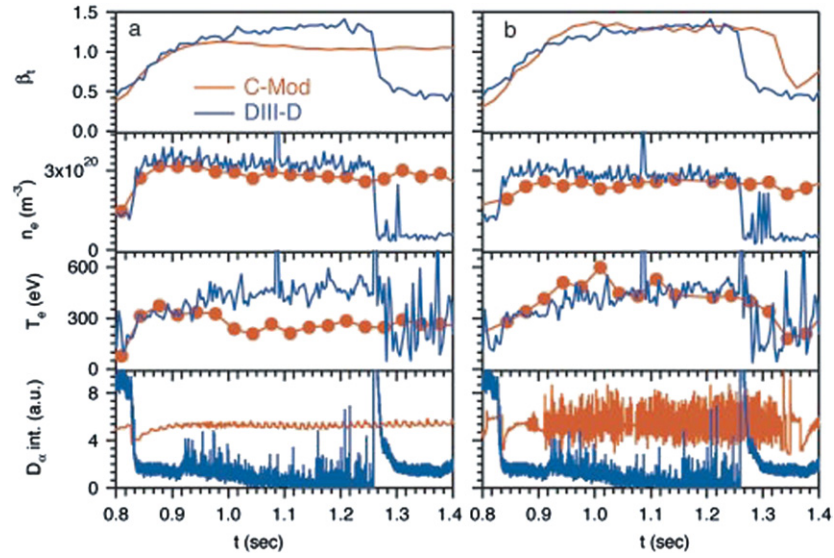


Figure 75. Example of a matching experiment between Alcator C-Mod and DIII-D. DIII-D pedestal parameters (blue) are scaled to the machine size of Alcator C-Mod (red). When parameters are matched, similar fluctuation and global behaviour is seen in both the EDA (left, 0.820–0.92 s) and small ELM regime (right, 0.92–1.25 s). Reprinted with permission from [530].

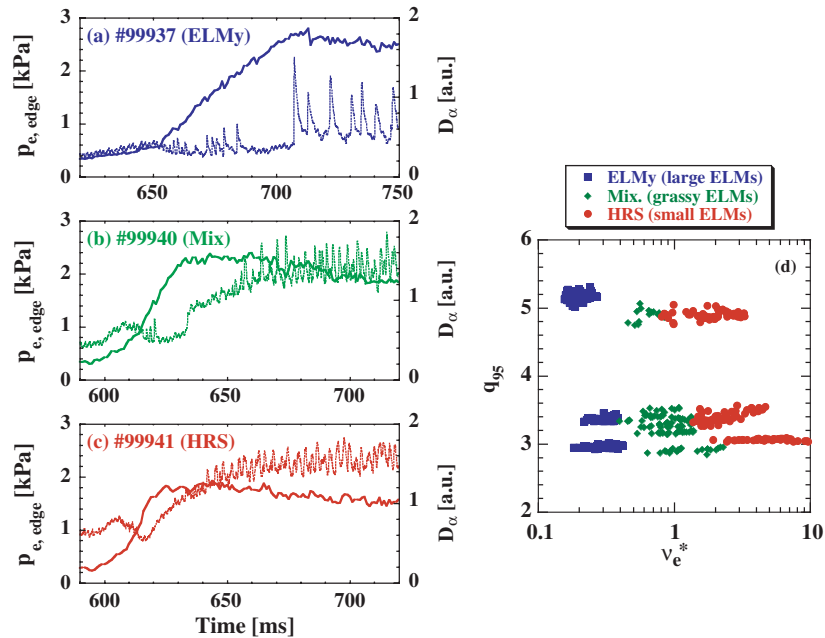


Figure 76. Time history of the edge electron pressure p_e^{edge} (solid) and D_α emission (dotted). (a) ‘ELMy’ (#99937), (b) ‘Mixture’ (#99940) and (c) ‘HRS’ (#99941). (d) Plot of ELMy (blue), Mix. (green) and HRS (red) operational regimes in safety factor at the 95% flux surface q_{95} versus edge normalized electron collisionality ν_{e*} . Reprinted with permission from [637].

also been seen during some counter-injection experiments on JET, though a steady-state QH regime has not yet been accessed. The mechanism and conditions for the EHO, and its relation to the HFO and fast particles, remain open questions.

Pedestal pressures and gradients in the QH regime are comparable to those in ELMy H-mode [388, 649]. In contrast to the EDA and HRS regimes, access to the QH regime is favoured by relatively low edge densities, in some cases requiring wall pumping and high pedestal temperatures; most discharges have low pedestal collisionality, with typical $\nu_{e*} \sim 0.04$ and $\nu_{i*} \sim 0.14$. However, recent DIII-D experiments

have shown that with stronger shaping [650, 651] the pedestal density and pressure can be increased; \bar{n}_e is in the range $(1.7\text{--}7.4) \times 10^{19} \text{ m}^{-3}$ and $q_{95} = 3.4\text{--}5.8$, raising the electron and ion collisionalities to 0.5 and 1.4, respectively. This presumably reflects changes in ELM stability. The limits of the operational space in this regime are thus not fully known. QH-mode also has been combined with internal transport barriers, and the resulting QDB regime has been extensively studied on DIII-D [200, 242, 466]. This high performance regime can be maintained for the duration of the plasma discharge. An issue for extrapolation to burning plasmas is that Z_{eff} tends to

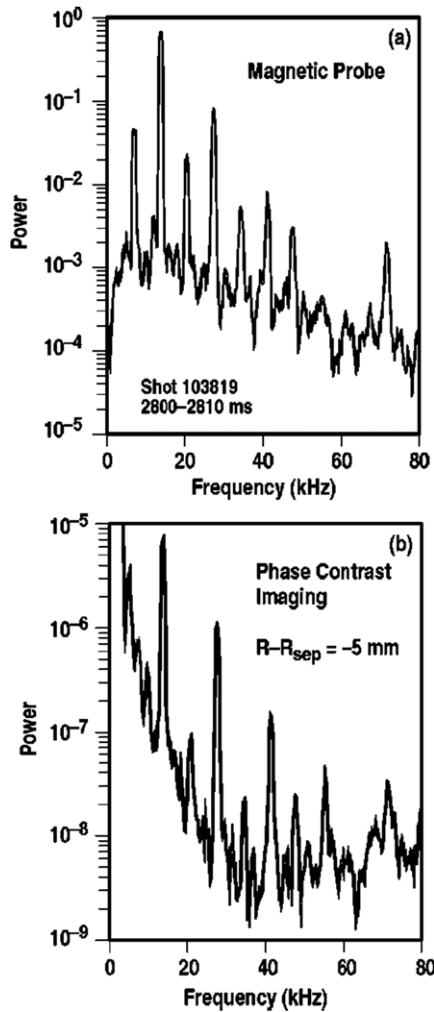


Figure 77. Frequency spectra of the edge-harmonic oscillation (EHO) as measured by magnetics and phase contrast imaging diagnostics, in a QH discharge on DIII-D. Reprinted with permission from [466].

be higher in QH than in Type I ELMy plasmas, typically in the range ~ 2 – 4 in both the DIII-D and ASDEX Upgrade QH discharges. Average Z_{eff} values do decrease as expected at higher operating density.

4.7.4. Type II ELMy H-modes. The first observation of a transition from Type I ELMy H-modes to small ELMy H-modes at high plasma confinement was reported by DIII-D in 1990 [652]. This transition was observed in a single-null discharge by increasing the plasma elongation at very high δ ($\kappa \geq 1.8$ and $\delta \sim 0.5$) and $q_{95} \sim 7$, and was attributed to a change of MHD stability in the plasma edge. The main characteristic of this regime was the co-existence of high pedestal pressure and high frequency/irregular, very small ELMy H-modes.

More recently [653], Type II ELMy H-modes have been identified in the ASDEX Upgrade tokamak and access conditions and plasma properties thoroughly characterized. Type II access has also been investigated in JET [497], and mixed Type I–II ELMy H-modes have been reproducibly obtained, although so far H-modes with a pure Type II ELMy H-mode have not yet been achieved [600]. Periods of small, apparently Type II

ELMs have also been identified in high power H-mode plasmas in Alcator C-Mod, with $\beta_N > 1.2$, in discharges that exhibit an EDA edge at lower input powers [624, 634].

The interest in Type II ELMy H-modes originates from the attractive global characteristics of these plasmas, combining a drastic reduction in ELM transient power loads to plasma facing components with steady-state high density (upto ~ 0.85 – $0.95n_G$), good global confinement ($H_{98(y,2)} \sim 0.95$, a reduction from standard ELMy H-mode confinement with Type I ELMs of $< 10\%$) and no impurity accumulation [653]. Type II ELMs do not cause a measurable perturbation of the pedestal temperature or density profiles and therefore are, in principle, compatible with ITBs.

Type II ELMs are characterized by a specific enhancement of MHD fluctuations in the plasma edge region. In ASDEX Upgrade, as well as in JET and Alcator C-Mod, Type II ELM activity is associated with an increase in broadband, low frequency magnetic fluctuations (30–50 kHz region). In the case of JET, these fluctuations are attributed to an increase in the intensity of so-called washboard modes [590], always observed between ELMs in standard ELMy H-modes. Enhanced density fluctuations in the plasma edge region are also observed both in the ASDEX Upgrade [653] and in JET [600, 654]. It is hypothesized that these enhanced fluctuations are responsible for the quasi-continuous power and particle losses associated with Type II ELMs, although direct measurements of turbulent fluxes are not yet available.

The gradual nature of the transition from Type I to Type II ELMs, and the fact that these two types of ELMs can co-exist, complicates somewhat the definition of exact access conditions. Analysis of ASDEX Upgrade results shows that the key element required to access a pure Type II ELMy H-mode is the proximity to quasi-double-null (QDN) configuration (the distance between the first and second separatrix at the midplane DX needs to be < 1 cm) and plasma densities $\sim 0.85n_G$ (or $n_{\text{ped}} \sim 0.65n_G$) [473, 653, 655]. In the case of medium β plasmas ($\beta_p \sim 1.1$ – 1.3 and $\beta_N \sim 1.9$ – 2.2), access to pure Type II ELMy H-modes requires high triangularity, as well as $q_{95} \geq 4.2$ – 4.5 . If the plasma δ is reduced, mixed Type I–II ELMs are also observed if the QDN configuration is approached, indicating that both the shaping and the proximity to double null play a role in the onset of Type II ELMs. Ideal MHD analysis of these discharges [656] indeed shows that the high δ and q_{95} tend to make the peeling modes more localized and stable, and the QDN configuration further improves the peeling mode stability (see section 4.8).

H-modes with Type II ELMy edge have been obtained in ASDEX Upgrade also at very high β ($\beta_N \sim 3$ – 3.5 and $\beta_p \sim 1.7$ – 2), in the so-called high β_N or hybrid scenario (these high values of β are obtained because $q_0 > 1$ and fishbones replace sawteeth, reducing the trigger for NTM destabilization, see section 2 of chapter 3 of this issue [657]) [473]. The onset of pure Type II ELM edge in this regime occurs for pedestal conditions and plasma geometry very similar to that of the medium β , standard H-modes (high density, high shaping and proximity to double null).

The comparison of access conditions to Type II ELMs for high and medium β plasmas in ASDEX Upgrade suggests a possible trade-off between β and q_{95} . In particular, for the highest β obtained ($\beta_N \sim 3.5$, $\beta_p \sim 2$, with $P_{\text{in}}/P_{\text{LH}} \sim 5$), the

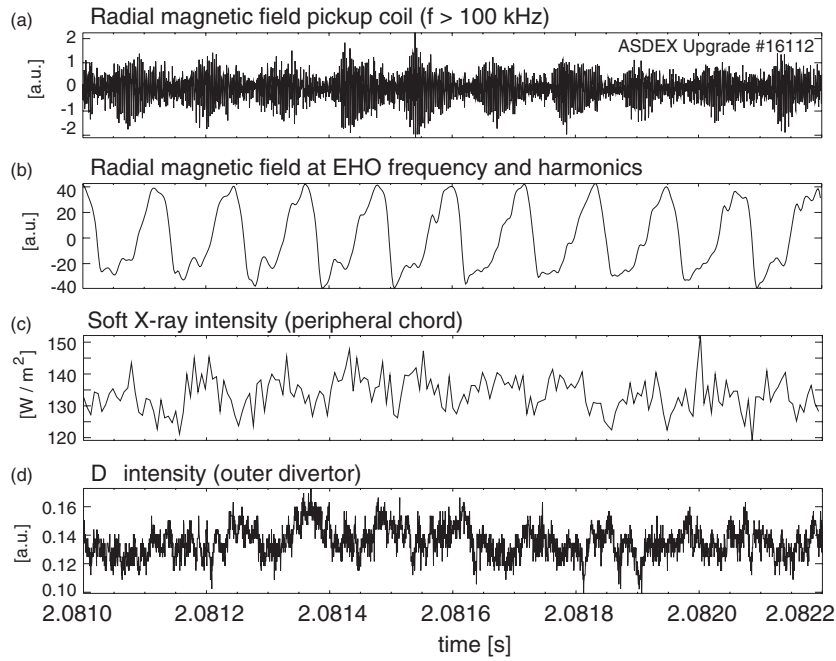


Figure 78. Measurements of (a) the high frequency HFO and the EHO in measurements of (b) B_r , (c) soft x-rays and (d) D_α , in a quiescent discharge on ASDEX Upgrade. Reprinted with permission from [646].

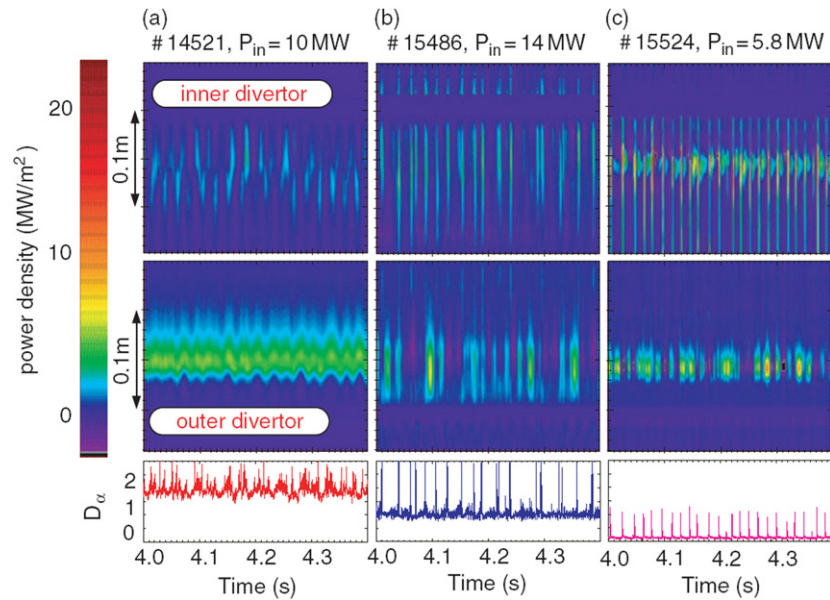


Figure 79. Heat load on the inner and outer lower divertor plates in ASDEX Upgrade for three plasma discharges in advanced scenarios, with increasing shaping, β and density ((c) to (a) in the figure). (a) #14521, $\delta = 0.43$, $n/n_{Gr} \sim 0.88$, $q_{95} = 3.6$, $\beta_N = 3.5$ (b) #15486, $\delta = 0.43$, $n/n_{Gr} \sim 0.83$, $q_{95} = 3.7$, $\beta_N = 3.2$ and (c), #15524 $\delta = 0.33$, $n/n_{Gr} \sim 0.50$, $q_{95} = 4.4$, $\beta_N = 2.3$. The short, high power loads measured by IR thermography are caused by Type I ELM crashes. For the highest density and β (case (a)), no such events are detected, while at intermediate β and densities (case (b)), mixed Type I–II Elms are observed. At low β /shape and density (case (c)) the plasma exhibits Type I ELMs, although $q_{95} > 4$. These plasmas have $DX \sim 1$ cm. Reprinted with permission from [468].

minimum q_{95} at which pure Type II are obtained is reduced to ~ 3.6 from $q_{95} \sim 4.3$ – 4.5 required at $\beta_N \sim 2$. The role of plasma shape, density and β in the onset of Type II ELMs is illustrated by the example in figure 79 (from [468]).

The extrapolation of Type II ELMy H-modes to burning plasma conditions and to ITER in particular is not yet clear. Although this ELM regime occurs in the right range of plasma densities, the typical pedestal temperatures are low (T_{ped} (Type

II) $\sim T_{crit}$ (Type I \rightarrow III transition)), with collisionality $\nu_* \sim 1$ at the top of the pedestal at low β , reduced to $\nu_* \sim 0.5$ at the highest β . Investigation of Type II ELM access in high-density/low collisionality conditions is a high priority for the validation of this regime for ITER.

A confident extrapolation of Type II ELMs to ITER conditions ($H_{98(y,2)} \sim 1$, $n/n_G \geq 0.85$ at $\beta_N \geq 1.8$ – 2), as well as the full understanding of the underlying physics,

would strongly benefit by the extension of the Type II ELM regime to other existing tokamaks. In JET, access to Type II ELM edge in high performance ELMy H-modes has been extensively investigated [497, 600]. Mixed Type I–II ELMy H-modes with the required global confinement and plasma β have been achieved routinely, in single-null plasmas with $0.35 \leq \delta \leq 0.5$, $\kappa > 1.75$ and $3 \leq q_{95} \leq 4$, with $0.7 \leq n_{\text{ped}}/n_G \leq 1$ ($v_* \sim 0.5$). In contrast to ASDEX Upgrade, QDN plasma configurations and increasing q_{95} have not produced, so far, suppression of Type I ELMs but rather an early transition (in terms of density) to Type III ELMs and reduced plasma confinement. Predictive MHD stability calculations indicate that the appearance of Type II ELMs in JET could be caused by a transition of a narrow region of the pedestal next to the separatrix from the second to first stability [658].

A small ELM regime has recently been observed in the National Spherical Torus Experiment (NSTX), which is characterized by a low B_t (< 0.6 T) and aspect ratio ($R/a \geq 1.26$). This regime is also characterized by small, rapid ELMs, occurring at higher pedestal pressures than Type III ELMs. The ELMs, observed on several edge diagnostics, have been designated as ‘Type V’ [595, 659]. They are characterized by an intermittent $n = 1$ mode rotating counter to the plasma current, which slightly precedes each ELM crash and vanishes between ELMs. In contrast to the EDA or QH regimes, there does not appear to be a persistent edge fluctuation controlling the pressure. Densities tend to rise slowly during Type V H-mode regimes, as is typical of other NSTX H-modes, and energy confinement is modestly reduced compared with ELM-free H-modes. NSTX H-modes to date have a pedestal collisionality $\nu_* > 1$. Further experiments will be required to understand the physical mechanism of these ELMs and how they may be related to Type II or other small ELMs. These should help to understand the extrapolability of the regime to other conditions and to a higher aspect ratio.

4.7.5. ‘Grassy’ ELMs. Small ELMs at high plasma confinement are also achieved in JT-60U [660, 661]. These ELMs are obtained in high triangularity, high β_p plasmas with a weak reversed shear (i.e. in plasmas that have both an ITB and an ETB). The pedestal pressure (T_{ped}) with ‘grassy’ ELMs is higher than in comparable standard Type I ELMy H-modes. As in the case of Type II ELMs, grassy ELMs do not perturb in a measurable way the pedestal profiles and cause very low power/continuous losses from the plasma.

The transition from a Type I ELMy edge to grassy ELMs H-modes is gradual, and similarly to the case of Type II ELMs, grassy and giant ELMs can co-exist, with transitions from one ELM type to another at (apparently) constant pedestal parameters. The disappearance of giant (Type I) ELMs and the onset of grassy ELMs occur when the plasma triangularity, q_{95} and β_p are high enough. Detailed experimental investigation of access conditions in JT-60U has found that β_p is the critical parameter to obtain grassy ELMs, and a threshold value of $\beta_p > 1.6$ – 1.7 has been established, although high δ and q are also required.

The transition from giant to grassy ELMs in a series of JT-60U discharges with increasing β_p , q_{95} and δ is

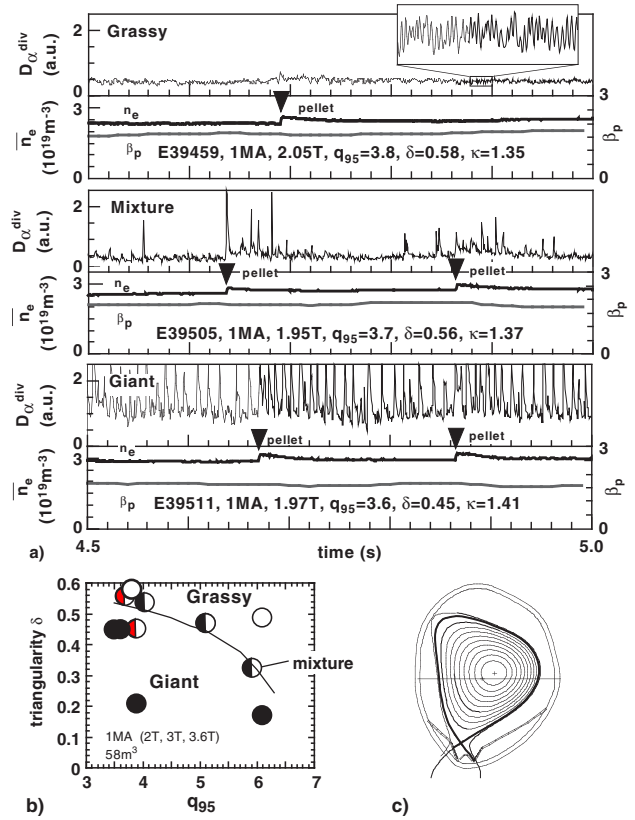


Figure 80. (a) The change of ELM behaviour from giant (#E39511), to mixed giant-grassy ELMS (#E39505) to pure grassy edge (#E39459) is obtained by gradual increase of plasma shaping, q_{95} (at constant I_p) and β_p . (b) q_{95} - δ existence diagram for the grassy ELM regime: all plasmas with pure grassy ELM edge have $\beta_p > 1.6$. (c): JT-60U equilibrium with $\delta = 0.6$. Reprinted with permission from [501].

illustrated in figure 80(a). Figure 80(b) shows the ‘trade-off’ between triangularity and q_{95} to obtain grassy ELMs edge; in particular, increasing δ to ~ 0.6 allows the reduction of the minimum q_{95} to less than 4 [501]. Even with this very high triangularity, the second X-point remains outside the vacuum vessel (figure 80(c)).

MHD stability analysis of the high β_p JT-60U plasmas (at high q_{95}) [662] indicates that the transition from giant to grassy ELMs is due to improved pedestal stability, with the pedestal accessing the second region of stability for ideal ballooning modes. A stability change in the edge could also be promoted by the strong Shafranov shift at high β_p .

Very small ELMs, reminiscent of the grassy ELMs of JT-60U, have been obtained in high β_p H-modes in JET [663]. The transition from Type I to grassy ELMs occurs at $\beta_p \sim 1.6$ – 1.7 , very similar to the critical threshold reported by JT-60U. So far, grassy ELMs in JET have been obtained only in H-modes with conventional q profile, very high edge q ($q_{95} \sim 7$) and in quasi-double-null configuration ($\delta \sim 0.5$).

Some features of the JT-60U high β_p regime with grassy ELMs are of clear relevance for ITER and burning plasmas, such as the demonstrated compatibility with ITBs, full non-inductive operation, low edge collisionality ($0.1 < \nu_* < 0.3$), good impurity transport and, as shown in figure 80(a), possible

compatibility with pellet injection. On the other hand, the extreme shape required for obtaining grassy ELMs at reasonable values of q_{95} , as well as the very high threshold in β_p (this issue is common to the hybrid/high β_N plasmas in ASDEX Upgrade and to JET) make a simple extrapolation to ITER conditions impossible. As with other small ELM regimes, the high β_p grassy ELMs regime needs to be investigated further, to gain more understanding of the basic physics mechanisms causing the transition in the pedestal behaviour, so as to learn how to obtain this very promising plasma regime in other devices and in ITER.

4.7.6. Summary and issues for extrapolation to burning plasmas. It is evident from the large number of recent experiments and publications that significant progress has been made since the ITER Physics Basis [1] in obtaining and documenting H-mode regimes which offer an alternative to Type I ELMs. As examples, the EDA regime has been extended from Alcator C-Mod to several other tokamaks, and the responsible quasi-coherent mode has been measured in detail and reproduced in simulations. The quiescent H-mode (QH) regime has been discovered on DIII-D and reproduced on other experiments. The operational regime of Type II ELMs has been expanded to $n/n_G \sim 0.85$ on ASDEX Upgrade and that of grassy ELMs to lower q_{95} and high β_p on JT-60U, as well as being reproduced in JET at high q_{95} . Each of the regimes has been successfully sustained for many τ_E and combined with internal transport barriers, making them attractive for advanced scenarios. It is also clear from inter-machine experiments that there is not yet the completeness of understanding which is required to confidently extrapolate any regime to a burning plasma experiment, though several routes look promising. Simply transferring an operational ‘recipe’ to a machine of different size often fails to reproduce the same behaviour (e.g. EDA and Type II ELM experiments on JET). On the other hand, if shape and edge dimensionless parameters are matched, similar fluctuations are generally seen. Each regime has accessibility issues which need to be further explored. The EDA H-mode tends to evolve to a Type II ELMy regime at higher edge temperatures and pressures, though there are indications of a quasi-coherent mode present between ELMs. There are limits to pedestal density in the quiescent H-mode which apparently depend on shaping. All present QH experiments use counter-injected NBI, and the role of fast ions versus rotation is not fully understood. Any burning plasma regime needs to be compatible with predominant heating, by alpha particles and RF, of electrons. Most regimes are presently found at somewhat higher q_{95} , and with stronger shaping and/or nearness to double null, than is envisioned for example in ITER reference scenarios. An exception is the Type III ELMy regime, which has been observed robustly on all divertor tokamaks and whose access conditions are now well documented and at least partially explained by theory. Continued study and extrapolation to burning plasmas is important since Type III ELMs tend to occur at power close to the L–H threshold and at low pedestal temperature or pressure; with limited power this regime may occur whether or not it is desired.

Just as important as the access requirements for alternative H-mode regimes is that of pedestal scaling, which is closely

linked to plasma confinement and fusion performance. To be attractive as an operating scenario, a regime should have energy confinement *at least* as great as that of the Type I ELMy H-mode. Lower confinement is the primary drawback of the Type III ELM regime. For the other small ELM regimes, high H-factors appear to be achievable in the limited parameter range of single devices. However, because each of the regimes described has only recently been reproduced on more than one or two experiments, there are not yet robust multi-machine scalings of pedestal widths and heights, or energy confinement, in H-mode regimes which do not have Type I ELMs. Other important parameters such as Z_{eff} , which tend to be higher in the low density, low v_* regimes, also need to be documented. This remains an important task in the coming years and will require coordinated experiments among devices with a range of sizes and plasma parameters. The issues of accessibility and performance are closely linked; for example if it is necessary to raise q , and lower I_p , to achieve Type II or other ELMs, confinement would need to be correspondingly higher to compensate. Lower pedestal pressure with small ELMs could in some operation scenarios be offset by improved core confinement. Given the promise of alternative regimes and the present uncertainties, they need to be actively pursued in parallel with the further studies of Type I ELMs discussed in sections 4.2 and 4.6 of this chapter and in chapter 4 of this issue [364]. Such experiments, together with an increased and coordinated effort to model possible instabilities responsible for the edge transport in each regime, offer the prospect of good physical understanding required for confident extrapolation.

4.8. Pedestal stability

It is now generally accepted that MHD stability has a large influence on the pedestal characteristics. Ideal MHD modes provide a limit to the maximum achievable pressure gradient and so, for a given pedestal width, determine the maximum height of the pressure pedestal. For stiff transport models, the pressure pedestal is predicted to have a significant impact on the confinement, and therefore fusion performance, of any burning plasma tokamak designed to operate in H-mode. Thus, understanding the pedestal stability constraints is crucial for performance predictions of future tokamaks.

The ELMs associated with the pedestal region are now also widely believed to be a consequence of MHD instabilities. To develop a predictive capability for their resulting heat loads, we therefore need to understand not only the onset criteria for these instabilities but also their non-linear evolution. This is a challenge, but significant progress has been made in recent years, as described in this section.

To understand fully the ELM dynamics and pedestal height constraints, it is necessary to integrate the stability calculations with transport codes. Such integrated modelling is covered in section 5.5 and will not be repeated here.

4.8.1. MHD instabilities in the pedestal. There are two ideal MHD instabilities associated with the pedestal region. High toroidal mode number, n , ballooning modes can be driven unstable if the pressure gradient exceeds a certain critical value. However, with sufficient shaping, and in the presence of sufficient current density, these ballooning modes

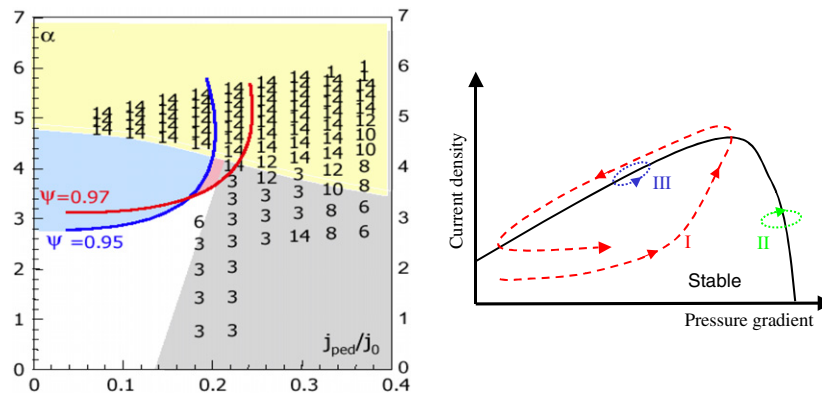


Figure 81. (a) Stability calculation for a JET discharge using the MISHKA code [670]. Shaded areas are unstable, numbers indicate the most unstable toroidal mode number calculated and the two curves indicate the $n = \infty$ ballooning stability boundary at two flux surfaces. α is the normalized pressure gradient and j_{ped} , j_0 are the current density in the pedestal region and centre, respectively. The unshaded region is stable. The grey area indicates the peeling or kink unstable region. (b) A sketch of the marginal stability curve (full curve), together with possible interpretations of large (I) and small (II and III) ELM cycles [666, 669].

can be stabilized, providing access to higher pressure gradients: the so-called second stability. The destabilizing effect of the pressure gradient is a consequence of the fact that the mode localizes on the outboard side, where the curvature is bad.

The second ideal MHD instability is the peeling mode, which can be thought of as an edge-localized kink mode [664]. The instability is driven by the current density (or its gradient) in the pedestal region. However, because it is approximately poloidally symmetric, it experiences the good average curvature of the tokamak so that pressure gradient is stabilizing for this mode. The stabilizing effect of the pressure gradient is less effective when the shaping is weak, and then one finds that the current density required to stabilize the ballooning modes destabilizes the peeling mode. The result is that there is no access to the second stability regime referred to above. Increasing the shaping both reduces the current density required to stabilize the ballooning mode and increases the current density required to destabilize the peeling mode, so access to the second stability can then be achieved. Nevertheless, the pressure gradient is ultimately limited by ideal MHD modes with an intermediate n , typically $n \sim 6$ –12, where both the pressure gradient and current density play a role in destabilizing the modes. In these situations, where both drives are operative, the modes have become known as the (coupled) peeling–ballooning modes [665–669].

In summary, the three factors that have most influence on the ideal MHD stability of the pedestal are current density, pressure gradient and shaping. These can therefore all influence the pedestal characteristics.

The importance of the current density is particularly interesting. For modern tokamaks, where the collisionality is relatively low, the bootstrap current is the dominant contribution in the pedestal, and this depends sensitively on the individual density and temperature profiles, not just the pressure profile. Thus, the ideal MHD stability can be significantly influenced by varying the plasma density.

Because of the importance of their role in determining the pedestal characteristics, significant effort has been invested in developing computer codes for quantitative ideal MHD stability analyses. MISHKA [670] can in principle deal with a range of toroidal mode numbers from $n = 1$ up

to $n \sim 20$ –30 but becomes increasingly computationally demanding at the higher n ; it also has the capability to explore diamagnetic effects [668]. KINX can cope with a similar range of toroidal mode numbers but has the unique capability to treat the separatrix geometry [671, 672]. ELITE has been developed specifically to treat intermediate to high n modes (typically accurate for $n > 5$) efficiently at the plasma edge [673]; it has been used for extensive parameter scans. As well as these ‘purpose-developed’ codes, the advances in computing capability have meant that the low n codes, such as GATO/ERATO [674], can now access toroidal mode numbers as high as $n \sim 8$. Extracting the fast variation through a phase factor permits even higher mode numbers to be explored [675]. As an example of the use of these codes, we show a stability diagram for a JET discharge, obtained using MISHKA in figure 81. Results from KINX show that when a separatrix is included, the results are broadly similar [672], but a higher current density is typically required to trigger a peeling mode.

4.8.2. Links of MHD stability calculations to ELM types.

The proximity of the pedestal parameters to the ideal stability boundaries in the cases where Type I and Type II ELMs are observed has led to the suggestion that these ELMs are a consequence of the ideal MHD instabilities (figure 81(b)). However, Type III ELMs typically occur at a pressure gradient significantly below the critical value for ballooning instability. While it has been suggested that peeling modes could be responsible in some situations, it is unlikely that all Type III ELMs can be interpreted in this way. One possibility is that resistive ballooning modes play a role here [676]. A challenge to this idea is to explain why such instabilities would lead to a large transient heat flux, rather than simply contribute to the steady turbulent transport.

It is now generally accepted that large Type I ELMs are triggered by intermediate n peeling–ballooning modes. Figure 82 shows an example of a DIII-D discharge which is found to be stable to ideal MHD modes throughout the ELM-free period, but just prior to the ELM the plasma edge becomes unstable to an $n = 10$ mode [669]. Allowing for the effects of diamagnetism, the coincidence between the time of instability

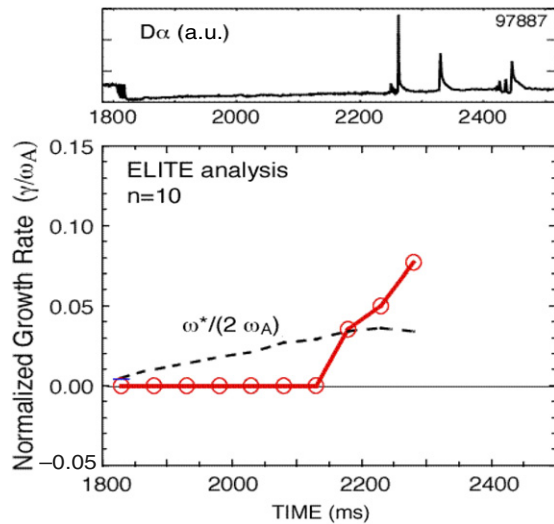


Figure 82. The upper trace shows the onset of the first ELM in a DIII-D discharge as a spike in the D_α emission. The lower trace shows the results of a sequence of stability analyses. The pedestal pressure gradient and current density rise continuously up to 2180 ms, when an $n = 10$ ideal MHD mode is predicted to go unstable just prior to the first ELM. Reprinted with permission from [669].

(when the growth rate $\gamma > \omega_*/2$, where ω_* is the diamagnetic frequency) and the ELM onset is remarkable.

It is natural to ask why we see such a range of different ELM types. One explanation that has been proposed is that the ELM size is related to the width of the linear eigenmode. Thus, a more extended eigenmode might be expected to affect more of the plasma, and hence result in a larger ELM. While such a model has little theoretical basis, and there is clearly more to the story [580], there is some experimental evidence that the ELM-affected area is indeed related to the linear eigenmode width. Figure 83 shows the radial distribution of the temperature perturbation due to ELMs, built up from a series of ELMs in a particular DIII-D discharge [669]. Also shown in that figure is the eigenmode structure for the most unstable toroidal mode number, from which it can be seen that the radial structure is similar to that observed for the temperature perturbation. Such a model would suggest that Type II ELM regimes originate from situations when the linear eigenmode is restricted to a narrow radial region. A study of this was performed using GATO for a range of discharges characteristic of ASDEX Upgrade [656]. It was found that a combination of high edge safety factor, q_{95} , and high triangularity leads to a reduction in the radial mode width (figure 84). This could provide a possible explanation for the observed transition to Type II ELMs in this regime. A similar result was obtained from JT-60U in their ‘grassy’ ELM regime (figure 85) [662] with $q_{95} = 3.4$ for large ELMs and $q_{95} = 6$ for small ELMs. The poloidal extent of the mode could also influence the resulting ELM size, and both JT-60U [584] and MAST [594] do indicate that ELMs predominantly affect the pressure on the outboard side.

As well as small ELM regimes, there are examples of regimes with no ELMs, in which density control is provided by a more benign feature observed in the pedestal region. There are two such modes of operation. The first is the enhanced

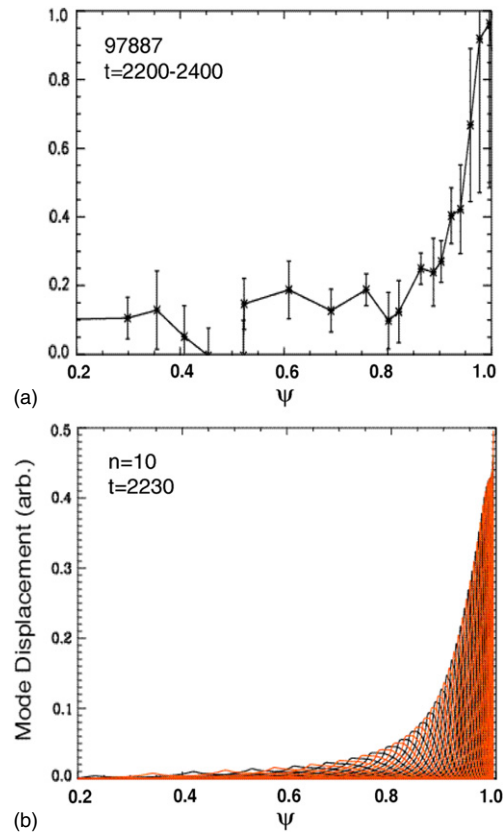


Figure 83. (a) Temperature perturbation built up from a sequence of ELMs in a DIII-D discharge. (b) The structure of the most unstable eigenmode, $n = 10$, calculated using ELITE. Reprinted with permission from [669].

D_α (EDA) mode observed in Alcator C-Mod [624]. Stability analyses (see figure 86) suggest that the EDA mode plasmas are stable to ideal MHD modes, and this could explain the absence of ELMs [634]. Nevertheless, a coherent mode is observed during the EDA, and it is believed that this provides the density control. Calculations with the BOUT code [19] (a non-linear code, based on a Braginskii fluid description of the plasma, treating the full divertor geometry) have led to the speculation that this coherent mode may be associated with a resistive ballooning mode [176].

The QH-mode [646, 647], which was first observed on DIII-D, is a second regime which provides density control, but without ELMs. The mode requires counter-neutral beam injection and low plasma density. ELMs disappear and an edge-harmonic oscillation appears to control the density instead. Precisely what the edge-harmonic oscillation is and why the ELMs disappear are still uncertain, but the latter may be related to the toroidal momentum input [648].

4.8.3. Non-linear MHD analyses. In order to model the crash phase of ELMs, it is clearly important to understand the non-linear evolution of the MHD instabilities. A non-linear theory for the ballooning mode predicts that the mode evolves into a flux tube, which narrows and twists to allow it to erupt explosively out into the scrape-off layer without reconnection [677, 678]. This helps to explain the rapid growth time of the ELM. It is then envisaged that the flux tube provides a direct

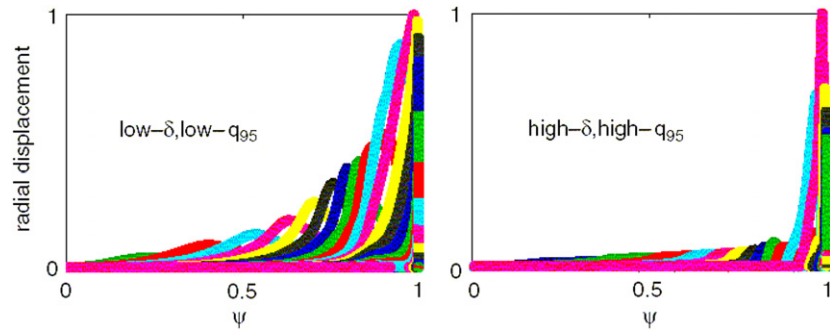


Figure 84. Eigenmode structures for a sequence of discharges with ASDEX Upgrade parameters, calculated using the GATO code [674]. High $\delta = 0.45$ and $q_{95} = 5$ lead to narrower radial mode widths than low $\delta = 0.15$ and $q_{95} = 4.3$, providing a possible interpretation of Type II ELMs. Reprinted with permission from [656].

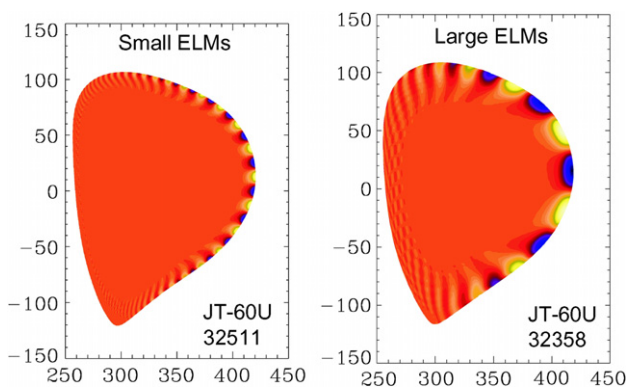


Figure 85. Eigenmode structures for the most unstable modes in two JT-60U discharges, showing a correlation between ELM size and radial eigenmode width [662].

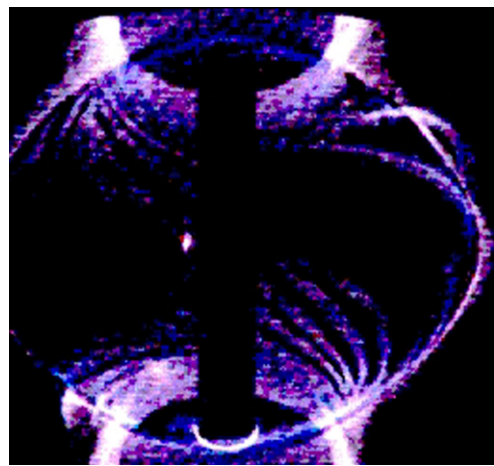


Figure 87. Filamentary structures observed in MAST during an ELM, consistent with the predictions of flux-tube eruptions from non-linear ballooning mode theory. Reprinted with permission from [555].

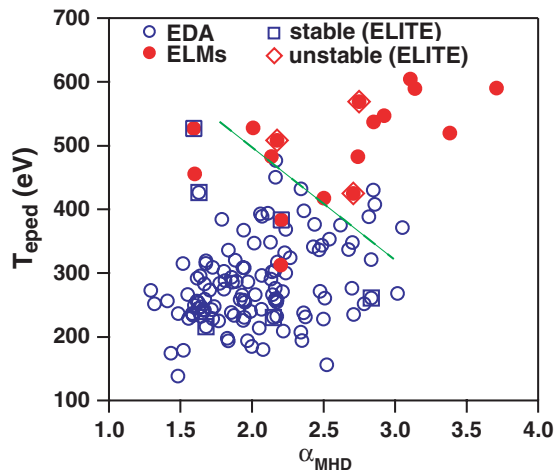


Figure 86. Observations of EDA and small ‘grassy’ ELMs in Alcator C-Mod, showing EDA occurs at low pedestal temperature (open circles). Stability analyses (squares and diamonds) are broadly consistent with the EDA mode plasmas being stable to ideal MHD modes. Reprinted with permission from [634].

route for the hot core plasma to escape into the scrape-off layer, though the precise mechanism for this remains unclear. Direct experimental evidence for such structures has been obtained from MAST (figure 87) [555, 679], and there are also signs of such structures in BOUT simulations [680].

4.8.4. Implications for ITER. Clearly the understanding of ELM dynamics and associated phenomena have progressed significantly since the ITER Physics Basis. Nevertheless, a fully quantitative model for ELM size remains elusive. There are clear trends which are observed experimentally and which have an interpretation in terms of the linear mode width. Thus we would expect smaller ELM sizes in discharges with higher triangularity and higher edge q_{95} . Flexibility to access these regimes on ITER is clearly of importance. The role of the flux-tube eruptions predicted by theory and observed in MAST needs to be understood for tokamaks with close-fitting walls to quantify the implications for ITER. These flux tubes would carry a high power density if they connect directly to the core plasma, so they could have significant implications if they were to strike the vessel wall. On the other hand, the presence of the wall itself may help to limit the radial extent of the flux-tube eruption.

Of the regimes where density control is possible without ELMs, it seems unlikely that the EDA will be a viable operating regime for ITER because of the low temperature that is apparently required. Nevertheless, the quasi-coherent mode should continue to be studied to understand whether it has a role for density control in ITER-like conditions. The QH-mode offers more promise, having now been observed on a number of

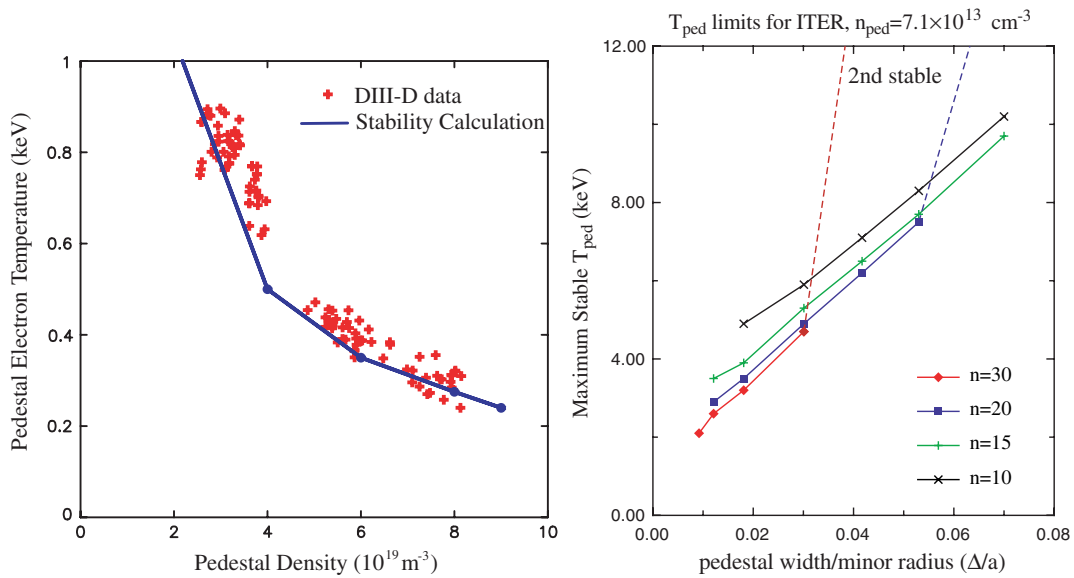


Figure 88. Comparison of the predicted temperature pedestal height as a function of density (left) from stability calculations (curve) and from a Type I ELMy H-mode DIII-D data set (with other parameters constrained to a specified narrow range). The figure on the right shows predictions of the maximum stable temperature pedestal for ITER as a function of pedestal width from the ideal MHD stability calculations for a range of n . The relevant n at any particular pedestal width is that for which the maximum stable T_{ped} is lowest. Reprinted with permission from [681].

tokamaks, but extrapolation to ITER is very uncertain without a reliable physics-based model for the phenomenon. The high impurity content of the QH-mode plasmas is also a concern.

Based on the qualitative understanding of ELM dynamics described here, it is also possible to suggest means for ELM control. Ramping the current up or down can trigger ELMs or suppress them as found experimentally and as expected theoretically from our picture of the role of peeling modes. Thus, some form of current profile control in the pedestal region would provide a control parameter for ELMs, but it remains to be seen how effective such a technique might be (if feasible). A means to degrade the pedestal confinement and so limit the pressure gradient a little below the ballooning stability boundary may also help to reduce the ELM size (the radial mode width would be more narrow).

A more quantitative use of the MHD stability results is to calculate the maximum achievable pressure pedestal in ITER. These calculations assume that the edge current density profile has reached steady state and is given by the bootstrap current. With this assumption, the pressure pedestal height can be calculated. This has been done for a range of DIII-D discharges and, provided only those discharges in a specified, narrow range of parameter space are chosen (including the pedestal width), a good agreement can be obtained, as shown in figure 88 [681]. Note that this comparison has no free fitting parameters. The predicted pedestal height for ITER as a function of pedestal width can be determined [498]. Note that a significant pedestal height can be achieved even down at quite low values of the pedestal width. This is presumably associated with the finite n stabilizing corrections for the ballooning modes, which are stronger when the pedestal is narrow [682]. An important conclusion is that estimates of the pedestal height for ITER based on a constant critical pressure gradient are inaccurate at a low pedestal width, predicting a lower height than we derive here.

We close with a few comments regarding the remaining areas of uncertainty in the theory of MHD in the pedestal and predictions for ITER. The importance of diamagnetic effects (including shear in the diamagnetic frequency) and also fast particle effects on the linear stability theory should be assessed, to complete the understanding of the trigger mechanism. The non-linear evolution should address how the pressure and current density evolve through the crash phase, which will require a model beyond ideal MHD, including transport effects. Without such a model it is difficult to predict the size of ELMs with accuracy. The role of the plasma filaments needs to be studied further, in particular whether or not they have any implications for the vessel wall.

In summary, there has been much progress in the area of pedestal MHD, but there is more work to be done to have a completely predictive model for ITER.

4.9. Possible pedestal control scenarios

A key feature of the control of burning and steady-state high beta plasmas is that the object plasma is a highly self-sustaining system. In this system, our goal is to maintain the integration of multiple performance criteria required for the reactor core. Since the pedestal area stands at the pivot of the multiple criteria discussed in the introduction to this section, we need to develop and evaluate pedestal control scenarios from the viewpoint of optimizing the whole plasma system. For ‘pedestal control’, which includes control of the structure/profile of the pedestal parameters and of the ELM activity, the possible approaches are based on modifying the plasma transport, the neutral distribution and MHD stability.

4.9.1. Control of pedestal height and structure. In burning plasma experiments, the basic requirement is to establish a favourable steady-state solution of the pedestal structure

without additional power to control the pedestal in order to maximize Q_{DT} . Therefore, the optimum choice of equilibrium shape, in combination with heating power and fuelling/pumping, is essentially important. This optimization should be conducted in a burning plasma experiment as the first step. According to present knowledge, high elongation with high triangularity seems to be a favourable equilibrium shape. The heating and current drive power should be applied to the core region (not to the pedestal directly) in order to maximize Q_{DT} . As for fuelling, the pellet injection seems to be favourable for high confinement at high density by reducing the neutrals surrounding the plasma and for minimizing the fuel circulation. In addition, some amount of gas puffing to the divertor area may be required to maintain the detached condition. Pumping from the inner strike point will be optimized under a trade-off with the required triangularity.

Once a steady-state operational point is achieved, real-time feedback control of the pedestal structure can be applied to a burning plasma. However, there are practical limitations to be considered. As for the shape control, the ac loss in the superconducting poloidal field coils has to be kept within a allowable level. Edge plasma current control is theoretically effective, but inductive drive is limited by the allowable ac loss. For non-inductive edge current drive, the problem is that the pedestal temperature is low. ECCD has a favourably localized driven current profile, however it requires a much better current drive efficiency, η_{CD} . LHCD has the highest η_{CD} , however the launcher–plasma interaction issue has to be solved. Another candidate is edge rotation/radial electric field drive. The edge transport barrier ELMs, the internal transport barrier and high beta MHD stability (such as due to resistive wall modes) can be controlled by rotation drive. The quantitative evaluation of the required rotation drive power using NBI and RF is quite an important issue to decide in order to determine whether these are both effective and practical in burning plasma experiments and reactors.

4.9.2. ELM control. In ITER, real-time ELM control scenarios are needed for ELM mitigation (for both reduction of the divertor heat load and compatibility with the ITB), impurity control and fuel control while keeping W_{ped} high enough to maintain burning plasma performance. See section 2.2 of chapter 4 of this issue [364] for discussion of ELM transport in the SOL. In addition, any negative impact on other key performance characteristics has to be minimized. At present, as discussed in the previous sections (e.g. see section 4.6.3), two means of ELM control are apparent. The first is to change the mode number or eigenfunction distribution of the instability. The second is to enhance other energy losses. And in some cases, such as in the small ELM regimes, these two seem to be mixed. In this context, this section summarizes active control schemes demonstrated in recent experiments [683].

Pellet injection. In ASDEX Upgrade, the Type I ELM frequency was controlled ($f_{ELM}/f_{pel} = 1$) by injecting small pellets (cubic $(1.4\text{ mm})^3 \sim 1 \times 10^{19}$ D-atoms, at 1 km s^{-1}) as shown in figure 89 [684, 685]. The ELM characteristics were similar to the intrinsic Type I ELMs with the same frequency, and confinement degradation was very mild. See

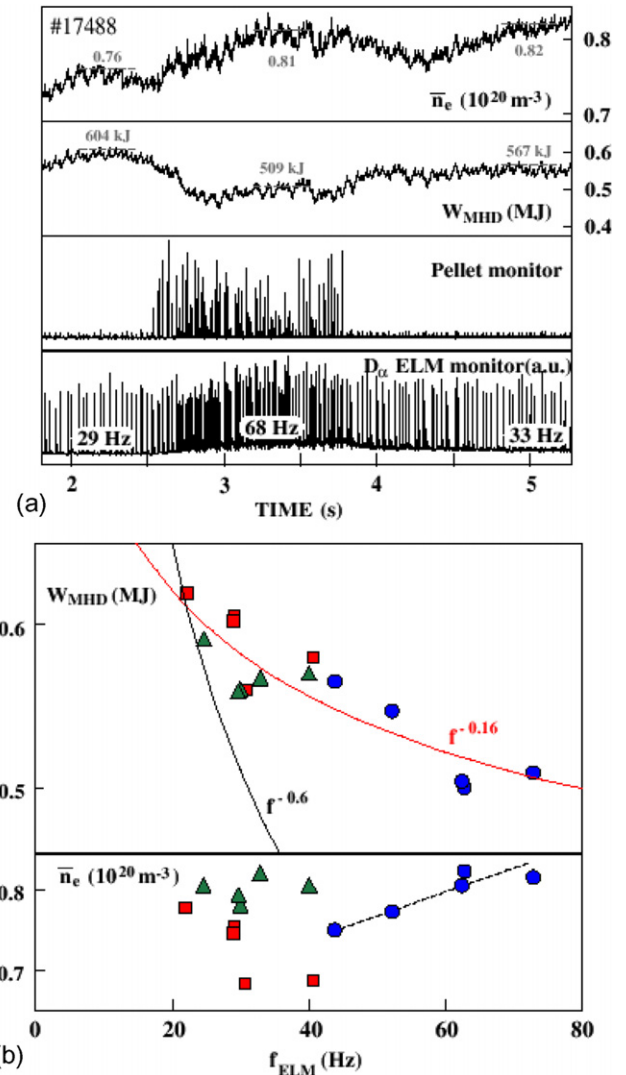


Figure 89. ELM control by pellet injection demonstrated in ASDEX Upgrade: (a) density, diamagnetic energy, pellet monitor and D_{α} signals during external gas puff without pellets ($f_{ELM} = 29$ Hz), small pellets and no puff ($f_{ELM} = 68$ Hz) and with external puff only ($f_{ELM} = 68$ Hz). (b): diamagnetic energy and line-averaged electron density dependence on ELM frequency without gas (squares), gas puffed (triangles) and pellet phases (circles). Increasing f_{pel} imposes slight refuelling and confinement degradation. A fit to data with pellets: $W_{MHD} \sim f_{ELM}^{-0.16}$. Experimental scaling with gas puff in ASDEX Upgrade: $W_{MHD} \sim f_{ELM}^{-0.6}$. Reprinted with permission from [684].

section 2.7.3 in chapter 4 of this issue [364] for more discussion of the effects of pellets on ELMs. Although the ELM trigger mechanism by pellets is a remaining issue, a study of the projection to ITER [609] determined that the minimum required pellet frequency, f_{pel} , is 3 Hz to restrict the allowable ELM energy loss to $\Delta W_{ELM} < 7\text{ MJ}$ with $P_{loss} \approx 100\text{ MW}$. And high field side injection of moderate sized ($d_{pel} < 7\text{ mm}$) pellets at 4 Hz would reduce ΔW_{ELM} to the acceptable level of $\sim 5\text{ MJ}$.

Edge current control. Changing the edge current can modify the stability boundary and ELM characteristics as predicted by the peeling–ballooning mode theory. In COMPASS-D

[602], Type I ELMs were triggered when the edge current was increased and vice versa. In TCV [604], using edge current drive with vertical plasma movement, ELMs were triggered when a positive edge current was driven (upwards for LSN). For application to ITER, however, we need to evaluate the practical effects within the ac loss and power supply limitations.

Application of external field. In JFT-2M, an ELM-free H-mode was controlled to be a steady ELMy H-mode by applying an ergodic magnetic field [686]. Testing many configurations with three sets of ergodic coils, they concluded that the helical field component of $n = 4$ is effective in producing ELMs [687]. COMPASS-D [602] also demonstrated the transition from ELM-free to ELMy H-mode when a radial magnetic perturbation was applied. On the other hand, in DIII-D [606], Type I ELMs were suppressed almost completely with an external helical magnetic perturbation (mainly $n = 3$ resonant at the plasma edge of $q_{95} = 3-4$) while keeping the confinement performance constant. In order to apply an edge ergodization scheme to ITER, however, further evaluation is needed not only for the effects on the pedestal but also for the stability of the low- n global mode at high beta.

Edge rotation control. As discussed in section 4.7, counter-rotation produces the QH-mode. In addition, by utilizing co-, counter- and perpendicular NBI, JT-60U demonstrated that the Type I ELM frequency increases with increasing counter toroidal rotation velocity, and the ELMs change from Type I to grassy while keeping almost constant pedestal pressure (figure 90) [661]. In addition to this ELM control scheme, rotation drive can expand the controllability of the burning plasma in many other aspects. However, for burning plasmas the required power has to be carefully evaluated quantitatively.

4.10. Summary of pedestal structure and transport

The edge pedestal is a key area determining the integrated performance required for burning steady-state plasmas. In the pedestal physics research field, the main issues identified in the ITER Physics Basis [1] were: (i) extension of the high confinement regime to high plasma density ($\sim n_G$); (ii) establishment of the predictive capability of the pedestal pressure and its radial structure for burning plasmas; (iii) mitigation of the giant (Type I) ELM amplitude; and (iv) development of control techniques for the pedestal pressure and ELMs. It was also emphasized that identification of the edge transport and stability processes and their interplay determining the pedestal structure and dynamics is essentially important.

Towards this goal, remarkable progress has been obtained in the intervening years. H-mode confinement has been maintained up to the Greenwald density with high triangularity. The peeling–ballooning mode theory explains the pedestal pressure gradient in the Type I ELM regime and its variation with plasma shape. Experimentally, the detailed structure of the ELM crash (poloidal asymmetry, radial distribution, three-dimensional propagation in the SOL, etc) has been clarified. Type I ELM control techniques (e.g. pellet pace making) have also been demonstrated. A variety of small

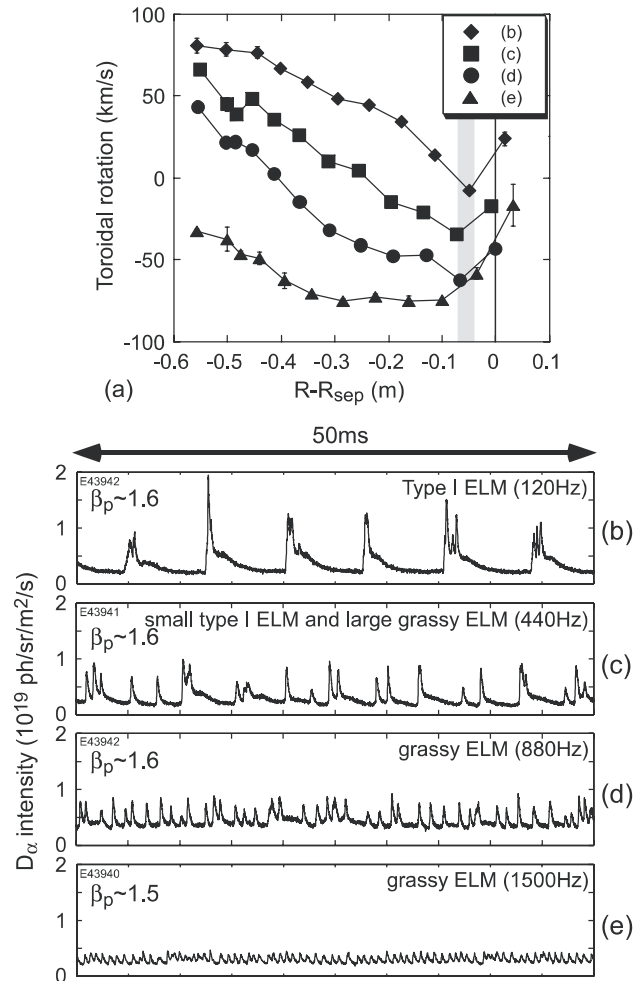


Figure 90. ELM control by rotation demonstrated in JT-60U: (a) Toroidal rotation profiles mapped into outer midplane measured with charge-exchange recombination spectroscopy. The shaded region shows the area at the top of the T_i pedestal. (b)–(e) Time evolution of the D_α signal during a plasma toroidal rotation scan ($q_{95} \sim 4.9$ and $\delta \sim 0.59$). Plasma rotation profiles were changed by using different beam combinations: (b) 2CO+2perp+2N–NB, (c) 2CO+3perp+1N–NB, (d) 2CO+5perp and (e) 1CO+1CTR+5perp. Reprinted with permission from [661].

and no-ELM regimes have been developed and some of them have been demonstrated in the low collisionality regime. High triangularity shape, safety factor, edge rotation, collisionality and harmonic oscillations have been found to play key roles in these regimes. Theory-based predictive capability has shown good progress by integrating plasma transport (in particular, turbulence suppression models based on zonal flows), neutral transport and MHD stability including the core, pedestal, SOL and divertor regions. These approaches reproduce most aspects of the L–H transition. Also, on the experimental front, high spatial and temporal resolution diagnostics have revealed the rapid change in the radial electric field and the threshold in temperature or its gradient for the L–H transition.

Finally, we list the remaining important issues. The most important is the uncertainty of the edge transport barrier width. Although establishing the inter-machine pedestal database has improved our understanding of the

pedestal structure, the width scaling has not been established. Recent efforts on inter-machine comparison experiments will clarify this issue. For the density profile shape, the effects of neutrals have been modelled but need to be verified systematically. As for the high-density operation near the Greenwald density, extension to the low collisionality regime is needed. For understanding the ELM crash dynamics, non-linear evolution of the MHD instabilities has to be clarified. Also, for understanding the ELM crash dynamics and the ELM period, time evolution of the edge current profile across an ELM crash and the inter-ELM transport has to be analysed together with the edge oscillations. These are also important for extending the small and no-ELM regimes to reactor-relevant conditions. In order to solve these issues, advanced diagnostics for the edge current density profile measurement with high spatial and temporal resolution is essentially important.

5. Predictive capability and projections for ITER

Three primary approaches are used to project the performance capabilities of ITER. The first is scaling from present machines using global parameters that encompass the collective effects of all the physics and machine conditions: the interactions between plasma confinement, MHD equilibrium and stability, particle, momentum, energy and current sources, as well as interactions between the plasma and the physical boundaries. The energy confinement time given by the ITERH-98(y,2) scaling for an inductive scenario with a plasma current of 15 MA and a plasma density 15% below the Greenwald density is 3.7 s with one estimated technical standard deviation of 14%. For levels of helium removal and impurity concentration that are expected to be attainable, this translates to $Q \sim 6\text{--}15$ with an auxiliary heating power, $P_{\text{aux}} = 40$ MW, and $Q \sim 6\text{--}30$ at the minimum heating power satisfying a good confinement ELMy H-mode [279]. The scatter in such projections from present machines is in part due to a variety of conditions that are not all directly relevant to ITER, which is not captured by the relatively few physics parameters in the fits. So the global studies are augmented by a second approach, dimensionless scaling experiments, that more closely resemble the ITER configuration and operating conditions. The third approach is the simulation of time-dependent plasma profiles. This requires enough understanding of the underlying physics to enable the construction of models for validation against existing data and extrapolation to ITER conditions. Over the past thirty years, the time-dependent simulation of plasma profiles has progressed from being dominated by empirical models to being dominated by models that are more closely connected to fundamental theoretical descriptions. Each of the three approaches has its own strengths and limitations. Collectively, they are used to find the scope of the potential operating domain within which we can explore the new physics and dynamics of burning plasmas.

We begin this section by reviewing the status of the confinement-related databases that are developed and maintained by the ITPA. These are absolutely necessary for validating models over a wide range of plasma conditions. They have undergone major changes since the publication of the ITER Physics Basis (IPB), including expanded coverage

of machines and physics as well as unification of structures and analysis tools. This is followed by a summary of our expectations for the plasma edge and H-mode pedestal conditions in ITER, then the performance projections from each of the three approaches described above. The pedestal conditions are used in global confinement projections as well as in profile modelling, which improves the confidence in our extrapolations to ITER over those used in the IPB report. But limitations still exist and are described to the best of our present knowledge.

5.1. Improved database resources for modelling and scaling studies

The results of the confinement modelling and scaling studies presented in this paper are based upon six international multi-machine databases that are currently maintained by ITPA working groups. These are the following.

1. Global L-mode confinement database [688–694].
2. H-mode power threshold database [559, 560, 689, 695–698].
3. Global H-mode confinement database [2, 689, 690, 698–709].
4. H-mode pedestal database [529, 534, 541, 702, 706, 707].
5. ITB database [25, 202, 263, 486, 710–716].
6. Profile database [2, 234].

The references included in this list refer to work related to the databases published after (or not included in) the publication of the ITER Physics Basis report [2]. The L-mode, threshold and H-mode databases are purely scalar whereas the pedestal and ITB databases have also a profile part that are kept in the same format as the profile database.

Table 3 summarizes which devices have contributed data to the databases and table 4 lists where the databases can be found and who manages them. In the following six sections more details will be given about each of the databases in turn.

5.1.1. ITPA global L-mode confinement database. The global L-mode confinement database contains 8749 entries from various tokamaks (see table 3), corresponding to Ohmic (6067 entries) and L-mode discharges (i.e. with additional heating and L-mode edge). Most of the discharges do not feature enhanced core confinement, except those specially marked in the database as corresponding to improved phases (189 entries). This database is however important for the operation of ITER, which will start with Ohmic and L-mode regimes.

The present version of the database is v2.9. Though a large number of new entries have been contributed since the previous major publication of this database, the L-mode scaling law derived in [688] has not yet been revisited and is still used for extrapolation to burning plasmas. However, it has been found that the same definition of elongation as in the IPB98(y,2) scaling expression [2] should be used and that this leads to a stronger inverse aspect ratio dependence [691]. But there is still a significant difference in the aspect ratio dependence of L-mode and H-mode scaling expressions that may explain why the difference in confinement is very small between the L-mode and H-mode in high aspect ratio tokamaks such as T-10 [694].

Table 3. Summary of tokamaks that have contributed data to the different databases.

Tokamaks	Database/Version					
	L-mode/ Ldb2v9	Threshold/ Thdb4v4	H-mode/ Hdb3v13	Pedestal/ Pdb3v3	ITB/ v1.8	Profile
Alcator C	×					
Alcator C-mod	×	×	×	×		×
ASDEX	×	×	×			
ASDEX Upgrade		×	×	×	×	×
COMPASS-D		×	×	×		
DIII	×					
DIII-D	×	×	×	×	×	×
FT	×					
FTU	×				×	×
HL-1M	×					
JET	×	×	×	×	×	×
JFT-2M	×	×	×	×		
JT-60	×					
JT-60U		×	×	×	×	×
MAST		×	×	×		
NSTX		×	×			
PBX-M	×	×	×			
PDX	×		×			
RTP	×				×	×
START	×		×			
TCV		×	×		×	
TdeV	×		×			
TEXTOR	×		×			×
TFTR	×		×		×	×
Tore Supra	×				×	×
TUMAN-3M		×	×			
T-10	×		×		×	×
No. of devices	20	13	19	8	10	11

Table 4. Database web access and managers.

ITPA DB	Online at http://	Manager	E-mail
L-mode	www-itpa0d.cea.fr/	F. Imbeaux	imbeaux@drfc.cad.cea.fr
Threshold	efdasql.ipp.mpg.de/threshold/	Y.R. Martin	Yves.Martin@epfl.ch
H-mode	efdasql.ipp.mpg.de/igd/	K. Thomsen	thomsek@ipp.mpg.de
Pedestal	efdasql.ipp.mpg.de/peddb/	L.D. Horton	ldh@ipp.mpg.de
ITB Global	www-itpa0d.cea.fr/	F. Imbeaux	imbeaux@drfc.cad.cea.fr
ITB Profile	tokamak-profiledb.ukaea.org.uk/	F. Imbeaux	imbeaux@drfc.cad.cea.fr
Profile	tokamak-profiledb.ukaea.org.uk/	C.M. Roach	colin.m.roach@ukaea.org.uk

The L-mode and H-mode scaling expressions also differ in their dependence upon normalized Larmor radius [692], with the L-mode closer to a Bohm-like dependence whereas the H-mode is more like a gyro-Bohm dependence [689]. Finally, a two-term scaling expression has been established to predict the confinement of high magnetic field devices [693]. The L-mode database also contains a significant amount of Ohmic data [717, 718] that could be used to establish the size scaling of an Ohmic confinement scaling expression [690].

The public versions of the L-mode database are accessible using a web browser at: <http://www-itpa0d.cea.fr> (common public website for ITPA 0D L-mode and ITB Global Databases). This site can be used to browse the database and to download it in various formats: U-File, CSV and SQL. Downloading the SQL dump file allows regenerating the database on the destination computer in the SQL format. The CSV format is recognized by most spreadsheet editors (such as Excel, OpenOffice, etc) and for this reason is very

convenient for downloading the database. This website also features a simplified SQL request editor, which allows data filtering and carrying out some preliminary analysis on the database. Further details about the ITPA 0D database servers and data submission can be obtained by e-mail to: webmaster.itpa0d@drfc.cad.cea.fr.

5.1.2. ITPA H-mode power threshold database. The H-mode power threshold database contains at present 7673 entries from 13 tokamaks: ASDEX (600), ASDEX Upgrade (636), Alcator C-Mod (1227), COMPASS-D (46), DIII-D (752), JET (3111), JFT-2M (1013), JT-60U (109), MAST (20), NSTX (8), PBX-M (5), TCV (131) and TUMAN-3M (15). The current version of the database is labelled IGDBTH4v4.

While H-mode threshold power scaling relations are based on data taken at the L–H transition only, it is worthwhile to have access to L-mode and H-mode data for comparison and analysis with different statistical analyses such as the

discriminant analysis. Therefore the database contains 2660 time slices taken at the L–H transition, 2345 L-mode time slices, 2261 H-mode time slices and 404 time slices taken at the H–L transition. A series of selection criteria has been applied to this collection of data in order to make the comparison between tokamaks reliable. For instance, only single-null discharges with the ion ∇B drift directed towards the X-point and operated in deuterium are kept. With these restrictions, the number of L–H transition data used in the calculation of the scaling is 1302: ASDEX (43), ASDEX Upgrade (232), Alcator C-Mod (184), COMPASS-D (21), DIII-D (58), JET (585), JFT-2M (53), JT-60U (58), MAST (5), NSTX (6) and TCV (7).

The threshold power is still found to scale, predominantly, with the plasma density, the magnetic field and the size of the device [559, 697, 698]. However, the potential effects of other parameters are currently being investigated, aiming at a reduction in the scatter between the actual threshold power and the estimation based on the scaling. For instance, the effect of the aspect ratio has now been addressed thanks to the recent contributions of MAST and NSTX. The roles of the effective Z (Z_{eff}), of the plasma shape and of low density have recently been studied as well [560]. Although these analyses resulted in a better estimation of the fit coefficients, the RMSE value of the fits remains larger than 20%. This implies a still larger uncertainty in the ITER H-mode threshold power.

A public version (IGDBTH3v2) of the database is available on the EFDA SQL server (efdasql.ipp.mpg.de). The database can be downloaded using any software equipped with a decent SQL request interface.

5.1.3. ITPA global H-mode confinement database. The H-mode database contains at present 10382 entries from 19 tokamaks (see table 3). The current version of the database is labelled DB3v13. The IPB98(y,2) scaling expression [2] is still recommended for the prediction of the ELMy H-mode confinement. The confidence interval of the ITER prediction using this scaling has been studied in detail [279, 690, 701, 703, 704]. See section 5.3.4 for a summary of ITER projections using global data. Improvements to the log-linear scaling expression by adding interaction terms as well as other effects such as density peaking, high density and triangularity have been studied [697, 704]. The effects of these improvements are included in the above confidence interval.

ASDEX Upgrade, Alcator C-Mod, DIII-D, JET, JFT-2M, JT-60U and MAST also provide data to the H-mode Pedestal Database and a significant overlap between the two databases has been achieved that has facilitated two-term scaling studies to be performed [698, 704, 706, 707]. See also the pedestal database section below.

There is now further experimental evidence [225, 228, 430, 432, 433] that the beta and v_* dependences of the H-mode confinement scaling expressions are not correct whereas the ρ_* dependence is confirmed. The strong beta degradation of the global scaling expressions has been a concern for a long time [700] and various causes have been suggested [699]. Recently it was recognized after measurement errors had been collected from all data providers that the smallest principal components have large measurement errors associated with them so that the log-linear regressions are affected

by a significant error bias. New regression studies using regression techniques that include measurements errors have shown that these indeed could be responsible for the observed discrepancies in the beta and v_* dependences [708, 709].

The various versions of the database are available on the EFDA SQL server (efdasql.ipp.mpg.de) and can be downloaded via a web interface [705].

5.1.4. ITPA H-mode pedestal scalar database. The ITPA pedestal scalar database was established with the goal of facilitating multi-machine comparisons of high resolution, plasma edge measurements. The profile information in the database is parametrized using either a hyperbolic tangent fit or a linear fit. Numerical tests have shown that the pedestal width deduced by the linear fit is approximately twice that of a tanh fit to the same data. For use in confinement studies, pedestal-top data are also stored for cases where profile information is not available. Data are presently available from the ASDEX Upgrade, Alcator C-Mod, COMPASS-D, DIII-D, JET, JFT-2M, JT-60U and MAST tokamaks.

With the increasing evidence that the pressure gradient in the pedestal region is limited by MHD stability, the focus of multi-machine analysis has been on the physics determining the pedestal width. Using the database, width scaling has been tested against models based on ion loss, neutral penetration and velocity shear turbulence stabilization due to a combination of magnetic and $E \times B$ shear [529, 534, 541]. Although some correlation is found between the data and the models, significant scatter remains in each of these theory-based fits to the database. Some of this scatter may be due to the simplified peeling–ballooning model, which is incorporated into the global scalings. In addition, the difficulty of making precise measurements leads to large scatter when a wide range of data is required. For these reasons, the Pedestal Group is presently constructing a profile database which will contain high quality data for a few discharges which can then be tested in detail against the various width models in parallel with the best available MHD stability calculations.

An additional goal of the pedestal scalar database is to determine the scaling of the pedestal energy confinement and its contribution to the global confinement. For this reason, the pedestal database was developed in close cooperation with the global confinement group and in such a way that the two databases can be easily combined. By separately fitting the core and pedestal energy, it has been possible to develop a two-term model for the scaling of energy confinement [707]. Two models for the pedestal confinement were tested: a thermal conduction model and an MHD stability limit model. When combined with a standard regression to the remaining core energy, the models result in similar predictions for the energy confinement in ITER, both within the 95% confidence limit of the IPB98(y,2) scaling [2]. The precision of the fit is limited by the conditioning of the database. More data from smaller machines and from different shapes and aspect ratios are required to improve the quality of the extrapolation to next generation machines and to differentiate between the conduction and MHD models for the pedestal confinement.

5.1.5. ITPA ITB database. The purpose of the ITB database is to provide a comprehensive multi-machine dataset for

the analysis of enhanced core confinement discharges. The database content corresponds mostly to discharges featuring internal transport barriers, but has been recently extended to the 'hybrid' regime, which also features enhanced core confinement.

The global (0D) database part contains 1777 entries from various tokamaks: ASDEX Upgrade, DIII-D, FT-U, JET, JT-60U, RTP, T10, TCV, TFTR and Tore Supra (public release v1.8). This global database is used to investigate the origin of the enhanced core confinement, by multi-machine analysis of local quantities such as the magnetic shear at the foot of the barrier [263, 486, 710] and by deducing a possible threshold in the heating power required to form an ITB [486]. Also, the 0D database has been used for mapping the performances and operational space of enhanced core confinement discharges in terms of dimensionless parameters [202]. The ITB databases feature an extended set of 128 0D variables, which also characterize 1D physical quantities such as safety factor at given positions and power deposition profiles.

The ITB profile database part is used for predictive modelling of enhanced core confinement discharges and studies that require profile analysis [711, 713–716]. Thanks to this database, transport model predictions and turbulence microstability calculations can be compared with experimental data from various tokamaks, which help in determining the common mechanisms underlying enhanced core confinement. Though the working versions of the ITB profile database and the general profile database are managed independently, their contents have been merged into a common database for public release.

The 0D ITB database part can be browsed and downloaded in various formats (U-File, CSV, SQL) at the URL: <http://www-itpa0d.cea.fr> (common public website for ITPA 0D L-mode and ITB databases). The ITB profile database part can be browsed and downloaded at the URL: <http://tokamak-profiledb.ukaea.org.uk> (common website for ITPA profile databases).

5.1.6. ITPA profile database. The international multi-tokamak profile database was developed in the late 1990s for the testing of local models of anomalous heat transport in tokamaks, and approximately two hundred tokamak discharges were collected from a large number of major devices including ASDEX Upgrade, Alcator C-Mod, DIII-D, FTU, JET, JT-60U, RTP, T10, TFTR, Tore Supra and TEXTOR. These discharges cover a wide range of confinement modes, heating schemes and plasma parameters, and a substantial subset was used in the testing of local transport models. This model validation exercise improved confidence in applying transport models to predict plasma performance in future devices such as ITER and placed such calculations in context. The transport model validation work has been reported in [2, 234] and in 1998 the resulting database was made publicly available to the wider fusion community.

The profile database has evolved considerably since then, both through the addition of discharges and through a number of major improvements to the database infrastructure. The database is available online at: <http://tokamak-profiledb.ukaea.org.uk>. Data is stored both in the original ASCII U-File format and in the more convenient

MDSplus system, which has been widely adopted by the fusion community. MDSplus simplifies interactions with the data and is interfaced to many standard tools. The website hosts the data itself, a range of analysis tools and documentation covering: data variable definitions and formats and descriptions of access and submission procedures. The tools add considerable value to the database and these include a powerful relational database search facility to help users find discharges of interest, data display tools and codes to interface the profile database to gyro-kinetic microstability codes (KINEZERO [719] and GS2 [147] see also <http://gs2.sourceforge.net/>).

The profile database has continued to grow under the ITPA framework, and more than 100 discharges have been submitted since June 2001, when the database was moved to Culham. The additional discharges have included electron heated plasmas, high performance ELMy H-modes with scans in density and shaping, high performing DT plasmas and discharges with pellet injection. There is a particular interest in testing models in high performance reference scenarios, as these discharges may be the most useful for extrapolating to next step devices. In addition, many machines have developed high performance scenarios with internal transport barriers (ITBs). Profile effects are known to be especially crucial in achieving these conditions, and such discharges may hold valuable clues to the basic mechanisms that underlie anomalous transport in tokamaks. Within the framework of the ITB profile database, profile data has been collected for ITB discharges from a number of machines, following closely the framework adopted for the profile data that was released in 1998.

The value of a coherent profile database, for testing physics models against experimental data from a wide variety of machines, is being increasingly appreciated by the fusion community. Fusion scientists, who are studying a wide variety of tokamak phenomena (e.g. internal transport barriers, the edge pedestal, steady-state scenarios, pellet injection, etc), need access to profile data so as to develop their models. There is great benefit in having uniform methods for accessing such data from a variety of machines. The ITPA profile database is broadening its scope to accommodate the type of profile data that is required in a wider range of tokamak physics analyses. As a first step in the broadening of the profile database, the ITB discharges with profile data are being incorporated, and when this task is completed, it is intended that the integrated database will be made publicly available.

5.2. Pedestal and edge characteristics

For the prediction of ITER performance, the prediction of pedestal pressure and/or temperature is one of the essential ingredients due to the strong link between the pedestal and the core through stiffness in the temperature profiles. In this section, various approaches to predicting the pedestal pressure and/or temperature developed in the past several years are summarized according to the details presented in section 4. Emphasis is placed on the Type I ELMy regime, which is the reference operation mode in ITER.

5.2.1. MHD approach. Recently, it has become widely accepted that the critical pressure gradient and trigger of Type I ELMs are governed by an ideal MHD stability. Both

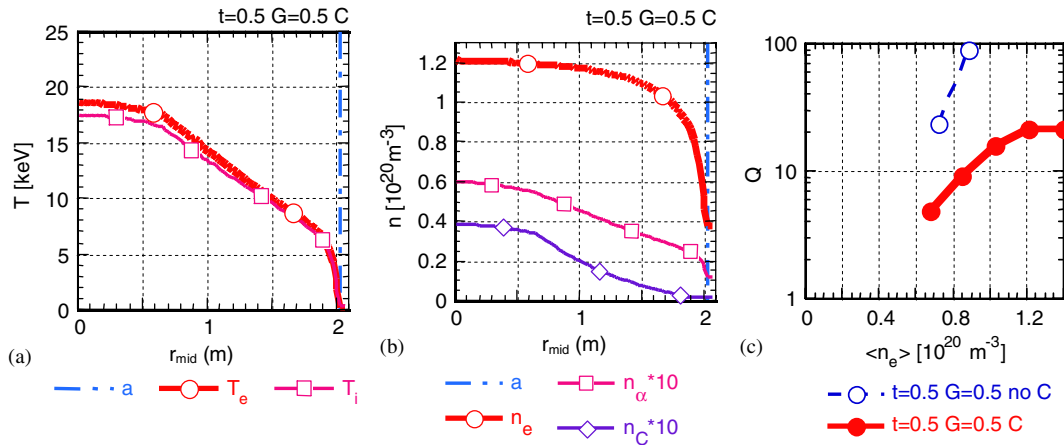


Figure 91. Predicted ITER pedestal structure and core, (a) temperature and (b) density, with the ICPS model in the ASTRA 1.5-D transport code, which models the critical pressure gradient by analytic formula derived from MHD calculation and the $\vec{E} \times \vec{B}$ shearing stabilization of the turbulence in the pedestal region. Fusion gain Q is also shown in (c) for the case with and without carbon impurities. Reprinted with permission from [516].

the pressure gradient and current density in the pedestal region play an essential role in determining the maximum achievable pressure gradient. The gradient is ultimately limited by ideal MHD modes with an intermediate toroidal mode number n , typically $n \sim 6$ –12, which are known as coupled peeling–ballooning modes. Detailed MHD codes have been developed to calculate these intermediate n modes, which include MISHKA [670], KINX [671] and ELITE [673]. MISHKA can in principle deal with a range from $n = 1$ up to $n \sim 20$ –30. It also has the capability to explore diamagnetic effects. KINX can cope with a similar range of toroidal mode numbers but has the unique capability to treat the separatrix geometry. ELITE has been developed specifically to treat intermediate to high n modes (typically accurate for $n > 5$) efficiently at the plasma edge; it has been used for extensive parameter scans. In addition to these codes, the low n codes, such as GATO/ERATO [674, 675], can now access modes as high as $n \sim 8$. Once the critical pressure gradient is calculated with these codes, the pedestal pressure/temperature can be evaluated by an appropriate assumption of the pedestal width.

Such a predictive calculation of the pedestal temperature (pedestal density is assumed as $7.1 \times 10^{19} \text{m}^{-3}$) for ITER is performed with the ELITE code and is shown in figure 88 (in section 4). In this figure, the maximum stable pedestal temperature is shown as a function of pedestal width for a range of toroidal mode numbers, n . The governing n that determines the maximum stable pedestal temperature differs from $n = 30$ for a narrow pedestal width ($\Delta/a \leq 3\%$) to $n = 15$ for a wide pedestal width ($\Delta/a \leq 5.5\%$). If $\Delta/a \approx 4$ –5% is assumed, the pedestal temperature for ITER is expected to be 6–7 keV. The remaining key point in this approach is an appropriate assumption of the pedestal width.

5.2.2. Transport modelling approach. In this approach, a 1.5D transport code is used to predict the pedestal pressure/temperature. Representative codes developed for this purpose are summarized in table 2 (in section 4). Since detailed MHD calculation for the critical pressure gradient is time consuming, it is calculated with an analytical formula derived from the MHD code calculation performed

separately in most of the codes. Thus, the condition for the critical gradient could be less accurate than the detailed MHD stand-alone calculations, whereas transport codes can calculate various aspects of the pedestal characteristics and their transient behaviours, e.g. the dynamic behaviour of ELMs, the integrated nature of the pedestal and core and separate treatment of temperature and density pedestals. For the prediction of the pedestal pressure/temperature with these transport codes, a model of the pedestal width is also necessary as in the MHD approach. An example of this model is to employ turbulence suppression by the $E \times B$ shearing rate together with the magnetic shear [516]. With this model, the pedestal structure is self-organizationally formed and accordingly the pedestal width and height are naturally determined. The ITER prediction by this code is shown in figure 91, in which temperature (a) and density (b) profiles for the average density of $\approx 10^{20} \text{m}^{-3}$ are calculated for the entire plasma region inside the separatrix. Here, the adjusting parameters t and G are calibrated with ASDEX upgrade and JET experiments as was explained in section 4.6. In figure 91(c), the fusion gain Q calculated for various average densities are also shown with and without carbon impurities.

In some codes [576], the pedestal width is artificially fixed. The emphasis of this method is placed on calculating the detailed behaviour of ELM dynamics instead of predicting the pedestal pressure/temperature accurately. In another code [568], the pedestal temperature is specified by scaling formulations derived from various models of the pedestal width to evaluate the core plasma performance, and thus this method can be categorized as a scaling approach discussed next.

5.2.3. Scaling approach. In this approach, scaling formulations of the pedestal pressure are derived based on the critical pressure gradient by an MHD model together with various models for the pedestal width. Unknown coefficients and exponents are determined by the least square error method using experimental data for the pedestal pressure or temperature. One of these approaches is described in section 4.2. In this method, a simple analytic expression for the critical pressure gradient is assumed to be modified by the

plasma shaping and beta, which is suggested by the coupled peeling–ballooning mode theory. Using the pedestal width model, $\Delta \propto \sqrt{\rho_{\text{pol}} a}$ [720], and fitting with the experimental data archived in the ITER pedestal database [534], the resulting scaling expression is given in equation (22) [540]. Fitting of the data and ITER prediction are shown in figure 63 (section 4). The predicted pedestal temperature for ITER is 5.3 keV, assuming a pedestal density of $7 \times 10^{19} \text{ m}^{-3}$.

A similar investigation has evaluated the pedestal temperature for a variety of pedestal width models using an analytic formula for the critical pressure gradient against the ballooning mode instability [721]. Numerical coefficients for each pedestal width model are determined by the least square error method using the ITER pedestal database [534]. Unfortunately, all these models provide rather large RMSE (typically 30–40%), and therefore the best model cannot be identified based on the present database. Although the pedestal temperatures predicted by some of the models are in a similar range, e.g. 2.9 keV for $\Delta \propto R\sqrt{\beta_p}$ [236] or 2.7 keV for $\Delta \propto \rho_{\text{tor}} S^2$ [722], further systematic improvement of the model of pedestal width is essential.

Although the predictive capability for the pedestal pressure/temperature in the Type I ELM regime has progressed significantly over the past several years, models for the pedestal width still have large uncertainty. Examinations of various models for the pedestal width are described in section 4.2 in detail. Further development of the model and its validation with a more solid database can greatly promote the predictive capability for all of the approaches listed above.

5.3. Global scaling

Global scaling expressions for the energy confinement time (τ_E), or the stored energy (W), are powerful tools for predicting the confinement performance of burning plasmas. These expressions are described using engineering parameters, such as the major radius (R), minor radius (a) or inverse aspect ratio ($\varepsilon = a/R$), elongation (κ), toroidal magnetic field (B_t), plasma current (I_p), electron density (n_e), heating power (P) or loss power ($P_L \equiv P - dW/dt$) and ion mass number (M). One of the most reliable scaling expressions since 1998 for the ELM regime thermal energy confinement time (τ_{th}) is the so-called IPB98(y,2) scaling [2]:

$$\tau_{\text{th},98y2} = 0.0562 I_p^{0.93} B_t^{0.15} n_{19}^{0.41} P_L^{-0.69} R^{1.97} \varepsilon^{0.58} \kappa_a^{0.78} M^{0.19} \quad (30)$$

(in s, MA, T, 10^{19} m^{-3} , MW, m). The effective elongation is defined as $\kappa_a = S_c/\pi a^2$, where S_c is the plasma cross-sectional area. The interval estimation of τ_{th} in the ITER FDR with the use of such scaling expressions was studied in detail [2, 701]. Later estimation for the present ITER design using the extended database ITERH.DB3 showed a smaller interval of a 95% log-linear uncertainty (+14% / –13%) than that for ITER FDR (+25% / –20%) [704].

5.3.1. H-mode in low aspect ratio tokamaks. The IPB98(y,2) scaling was obtained from the data of standard tokamaks with $0.15 < \varepsilon < 0.45$. The later H-mode experiments in tight aspect ratio tokamaks expanded the database significantly to $0.65 < \varepsilon < 0.8$ and towards higher toroidal beta values. To

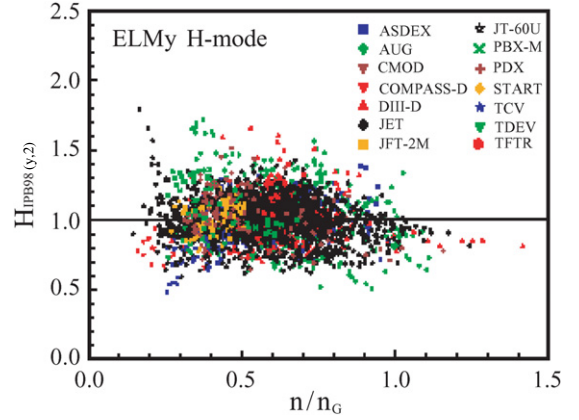


Figure 92. HH factor ($\equiv \tau_{\text{th}}/\tau_{\text{th},98y2}$) versus n/n_G . Reprinted with permission from [698].

the first approximation τ_{th} is in agreement with values given by the above scaling (MAST [723]), although τ_{th} can reach values of more than 20% greater than those given by IPB98(y,2) and indicates a non-linear behaviour of the power degradation on plasma current (NSTX [724]). The detailed dependence on ε and on other parameters is currently being assessed.

5.3.2. High-density H-mode. As for the density dependence of τ_{th} , the favourable dependence, $\tau_{\text{th}} \sim n_{19}^{0.4}$, is lost when the average density approaches the Greenwald density, $n_G (10^{20} \text{ m}^{-3}) = I_p/\pi a^2 (\text{MA}, \text{m})$, and the confinement enhancement factor, $H_{H98(y,2)} \equiv \tau_{\text{th}}/\tau_{\text{th},98y2}$, decreases below unity. This degrading nature has been widely observed in various tokamaks. It has also been found that strong shaping of the plasma cross-section, such as increasing triangularity, can mitigate this degradation at high n/n_G values [273, 494, 725]. Figure 92 shows the behaviour of $H_{H98(y,2)}$ against n/n_G for the ITPA global energy confinement database, where the degradation is seen for $n/n_G > 0.8$ [698]. Although the averaged density becomes high, the peripheral density stays low and the high confinement can be maintained. Spontaneous peaking of the density profile with simultaneous gas fuelling and good divertor pumping in DIII-D [365], or with reduced gas puffing and allowing for longer timescale in JET [355], was found to be important for achieving good confinement at high density. Introducing a density peaking factor, $\gamma_n = (n_0/\bar{n} + \bar{n}/\langle n \rangle)/2$ (n_0 is the central density, \bar{n} the line-averaged density and $\langle n \rangle$ the volume-averaged density) [690], the enhancement factor was roughly given by $H_{H98(y,2)} = 1 - 0.07(\bar{n}/n_G) + 0.17\gamma_n$ [698]. Methods to control the density peaking have not yet been fully established. The good confinement can be achieved even when the loss power, P_L , is near the L–H transition threshold, P_{LH} . The enhancement factor was found to lie around unity for a wide range of P_L/P_{LH} values [698].

5.3.3. Two-term scaling and beta dependence of ELM regime H-mode confinement. The expression of IPB98(y,2) is converted to a physics form [2]:

$$\tau_{H98(y,2)} \propto \tau_B \rho_*^{-0.7} \beta^{-0.9} v_*^{-0.01}, \quad (31)$$

where $\tau_B \propto a^2 B_t/T$ is the Bohm confinement time (T is the plasma temperature), $\rho_* \propto T^{0.5}/a B_t$ is the normalized Larmor

radius, $\beta \propto nT/B_t^2$ is the beta value and $\nu_* \propto na/T^2$ is the collisionality. Strong degradation of τ_{th} with increasing β was at first considered a result of the MHD limitation in the pedestal stored energy, W_{ped} , in ELMy H-mode plasmas. If $W = \tau_{core} P_L + W_{ped}$ and W_{ped} (or β_{ped}) is assumed independent of P_L , $\tau_E (\equiv W/P_L) = \tau_{core}/(1 - \beta_{ped}/\beta)$ deteriorates with β even when the core energy confinement time, τ_{core} , is independent of β . According to such a consideration two-term models or offset non-linear models have been developed. An early-proposed expression for the MHD-limited W_{ped} is given as $W_{ped(1)} = 0.082 I_p B_t R^2 \varepsilon \kappa (B_t R^{1.25})^{-0.1}$ (MJ), and the core thermal energy confinement time $\tau_{core,th(1)} = 0.043 I_p^{0.6} n_{19}^{0.6} P_L^{-0.4} R^{2.3} \varepsilon (B_t R^{1.25})^{-0.15}$ [2, 495]. This was obtained from the H-mode global confinement database without using the pedestal database. An international pedestal database has been assembled [534], as described in section 5.2, and various scalings for W_{ped} have been developed from it. It has been found obviously from H-mode experiments and the database that W_{ped} increases with strong shaping of the plasma cross-section, such as high elongation and high triangularity. In order to include this shaping effect, a shaping factor $F_q \equiv q_{95}/q_{cyl}$ was introduced, where q_{95} is the safety factor at 95% poloidal flux surface and $q_{cyl} = 2\pi B_t \kappa a^2 / \mu_0 I_p R$ is the cylindrical safety factor [690, 726]. One of the scaling expressions of the MHD-limited W_{ped} including this F_q variable is given as [706]

$$W_{ped(2)} = 0.01 I_p^2 R \varepsilon^{-1.68} (M/n_{19} R^2)^{0.13} F_q^{1.28} \quad (32)$$

and

$$\tau_{core,th(2)} = 0.065 I_p^{0.45} B_t^{0.35} n_{19}^{0.6} P_L^{-0.6} R^{2.55} \varepsilon^{1.87} \kappa_a^{0.88} M^{0.2}. \quad (33)$$

This $\tau_{core,th(2)} \propto \tau_B/\rho_*$ is just a pure gyro-Bohm confinement time, while $\tau_{core,th(1)} \propto \tau_B/\rho_*^{0.78}$.

It has been known from H-mode experiments that the pedestal stored energy and the core stored energy link with each other in many cases [2]. This means that W_{ped} is not always independent of P_L . Several expressions for W_{ped} dependent on P_L as well as on F_q have been proposed; $W_{ped(3)} \sim P_L^{0.2} F_q^{1.67}$ [690, 706] and $W_{ped(4)} \sim P_L^{0.42} F_q^{2.09}$ [707]. For both the expressions, the weak density dependence of W_{ped} is a distinct feature from the global W . Since W_{ped} increases with P_L , this type of W_{ped} expression was called a ‘thermal conduction model’ [707]. The physics mechanism of the P_L -dependent W_{ped} , however, is not so simple. The enhancement of the edge MHD stability in high- β_p plasmas is also a cause for the explicit P_L dependence of W_{ped} [501]. When these W_{ped} scalings are adopted in the analysis of the core confinement, the stronger power degradation of $\tau_{core,th}$ compared with $\tau_{core,th(1,2)}$ is found, i.e. $\tau_{core,th(3)} \sim P_L^{-0.65}$ [690, 706] and $\tau_{core,th(4)} \sim P_L^{-0.75}$ [707]. It is noted that $\tau_{core,th(3)}$ is close to a gyro-Bohm one, $\tau_{core,th(3)} \propto \tau_B \rho_*^{-0.8} \beta^{-0.11} \nu_*^{0.17}$, while $\tau_{core,th(4)}$ is a weak gyro-Bohm one with strong β degradation, $\tau_{core,th(4)} \propto \tau_B \rho_*^{-0.4} \beta^{-1.3}$. The latter result of the two-term modelling does not agree with the result of non-dimensional transport experiments. One of the causes for this difference comes from the different data sets between pedestal and global databases. Matching of the pedestal and global databases are planned for future work.

Recent analysis based on the ITPA H-mode database DB3v12 [709] brought a similar scaling to the IPB98(y,2)

scaling based on the database ITERH.DB2.8 [2]. Data from ASDEX, ASDEX Upgrade, Alcator C-Mod, COMPASS-D, DIII-D, JET, JFT-2M, JT-60U, MAST, NSTX, PBX-M, PDX, START, TCV, TdeV and TFTR were used. In this analysis a weighting factor inversely proportional to the square root of the number of observations from each tokamak was applied. A straightforward regression gives [709]

$$\tau_{th,04(1)} = 0.0596 I_p^{0.86} B_t^{0.21} n_{19}^{0.40} P_L^{-0.65} R^{2.00} \varepsilon^{0.69} \kappa_a^{0.84} M^{0.08}. \quad (34)$$

The physics expression is $\tau_{th,04(1)} \propto \tau_B \rho_*^{-0.8} \beta^{-0.66} \nu_*^{-0.09}$, which has a β -degradation nature, a little weaker than $\tau_{H98(y,2)}$. The condition of the dataset was examined in detail to study the accuracy of $\tau_{th,04(1)}$ and $\tau_{H98(y,2)}$. When eight variables are used, as in equations (30) and (34), there is strong collinearity between variables. As a result, three principal components among eight do not have enough spread, being less than the spread of experimental measurement errors. To exclude these three smallest principal components, an ITER-like subset of the data was selected by windowing on the parameters $1.8 < M < 2.2$, $1.6 < q_{cyl} < 2.8$ and $1.4 < \kappa_a < 1.9$, and only five variables (I_p , n , P_L , R , ε) were used for the regression analysis. Now all five principal components have enough spread. A scaling expression for this ITER-like subset is given as [709]

$$\tau_{th,04(2)} = 0.095 I_p^{1.00} n_{19}^{0.37} P_L^{-0.55} R^{1.73} \varepsilon^{0.56}. \quad (35)$$

The physics form of this scaling is $\tau_{th,04(2)} \propto \tau_B \rho_*^{-0.78} \beta^{-0.2} \nu_*^{-0.2}$. A weaker β and stronger ν_* dependence agrees fairly well with the non-dimensional transport experiments reviewed in sections 3.6 and 5.4 of this chapter.

5.3.4. Prediction for ITER. The predicted values of τ_{th} in the ITER standard operation ($I_p = 15$ MA, $B_t = 5.3$ T, $n_{19} = 10 \times 10^{19} \text{ m}^{-3}$, $P_L = 87$ MW, $R = 6.2$ m, $\varepsilon = 0.32$, $\kappa_a = 1.7$, $M = 2.5$, $F_q = 1.5$) are summarized here: $\tau_{H98(y,2)} = 3.6$ s, $\tau_{th-t(2)} = 3.5$ s (0.9 s+2.6 s), $\tau_{th-t(4)} = 3.9$ s (1.9 s+2.0 s), $\tau_{th,04(1)} = 3.4$ s and $\tau_{th,04(2)} = 3.5$ s. The global thermal confinement time for two-term models is defined as $\tau_{th,t-t} = W_{ped}/P_L + \tau_{th,core}$. In contrast to the above coincidence, the prediction of τ_{th} for higher beta operation (or higher heating power operation) in ITER is rather uncertain. Superiority among the above scaling expressions is not defined at present. Consequently, the recommended scaling for ITER operation remains the IPB98 scaling law, while this issue is further investigated. More comprehensive studies in experiments and analyses are required to clarify the beta dependence of ELMy H-mode confinement characteristics.

5.3.5. Scaling for higher confinement plasmas with ITBs. A scaling study for higher confinement plasmas with internal transport barriers (ITBs) has been started. Relations between the H -factor ($H_{L89} \equiv \tau_E/\tau_{ITER-89p}$) and plasma parameters were surveyed based on the international ITB database [202]. Explicit scaling expressions for the global energy confinement based on this database have not been obtained so far (before 2004). With the use of a confinement database of reversed-shear plasmas with box-type ITB in JT-60U, a scaling expression of the core stored energy inside ITB region was

Table 5. ITER confinement projections scaled from DIII-D and JET results using non-dimensional parameters.

Tokamak	β_N^{th}	$\rho_*/\rho_*^{\text{ITER}}$	α	$\delta\alpha$	$\tau_{\text{th}}^{\text{ITER}}(\text{s})$	$\delta\tau(\sigma)$ (S)
DIII-D	2.1	5.5	1.1	± 0.4	12	± 6
JET	2.2	4.2	0.7	± 0.3	3.3	± 1.8

shown [727]. The core stored energy W_{core} does not simply increase with P_L . A scaling of W_{core} was given as $W_{\text{scale}} = C \varepsilon_f^{-1} B_{\text{pf}}^2 V_{\text{core}}$, where ε_f is the inverse aspect ratio at the ITB foot, B_{pf} is the poloidal magnetic field at the outer midplane ITB foot and V_{core} is the core volume inside the ITB foot. This scaling is equivalent to the condition for the core poloidal beta $\varepsilon_f \beta_{\text{p,core}} = C_1$ with $C_1 \approx 1/4$. It becomes clear that the confinement scaling of ITB plasmas cannot be described only with external engineering parameters. Development of the scaling of $\tau_{E,\text{core}}$ for these plasmas is left for future work.

5.4. Non-dimensional scaling

From ρ_* scans in present devices, in which the other dimensionless parameters β , v_* and q are fixed at their values in ITER, it is possible to predict the confinement time in ITER by projecting to the value of ρ_* in ITER. This technique is described in more detail in [2, 728]. Using the scaling relation for the dimensionless confinement time

$$B_T \tau_{\text{th}} = \rho_*^{-(2+\alpha)} F(v_*, q, \dots) \quad (36)$$

and taking into account the error in the determination of α from the errors in the measurement of the thermal energy confinement time, τ_{th} , one can derive the ITER confinement time using the DIII-D and JET ρ_* scans. The results for the present version of ITER are given in table 5. The reason that the errors in τ_{th} are so large is the fact that the range in ρ_* is very small in the experiments (for toroidal magnetic field values of 1 and 2 T in DIII-D: $\rho_{*1\text{T}}/\rho_{*2\text{T}} = 1.6$ and for 1 and 2.6 T in JET: $\rho_{*1\text{T}}/\rho_{*2.6\text{T}} = 1.9$).

The results from the dimensionless scaling experiments have also been used in conjunction with the ELMy H-mode database to predict the confinement time in ITER. In this technique the regression is constrained to give the dimensionless scaling form of the single scan experiments. For example Petty *et al* [729] constrained the fit such that it satisfied the electrostatic gyro-Bohm constraints

$$B_T \tau_{\text{th}}^{\text{EGB}} \propto \rho_*^{-3} \beta^0 F(v_*, q, \dots). \quad (37)$$

The expression had the form

$$\tau_{\text{th}}^{\text{EGB}} = 0.028 I_p^{0.83} B_T^{0.07} n_{19}^{0.49} P_L^{-0.55} R^{1.81} a^{0.3} \kappa_a^{1.75} M^{0.14} \quad (38)$$

in engineering variables.

Similarly, McDonald *et al* [351] have derived an expression which satisfied the dimensionless electrostatic constraint only:

$$B_T \tau_{\text{th}}^{\text{ES}} \propto \rho_*^{-2.8} \beta^0 v_*^{-0.09}. \quad (39)$$

In engineering units this expression has the form

$$\tau_{\text{th}}^{\text{ES}} = 0.0487 I_p^{0.72} B_T^{0.09} n_{19}^{0.51} P_L^{-0.55} R^{2.14} \kappa_a^{0.74} \varepsilon^{0.78} M^{0.1}. \quad (40)$$

Table 6. The ITER parameters are taken as: $I_p = 15$ MA, $B_T = 5.3$ T, $n = 10^{20} \text{ m}^{-3}$, $R = 6.2$ m, $a = 2$ m, $\kappa = \kappa_a = 1.75$, $M = 2.5$ AMU and $P_L = 87$ MW for $\beta_N^{\text{th}} = 1.6$ and $P_L = 348$ MW for the $\beta_N^{\text{th}} = 2.5$ case.

β_N^{th}	$\tau_{\text{th},98\text{y}2}(\text{s})$	$\tau_{\text{th}}^{\text{EGB}}(\text{s})$	$\tau_{\text{th}}^{\text{ES}}(\text{s})$
1.6	3.67	4.57	3.75
2.5	1.38	3.46	2.25

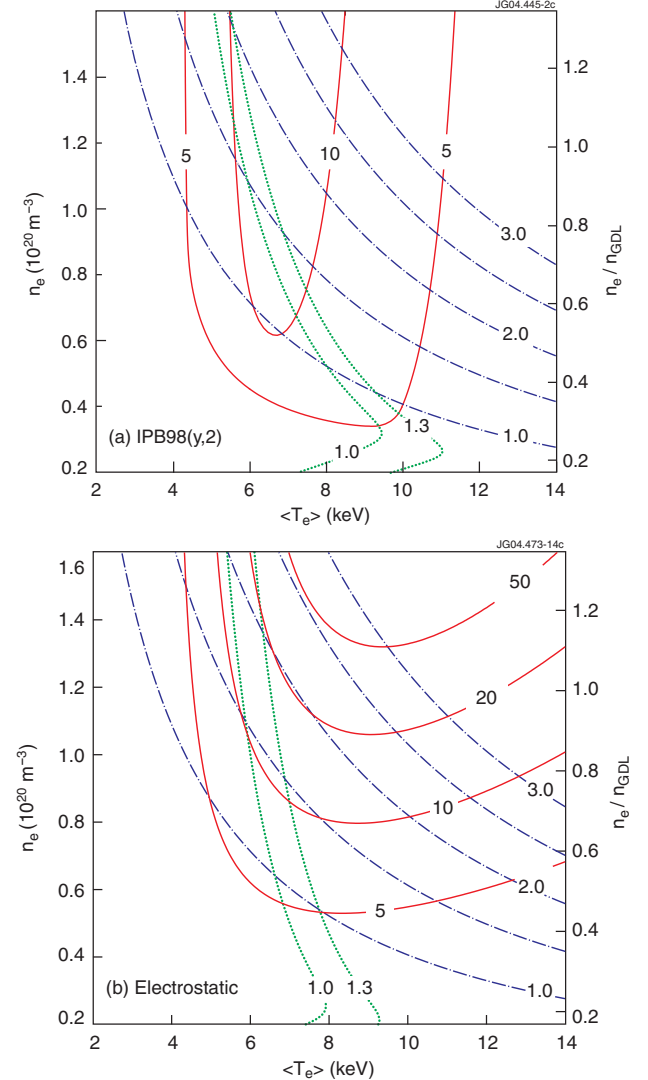


Figure 93. POPCON plots of the ITER operation space in volume averaged density and temperature showing contours of fusion gain Q (red solid lines), normalized β_N^{th} (blue dashed and dotted lines) and power relative to the L–H threshold (green dotted lines). Energy confinement is assumed to scale as (a) IPB98(y,2) and (b) the electrostatic model of equation (40). n_{GDL} designates the Greenwald density in this case.

For the ITER standard operating condition (thermal $\beta_N^{\text{th}} = 1.6$), equations (38) and (40) give a slightly higher value for τ_{th} in ITER than the standard IPB98(y,2) scaling as can be seen in table 6. However by operating at higher β_N^{th} and fusion power output, a substantial improvement in the predicted τ_{th} is given by equations (38) and (40), as also shown in table 6.

In figure 93 POPCON plots comparing the operational range for ITER with the conventional IPB98(y, 2) scaling and

that of equation (40), the scaling with zero β dependence, are presented. The main difference is that high Q s are now accessible at high temperatures with the β independent scaling. The optimum operational point for $Q = 10$ is at higher values of β_N^{th} (~ 2.5) and average temperature (~ 10 keV). This means that the steady-state operation with full current drive would be more feasible with this type of scaling.

5.5. Modelling codes, including edge modelling capability

The higher dimensional treatments (1.5D and 2D) in modelling codes introduce the next level of complexity over global analyses and are used to predict more details of plasma performance. Such modelling ultimately allows the prediction of the distribution of all relevant plasma parameters across closed magnetic surfaces in the plasma core and both across and along open magnetic field lines in the SOL. A complete picture of the plasma evolution and access to quasi-steady solutions requires modelling of electron and ion temperatures, all hydrogenic and impurity ion densities and neutrals, sources, sinks, MHD equilibria, as well as the current distribution and plasma rotation. Such a fully self-consistent simulation is an enormous challenge and is far from being fully implemented. Nonetheless, significant progress in understanding the physics of the underlying transport processes and its implementation in integrated core-edge transport codes has been reported in the past few years, which improves our comprehension of plasma dynamics and advances our predictive capabilities.

At the time the IPB was published, several core confinement models were able to model the temperature profiles of a series of H-mode and L-mode plasmas in the profile database [234] with comparable accuracy when the boundary conditions and density profiles were given by experimental values. Reference ITER confinement projections from these models were then primarily based on the assumption of flat density profiles with boundary conditions for densities and temperatures based on rough approximations to the expected pedestal height. But sensitivity studies also showed that ITER performance was very sensitive to the boundary conditions and density profile. In the following four subsections we review the progress on the implementation and validation of some of the most advanced physics components for improving those projections: core transport, the H-mode pedestal, ELMs and the scrape-off layer. Then we summarize analyses that use at least a subset of these more advanced models to evaluate ITER performance in the areas of energy confinement, density peaking and impurity profiles. Applications to steady-state and hybrid scenarios are reported in chapter 6 of this issue [199].

5.5.1. Developments in core transport models. Core transport code models necessarily started with simplified theoretically motivated models with several coefficients adjusted to best fit the experimentally measured profiles, given the calculated sources. The multi-mode model (MMM95) [238] is a good example. Various strength coefficients are assigned to the diffusivities of various component modes: ITG and TEM from the Weiland model [154] plus kinetic Alfvén and resistive ballooning mode contributions. MMM95 was

much more comprehensive than its predecessors in covering many transport regimes. Some closed form expressions were used for some diffusivities, but others required concurrent solutions of simplified dispersion relations followed by quasilinear substitution and mixing length rules. The IFS-PPPL model [237] used a linear gyro-kinetic stability code to fit a complicated parametric formula for the ITG threshold and the early gyro-fluid ITG simulations to fit a heuristic model for the diffusivity. Taking nothing from experimental fits, this was the first example of a ‘first principles’ model. The GLF23 [20] used many of the methods from MMM95 and IFS-PPPL to develop a comprehensive model covering ITG/TEM as well as ETG fit solely to ITG (with adiabatic electrons) and ETG (with adiabatic ions) simulations but checked against ITG/TEM gyro-fluid simulations. All these models are local transport models (diffusivities dependent only on local plasma gradients) and have local gyro-Bohm scaling strictly accurate only at vanishingly small ρ_* .

As noted earlier, several core transport models yielded comparable agreement with the profile database at the time the IPB was published. It was suspected that much of the remaining scatter was due to $E \times B$ rotational shear damping, geometry and other effects that were being explored in more comprehensive kinetic models but not adequately expressed in the core transport models used in 1.5D simulations. Since then there has been a continuing effort to upgrade these models. One of the more sophisticated and widely used of these is the GLF23 model; its development history is summarized here briefly to illustrate the improvements being made in core models.

The GLF23 model has been retuned recently [236] in order to extend its validity to negative magnetic shear and pedestal parameters for low to moderate values of MHD α . The retuning yields improved agreement with the linear gyro-kinetic growth rates for reversed magnetic shear and H-mode pedestal parameters, particularly for large values of MHD α . The retuned model has been tested against a variety of L- and H-mode discharges with and without negative magnetic shear [533]. Modelling results using the XPTOR code have yielded good agreement with the temperature profiles for several DIII-D ITB discharges with strongly reversed magnetic shear (see figure 94). Simulations have also demonstrated that the model is successful in predicting the density profile in discharges without ITBs. In discharges with ITBs, it was found that some additional background particle diffusivity is needed in order to reproduce the measured density profiles within the barrier region where the ITG and TEM transport has been quenched by rotational shear stabilization. The saturation levels in the original GLF23 model [20] were normalized to non-linear gyro-fluid simulations. The new version of GLF23 has been renormalized using non-linear GYRO gyro-kinetic simulations (see figure 21). As a result, the stiffness of the model has been reduced.

It is worth noting here that although self-consistent modelling of all main plasma parameters, including ion density and toroidal rotation, is an ultimate goal of any predictive modelling, its role is paramount in a self-consistent description of the radial electric field. The latter determines the shearing rate of plasma rotation, seen as one of the main factors in suppressing plasma turbulence and developing both edge and internal transport barriers (ETBs and ITBs).

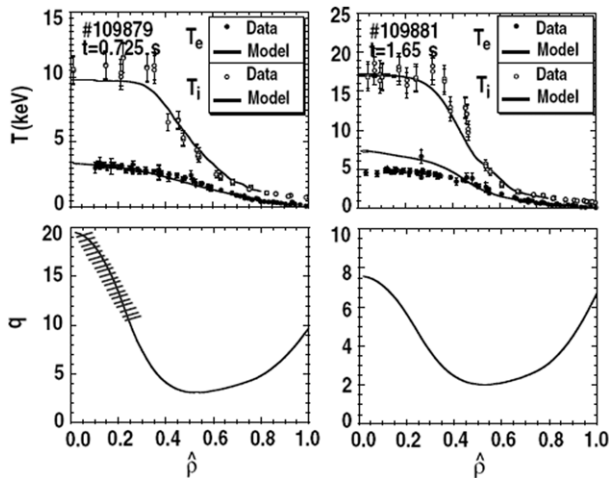


Figure 94. Experimental profiles for a strong NCS DIII-D plasmas with an L-mode edge are compared with a simulation using the retuned GLF23 transport model. The points represent the measured temperatures and the lines represent the mode predictions. Reprinted with permission from [533].

Fully self-consistent modelling of the radial electric field (including toroidal rotation) and its role in the formation of an ITB has been recently reported [253, 716]. Three pairs of shots from JET, JT-60U and DIII-D with ITBs (one shot with and another without negative magnetic shear) were simulated, using either the mixed Bohm/gyro-Bohm [397, 730] or Weiland [731] models. One of the main results of this study was the recognition of high sensitivity of the ITB formation and its further evolution with respect to a wide range of plasma parameters. Many researchers use a somewhat simplified, not fully self-consistent approach to ITB modelling [253, 714, 715, 732]. Figure 95 shows an example of the modelling of a JET ITB plasma from [714]. The Bohm term was assumed to have a threshold represented by a Heaviside step function, $H(0.5 - s - C\omega_{E \times B}/\gamma)$, where s is the magnetic shear, C an adjustable factor of order unity, γ the growth rate and $\omega_{E \times B}$ the rotational shearing rate. Only electron and ion temperatures were allowed to evolve in this simulation. The rest of the plasma parameters (density of ions and impurities and toroidal rotation) were taken from experiment. Although these studies indicate that progress has been made in modelling some aspects of ITBs, further model development is necessary before a fully predictive capability exists for ITER advanced scenarios.

5.5.2. Transport simulations using models for the H-mode pedestal. Modelling of ELMy H-mode has advanced much during the past few years as well. First of all, several groups now explicitly include the edge transport barrier in their simulations [193, 516, 533, 566] with a range of assumptions about the mechanism of the barrier formation and about transport coefficients within the ETB. One approach [533] calculates the radial electric field near the separatrix (using a neoclassical approximation for poloidal rotation and neglecting toroidal rotation) that suppresses ITG and TEM turbulence in the GLF23 model if the shearing rate exceeds the corresponding growth rates. Experimental temperatures and densities at normalized minor radius $\rho = 0.9625$ (halfway

through the ETB) are used as boundary conditions. This is the outermost flux surface, where drift wave turbulence still makes a significant contribution to anomalous transport. Another group [566] uses a combination of shear in plasma rotation and strong magnetic shear as two stabilizing factors to induce the ETB. The MMM transport model [236, 238, 239], combined with the NCLASS neoclassical model [185], was used in the simulations. It is worth noting that the presence of a drift-resistive ballooning mode in MMM95 (or drift Alfvén waves in its later realization [145]) allows setting boundary conditions just inside the separatrix. Finally, two other groups [576, 733] prescribe the ETB width using a number of theory-motivated scalings [721]. Different assumptions about transport within the ETB are used, but the most common is that the long wavelength turbulence (responsible for ion transport) is fully suppressed so that ion heat flux is controlled by a collisional transport only.

5.5.3. Modelling the effect of ELMs. Simulation of ELMs is another area of active research in predictive modelling, with the various types and effort to model them described in section 4. Simulation of ELMs introduces two additional ingredients, which were not previously used in predictive modelling. The first one is an incorporation of MHD stability analysis of the plasma within the ETB into the simulation. The simplest approach, used by all participating parties [566, 567] is to use analytical formulae for ballooning and peeling mode stability. If one of the stability criteria is violated, either the transport coefficients within the barrier are temporarily increased to simulate an ELM [567, 658, 734] or the plasma parameters within the ETB are reconstructed to take into account the edge losses during the ELM [735]. Another option, used in [566, 574] is to use a pressure gradient that corresponds to the ideal ballooning stability limit as a boundary condition for the plasma pressure at the top of the ETB. Whatever approach is used, it is very important to check the validity of simple analytical MHD stability criteria with comprehensive MHD stability codes. This requires an interface between transport and MHD stability codes. Because of a strong disparity in CPU time needed to evolve transport equations (a few minutes) and to perform a comprehensive MHD stability analysis (a few hours for peeling and finite ballooning modes), these two simulations are not used in a feedback loop at present. Instead, results of transport simulation taken shortly before the ELM crash are stored in a special file and transferred to MHD stability codes. This file contains information about simulated pressure and current profiles as well as details of the plasma equilibrium. A high quality equilibrium solver in the transport code is therefore needed in order to have a meaningful comparison between the simplified stability analysis, used by the transport code, and the one generated by a dedicated MHD stability code. Comparison between transport and MHD codes in terms of the MHD stability is then used to re-adjust analytical MHD stability formulae implemented in transport codes.

5.5.4. Modelling the connection between the ETB and the SOL. The edge transport barrier is a narrow region that separates the plasma core from the scrape-off layer and both areas influence the ETB structure and behaviour as a result.

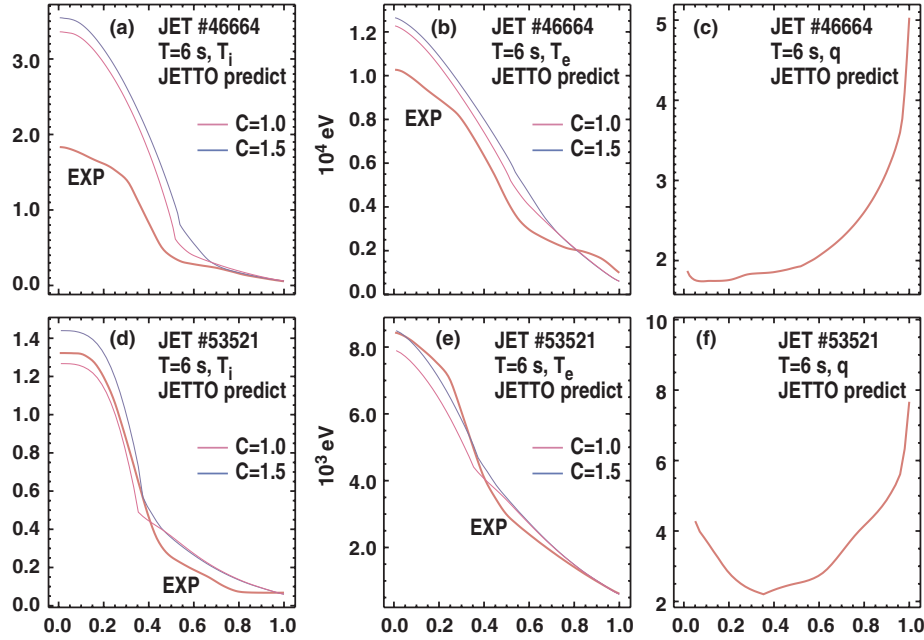


Figure 95. Predicted temperatures using the JETTO model compared against the experimental profiles for JET discharges #46664 (optimized shear) and #53521 (reversed shear). Reprinted with permission from [714].

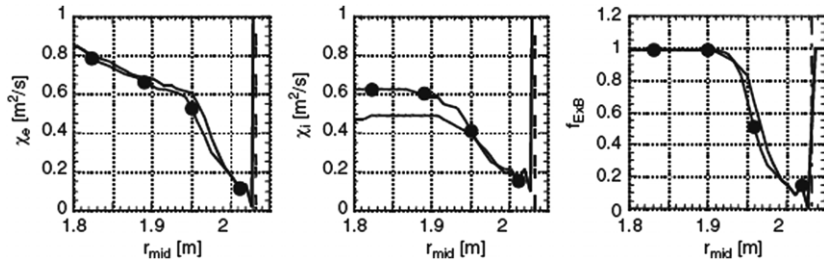


Figure 96. Expanded profiles of total electron and ion transport coefficients and the $\vec{E} \times \vec{B}$ shear reduction factor near the edge in ITER (without symbols at 100 s, with symbols at 400 s) using boundary conditions implemented as a set of scaling relations derived from B2-Eirene modelling of the divertor. Reprinted with permission from [574].

Modelling of the pedestal structure is discussed in more detail in section 4.5. Here we will try to highlight the role of the SOL in the ETB formation and its evolution, as well as the importance of an integrated approach towards modelling of ETBs. The radial distribution of cold neutrals is probably the most important ingredient of predictive modelling that is influenced by the SOL. It has been recognized that penetration of cold neutrals through the SOL may influence the structure of the ETB [538] as well as ELM dynamics [736]. Therefore self-consistent predictive modelling of ELMy H-mode plasmas requires 2D modelling of the SOL as well as the plasma core. Few attempts have been reported, first of all because of the complexity of the interface between a 1D core transport code and 2D SOL codes [514, 734, 737]. Probably the most important finding has been that the penetration of cold neutrals from external gas puffing through the separatrix is a very non-linear function of plasma density and machine size [737]. Predictive modelling of the SOL plasma for an ITER configuration shows that gas puffing cannot provide adequate core fuelling of ITER independently of the level of gas puffing [514].

The next important finding of integrated core–edge modelling comes from the realization that gas puffing controls the density within the ETB rather than in the core. And that the radial distribution of the ion density within the ETB can vary in accordance with the gas puffing even if the ion density inside the ETB does not change. It was shown that the de-coupling between core and edge density influences MHD stability of the ETB and dynamics of ELMs [734]. The somewhat simplified integrated core–pedestal SOL (ICPS) model has been used in the ASTRA code for ITER studies [574]. In ICPS the conditions at the separatrix are parametrized for different ITER scenarios based on an extensive modelling of the SOL plasma with the 2D SOL transport code B2/EIRENE. The suppression of transport coefficients near the plasma edge by $E \times B$ shear damping is shown in figure 96.

5.5.5. Confinement projections for ITER. Here we focus on a few aspects of modelling confinement in ITER standard inductive H-mode plasmas that have been influenced by progress or new information since the IPB. (1) Although the most commonly exercised physics-based models for core

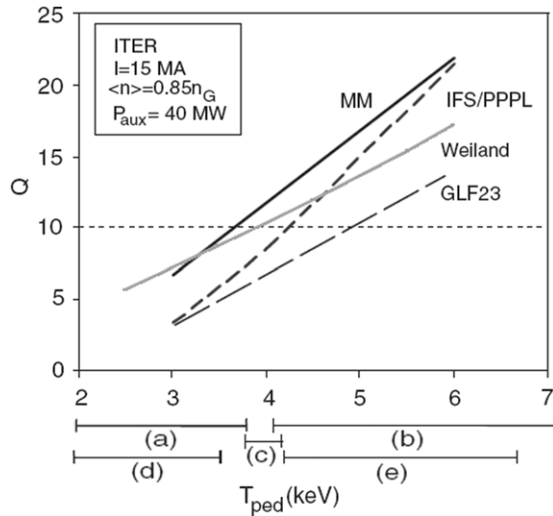


Figure 97. Fusion gain Q predicted for ITER by the MMM95 (MM) [238], IFS/PPPL [237] and GLF23 [20] transport models at the same input parameters using the ASTRA code [738]. Also shown are predictions of the Weiland model at similar input parameters [739]. Along the horizontal axis are indicated the ranges of expected pedestal temperatures from various models (a) and (b) [707], (c) [541], (d) [722], (e) [540]. Reprinted with permission from [750]. © 2003 Institute of Physics.

transport generally exhibit less stiffness than the range of models considered in the IPB, there is still a large uncertainty in the projections due to the uncertainty in the pedestal. (2) New evidence for an anomalous pinch that generally increases with decreasing collisionality influences many aspects of performance: the fusion production, edge density at a given power and turbulence growth rates. (3) Transport of low Z impurities, especially He ash, is dominated by turbulence and impurities are not expected to accumulate to very high levels, and although higher Z impurities are increasingly influenced by neoclassical effects, the neoclassical ion temperature gradient screening and turbulence-driven diffusion may help reduce the possibility of their accumulation in the core. Projections for steady-state and hybrid scenarios are discussed in section 6 of chapter 6 of this issue [199].

Energy confinement and sensitivity to the pedestal. Drift wave transport models have demonstrated success in predicting the experimental profiles in a variety of tokamaks when using experimental data for the temperatures, densities and rotation near the plasma boundary. But improved models for the ETB are clearly needed in order to increase confidence in predicting the performance of burning plasmas. Simulations using various core transport models in combination with various models for the pedestal illustrate the sensitivity of ITER performance to uncertainties in the projected pedestal characteristics. Figure 97 shows the resulting fusion Q as a function of pedestal temperature for the MMM95 [238], IFS/PPPL [237] and GLF23 [20] transport models at the same input parameters using the ASTRA code [738]. Also shown are predictions of the Weiland model at similar input parameters [739]. Along the horizontal axis are indicated the predicted ranges of several pedestal models discussed in section 5.2. The retuned GLF23 model would be expected to yield somewhat higher Q values than indicated for the earlier version of GLF23

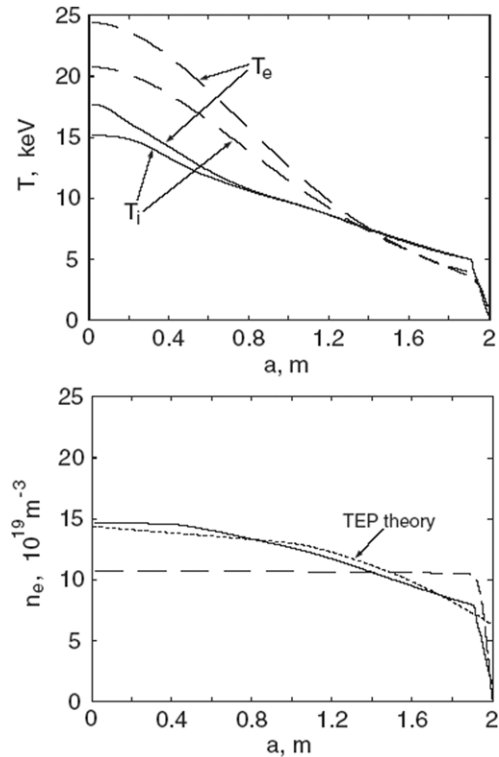


Figure 98. Steady-state distributions of the plasma density, n_e , and electron and ion temperatures, T_e and T_i , respectively, as functions of the minor radius a in the midplane. Full curves show the results of the GLF23 model with the boundary conditions $n_{e,ped} = 7.8 \times 10^{20} \text{ m}^{-3}$ and $T_{e,ped} = T_{i,ped} = 5 \text{ keV}$ at the pedestal top. Results of the ITER reference model are shown as broken lines. The dotted line shows the prediction of the turbulent equipartition (TEP) theory where the shear profile is defined by the GLF23 modelling. Reprinted with permission from [373].

because it is now less stiff. This illustrates that they yield very similar projections for a given pedestal temperature. The uncertainty in the pedestal temperature appears to be more critical than differences between the models.

In the ITER studies by Pacher *et al* [574] using the ICPS model discussed above, Q values were found to range between 5 and 20 depending on pumping speed, heat flow across the separatrix, average plasma density and allowable peak heat power on the divertor plate. So it is very clear that core, edge and SOL simulations need to be integrated to reduce the overall uncertainty in ITER performance.

Density peaking. As described in section 3.4.6, recent studies provide evidence of density peaking at low collisionality that is apparently governed by turbulence. This may impact ITER performance in many ways, including energy confinement (density-gradient-dependent turbulence), pedestal densities, fusion power production and impurity accumulation. Pereverzev *et al* [373] have recently employed the GLF23 model as well as the turbulent equipartition (TEP) theory [374] in a study of their effects on ITER density and temperature profiles as well as performance. They compare the profiles with the results of an often-used ITER reference model [372], which uses a fixed diffusivity profile shape with amplitude normalized to match the ITERH-98P(y,2) global confinement scaling. The differences in the profiles are

shown in figure 98. The density profiles for these cases were discussed in section 3.4 and shown in figure 34, but here we have added the temperature profiles to show that there are corresponding changes in the temperature profiles, i.e. they are not independent. It is seen that the GLF23 and TEP models both show more peaked density profiles and flatter temperature profiles than the scaling model and consequently yield $\sim 30\%$ more fusion power when the impurity profiles were kept fixed. But, as we discuss next, peaking of the impurity profile may cancel this benefit.

Impurities. Important impurity issues to be examined with core–edge integrated modelling include the profiles and amounts of intrinsic or seeded impurities and He ash in the core. Both processes involve successive impurity transport through the core and the SOL and, as such, require a link between 1D and 2D transport codes. A number of stand-alone simulations for either core or SOL have been reported previously [737, 740–743]. An attempt at self-consistent modelling of ITER-EDA using coupling between the 1.5D core transport code JETTO/SANCO and the 2D SOL code EDGE2D/NIMBUS has been reported [742]. As expected from such complicated simulations, they observed a strong sensitivity of the predicted impurity and He confinement to assumptions about anomalous transport both in the core and the SOL.

More recently, Pacher *et al* [744] examined intrinsic carbon in ITER with the ICPS model in ASTRA. Using the MMM95 model for the anomalous thermal conductivity with $E \times B$ shear stabilization fitted to JET and ASDEX Upgrade experimental results plus a simplified model for neoclassical transport, the authors found that the increased peaking of the carbon density essentially cancelled out any increases in performance that might be expected as improved core confinement (there was no anomalous particle pinch). Leonov and Zhogolev [745] examined higher Z impurities (tungsten and argon) with a much more sophisticated model for the impurities in ASTRA: the multi-species dynamic impurity code ZIMPUR was used to model the ionization states of up to three impurity fluxes simultaneously and NCLASS [185] was used for the full neoclassical transport of each charge state. Even in the cases of high anomalous transport, both the Ar and W densities were peaked towards the edge where they radiated a large fraction of the power without significant contamination of the core. This was because the neoclassical ion temperature gradient screening effect provided a stronger outward flux than the inward flux driven by the very flat fuel density profiles, as described in section 3.4.8, and because it was assumed that there was no anomalous pinch. Polevoi *et al* [746] performed a survey of the sensitivity of ITER performance to variations in the particle diffusivity and pinch while using high field side pellet launch for deeper fuelling and shallow pellets for ELM control. The opposing consequences of fuel ion and impurity peaking resulted in very little net change in plasma performance over the range of parameters considered.

These studies highlight the many competing effects to consider in modelling the density and impurity profiles and their effects on performance. Recent emphasis in the experimental program to identify the parameters that govern density peaking, even in the extreme conditions of non-inductive operation (no Ware pinch) and no central sources,

should improve our understanding of particle transport and how peaked we can expect the density and impurity profiles to be in ITER.

5.6. Summary of progress and remaining issues

Our various approaches to projecting ITER confinement capabilities have progressed well since the IPB, supported by improvements in diagnostic measurements, theoretical understanding and computational models. The six international multi-machine databases developed and maintained by the ITPA confinement-related topical groups have been a vital resource for developing improved qualitative and quantitative understanding of confinement over a broad range of parameters. We expect these to continue to be an important bridge between the present experimental program and burning plasmas in ITER—by providing a basis for validating more comprehensive physics models and for designing the experimental program.

Some of our greatest progress has been in an improved qualitative understanding of the physics of the plasma edge. The interactions between MHD and transport processes in the edge are very complex. The dynamics takes place over a wide range of timescales from the fast ELM crashes and bifurcations of L–H transitions to the slower evolution of the bootstrap current during the quiescent periods in between. But, we still need to develop more reliable physics-based models for the L–H transition, the pedestal width and for the full range of ELM types. Such knowledge would give us not only a better predictive capability but would allow us also to identify opportunities to intervene with external control techniques for controlling the pedestal and ELM characteristics consistent with optimal SOL and divertor performance.

Global scaling, identity experiments and detailed modelling all show general agreement on ITER’s performance and have similar uncertainties. Global scaling studies have historically provided the first step in evaluating performance characteristics of machines during their design phases and generally have proven to be very reliable for moderate projections beyond the existing experimental physics base. More recently, these have been augmented with dimensionless scaling experiments that constrain the geometry and a few other parameters to be more closely aligned with the target design. The dimensionless scaling experiments allow us to identify trends that may be more critical in the direction of extrapolation than in the broader database. Several issues that have been identified through these comparisons are: (1) how global confinement scales with beta, (2) whether collisionality or proximity to the Greenwald density is more important in governing confinement degradation at higher densities and (3) the effects of strong shaping (e.g. elongation and triangularity) on confinement. A better understanding of these trends will reduce the uncertainty in projecting ITER performance.

Time-dependent modelling of the plasma profiles has often used assumed profiles for transport coefficients with amplitudes constrained by global fits. Although use of these models allowed the investigation of issues of dynamics, access to interesting regimes and superposition of expected new physics, they did not add substantially new perspective on the overall expected confinement. The success of theory-based turbulence models in simulating experimental plasmas,

which was highlighted in the IPB, has continued. They are now viewed as a very strong complement to the global scaling models and identity experiments in projecting to ITER. Since the IPB, the theory-based models have converged somewhat on their stiffness and thereby yield a narrower range of projections when using a common set of boundary conditions at the top of the pedestal. Narrowing the uncertainty in the overall confinement projections will be heavily based on integrating with improved models for the edge. Experimental observations and theory also tell us to be cautious about the present extrapolations with these models until we strengthen them in the areas where they require the most extrapolation to ITER. These include: (1) electron transport in plasmas with predominant electron heating, (2) density peaking at low collisionality in plasmas with small or negligible sources in the core, (3) rotation in low torque plasmas and (4) the formation and sustainment of ITBs. The ITB issue is of particular relevance for the enhanced confinement that will be needed for the steady-state and hybrid scenarios discussed in chapter 6 of this issue [199]. Although they appear to have many characteristics in common with ETBs, their onset, location and strength is much more variable than ETBs, and they therefore present an even greater theoretical and computational challenge.

6. Summary

Transport in tokamak plasmas is primarily governed by non-linear turbulence processes, with multiple turbulence drives and suppression mechanisms, occurring on multiple scales. Despite this intrinsic complexity, very considerable progress has been made in understanding, controlling and predicting tokamak transport across a wide variety of plasma conditions and regimes since the publication of the ITER Physics Basis (IPB) document [1].

The understanding of fundamental transport processes has been considerably advanced by analytic theory, numerical turbulence simulations and neoclassical transport theory, as well as by efforts to benchmark theory via direct comparisons to turbulence measurements. A major step forward here is in the capability of non-linear, gyro-kinetic turbulence simulation codes. These codes can now treat large fractions of the plasma radius, a , on relevant turbulence time scales (100s of a/c_s , where c_s is the sound speed) and with expanded physics content, such as non-adiabatic electrons and electromagnetic effects. Consequently, such simulation codes are now being used to model and interpret experimental discharges, as well as to benchmark transport models which contain simplified physics content. With regard to turbulence regulation and suppression, the critical role of $E \times B$ sheared flows and zonal flows, as well as the effect of magnetic shear, is now generally accepted. Significant progress has been made in quantitative comparisons of turbulence measurements of fluctuation amplitude, spectra and correlation lengths to theory and simulation predictions, showing reasonable agreement, and essential features of the turbulence theory such as zonal flows have been identified in multiple devices. However, multiple outstanding issues still remain with regard to fundamental transport understanding, such as obtaining a successful physics description of electron thermal, particle and

momentum transport to match that which exists for ion thermal transport.

Remarkable progress has also been made in developing and understanding regimes of improved core confinement since the publication of the IPB. Internal transport barriers and other forms of reduced core transport are now routinely obtained in all the leading tokamak devices worldwide. Reduced transport has been achieved in all four transport channels (ion and electron thermal, particle and momentum transport channels), sometimes simultaneously, and ion thermal transport is often reduced to neoclassical levels. A wide range of transport dynamics in these reduced transport modes can be understood in terms of the interplay between turbulence drive and suppression mechanisms, the latter including $E \times B$ sheared flows, magnetic shear reversal, α -stabilization and impurity effects on turbulence growth rates. These mechanisms can successfully explain regimes such as the radiation-improved confinement (RI) mode, which were poorly understood at the time of the IPB. This rapid progress in the development of enhanced confinement modes of operation has contributed to an increased emphasis on developing both hybrid and steady-state operation modes for ITER. However, a concern about these operating regimes on present devices is that they are typically hot ion modes, at moderate density, with high plasma rotation rates due to external momentum input, i.e. they typically operate under non-reactor conditions. Progress has been made with regard to extrapolation to reactor conditions, though in all cases further investigation and experimental demonstration of robust high confinement operation are desirable. Ion thermal transport is now relatively well understood and is believed to be regulated by ITG-type turbulence. Theory-based modelling can qualitatively replicate ion transport across a wide range of operating regimes with quantitative agreement in many cases. However, transport in the other channels (electron thermal, particle and momentum) is relatively not as well understood as ion transport, either experimentally or theoretically. In particular, momentum transport and plasma rotation are less well understood than the other plasma transport channels; an ability to predict momentum transport and rotation for ITER is currently lacking. Using non-dimensional scaling techniques, significant new work on the scaling of energy transport with β has been performed, showing a weak or null dependence of the transport on beta, in contrast to both theoretical expectations and global database scalings. This discrepancy is an outstanding issue.

The critical importance of the edge H-mode pedestal to overall plasma performance is increasingly recognized, and H-mode access is of course essential for ITER. Theory and modelling can now reproduce many aspects of the L–H transition but have not yet produced a reliable quantitative prediction for the power threshold. Consequently, global scaling techniques employing fits to experimental multi-machine data are still employed to project the L–H transition threshold power. Using an improved and expanded database the latest projection for ITER is a threshold power in the range ~ 40 – 50 MW, within the capability of the ITER heating system (70 MW). Once in H-mode, global fusion performance is strongly influenced by the height of the edge temperature and density pedestals; with relatively stiff central

profiles the pedestal parameters have a large impact on global performance. In predicting pedestal parameters, the most important unresolved issue is determining the pedestal width, i.e. the width of the edge transport barrier. Multiple models for the width, which have divergent predictions for ITER, have been tested versus data from present devices, but this testing has failed to discriminate between the models. It is hoped that further inter-machine comparisons will clarify this issue. A successful, quantitative theoretical model has been developed for the pressure limit in Type I ELMs, in terms of the stability of peeling–ballooning modes. However, a full understanding of the ELM crash dynamics requires further clarification of the non-linear evolution of the MHD instabilities. Several successful methods have been demonstrated to either mitigate or eliminate Type I ELMs, in order to avoid unacceptable erosion of the first wall material (ELMs generate transient pulsed heat and particle fluxes to the wall and divertor). These mitigated and no-ELM regimes need to be extended to reactor-relevant conditions. Also with regard to reactor compatibility, high confinement at high density has now been robustly demonstrated, as required for the ITER operating point. However, extension of these results to lower, ITER-like collisionality is desired.

Predictive capabilities for transport and confinement projections to ITER have improved. Multi-machine experimental scalar and profile databases for constructing global confinement scalings and local transport modelling have been expanded and are now administered under the auspices of the ITPA. The three primary predictive techniques—global scaling, transport modelling and non-dimensional scaling—have each been refined and extended in scope since the publication of the ITB. Empirical scaling, using parameter fits to global experimental transport data from present devices, was previously the primary predictive approach, but it is now extensively complemented by theory-based transport modelling. The capability and reliability of transport models has been substantially increased, and the models are benchmarked via comparison to both present experiments and to more physically comprehensive transport simulation codes. The non-dimensional scaling technique, in which plasma parameters are matched in dimensionless fashion across devices, leaving only a single parameter extrapolation to be made to ITER, e.g. in ρ_* , has also been refined, especially with regard to the beta scaling of transport.

For the ITER base case or reference scenario (conventional ELMy H-mode operation), all three predictive techniques show that ITER will have sufficient confinement to meet its design target of $Q = 10$ operation, within similar ranges of uncertainties. Specifically, while several new global scalings have been developed, the recommended scaling for ITER remains the IPB98(y,2) scaling law [2]. For the ITER design operating point this scaling predicts $\tau_{th} = 3.6$ s. However, the estimated 95% log-linear uncertainty interval for the ITER projection has been significantly reduced; using a revised, expanded database the interval is now (+14%/–13%), as compared with (+25%/–20%) for the earlier ITER design [1]. The non-dimensional scaling projection for ITER is very similar, with a minimum $\tau_{th} = 3.3$ s. However, the non-dimensional and global scaling results differ with regard to

the beta scaling of transport, β^0 versus $\beta^{-0.9}$, respectively. At the ITER design operating point of $\beta_N = 1.6$ this different scaling has little effect on confinement projections, but this would become important for advanced operation at higher beta, with the non-dimensional result being more optimistic. This discrepancy is not currently understood and is under active investigation. Other areas of current research with regard to scaling projections include the effect of shaping on confinement and whether collisionality or proximity to the Greenwald density is more important in determining confinement at high density. With regard to projections by the transport models, a comparison of four leading models (MM, IFS/PPPL, Weiland and GLF23) shows ITER achieving $Q = 10$ operation for edge pedestal temperatures in the range 3.5–5 keV, depending on the model. In general, the predictions of the transport models have converged since the publication of the IPB but still differ in detail due to varying levels of ‘stiffness’ in the models. Also, these models are more accurate in replicating ion thermal as compared with electron thermal, particle or momentum transport, all of which are critical to ITER performance, so caution is still required in using these projections. In further extending the applicability of these models the current focus is on developing and integrating models of the edge pedestal with the core plasma.

With regard to operation of ITER in regimes with enhanced core confinement, such as with ITBs, none of the predictive techniques are as yet in a position to make reliable projections. For the global scaling approach the limitation may be intrinsic, in that the development and sustainment of ITBs depends on local plasma parameters (i.e. on detailed plasma profiles), which are not captured in scalar databases. For the transport models, while progress has been made in replicating ITB formation and sustainment, further work is required before projections can be made with confidence.

In an overall summary, it may be stated that both experimental and transport modelling/simulation indicate that ITER will meet its baseline design confinement requirements. Advanced operation on ITER with enhanced core confinement is becoming an increasingly realistic and attractive prospect, but a major experimental emphasis is required to demonstrate that such an advanced operation is compatible with reactor operating conditions. Substantial advances have been made in improving the physics content and reliability of transport modelling and simulation codes, but a fully consistent and integrated (core and edge) predictive capability which can accurately describe all transport channels is still some way in the future.

Reference

- [1] ITER Physics Basis Editors *et al* 1999 *Nucl. Fusion* **39** 2137
- [2] ITER Physics Expert Groups on Confinement and Transport and Confinement Modelling and Database, ITER Physics Basis Editors and ITER EDA 1999 *Nucl. Fusion* **39** 2175
- [3] Itoh K. 2003 *Nucl. Fusion* **43** 1710
- [4] Diamond P.H. *et al* 2004 *Fusion Energy 2004: Proc. 20th Int. Conf. (Vilamoura, 2004)* (Vienna: IAEA) CD-ROM file OV/2-1 and <http://www-naweb.iaea.org/naweb/physics/fec/fec2004/datasets/index.html>

- [5] Shaing K.C. *et al* 2003 *Nucl. Fusion* **43** 258
- [6] Joffrin E. *et al* 2003 *Nucl. Fusion* **43** 1167
- [7] Connor J.W. *et al* 2005 *Plasma Phys. Control. Fusion* **47** 941
- [8] Terry P.W. 2000 *Rev. Mod. Phys.* **72** 109
- [9] Connor J.W. and Pogutse O.P. 2001 *Plasma Phys. Control. Fusion* **43** 155
- [10] Horton W. *et al* 2003 *New J. Phys.* **5** 14.1
- [11] Parail V.V. 2002 *Plasma Phys. Control. Fusion* **44** A63
- [12] Horton W. *et al* 2000 *Phys. Plasmas* **7** 1494
- [13] Garbet X. *et al* 2003 *Nucl. Fusion* **43** 975
- [14] Baker D.R. *et al* 2001 *Phys. Plasmas* **8** 1565
- [15] Kaw P.K. 1982 *Phys. Rev. A* **90A** 290
- [16] Li J. and Kishimoto Y. 2002 *Plasma Phys. Control. Fusion* **44** A479
- [17] Itoh K., Itoh S.-I. and Fukuyama A. 1999 *Transport and Structural Formation in Plasmas* (Bristol: Institute of Physics Publishing)
- [18] Hahn T.S., Lee W.W. and Brizard A. 1988 *Phys. Fluids* **31** 1940
- [19] Xu X.Q. and Cohen R.H. 1998 *Contrib. Plasma Phys.* **38** 158
- [20] Waltz R.E. *et al* 1997 *Phys. Plasmas* **4** 2482
- [21] Dorland W. and Hammett G.W. 1993 *Phys. Fluids B* **5** 812
- [22] Doyle E.J. *et al* 2000 *Fusion Energy 2000: Proc. 18th Int. Conf. (Sorrento, 2000)* (Vienna: IAEA) CD-ROM file EX6/2 and <http://www.iaea.org/programmes/ripc/physics/fec2000/html/fec2000.htm>
- [23] Garbet X. *et al* 2004 *Plasma Phys. Control. Fusion* **46** 1351
- [24] Wolf R.C. 2003 *Plasma Phys. Control. Fusion* **45** R1
- [25] Connor J.W. *et al* 2004 *Nucl. Fusion* **44** R1
- [26] Biglari H., Diamond P.H. and Terry P.W. 1990 *Phys. Fluid B* **2** 1
- [27] Hahn T.S. and Burrell K.H. 1995 *Phys. Plasmas* **2** 1648
- [28] Horton W. 1999 *Rev. Mod. Phys.* **71** 735
- [29] Ottaviani M. and Manfredi G. 1999 *Phys. Plasmas* **6** 3267
- [30] Labit B. and Ottaviani M. 2003 *Phys. Plasmas* **10** 126
- [31] Kishimoto Y. *et al* 1996 *Phys. Plasmas* **3** 1289
- [32] Candy J. and Waltz R.E. 2003 *Phys. Rev. Lett.* **91** 045001
- [33] Lin Z. *et al* 2002 *Phys. Rev. Lett.* **88** 195004
- [34] Waltz R.E., Candy J.M. and Rosenbluth M.N. 2002 *Phys. Plasmas* **9** 1938
- [35] Kim E. *et al* 2003 *Nucl. Fusion* **43** 961
- [36] Hahn T.S. *et al* 2004 *Plasma Phys. Control. Fusion* **46** A323
- [37] Stallard B.W. *et al* 1999 *Phys. Plasmas* **6** 1978
- [38] Roach C.M., Connor J.W. and Janjuat S. 1995 *Plasma Phys. Control. Fusion* **37** 679
- [39] Krommes J.A. and Kim C.B. 2000 *Phys. Rev. E* **62** 8508
- [40] Itoh S.-I. *et al* 2002 *Plasma Phys. Control. Fusion* **44** 1311
- [41] Diamond P.H. and Hahn T.S. 1995 *Phys. Plasmas* **2** 3640
- [42] Lin Z. *et al* 1999 *Phys. Rev. Lett.* **83** 3645
- [43] Malkov M.A., Diamond P.H. and Rosenbluth M.N. 2001 *Phys. Plasmas* **8** 5073
- [44] Li J.Q. and Kishimoto Y. 2002 *Phys. Rev. Lett.* **89** 115002
- [45] Diamond P.H. *et al* 2001 *Nucl. Fusion* **41** 1067
- [46] Dorland W. *et al* 2000 *Phys. Rev. Lett.* **85** 5579
- [47] Jenko F. and Dorland W. 2002 *Phys. Rev. Lett.* **89** 225001
- [48] Idomura Y. *et al* 2001 *Nucl. Fusion* **41** 437
- [49] Kishimoto Y. *et al* 2002 *Fusion Energy 2002: Proc. 19th Int. Conf. (Lyon, 2002)* (Vienna: IAEA) CD-ROM file TH/1-5 and <http://www.iaea.org/programmes/ripc/physics/fec2002/html/fec2002.htm>
- [50] Rogers B.N., Dorland W. and Kotschenreuther M. 2000 *Phys. Rev. Lett.* **85** 5336
- [51] Kim E. and Diamond P.H. 2003 *Phys. Rev. Lett.* **90** 185006
- [52] Kim E. and Diamond P.H. 2003 *Phys. Plasmas* **10** 1698
- [53] Staebler G.M. 2000 *Phys. Rev. Lett.* **84** 3610
- [54] D'Ippolito D.A. and Myra J.R. 2003 *Phys. Plasmas* **10** 4029
- [55] Yu G.Q. and Krasheninnikov S.I. 2003 *Phys. Plasmas* **10** 4413
- [56] Chen L., Lin Z. and White R. 2000 *Phys. Plasmas* **7** 3129
- [57] Guzdar P.N., Kleva R.G. and Chen L. 2002 *Phys. Plasmas* **8** 459
- [58] Guzdar P.N. *et al* 2002 *Phys. Plasmas* **8** 3907
- [59] Lashmore-Davies C.N., McCarthy D.R. and Thyagaraja A. 2001 *Phys. Plasmas* **8** 5121
- [60] Smolyakov A.I., Diamond P.H. and Malkov M. 2000 *Phys. Rev. Lett.* **84** 491
- [61] Champeaux S. and Diamond P.H. 2001 *Phys. Lett.* **288** 214
- [62] Holland C. and Diamond P.H. 2002 *Phys. Plasmas* **9** 3857
- [63] Holland C. *et al* 2003 *Nucl. Fusion* **43** 761
- [64] Li J. and Kishimoto Y. 2002 *Phys. Plasmas* **9** 1241
- [65] Manfredi G., Roach C.M. and Dendy R.O. 2001 *Plasma Phys. Control. Fusion* **43** 825
- [66] Diamond P.H. *et al* 2005 *Plasma Phys. Control. Fusion* **47** R35
- [67] Hahn T.S. *et al* 1999 *Phys. Plasmas* **6** 922
- [68] Winsor N., Johnson J.L. and Dawson J.M. 1968 *Phys. Fluids* **11** 2448
- [69] Miyato N., Kishimoto Y. and Li J. 2004 *Phys. Plasmas* **11** 5557
- [70] Hallatschek K. and Biskamp D. 2001 *Phys. Rev. Lett.* **86** 1223
- [71] Scott B. 2003 *Phys. Lett. A* **320** 53
- [72] Krommes J.A. 2002 *Phys. Rep.* **360** 1
- [73] Yagi M. *et al* 2002 *Fusion Energy 2002: Proc. 19th Int. Conf. (Lyon, 2002)* (Vienna: IAEA) CD-ROM file TH/1-4 and <http://www.iaea.org/programmes/ripc/physics/fec2002/html/fec2002.htm>
- [74] Idomura Y., Tokuda S. and Kishimoto Y. 2002 *Fusion Energy 2002: Proc. 19th Int. Conf. (Lyon, 2002)* (Vienna: IAEA) CD-ROM file TH/P1-08 and <http://www.iaea.org/programmes/ripc/physics/fec2002/html/fec2002.htm>
- [75] Jenko F. *et al* 2002 *Fusion Energy 2002: Proc. 19th Int. Conf. (Lyon, 2002)* (Vienna: IAEA) CD-ROM file TH/1-2 and <http://www.iaea.org/programmes/ripc/physics/fec2002/html/fec2002.htm>
- [76] Roach C.M. *et al* 2005 *Plasma Phys. Control. Fusion* **47** B323
- [77] Thyagaraja A. 2000 *Plasma Phys. Control. Fusion* **42** B255
- [78] McClements K.G. *et al* 2002 *Nucl. Fusion* **42** 1155
- [79] deBaar M.R. *et al* 2005 *Phys. Rev. Lett.* **94** 035002
- [80] Itoh S.-I. *et al* 2002 *Phys. Plasmas* **9** 1947
- [81] Itoh S.-I. and Itoh K. 2001 *Plasma Phys. Control. Fusion* **43** 1055
- [82] Estrada-Mila C., Candy J. and Waltz R.E. 2005 *Phys. Plasmas* **12** 022305
- [83] Hammett G.W. and Perkins F.W. 1990 *Phys. Rev. Lett.* **64** 3019
- [84] Hammett G.W., Dorland W. and Perkins F.W. 1992 *Phys. Fluids B* **4** 2052
- [85] Waltz R.E., Dominguez R.R. and Hammett G.W. 1992 *Phys. Fluids B* **4** 3138
- [86] Rosenbluth M.N. and Hinton F.L. 1998 *Phys. Rev. Lett.* **80** 724
- [87] Dastgeer S., Mahajan S. and Weiland J. 2002 *Phys. Plasmas* **9** 4911
- [88] Sugama H., Watanabe T.H. and Horton W. 2003 *Phys. Plasmas* **10** 726
- [89] Snyder P.B. and Hammett G.W. 2001 *Phys. Plasmas* **8** 3199
- [90] Beer M.A. and Hammett G.W. 1996 *Phys. Plasmas* **3** 4046
- [91] Scott B.D. 2005 *Phys. Plasmas* **12** 102307
- [92] Idomura Y., Tokuda S. and Kishimoto Y. 2003 *Nucl. Fusion* **43** 234
- [93] Villard L. *et al* 2004 *Nucl. Fusion* **44** 172
- [94] Lin Z. and Chen L. 2001 *Phys. Plasmas* **8** 1447
- [95] Cohen B.I. *et al* 2002 *Phys. Plasmas* **9** 1915
- [96] Cohen B.I. *et al* 2002 *Phys. Plasmas* **9** 251
- [97] Chen Y. and Parker S.E. 2003 *J. Comput. Phys.* **189** 463
- [98] Chen Y. *et al* 2003 *Nucl. Fusion* **43** 1121
- [99] Allfrey S.J. and Hatzky R. 2003 *Comput. Phys. Commun.* **154** 98
- [100] Aydemir A.Y. 1994 *Phys. Plasmas* **1** 822
- [101] Denton R.E. and Kotschenreuther M. 1995 *J. Comput. Phys.* **119** 283
- [102] Kotschenreuther M. 1988 *Bull. Am. Phys. Soc.* **33** 2107

- [103] Dimits A.M. and Lee W.W. 1993 *J. Comput. Phys.* **107** 309
- [104] Parker S.E. and Lee W.W. 1993 *Phys. Fluids B* **5** 77
- [105] Manuilskiy I. and Lee W.W. 2000 *Phys. Plasmas* **7** 1381
- [106] Lee W.W. *et al* 2001 *Phys. Plasmas* **8** 4435
- [107] Hatzky R. *et al* 2002 *Phys. Plasmas* **9** 898
- [108] Nevins W.M. *et al* 2005 *Phys. Plasmas* **12** 122305
- [109] Candy J. and Waltz R.E. 2003 *J. Comput. Phys.* **186** 545
- [110] Dimits A.M. *et al* 2000 *Phys. Plasmas* **7** 969
- [111] Lin Z. *et al* 1998 *Science* **281** 1835
- [112] Hammett G.W. *et al* 1993 *Plasma Phys. Control. Fusion* **35** 973
- [113] Beer M.A. 1995 Gyrofluid models of turbulent transport in tokamaks, *PhD Thesis*, Princeton University
- [114] Waltz R.E., Kerbel G.D. and Milovich J. 1994 *Phys. Plasmas* **1** 2229
- [115] Dimits A.M. *et al* 1996 *Phys. Rev. Lett.* **77** 71
- [116] Sydora R.D., Decyk V.K. and Dawson J.M. 1996 *Plasma Phys. Control. Fusion* **38** A281
- [117] Lin Z. *et al* 2000 *Phys. Plasmas* **7** 1857
- [118] Candy J., Waltz R.E. and Dorland W. 2004 *Phys. Plasmas* **11** L25
- [119] Jenko F., Dannert T. and Angioni C. 2005 *Plasma Phys. Control. Fusion* **47** B195
- [120] Beer M.A. and Hammett G.W. 1996 *Phys. Plasmas* **3** 4018
- [121] Ross D.W. and Dorland W. 2002 *Phys. Plasmas* **9** 5031
- [122] Dannert T. and Jenko F. 2005 *Phys. Plasmas* **12** 072309
- [123] Ernst D.R. *et al* 2004 *Phys. Plasmas* **11** 2637
- [124] Garbet X. *et al* 2003 *Phys. Rev. Lett.* **91** 035001
- [125] Yankov V.V. 1995 *Plasma Phys. Rep.* **21** 719
- [126] Isichenko M.B. *et al* 1996 *Phys. Plasmas* **3** 1916
- [127] Garbet X. *et al* 2002 *Phys. Plasmas* **9** 3893
- [128] Hallatschek K. and Dorland W. 2005 *Phys. Rev. Lett.* **95** 055002
- [129] Angioni C. *et al* 2005 *Phys. Plasmas* **12** 040701
- [130] Snyder P.B. and Hammett G.W. 2001 *Phys. Plasmas* **8** 744
- [131] Parker S.E. *et al* 2004 *Phys. Plasmas* **11** 2594
- [132] Candy J. 2005 *Phys. Plasmas* **2005** 072307
- [133] Jenko F. and Dorland W. 2001 *Plasma Phys. Control. Fusion* **43** A141
- [134] Applegate D.J. *et al* 2004 *Phys. Plasmas* **12** 5085
- [135] Jenko F. *et al* 2000 *Phys. Plasmas* **7** 1904
- [136] Beyer P. *et al* 2000 *Phys. Rev. Lett.* **85** 4892
- [137] Lin Z., Chen L. and Zonca F. 2005 *Phys. Plasmas* **12** 056125
- [138] Idomura Y., Wakatani M. and Tokuda S. 2000 *Phys. Plasmas* **7** 3551
- [139] Li J.Q. and Kishimoto Y. 2003 *Phys. Plasmas* **10** 683
- [140] Jenko F. 2004 *J. Plasma Fusion Res. Series* **6** 11
- [141] Waltz R.E. and Miller R.L. 1999 *Phys. Plasmas* **6** 4265
- [142] Scott B.D. 2002 *New J. Phys.* **4** 52.1
- [143] Carreras B.A. 1997 *IEEE Trans. Plasma Sci.* **25** 1281
- [144] Conway G.D. *et al* 2002 *Plasma Phys. Control. Fusion* **44** 451
- [145] Scott B. 1998 *Plasma Phys. Control. Fusion* **40** 823
- [146] Rettig C.L. *et al* 2001 *Phys. Plasmas* **8** 2232
- [147] Kotschenreuther M., Rewoldt G. and Tang W.M. 1995 *Comput. Phys. Commun.* **88** 128
- [148] Rhodes T.L. *et al* 2002 *Phys. Plasmas* **9** 2142
- [149] McKee G.R. *et al* 2001 *Nucl. Fusion* **41** 1235
- [150] Ross D.W. *et al* 2002 *Phys. Plasmas* **9** 177
- [151] McKee G.R. 2004 private communication, General Atomics
- [152] Xu X.Q. *et al* 1999 *J. Nucl. Mater.* **266–269** 993
- [153] Vershkov V.A. *et al* 2002 *Fusion Energy 2002: Proc. 19th Int. Conf. (Lyon, 2002)* (Vienna: IAEA) CD-ROM file EX/P3-04 and <http://www.iaea.org/programmes/rip/physics/fec2002/html/fec2002.htm>
- [154] Weiland J. and Nordman H. 1991 *Nucl. Fusion* **31** 390
- [155] Ossipenko M.V. and Tsaun S.V. 2001 *Plasma Phys. Rep.* **27** 1
- [156] Evensen H.T. *et al* 1998 *Nucl. Fusion* **38** 237
- [157] Colas L. *et al* 1998 *Nucl. Fusion* **38** 903
- [158] Entrop I. *et al* 2000 *Phys. Rev. Lett.* **84** 3606
- [159] Wong K.-L. *et al* 1997 *Phys. Lett.* **236** 339
- [160] Itoh K. *et al* 1994 *Plasma Phys. Control. Fusion* **36** 279
- [161] Rhodes T.L. *et al* 2004 *Fusion Energy 2004: Proc. 20th Int. Conf. (Vilamoura, 2004)* (Vienna: IAEA) CD-ROM file EX/P6-23 and <http://www-naweb.iaea.org/napc/physics/fec/fec2004/datasets/index.html>
- [162] Burrell K.H. 1999 *Phys. Plasmas* **6** 4418
- [163] Boedo J.A. *et al* 2002 *Nucl. Fusion* **42** 117
- [164] Ware A.S. *et al* 1998 *Phys. Plasmas* **5** 173
- [165] Zhang Y.Z. and Mahajan S.M. 1992 *Phys. Fluids B* **4** 1385
- [166] Budny R.V. *et al* 2002 *Plasma Phys. Control. Fusion* **44** 1215
- [167] Conway G.D. *et al* 2000 *Phys. Rev. Lett.* **84** 1463
- [168] Greenfield C.M. *et al* 1997 *Phys. Plasmas* **4** 1596
- [169] Greenfield C.M. *et al* 1999 *Nucl. Fusion* **39** 1723
- [170] McKee G.R. *et al* 2000 *Phys. Plasmas* **7** 1870
- [171] Murakami M. *et al* 2001 *Nucl. Fusion* **41** 317
- [172] Jackson G.L. *et al* 2002 *Plasma Phys. Control. Fusion* **44** 1893
- [173] Jakubowski M., Fonck R.J. and McKee G.R. 2002 *Phys. Rev. Lett.* **89** 265003
- [174] McKee G.R. *et al* 2003 *Phys. Plasmas* **10** 1712
- [175] Xu X.Q. *et al* 2002 *New J. Phys.* **4** 53.1
- [176] Mazurenko A. *et al* 2002 *Phys. Rev. Lett.* **89** 225004
- [177] Terry J.L. *et al* 2003 *Phys. Plasmas* **10** 1739
- [178] Hinton F.L. and Hazeltine R.D. 1976 *Rev. Mod. Phys.* **48** 239
- [179] Hirshman S.P. and Sigmar D.J. 1981 *Nucl. Fusion* **21** 1079
- [180] Shaing K.C., Hsu C.T. and Hazeltine R.D. 1994 *Phys. Plasmas* **1** 3365
- [181] Urano H. *et al* 2005 *Phys. Rev. Lett.* **95** 035003
- [182] Gates D. and NSTX National Research Team 2003 *Phys. Plasmas* **10** 1659
- [183] Wade M.R., Murakami M. and Politzer P.A. 2004 *Phys. Rev. Lett.* **92** 235005
- [184] Thomas D.M. *et al* 2004 *Phys. Rev. Lett.* **93** 065003
- [185] Houlberg W.A. *et al* 1997 *Phys. Plasmas* **4** 3230
- [186] Sauter O., Angioni C. and Lin-Liu Y.R. 1999 *Phys. Plasmas* **6** 2834
- [187] Sauter O., Angioni C. and Lin-Liu Y.R. 2002 *Phys. Plasmas* **9** 5140
- [188] Shaing K.C., Hazeltine R.D. and Zarnstorff M.C. 1997 *Phys. Plasmas* **4** 1375
- [189] Fujita T. *et al* 2001 *Phys. Rev. Lett.* **87** 245001
- [190] Hawkes N.C. *et al* 2001 *Phys. Rev. Lett.* **87** 115001
- [191] Baylor L.R. *et al* 2004 *Phys. Plasmas* **11** 3100
- [192] Severo J.H.F. *et al* 2004 *Phys. Plasmas* **11** 846
- [193] Rozhansky V. 2004 *Plasma Phys. Control. Fusion* **46** A1
- [194] Rozhansky V. *et al* 2002 *Nucl. Fusion* **42** 1110
- [195] Solomon W.M. *et al* 2004 *Fusion Energy 2004: Proc. 20th Int. Conf. (Vilamoura, 2004)* (Vienna: IAEA) CD-ROM file EX/P4-10 and <http://www-naweb.iaea.org/napc/physics/fec/fec2004/datasets/index.html>
- [196] Bell R.E. *et al* 1998 *Phys. Rev. Lett.* **81** 1429
- [197] Shaing K.C. *et al* 1999 *Phys. Rev. Lett.* **83** 3840
- [198] Shaing K.C. 1992 *Phys. Fluids B* **4** 290
- [199] Gormezano C. *et al* 2007 Progress in the ITER Physics Basis *Nucl. Fusion* **47** S285–S336
- [200] Doyle E.J. *et al* 2002 *Nucl. Fusion* **42** 333
- [201] Lao L.L. *et al* 1999 *Bull. Am. Phys. Soc.* **44** 77
- [202] Litaudon X. *et al* 2004 *Plasma Phys. Control. Fusion* **46** A19
- [203] Sips A.C.C. *et al* 2004 *Fusion Energy 2004: Proc. 20th Int. Conf. (Vilamoura, 2004)* (Vienna: IAEA) CD-ROM file IT/P3-36 and <http://www-naweb.iaea.org/napc/physics/fec/fec2004/datasets/index.html>
- [204] Politzer P.A. *et al* 2004 *Fusion Energy 2004: Proc. 20th Int. Conf. (Vilamoura, 2004)* (Vienna: IAEA) CD-ROM file EX/P2-7 and <http://www-naweb.iaea.org/napc/physics/fec/fec2004/datasets/index.html>
- [205] Dux R. *et al* 2004 *Nucl. Fusion* **44** 260
- [206] Stober J. *et al* 2003 *Nucl. Fusion* **43** 1265
- [207] Doyle E.J. *et al* 2002 *Fusion Energy 2002: Proc. 19th Int. Conf. (Lyon, 2002)* (Vienna: IAEA) CD-ROM file EX/C3-2 and <http://www.iaea.org/programmes/rip/physics/fec2002/html/fec2002.htm>

- [208] Takenaga H. *et al* 2003 *Nucl. Fusion* **43** 1235
- [209] Synakowski E.J. *et al* 1999 *Nucl. Fusion* **39** 1733
- [210] Sakamoto Y. *et al* 2004 *Nucl. Fusion* **44** 876
- [211] Synakowski E.J. *et al* 1997 *Phys. Rev. Lett.* **78** 2972
- [212] Sakamoto Y. *et al* 2001 *Nucl. Fusion* **41** 865
- [213] Tokar M.Z. *et al* 2000 *Phys. Rev. Lett.* **84** 895
- [214] McKee G. *et al* 2000 *Phys. Rev. Lett.* **84** 1922
- [215] Tokar M.Z. *et al* 2002 *Plasma Phys. Control. Fusion* **44** 1903
- [216] Synakowski E.J. 1998 *Plasma Phys. Control. Fusion* **40** 581
- [217] Turnbull A.D. *et al* 1995 *Phys. Rev. Lett.* **74** 718
- [218] Burrell K.H. 1997 *Phys. Plasmas* **4** 1499
- [219] Ida K. *et al* 2002 *Phys. Rev. Lett.* **88** 015002
- [220] Petty C.C. *et al* 2002 *Phys. Plasmas* **9** 128
- [221] Balet B. *et al* 1995 *Europhysics Conference Abstracts: Proc. 22nd EPS Conf. on Controlled Fusion and Plasma Physics (Bournemouth, 1995)* (Geneva: European Physical Society) vol 19C part I (ECA) p 9
- [222] Cordey J.G. *et al* 1996 *Plasma Phys. Control. Fusion* **38** A67
- [223] Perkins F.W. *et al* 1993 *Phys. Fluids B* **5** 477
- [224] Scott S.D. *et al* 1993 *Plasma Physics and Controlled Nuclear Fusion Research 1992: Proc. 14th Int. Conf. (Würzburg, 1992)* (Vienna: IAEA) vol 3 p 427
- [225] Petty C.C. *et al* 1998 *Nucl. Fusion* **38** 1183
- [226] Christiansen J.P. *et al* 1997 *Europhysics Conference Abstracts: Proc. 24th EPS Conf. on Controlled Fusion and Plasma Physics (Berchtesgaden, 1997)* (Geneva: European Physical Society) vol 21A part I (ECA) p 89
- [227] Petty C.C. and Luce T.C. 1999 *Phys. Plasmas* **6** 909
- [228] JET Team (presented by J.G. Cordey) 1997 *Fusion Energy 1996: Proc. 16th Int. Conf. (Montreal, 1996)* (Vienna: IAEA) vol 1 p 603
- [229] Greenwald M. *et al* 1998 *Plasma Phys. Control. Fusion* **40** 789
- [230] Shirai H. *et al* 2000 *Plasma Phys. Control. Fusion* **42** 1193
- [231] Petty C.C. *et al* 1998 *Phys. Plasmas* **5** 1695
- [232] Petty C.C. *et al* 2000 *Plasma Phys. Control. Fusion* **42** B75
- [233] Petty C.C. *et al* 1999 *Phys. Rev. Lett.* **83** 3661
- [234] ITER 1D Modelling Working Group: *et al* 2000 *Nucl. Fusion* **40** 1955
- [235] Mikkelsen D.R. *et al* 1999 *Fusion Energy 1998: Proc. 17th Int. Conf. (Yokohama, 1998)* (Vienna: IAEA) CD-ROM file IAEA-F1-CN-69/ITERP1/08 and www.iaea.org/programmes/ripc/physics/start.htm
- [236] Kinsey J.E. *et al* 2003 *Nucl. Fusion* **43** 1845
- [237] Kotschenreuther M. *et al* 1995 *Phys. Plasmas* **2** 2381
- [238] Bateman G. *et al* 1998 *Phys. Plasmas* **5** 1793
- [239] Kinsey J.E. and Bateman G. 1996 *Phys. Plasmas* **3** 3344
- [240] Dimits A.M. *et al* 2000 *Fusion Energy 2000: Proc. 18th Int. Conf. (Sorrento, 2000)* (Vienna: IAEA) CD-ROM file THP1/03 and <http://www.iaea.org/programmes/ripc/physics/fec2000/html/fec2000.htm>
- [241] Kinsey J.E., Waltz R.E. and Candy J. 2005 *Phys. Plasmas* **12** 062302
- [242] Greenfield C.M. *et al* 2001 *Phys. Rev. Lett.* **86** 4544
- [243] Strait E.J. *et al* 1995 *Phys. Rev. Lett.* **75** 4421
- [244] Levinton F.M. *et al* 1995 *Phys. Rev. Lett.* **75** 4417
- [245] Synakowski E.J. *et al* 1997 *Phys. Plasmas* **4** 1736
- [246] Challis C.D. *et al* 2001 *Plasma Phys. Control. Fusion* **43** 861
- [247] Gormezano C. *et al* 1998 *Phys. Rev. Lett.* **80** 5544
- [248] Gruber O. *et al* 2001 *Nucl. Fusion* **41** 1369
- [249] Wolf R.C. *et al* 2003 *Plasma Phys. Control. Fusion* **45** 1757
- [250] Koide Y. *et al* 1994 *Phys. Rev. Lett.* **72** 3662
- [251] Shirai H. *et al* 1999 *Nucl. Fusion* **39** 1713
- [252] Beer M. *et al* 1997 *Phys. Plasmas* **4** 1792
- [253] Kinsey J.E., Staebler G.M. and Waltz R.E. 2002 *Phys. Plasmas* **9** 1676
- [254] Bourdelle C. *et al* 2003 *Phys. Plasmas* **10** 2881
- [255] Gormezano C. 1999 *Plasma Phys. Control. Fusion* **41** B367
- [256] Challis C.D. *et al* 2002 *Plasma Phys. Control. Fusion* **44** 1031
- [257] Fujita T. *et al* 1997 *Phys. Rev. Lett.* **78** 2377
- [258] Litaudon X. *et al* 1996 *Plasma Phys. Control. Fusion* **38** 1603
- [259] Koide Y. 1997 *Phys. Plasmas* **4** 1623
- [260] Doyle E.J. *et al* 2000 *Plasma Phys. Control. Fusion* **42** A237
- [261] Burrell K.H. and DIII-D Team 2003 *Nucl. Fusion* **43** 1555
- [262] Kinsey J.E. *et al* 2005 *Nucl. Fusion* **45** 450
- [263] Fukuda T. and International ITB Database Working Group 2001 *Europhysics Conference Abstracts: Proc. 28th EPS Conf. on Controlled Fusion and Plasma Physics (Madeira, 2001)* (Geneva: European Physical Society) vol 25A (ECA) p 1349
- [264] Wade M.R. *et al* 2003 *Nucl. Fusion* **43** 634
- [265] Luce T.C. *et al* 2003 *Nucl. Fusion* **43** 321
- [266] DeBoo J.C. *et al* 1999 *Nucl. Fusion* **39** 1935
- [267] Kinsey J.E., Waltz R.E. and DeBoo J.C. 1999 *Phys. Plasmas* **6** 1865
- [268] Gentle K.W. *et al* 1995 *Phys. Rev. Lett.* **74** 3620
- [269] Kissick M.W. *et al* 1996 *Nucl. Fusion* **36** 1691
- [270] Ryter F. *et al* 2000 *Nucl. Fusion* **40** 1917
- [271] Galli P. *et al* 1999 *Nucl. Fusion* **39** 1355
- [272] Kubo H. *et al* 2001 *Nucl. Fusion* **41** 227
- [273] Stober J. *et al* 2000 *Plasma Phys. Control. Fusion* **42** A211
- [274] Suttrop W. *et al* 1997 *Plasma Phys. Control. Fusion* **39** 2051
- [275] Tardini G. *et al* 2002 *Nucl. Fusion* **42** 258
- [276] Baker D.R. *et al* 2001 *Phys. Plasmas* **8** 4128
- [277] Mikkelsen D.R. *et al* 2003 *Nucl. Fusion* **43** 30
- [278] Nordman H., Weiland J. and Jarmen A. 1990 *Nucl. Fusion* **30** 983
- [279] Mukhovatov V. *et al* 2003 *Nucl. Fusion* **43** 942
- [280] Onjun T. *et al* 2001 *Phys. Plasmas* **8** 975
- [281] Garbet X. and Waltz R.E. 1996 *Phys. Plasmas* **3** 1898
- [282] Neu R. *et al* 2000 *Fusion Energy 2000: Proc. 18th Int. Conf. (Sorrento, 2000)* (Vienna: IAEA) CD-ROM file EXP5/33 and <http://www.iaea.org/programmes/ripc/physics/fec2000/html/fec2000.htm>
- [283] Mantica P. *et al* 2002 *Plasma Phys. Control. Fusion* **44** 2185
- [284] Synakowski E.J. *et al* 2003 *Nucl. Fusion* **43** 1653
- [285] Goldston R.J. *et al* 1987 *Plasma Physics and Controlled Nuclear Fusion Research: Proc. 11th Int. Conf. (Kyoto, 1986)* (Vienna: IAEA) vol 1 p 75
- [286] Alikae V.V. *et al* 1987 *Plasma Physics and Controlled Nuclear Fusion Research 1986: Proc. 11th Int. Conf. (Kyoto, 1986)* (Vienna: IAEA) vol 1 p 111
- [287] Wagner F. *et al* 1986 *Phys. Rev. Lett.* **56** 2187
- [288] Callen J.D. *et al* 1987 *Nucl. Fusion* **27** 1857
- [289] Taylor G. *et al* 1989 *Nucl. Fusion* **29** 3
- [290] Luce T.C., Petty C.C. and de Haas J.C.M. 1992 *Phys. Rev. Lett.* **68** 52
- [291] Petty C.C. and Luce T.C. 1994 *Nucl. Fusion* **34** 121
- [292] Gohil P., Burrell K.H. and Osborne T.H. 1998 *Nucl. Fusion* **38** 425
- [293] Horton L.D. *et al* 1999 *Plasma Phys. Control. Fusion* **41** B329
- [294] Urano H. *et al* 2002 *Nucl. Fusion* **42** 76
- [295] Watkins M.L. 2002 *Plasma Phys. Control. Fusion* **44** B173
- [296] Coppi B. 1980 *Comm. on Plasma Phys. Control. Fusion* **5** 261
- [297] Ryter F. *et al* 2001 *Plasma Phys. Control. Fusion* **43** A323
- [298] Ryter F. *et al* 2001 *Phys. Rev. Lett.* **86** 2325
- [299] Ryter F. *et al* 2001 *Phys. Rev. Lett.* **86** 5498
- [300] Hoang G.T. *et al* 2001 *Phys. Rev. Lett.* **87** 125001
- [301] Suttrop W. *et al* 2001 *Europhysics Conference Abstracts: Proc. 28th EPS Conf. on Controlled Fusion and Plasma Physics (Madeira, 2001)* (Geneva: European Physical Society) vol 25A (ECA) p 989
- [302] Jacchia A. *et al* 2002 *Nucl. Fusion* **42** 1116
- [303] Cirant S. *et al* 2003 *Nucl. Fusion* **43** 1384
- [304] Ryter F.R. *et al* 2005 *Phys. Rev. Lett.* **95** 085001
- [305] Waltz R.E., DeBoo J.C. and Osborne T.H. 1992 *Nucl. Fusion* **32** 1051
- [306] Jenko F. 2000 *Phys. Plasmas* **7** 514
- [307] Jenko F., Dorland W. and Hammett G.W. 2001 *Phys. Plasmas* **8** 4096

- [308] Peeters A.G. *et al* 2005 *Phys. Plasmas* **12** 022505
- [309] Baker D.R. *et al* 2003 *Phys. Plasmas* **10** 4419
- [310] Imbeaux F., Ryter F. and Garbet X. 2001 *Plasma Phys. Control. Fusion* **43** 1503
- [311] Leuterer F. *et al* 2003 *Nucl. Fusion* **43** 1329
- [312] Ryter F. *et al* 2003 *Nucl. Fusion* **43** 1396
- [313] DeBoo J.C. *et al* 2005 *Nucl. Fusion* **45** 494
- [314] Pochelon A. *et al* 2004 *Fusion Energy 2004: Proc. 20th Int. Conf. (Vilamoura, 2004)* (Vienna: IAEA) CD-ROM file EX/9-1 and <http://www.naweb.iaea.org/naweb/physics/fec/fec2004/datasets/index.html>
- [315] Lopes Cardozo N.J. 1995 *Plasma Phys. Control. Fusion* **37** 799
- [316] Callen J.D. and Kissick M.W. 1997 *Plasma Phys. Control. Fusion* **39** B173
- [317] Lopes Cardozo N.J. *et al* 1990 *Plasma Phys. Control. Fusion* **32** 983
- [318] Jacchia A. *et al* 2003 *Europhysics Conference Abstracts: Proc. 30th EPS Conf. on Controlled Fusion and Plasma Physics (St Petersburg, 2003)* (Geneva: European Physical Society) vol 27A (ECA) paper P-1.117
- [319] Romanelli M., Bourdelle C. and Dorland W. 2004 *Phys. Plasmas* **11** 3845
- [320] Kinsey J.E. *et al* 2002 *Fusion Energy 2002: Proc. 19th Int. Conf. (Lyon, 2002)* (Vienna: IAEA) CD-ROM file TH/P1-09 and <http://www.iaea.org/programmes/ripc/physics/fec2002/html/fec2002.htm>
- [321] Manini A. *et al* 2004 *Plasma Phys. Control. Fusion* **46** 1723
- [322] Gentle K.W., Austin M.E. and Phillips P.E. 2003 *Phys. Rev. Lett.* **91** 255001
- [323] Barbato E. 2001 *Plasma Phys. Control. Fusion* **43** A287
- [324] Günter S. *et al* 2000 *Phys. Rev. Lett.* **84** 3097
- [325] Wolf R.C. *et al* 2001 *Nucl. Fusion* **41** 1259
- [326] Leuterer F. *et al* 2003 *Nucl. Fusion* **43** 744
- [327] Pericoli Ridolfini V. *et al* 2003 *Nucl. Fusion* **43** 469
- [328] Hogewij G.M.D. *et al* 2002 *Plasma Phys. Control. Fusion* **44** 1155
- [329] Mailloux J. *et al* 2002 *Phys. Plasmas* **9** 2156
- [330] Baranov Y.F. *et al* 2004 *Plasma Phys. Control. Fusion* **46** 1181
- [331] Ide S. *et al* 2000 *Nucl. Fusion* **40** 445
- [332] Ide S. *et al* 2004 *Nucl. Fusion* **44** 87
- [333] Fujita T. *et al* 2004 *Plasma Phys. Control. Fusion* **46** A35
- [334] Hoang G.T. *et al* 2000 *Nucl. Fusion* **40** 913
- [335] Litaudon X. *et al* 2001 *Plasma Phys. Control. Fusion* **43** 677
- [336] Pietrzyk Z.A. *et al* 2000 *Phys. Plasmas* **7** 2909
- [337] Sauter O. *et al* 2001 *Phys. Plasmas* **8** 2199
- [338] Henderson M.A. *et al* 2003 *Phys. Plasmas* **10** 1796
- [339] Henderson M.A. *et al* 2004 *Plasma Phys. Control. Fusion* **46** A275
- [340] Razumova K.A. *et al* 2000 *Plasma Phys. Control. Fusion* **42** 973
- [341] Sauter O. *et al* 2005 *Phys. Rev. Lett.* **94** 105002
- [342] Conway G.D. *et al* 2002 *Plasma Phys. Control. Fusion* **44** 1167
- [343] Fourment C. *et al* 2003 *Plasma Phys. Control. Fusion* **45** 233
- [344] Ide S. *et al* 2002 *Plasma Phys. Control. Fusion* **44** A137
- [345] Takenaga H. *et al* 1999 *Nucl. Fusion* **39** 1917
- [346] Takenaga H., Mahdavi M.A. and Baker D.R. 2001 *Phys. Plasmas* **8** 1607
- [347] Baker D.R. *et al* 1998 *Nucl. Fusion* **38** 485
- [348] Efthimion P.C. *et al* 1998 *Phys. Plasmas* **5** 1832
- [349] JET Team (prepared by K.-D. Zastrow) 1999 *Nucl. Fusion* **39** 1891
- [350] Stork D. *et al* 2004 *Fusion Energy 2004: Proc. 20th Int. Conf. (Vilamoura, 2004)* (Vienna: IAEA) CD-ROM file OV/4-1 and <http://www.naweb.iaea.org/naweb/physics/fec/fec2004/datasets/index.html>
- [351] McDonald D.C. *et al* 2004 *Fusion Energy 2004: Proc. 20th Int. Conf. (Vilamoura, 2004)* (Vienna: IAEA) CD-ROM file EX/6-6 and <http://www.naweb.iaea.org/naweb/physics/fec/fec2004/datasets/index.html>
- [352] Zastrow K.-D. *et al* 2004 *Plasma Phys. Control. Fusion* **46** B255
- [353] Stober J. *et al* 2002 *Plasma Phys. Control. Fusion* **44** A159
- [354] Baker D.R. *et al* 2000 *Nucl. Fusion* **40** 1003
- [355] Valovic M. *et al* 2002 *Plasma Phys. Control. Fusion* **44** 1911
- [356] Garzotti L. *et al* 2003 *Nucl. Fusion* **43** 1829
- [357] Hoang G.T. *et al* 2003 *Phys. Rev. Lett.* **90** 155002
- [358] Zabolotsky A., Weisen H. and TCV Team 2003 *Plasma Phys. Control. Fusion* **45** 735
- [359] Angioni C. *et al* 2003 *Phys. Rev. Lett.* **90** 205003
- [360] Angioni C. *et al* 2003 *Phys. Plasmas* **10** 3225
- [361] Weisen H. *et al* 2005 *Nucl. Fusion* **45** L1
- [362] Becker G. 2004 *Nucl. Fusion* **44** 933
- [363] Baker D.R. and Rosenbluth M.N. 1998 *Phys. Plasmas* **5** 2936
- [364] Lorate A. *et al* 2007 *Progress in the ITER Physics Basis* **47** S203–S263
- [365] Mahdavi M.A. *et al* 2002 *Nucl. Fusion* **42** 52
- [366] Takenaga H. *et al* 2004 *Fusion Energy 2004: Proc. 20th Int. Conf. (Vilamoura, 2004)* (Vienna: IAEA) CD-ROM file EX/6-1 and <http://www.naweb.iaea.org/naweb/physics/fec/fec2004/datasets/index.html>
- [367] Lang P.T. *et al* 2000 *Nucl. Fusion* **40** 245
- [368] Messiaen A. *et al* 1996 *Phys. Rev. Lett.* **77** 2487
- [369] Jackson G.L. *et al* 2002 *Nucl. Fusion* **42** 28
- [370] Ongena J. *et al* 2004 *Nucl. Fusion* **44** 124
- [371] Tokar M.Z. 2003 *Plasma Phys. Control. Fusion* **45** 1323
- [372] Polevoi A.R. *et al* 2002 *J. Plasma Fusion Res. Ser.* **5** 82
- [373] Pereverzev G.V. *et al* 2005 *Nucl. Fusion* **45** 221
- [374] Yankov V.V. 1994 *JETP Lett.* **60** 171
- [375] Isichenko M.B., Gruzinov A.V. and Diamond P.H. 1996 *Phys. Rev. Lett.* **74** 4436
- [376] Weisen H., Furno I. and TCV Team 2001 *Nucl. Fusion* **41** 1227
- [377] Gohil P. *et al* 2003 *Plasma Phys. Control. Fusion* **45** 601
- [378] Rice J.E. *et al* 2002 *Nucl. Fusion* **42** 510
- [379] Ossipenko M.V. and T-10 team 2003 *Nucl. Fusion* **43** 1641
- [380] Chen H. *et al* 2001 *Plasma Phys. Control. Fusion* **43** 1
- [381] Baker D.R. *et al* 2000 *Fusion Energy 2000: Proc. 18th Int. Conf. (Sorrento, 2000)* (Vienna: IAEA) CD-ROM file EXP5/03 and <http://www.iaea.org/programmes/ripc/physics/fec2000/html/fec2000.htm>
- [382] Dux R. *et al* 1999 *Nucl. Fusion* **39** 1509
- [383] Wade M.R., Houlberg W.A. and Baylor L.R. 2000 *Phys. Rev. Lett.* **84** 282
- [384] Houlberg W.A. and Baylor L.R. 1998 *Fusion Technol.* **34** 591
- [385] Efthimion P.C. *et al* 1999 *Nucl. Fusion* **39** 1905
- [386] Takenaga H. and JT-60 Team 2001 *Phys. Plasmas* **8** 2217
- [387] Chen H. *et al* 2001 *Nucl. Fusion* **41** 31
- [388] West W.P. *et al* 2002 *Phys. Plasmas* **9** 1970
- [389] Fujita T. and JT-60 Team 2003 *Nucl. Fusion* **43** 1527
- [390] Wade M.R. *et al* 2001 *J. Nucl. Mater.* **290–293** 773
- [391] Puiatti M.E. *et al* 2002 *Plasma Phys. Control. Fusion* **44** 1863
- [392] Scott S.D. *et al* 1990 *Phys. Rev. Lett.* **64** 531
- [393] Nishijima D. *et al* 2005 *Plasma Phys. Control. Fusion* **47** 89
- [394] Staebler G.M., Waltz R.E. and Wiley J.C. 1997 *Nucl. Fusion* **37** 287
- [395] Staebler G.M., Kinsey J.E. and Waltz R.E. 2004 *Plasma Phys. Control. Fusion* **46** A265
- [396] Parail V.V. *et al* 1999 *Nucl. Fusion* **39** 429
- [397] Tala T.J.J. *et al* 2001 *Plasma Phys. Control. Fusion* **43** 507
- [398] Rice J.E. *et al* 2001 *Nucl. Fusion* **41** 277
- [399] Meyer H. *et al* 2004 *Plasma Phys. Control. Fusion* **46** A291
- [400] Hutchinson I.H. 2000 *Phys. Rev. Lett.* **84** 3330
- [401] Rice J.E. *et al* 1998 *Nucl. Fusion* **38** 75
- [402] Rice J.E. *et al* 1999 *Nucl. Fusion* **39** 1175
- [403] Field A.R. *et al* 2004 *Plasma Phys. Control. Fusion* **46** 981
- [404] Field A.R. *et al* 2003 *Europhysics Conference Abstracts: Proc. 30th EPS Conf. on Controlled Fusion and Plasma Physics (St Petersburg, 2003)* (Geneva: European Physical Society) vol 27A (ECA) paper P-2.148
- [405] Eriksson L.-G., Righi E. and Zastrow K.-D. 1997 *Plasma Phys. Control. Fusion* **39** 27

- [406] Noterdaeme J.-M. *et al* 2003 *Nucl. Fusion* **43** 274
- [407] Assas S. *et al* 2003 *Europhysics Conference Abstracts: Proc. 30th EPS Conf. on Controlled Fusion and Plasma Physics (St Petersburg, 2003)* (Geneva: European Physical Society) vol 27A (ECA) paper P-1.138
- [408] Eriksson L.-G., Hoang G.T. and Bergeaud V. 2001 *Nucl. Fusion* **41** 91
- [409] DeGrassie J. *et al* 2004 *Phys. Plasmas* **11** 4323
- [410] Claassen H.A. *et al* 2000 *Phys. Plasmas* **7** 3699
- [411] Rogister A.L. 1999 *Phys. Plasmas* **6** 200
- [412] Fülöp T., Helander P. and Catto P.J. 2002 *Phys. Rev. Lett.* **89** 225003
- [413] Helander P., Fülöp T. and Catto P.J. 2003 *Phys. Plasmas* **10** 4396
- [414] Rozhansky V. *et al* 2005 *J. Nucl. Mater.* **337–339** 291
- [415] Coppi B. 2002 *Nucl. Fusion* **42** 1
- [416] Shaing K.C. 2001 *Phys. Rev. Lett.* **86** 640
- [417] Chang C.S. *et al* 1999 *Phys. Plasmas* **6** 1969
- [418] Perkins F.W. *et al* 2001 *Phys. Plasmas* **8** 2181
- [419] Chan V.S., Chiu S.C. and Omelchenko Y.A. 2002 *Phys. Plasmas* **9** 501
- [420] Eriksson L.-G. and Porcelli F. 2002 *Nucl. Fusion* **42** 959
- [421] Rice J.E. *et al* 2004 *Nucl. Fusion* **44** 379
- [422] Lee W.D. *et al* 2003 *Phys. Rev. Lett.* **91** 205003
- [423] LaBombard B. *et al* 2004 *Nucl. Fusion* **44** 1047
- [424] Rice J.E. *et al* 2005 *Nucl. Fusion* **45** 251
- [425] Rice J.E. *et al* 2003 *Nucl. Fusion* **43** 781
- [426] Connor J.W. 1988 *Plasma Phys. Control. Fusion* **30** 619
- [427] Waltz R.E., DeBoo J.C. and Rosenbluth M.N. 1990 *Phys. Rev. Lett.* **65** 2390
- [428] Buckingham E. 1914 *Phys. Rev.* **4** 345
- [429] Luce T.C. *et al* 2002 *Nucl. Fusion* **42** 1193
- [430] Petty C.C. *et al* 2004 *Plasma Phys. Control. Fusion* **46** A207
- [431] Greenwald M. 2002 *Plasma Phys. Control. Fusion* **44** R27
- [432] Petty C.C. *et al* 2004 *Phys. Plasmas* **11** 2514
- [433] McDonald D.C. *et al* 2004 *Plasma Phys. Control. Fusion* **46** A215
- [434] Cordey J.G. *et al* 2005 *Nucl. Fusion* **45** 1078
- [435] Batha S.H. *et al* 1997 *Europhysics Conference Abstracts: Proc. 24th EPS Conf. on Controlled Fusion and Plasma Physics (Berchtesgaden, 1997)* (Geneva: European Physical Society) vol 21A part III (ECA) p 1057
- [436] Cordey J.G. *et al* 2000 *Plasma Phys. Control. Fusion* **42** A127
- [437] Luce T.C., Petty C.C. and Kinsey J.E. 2001 *Europhysics Conference Abstracts: Proc. 28th EPS Conf. on Controlled Fusion and Plasma Physics (Madeira, 2001)* (Geneva: European Physical Society) vol 25A (ECA) p 1377
- [438] Luce T.C., Petty C.C. and Cordey J.G. 2007 Application of dimensionless parameter scaling techniques to the design and interpretation of magnetic fusion experiments *Plasma Phys. Control. Fusion* submitted
- [439] Bourdelle C. *et al* 2005 *Nucl. Fusion* **45** 110
- [440] Ide S. *et al* 2002 *Plasma Phys. Control. Fusion* **44** L63
- [441] Joffrin E. *et al* 2002 *Plasma Phys. Control. Fusion* **44** 1739
- [442] Wolf R.C. *et al* 1999 *Plasma Phys. Control. Fusion* **41** B93
- [443] Quigley E.D. *et al* 2004 *Nucl. Fusion* **44** 1189
- [444] Fujita T. *et al* 1999 *Nucl. Fusion* **39** 1627
- [445] Huysmans G.T.A. *et al* 2001 *Phys. Rev. Lett.* **87** 245002
- [446] Breslau J.A., Jardin S.C. and Park W. 2003 *Phys. Plasmas* **10** 1665
- [447] Fujita T. *et al* 2004 *Proc. 20th Int. Conf. on Fusion Energy 2004: (Vilamoura, 2004)* (Vienna: IAEA) CD-ROM file EX/P4-3 and <http://www-naweb.iaea.org/napc/physics/fec/fec2004/datasets/index.html>
- [448] Fujita T. 2002 *Plasma Phys. Control. Fusion* **44** A19
- [449] Fujita T. *et al* 2001 *Phys. Rev. Lett.* **87** 085001
- [450] Murakami M. *et al* 2003 *Phys. Rev. Lett.* **90** 255001
- [451] Joffrin E. *et al* 2002 *Nucl. Fusion* **42** 235
- [452] Sips A.C.C. *et al* 1998 *Plasma Phys. Control. Fusion* **40** 1171
- [453] Keilhacker M. *et al* 1999 *Nucl. Fusion* **39** 209
- [454] Crisanti F. *et al* 2002 *Phys. Rev. Lett.* **88** 145004
- [455] Litaudon X. *et al* 2002 *Plasma Phys. Control. Fusion* **44** 1057
- [456] Kamada Y. *et al* 1999 *Nucl. Fusion* **39** 1845
- [457] Isayama A. *et al* 2001 *Nucl. Fusion* **41** 761
- [458] Rice B.W. *et al* 1999 *Nucl. Fusion* **39** 1855
- [459] Wade M.R. *et al* 2001 *Phys. Plasmas* **8** 2208
- [460] Luce T.C. *et al* 2001 *Nucl. Fusion* **41** 1585
- [461] Waltz R.E., Dewar R.L. and Garbet X. 1998 *Phys. Plasmas* **5** 1784
- [462] Greenfield C.M. *et al* 2004 *Plasma Phys. Control. Fusion* **46** B213
- [463] Murakami M. *et al* 2004 *Proc. 20th Int. Conf. on Fusion Energy 2004: (Vilamoura, 2004)* (Vienna: IAEA) CD-ROM file EX/1-2 and <http://www-naweb.iaea.org/napc/physics/fec/fec2004/datasets/index.html>
- [464] JET Team (prepared by Gormezano C.) 1999 *Nucl. Fusion* **39** 1875
- [465] JET Team (prepared by Söldner F.X.) 1999 *Nucl. Fusion* **39** 1883
- [466] Burrell K.H. *et al* 2001 *Phys. Plasmas* **8** 2153
- [467] Burrell K.H. *et al* 2005 *Phys. Plasmas* **12** 056121
- [468] Sips A.C.C. *et al* 2002 *Plasma Phys. Control. Fusion* **44** B69
- [469] Wade M.R. *et al* 2004 *Proc. 20th Int. Conf. on Fusion Energy 2004: (Vilamoura, 2004)* (Vienna: IAEA) CD-ROM file EX/4-1 and <http://www-naweb.iaea.org/napc/physics/fec/fec2004/datasets/index.html>
- [470] Luce T.C. *et al* 2004 *Phys. Plasmas* **11** 2627
- [471] Gruber O. *et al* 1999 *Phys. Rev. Lett.* **83** 1787
- [472] Peeters A.G. *et al* 2002 *Nucl. Fusion* **42** 1376
- [473] Sips A.C.C. *et al* 2002 *Plasma Phys. Control. Fusion* **44** A151
- [474] Na Y.-S. *et al* 2002 *Plasma Phys. Control. Fusion* **44** 1285
- [475] Staebler A. *et al* 2004 *Proc. 20th Int. Conf. on Fusion Energy 2004: (Vilamoura, 2004)* (Vienna: IAEA) CD-ROM file EX/4-5 and <http://www-naweb.iaea.org/napc/physics/fec/fec2004/datasets/index.html>
- [476] Joffrin E. *et al* 2002 *Plasma Phys. Control. Fusion* **44** 1203
- [477] Sips A.C.C. *et al* 2003 *Europhysics Conference Abstracts: Proc. 30th EPS Conf. on Controlled Fusion and Plasma Physics (St Petersburg, 2003)* (Geneva: European Physical Society) vol 27A (ECA) paper O-1.3A
- [478] Joffrin E.H. *et al* 2004 *Proc. 20th Int. Conf. on Fusion Energy 2004: (Vilamoura, 2004)* (Vienna: IAEA) CD-ROM file EX/4-2 and <http://www-naweb.iaea.org/napc/physics/fec/fec2004/datasets/index.html>
- [479] Isayama A. *et al* 2003 *Nucl. Fusion* **43** 1272
- [480] Ide S. and JT-60 Team 2004 *Proc. 20th Int. Conf. on Fusion Energy 2004: (Vilamoura, 2004)* (Vienna: IAEA) CD-ROM file OV/1-1 and <http://www-naweb.iaea.org/napc/physics/fec/fec2004/datasets/index.html>
- [481] Isayama A. and JT-60 Team 2005 *Phys. Plasmas* **12** 056117
- [482] Suzuki T. *et al* 2004 *Proc. 20th Int. Conf. on Fusion Energy 2004: (Vilamoura, 2004)* (Vienna: IAEA) CD-ROM file EX/1-3 and <http://www-naweb.iaea.org/napc/physics/fec/fec2004/datasets/index.html>
- [483] Guo S.C. and Romanelli F. 1993 *Phys. Fluids B* **5** 520
- [484] Crisanti F. *et al* 2004 *Fusion Energy 2004: Proc. 20th Int. Conf. (Vilamoura, 2004)* (Vienna: IAEA) CD-ROM file EX/P2-1 and <http://www-naweb.iaea.org/napc/physics/fec/fec2004/datasets/index.html>
- [485] Gormezano C. *et al* 2004 *Plasma Phys. Control. Fusion* **46** B435
- [486] Sips A.C.C. *et al* 2002 *Plasma Phys. Control. Fusion* **44** A391
- [487] Tuccillo A.A. *et al* 2004 *Proc. 20th Int. Conf. on Fusion Energy 2004: (Vilamoura, 2004)* (Vienna: IAEA) CD-ROM file EX/1-1 and <http://www-naweb.iaea.org/napc/physics/fec/fec2004/datasets/index.html>
- [488] Fujita T. and JT-60 Team 1997 *Plasma Phys. Control. Fusion* **39** B75
- [489] Kamada Y. and JT-60 Team 2001 *Nucl. Fusion* **41** 1311
- [490] Suttrop W. 2000 *Plasma Phys. Control. Fusion* **42** A1
- [491] Hubbard A.E. 2000 *Plasma Phys. Control. Fusion* **42** A15

- [492] Horton L.D. 2000 *Plasma Phys. Control. Fusion* **42** A37
- [493] Lao L.L. 2000 *Plasma Phys. Control. Fusion* **42** A51
- [494] Saibene G. *et al* 1999 *Nucl. Fusion* **39** 1133
- [495] Takizuka T. 1998 *Plasma Phys. Control. Fusion* **40** 851
- [496] Kamada Y. *et al* 1997 *Proc. 16th Int. Conf. on Fusion Energy 1996: (Montreal, 1996)* (Vienna: IAEA) vol 1 p 247
- [497] Saibene G. *et al* 2002 *Plasma Phys. Control. Fusion* **44** 1769
- [498] Snyder P.B. and Wilson H.R. 2003 *Plasma Phys. Control. Fusion* **45** 1671
- [499] Urano H. *et al* 2002 *Plasma Phys. Control. Fusion* **44** 11
- [500] Sartori R. *et al* 2004 *Proc. 20th Int. Conf. on Fusion Energy 2004: (Vilamoura, 2004)* (Vienna: IAEA) CD-ROM file EX/6-3 and <http://www.naweb.iaea.org/naweb/physics/fec/fec2004/datasets/index.html>
- [501] Kamada Y. *et al* 2002 *Plasma Phys. Control. Fusion* **44** A279
- [502] Lang P.T. *et al* 2002 *Plasma Phys. Control. Fusion* **44** 1919
- [503] Sartori R. *et al* 2002 *Plasma Phys. Control. Fusion* **44** 1801
- [504] Borrass K., Schneider R. and Farengo R. 1997 *Nucl. Fusion* **37** 523
- [505] Borrass K., Lingertat J. and Schneider R. 1998 *Contrib. Plasma Phys.* **38** 130
- [506] Coster D.P. *et al* 1999 *J. Nucl. Mater.* **266–269** 804
- [507] Reiter D. 1992 *J. Nucl. Mater.* **196–198** 80
- [508] Schneider R. *et al* 1992 *J. Nucl. Mater.* **196–198** 810
- [509] Borrass K. *et al* 2001 *Europhysics Conference Abstracts: Proc. 28th EPS Conf. on Controlled Fusion and Plasma Physics (Madeira, 2001)* (Geneva: European Physical Society) vol 25A (ECA) p 501
- [510] Borrass K. *et al* 2004 *Nucl. Fusion* **44** 752
- [511] Chankin A.V., Itami K. and Asakura N. 2002 *Plasma Phys. Control. Fusion* **44** A399
- [512] Maingi R. *et al* 1999 *J. Nucl. Mater.* **266–269** 598
- [513] Mahdavi M.A. *et al* 2003 *Phys. Plasmas* **10** 3984
- [514] Kukushkin A.S. *et al* 2001 *Europhysics Conference Abstracts: Proc. 28th EPS Conf. on Controlled Fusion and Plasma Physics (Madeira, 2001)* (Geneva: European Physical Society) vol 25A (ECA) p 2113
- [515] Kukushkin A.S. and Pacher H.D. 2002 *Plasma Phys. Control. Fusion* **44** 931
- [516] Pacher G.W. *et al* 2004 *Plasma Phys. Control. Fusion* **46** A257
- [517] LaBombard B. *et al* 2002 *Proc. 19th Int. Conf. on Fusion Energy 2002: (Lyon, 2002)* (Vienna: IAEA) CD-ROM file EX/D2-1 and <http://www.iaea.org/programmes/ripc/physics/fec2002/html/fec2002.htm>
- [518] Myra J.R. *et al* 2002 *Europhysics Conference Abstracts: Proc. 29th EPS Conf. on Controlled Fusion and Plasma Physics (Montreux, 2002)* (Geneva: European Physical Society) vol 26B (ECA) paper O-3.23
- [519] Rudakov D.L. *et al* 2002 *Plasma Phys. Control. Fusion* **44** 717
- [520] Rogers B.N. and Drake J.F. 1998 *Phys. Rev. Lett.* **81** 4396
- [521] Russell D.A. *et al* 2004 *Phys. Rev. Lett.* **93** 265001
- [522] Tokar M.Z. 2003 *Phys. Rev. Lett.* **91** 095001
- [523] Kotschenreuther M. *et al* 1997 *Proc. 16th Int. Conf. on Fusion Energy 1996: (Montreal, 1996)* (Vienna: IAEA) vol 2 p 371
- [524] Waltz R.E. *et al* 1997 *Proc. 16th Int. Conf. on Fusion Energy 1996: (Montreal, 1996)* (Vienna: IAEA) vol 2 p 385
- [525] Kinsey J.E., Waltz R.E. and Schissel D.P. 1997 *Europhysics Conference Abstracts: Proc. 24th EPS Conf. on Controlled Fusion and Plasma Physics (Berchtesgaden, 1997)* (Geneva: European Physical Society) vol 21A part III (ECA) p 1081
- [526] Hatae T. *et al* 1998 *Plasma Phys. Control. Fusion* **40** 1073
- [527] Hughes J.W. *et al* 2002 *Phys. Plasmas* **9** 3019
- [528] Groebner R.J. and Osborne T.H. 1998 *Phys. Plasmas* **5** 1800
- [529] Osborne T.H. *et al* 2002 *Proc. 19th Int. Conf. on Fusion Energy 2002: (Lyon, 2002)* (Vienna: IAEA) CD-ROM file CT/3 and <http://www.iaea.org/programmes/ripc/physics/fec2002/html/fec2002.htm>
- [530] Mossessian D.A. *et al* 2003 *Phys. Plasmas* **10** 689
- [531] Mossessian D.A. *et al* 2003 *Europhysics Conference Abstracts: Proc. 30th EPS Conf. on Controlled Fusion and Plasma Physics (St Petersburg, 2003)* (Geneva: European Physical Society) vol 27A (ECA) paper P-3.182
- [532] Fenstermacher M.E. *et al* 2005 *Nucl. Fusion* **45** 1493
- [533] Kinsey J.E., Staebler G.M. and Waltz R.E. 2005 *Phys. Plasmas* **12** 052503
- [534] Hatae T. *et al* 2001 *Nucl. Fusion* **41** 285
- [535] Shaing K.C. and Crume E.C. 1989 *Phys. Rev. Lett.* **63** 2369
- [536] Itoh S.-I. *et al* 1994 *Phys. Rev. Lett.* **72** 1200
- [537] Hinton F.L. and Staebler G.M. 1993 *Phys. Fluids B* **5** 1281
- [538] Groebner R.J. *et al* 2002 *Phys. Plasmas* **9** 2134
- [539] Hatae T. *et al* 2000 *Plasma Phys. Control. Fusion* **42** A283
- [540] Sugihara M. *et al* 2003 *Plasma Phys. Control. Fusion* **45** L55
- [541] Sugihara M. *et al* 2000 *Nucl. Fusion* **40** 1743
- [542] Guzdar P.N. *et al* 2001 *Phys. Rev. Lett.* **87** 015001
- [543] Guzdar P.N. *et al* 2002 *Phys. Rev. Lett.* **89** 265004
- [544] Hubbard A.E. *et al* 2004 *Plasma Phys. Control. Fusion* **46** A95
- [545] Fielding S.J. *et al* 2001 *Nucl. Fusion* **41** 909
- [546] Ido T. *et al* 2000 *Plasma Phys. Control. Fusion* **42** A309
- [547] Miura Y. *et al* 2001 *Nucl. Fusion* **41** 973
- [548] Hubbard A.E. *et al* 1998 *Plasma Phys. Control. Fusion* **40** 689
- [549] Hubbard A.E. *et al* 2002 *Plasma Phys. Control. Fusion* **44** A359
- [550] Righi E. *et al* 2000 *Plasma Phys. Control. Fusion* **42** A199
- [551] Andrew Y. *et al* 2004 *Plasma Phys. Control. Fusion* **46** 337
- [552] Carlstrom T.N. *et al* 2002 *Plasma Phys. Control. Fusion* **44** A333
- [553] Andrew Y. *et al* 2004 *Plasma Phys. Control. Fusion* **46** A87
- [554] Martin Y.R. and TCV Team 2002 *Plasma Phys. Control. Fusion* **44** A143
- [555] Akers R.J. *et al* 2003 *Plasma Phys. Control. Fusion* **45** A175
- [556] Bush C.E. *et al* 2003 *Phys. Plasmas* **10** 1755
- [557] Martin Y.R. and TCV team 2004 *Plasma Phys. Control. Fusion* **46** A77
- [558] Ryter F. *et al* 2002 *Plasma Phys. Control. Fusion* **44** A407
- [559] Ryter F. and H-mode Threshold Database Group 2002 *Plasma Phys. Control. Fusion* **44** A415
- [560] ITPA H-mode Power Threshold Database Working Group (presented by T. Takizuka) 2004 *Plasma Phys. Control. Fusion* **46** A227
- [561] Connor J.W. and Wilson H.R. 2000 *Plasma Phys. Control. Fusion* **42** R1
- [562] Ossipenko M.V. and Tsaun S.V. 2000 *Plasma Phys. Rep.* **26** 465
- [563] Groebner R.J. *et al* 2002 *Proc. 19th Int. Conf. on Fusion Energy 2002: (Lyon, 2002)* (Vienna: IAEA) CD-ROM file EX/C2-3 and <http://www.iaea.org/programmes/ripc/physics/fec2002/html/fec2002.htm>
- [564] Xu X.Q. *et al* 2000 *Phys. Plasmas* **7** 1951
- [565] Connor J.W. and Pogutse O.P. 2001 *Plasma Phys. Control. Fusion* **43** 281
- [566] Janeschitz G. *et al* 2002 *Plasma Phys. Control. Fusion* **44** A459
- [567] Parail V. *et al* 2002 *Proc. 19th Int. Conf. on Fusion Energy 2002: (Lyon, 2002)* (Vienna: IAEA) CD-ROM file TH/P3-08 and <http://www.iaea.org/programmes/ripc/physics/fec2002/html/fec2002.htm>
- [568] Bateman G., Onjun T. and Kritz A.H. 2003 *Plasma Phys. Control. Fusion* **45** 1939
- [569] Roglien T.D. *et al* 2004 *Contrib. Plasma Phys.* **44** 188
- [570] Xu X.Q. *et al* 2004 *Contrib. Plasma Phys.* **44** 105
- [571] Kukushkin A.S. *et al* 2003 *Nucl. Fusion* **43** 716
- [572] Pacher H.D. *et al* 2003 *J. Nucl. Mater.* **313–316** 657
- [573] Pacher G.W. *et al* 2001 *Europhysics Conference Abstracts: Proc. 28th EPS Conf. on Controlled Fusion and Plasma Physics (Madeira, 2001)* (Geneva: European Physical Society) vol 25A (ECA) p 625

- [574] Pacher G.W. *et al* 2003 *Nucl. Fusion* **43** 188
- [575] Pacher G.W. *et al* 2003 *Europhysics Conference Abstracts: Proc. 30th EPS Conf. on Controlled Fusion and Plasma Physics (St Petersburg, 2003)* (Geneva: European Physical Society) vol 27A (ECA) paper P-3.139
- [576] Parail V.V. *et al* 2003 *Plasma Phys. Rep.* **29** 539
- [577] Sartori R. *et al* 1998 *Plasma Phys. Control. Fusion* **40** 757
- [578] Sartori R. *et al* 1999 *Europhysics Conference Abstracts: Proc. 26th EPS Conf. on Controlled Fusion and Plasma Physics (Maastricht, 1999)* (Geneva: European Physical Society) vol 23J (ECA) p 197
- [579] Leonard A.W. *et al* 2001 *J. Nucl. Mater.* **290-293** 1097
- [580] Loarte A. *et al* 2002 *Plasma Phys. Control. Fusion* **44** 1815
- [581] Oyama N. *et al* 2001 *Plasma Phys. Control. Fusion* **43** 717
- [582] Oyama N. *et al* 2004 *Nucl. Fusion* **44** 582
- [583] Nunes I. *et al* 2003 *Europhysics Conference Abstracts: Proc. 30th EPS Conf. on Controlled Fusion and Plasma Physics (St Petersburg, 2003)* (Geneva: European Physical Society) vol 27A (ECA) paper P-1.157
- [584] Oyama N. *et al* 2003 *Nucl. Fusion* **43** 1250
- [585] Kirk A. *et al* 2004 *Plasma Phys. Control. Fusion* **46** 551
- [586] Connor J.W. 1998 *Plasma Phys. Control. Fusion* **40** 531
- [587] Kass T. *et al* 1998 *Nucl. Fusion* **38** 111
- [588] Zohm H. *et al* 1995 *Nucl. Fusion* **35** 543
- [589] Perez C.P. *et al* 2004 *Nucl. Fusion* **44** 609
- [590] Perez C.P. *et al* 2004 *Plasma Phys. Control. Fusion* **46** 61
- [591] Loarte A. *et al* 2004 *Phys. Plasmas* **11** 2668
- [592] Loarte A. *et al* 2003 *Plasma Phys. Control. Fusion* **45** 1549
- [593] Leonard A.W. *et al* 2002 *Plasma Phys. Control. Fusion* **44** 945
- [594] Counsell G.F. *et al* 2003 *Nucl. Fusion* **43** 1197
- [595] Maingi R. *et al* 2005 *J. Nucl. Mater.* **337-339** 727
- [596] Saibene G. *et al* 2002 Transport in fusion plasmas: transport near operational limits *Proc. 9th EU-US Transport Task Force Workshop (Córdoba, 2002)* <http://www-fusion.ciemat.es/ttf2002/>
- [597] Urano H. *et al* 2003 *Plasma Phys. Control. Fusion* **45** 1571
- [598] Lao L.L. *et al* 1999 *Nucl. Fusion* **39** 1785
- [599] Ferron J.R. *et al* 2000 *Nucl. Fusion* **40** 1411
- [600] Saibene G. *et al* 2003 *Europhysics Conference Abstracts: Proc. 30th EPS Conf. on Controlled Fusion and Plasma Physics (St Petersburg, 2003)* (European Physical Society) vol 27A (ECA) paper P-1.192
- [601] Federici G., Loarte A. and Strohmayer G. 2003 *Plasma Phys. Control. Fusion* **45** 1523
- [602] Fielding S.J. *et al* 2001 *Europhysics Conference Abstracts: Proc. 28th EPS Conf. on Controlled Fusion and Plasma Physics (Madeira, 2001)* (Geneva: European Physical Society) vol 25A (ECA) p 1825
- [603] Becoulet M. *et al* 2003 *Plasma Phys. Control. Fusion* **45** A93
- [604] Degeling A.W. *et al* 2003 *Plasma Phys. Control. Fusion* **45** 1637
- [605] Horton L. *et al* 2004 *Plasma Phys. Control. Fusion* **46** B511
- [606] Evans T.E. *et al* 2004 *Phys. Rev. Lett.* **92** 235003
- [607] Kupschus P. *et al* 1997 *Europhysics Conference Abstracts: Proc. 24th EPS Conf. on Controlled Fusion and Plasma Physics (Berchtesgaden, 1997)* (Geneva: European Physical Society) vol 21A, part I (ECA) p 45
- [608] Lang P.T. *et al* 2003 *Nucl. Fusion* **43** 1110
- [609] Polevoi A.R. *et al* 2003 *Nucl. Fusion* **43** 1072
- [610] Turnbull A.D. *et al* 2003 *Plasma Phys. Control. Fusion* **45** 1845
- [611] JET Team (prepared by A.C.C. Sips) 2001 *Nucl. Fusion* **41** 1559
- [612] Sarazin Y. *et al* 2002 *Plasma Phys. Control. Fusion* **44** 2445
- [613] Becoulet M. *et al* 2002 *Plasma Phys. Control. Fusion* **44** A103
- [614] Osborne T.H. *et al* 1997 *Europhysics Conference Abstracts: Proc. 24th EPS Conf. on Controlled Fusion and Plasma Physics (Berchtesgaden, 1997)* (Geneva: European Physical Society) vol 21A part III (ECA) p 1101
- [615] Hubbard A.E. *et al* 1998 *Phys. Plasmas* **5** 1744
- [616] Sartori R. *et al* 2004 *Plasma Phys. Control. Fusion* **46** 723
- [617] Suttrop W. *et al* 2002 *Proc. 19th Int. Conf. on Fusion Energy 2002: (Lyon, 2002)* (Vienna: IAEA) CD-ROM file EX/P5-07 and <http://www.iaea.org/programmes/ripc/physics/fec2002/html/fec2002.htm>
- [618] Igitkhanov Y. *et al* 2000 *Contrib. Plasma Phys.* **40** 368
- [619] Chankin A.V. and Saibene G. 1999 *Plasma Phys. Control. Fusion* **41** 913
- [620] Rapp J. *et al* 2004 *Nucl. Fusion* **44** 312
- [621] Takase Y. *et al* 1997 *Proc. 16th Int. Conf. on Fusion Energy 1996: (Montreal, 1996)* (Vienna: IAEA) vol 1 p 475
- [622] Greenwald M. *et al* 1997 *Nucl. Fusion* **37** 793
- [623] Takase Y. *et al* 1997 *Phys. Plasmas* **4** 1647
- [624] Greenwald M. *et al* 1999 *Phys. Plasmas* **6** 1943
- [625] Hubbard A.E. *et al* 2001 *Phys. Plasmas* **8** 2033
- [626] Lin Y. *et al* 1999 *Rev. Sci. Instrum.* **70** 1078
- [627] Greenwald M. *et al* 2000 *Plasma Phys. Control. Fusion* **42** A263
- [628] Marmar E.S. *et al* 2000 *Proc. 18th Int. Conf. on Fusion Energy 2000: (Sorrento, 2000)* (Vienna: IAEA) CD-ROM file EX2/5 and <http://www.iaea.org/programmes/ripc/physics/fec2000/html/fec2000.htm>
- [629] Snipes J.A. *et al* 2001 *Plasma Phys. Control. Fusion* **43** L23
- [630] Rogers B. and Drake J.F. 1999 *Phys. Plasmas* **6** 2797
- [631] Mossessian D.A. *et al* 2002 *Plasma Phys. Control. Fusion* **44** 423
- [632] Mossessian D. *et al* 2000 *Plasma Phys. Control. Fusion* **42** A255
- [633] Sunn Pedersen T. *et al* 2000 *Nucl. Fusion* **40** 1795
- [634] Mossessian D.A. *et al* 2003 *Phys. Plasmas* **10** 1720
- [635] Maddison G. *et al* 2002 *Plasma Phys. Control. Fusion* **44** 1937
- [636] Kamiya K. *et al* 2003 *Nucl. Fusion* **43** 1214
- [637] Kamiya K. *et al* 2004 *Plasma Phys. Control. Fusion* **46** 1745
- [638] Kamiya K. *et al* 2004 *Plasma Phys. Control. Fusion* **46** A157
- [639] Nagashima N. *et al* 2004 *Plasma Phys. Control. Fusion* **46** A381
- [640] Hubbard A.E. *et al* 2006 *Plasma Phys. Control. Fusion* **A121**
- [641] Fiore C.L. *et al* 2004 *Phys. Plasmas* **11** 2480
- [642] Fiore C.L. *et al* 2001 *Phys. Plasmas* **8** 2023
- [643] Wukitch S.J. *et al* 2002 *Phys. Plasmas* **9** 2149
- [644] Burrell K.H. *et al* 1999 *Bull. Am. Phys. Soc.* **44** 127
- [645] Suttrop W. *et al* 2004 *Plasma Phys. Control. Fusion* **46** A151
- [646] Suttrop W. *et al* 2003 *Plasma Phys. Control. Fusion* **45** 1399
- [647] Burrell K.H. *et al* 2002 *Plasma Phys. Control. Fusion* **44** A253
- [648] Sakamoto Y. *et al* 2004 *Plasma Phys. Control. Fusion* **46** A299
- [649] Groebner R.J. *et al* 2001 *Nucl. Fusion* **41** 1789
- [650] Burrell K.H. *et al* 2004 *Plasma Phys. Control. Fusion* **46** A165
- [651] West W.P. *et al* 2004 *Plasma Phys. Control. Fusion* **46** A179
- [652] Ozeki T. *et al* 1990 *Nucl. Fusion* **30** 1425
- [653] Stober J. *et al* 2001 *Nucl. Fusion* **41** 1123
- [654] Koslowski H.R. *et al* 2003 *Europhysics Conference Abstracts: Proc. 30th EPS Conf. on Controlled Fusion and Plasma Physics (St Petersburg, 2003)* (Geneva: European Physical Society) vol 27A (ECA) paper P-1.102
- [655] Stober J. *et al* 2001 *Plasma Phys. Control. Fusion* **43** A39
- [656] Saarelma S. *et al* 2003 *Nucl. Fusion* **43** 262
- [657] Hender T.C. *et al* 2007 Progress in the ITER Physics Basis *Nucl. Fusion* **47** S128-S202
- [658] Lönnerth J.-S. *et al* 2004 *Plasma Phys. Control. Fusion* **46** A249
- [659] Maingi R. *et al* 2004 *Europhysics Conference Abstracts: Proc. 31st EPS Conf. on Plasma Physics (London, 2004)* (Geneva: European Physical Society) vol 28G (ECA) paper P-2.189
- [660] Kamada Y. *et al* 2000 *Plasma Phys. Control. Fusion* **42** A247
- [661] Oyama N. *et al* 2004 *Proc. 20th Int. Conf. on Fusion Energy 2004: (Vilamoura, 2004)* (Vienna: IAEA) CD-ROM file

- EX/2-1 and <http://www-naweb.iaea.org/naweb/physics/fec/fec2004/datasets/index.html>
- [662] Lao L.L. *et al* 2001 *Nucl. Fusion* **41** 295
- [663] Saibene G. *et al* 2005 *Nucl. Fusion* **45** 297
- [664] Manickam J. 1992 *Phys. Fluids B* **4** 1901
- [665] Hegna C.C. *et al* 1996 *Phys. Plasmas* **3** 584
- [666] Connor J.W. *et al* 1998 *Phys. Plasmas* **5** 2687
- [667] Wilson H.R. *et al* 2000 *Nucl. Fusion* **40** 713
- [668] Huysmans G.T.A. *et al* 2001 *Phys. Plasmas* **8** 4292
- [669] Snyder P.B. *et al* 2002 *Phys. Plasmas* **9** 2037
- [670] Mikhailovskii A.B. *et al* 1997 *Plasma Phys. Rep.* **23** 844
- [671] Degtyarev L. *et al* 1997 *Comput. Phys. Commun.* **103** 10
- [672] Medvedev S.Y. *et al* 2003 *Europhysics Conference Abstracts: Proc. 30th EPS Conf. on Controlled Fusion and Plasma Physics (St Petersburg, 2003)* (Geneva: European Physical Society) vol 27A (ECA) paper P-3.129
- [673] Wilson H.R. *et al* 2002 *Phys. Plasmas* **9** 1277
- [674] Gruber R. *et al* 1981 *Comput. Phys. Commun.* **21** 323
- [675] Gruber R. *et al* 1981 *Comput. Phys. Commun.* **24** 363
- [676] Igitkhanov Y. *et al* 1998 *Plasma Phys. Control. Fusion* **40** 837
- [677] Cowley S.C. *et al* 2003 *Plasma Phys. Control. Fusion* **45** A31
- [678] Wilson H.R. and Cowley S.C. 2004 *Phys. Rev. Lett.* **92** 175006
- [679] Kirk A. *et al* 2004 *Phys. Rev. Lett.* **92** 245002
- [680] Snyder P.B. *et al* 2004 *Plasma Phys. Control. Fusion* **46** A131
- [681] Snyder P.B. *et al* 2004 *Nucl. Fusion* **44** 320
- [682] Connor J.W., Hastie R.J. and Taylor J.B. 1979 *Proc. R. Soc. Lond., Ser. A (Math. Phys. Sci.)* **A365** 1
- [683] Becoulet M. *et al* 2005 *J. Nucl. Mater.* **337–339** 677
- [684] Lang P.T. *et al* 2003 *Europhysics Conference Abstracts: Proc. 30th EPS Conf. on Controlled Fusion and Plasma Physics (St Petersburg, 2003)* (Geneva: European Physical Society) vol 27A (ECA) paper P-1.129
- [685] Urano H. *et al* 2004 *Plasma Phys. Control. Fusion* **46** A315
- [686] Miura Y. *et al* 1991 *Proc. 13th Int. Conf. on Plasma Physics and Controlled Nuclear Fusion Research (Washington, D.C., 1990)* (Vienna: IAEA) vol 1 p 325
- [687] Mori M. *et al* 1993 *Proc. 14th Int. Conf. on Plasma Physics and Controlled Nuclear Fusion Research 1992 (Würzburg, 1992)* (Vienna: IAEA) vol 2 p 567
- [688] Kaye S.M. *et al* 1997 *Nucl. Fusion* **37** 1303
- [689] Thomsen K. *et al* 1999 *Proc. 17th Int. Conf. on Fusion Energy 1998: (Yokohama, 1998)* (Vienna: IAEA) CD-ROM file IAEA-F1-CN-69/ITERP1/07 and <http://www.iaea.org/programmes/ripc/physics/start.htm>
- [690] Kardaun O.J.W.F. *et al* 2000 *Proc. 18th Int. Conf. on Fusion Energy 2000: (Sorrento, 2000)* (Vienna: IAEA) CD-ROM file ITERP/04 and <http://www.iaea.org/programmes/ripc/physics/fec2000/html/fec2000.htm>
- [691] Bracco G. 2001 *Proc. 1st ITPA Confinement Database and Modelling Group Meeting (Toki, 2001)* <http://efdsql.ipp.mpg.de/igd/PublicH-Mode/ExpertMeetings/Toki2001/Toki2001.htm>
- [692] Kardaun O.J.W.F. 2002 *Proc. 3rd ITPA Confinement Database and Modelling Meeting (Cadache, 2002)* <http://efdsql.ipp.mpg.de/igd/PublicH-Mode/ExpertMeetings/Cadache2002/Cadache2002.htm>
- [693] Sugiyama L.E. 2002 *Cambridge Report PTP-02/02*, Massachusetts Institute of Technology
- [694] Leonov V.M. and Chudnovskiy A.N. 2003 *Plasma Phys. Rep.* **29** 97
- [695] Martin Y.R. and ITER H-mode Threshold Database Working Group 1998 *Europhysics Conference Abstracts: Proc. 1998 International Congress on Plasma Physics combined with the 25th EPS Conf. on Controlled Fusion and Plasma Physics (Praha, 1998)* (Geneva: European Physical Society) vol 22C (ECA) 667
- [696] ITER H-mode Threshold Database Working Group presented by E. Righi 1998 *Plasma Phys. Control. Fusion* **40** 857
- [697] Snipes J.A. and International H-mode Threshold Database Working Group 2000 *Plasma Phys. Control. Fusion* **42** A299
- [698] Snipes J.A. *et al* 2002 *Proc. 19th Int. Conf. on Fusion Energy 2002: (Lyon, 2002)* (Vienna: IAEA) CD-ROM file CT/P-04 and <http://www.iaea.org/programmes/ripc/physics/fec2002/html/fec2002.htm>
- [699] Christiansen J.P. and Cordey J.G. 1998 *Nucl. Fusion* **38** 1757
- [700] Valovic M. and ITER H-mode Confinement Database Working Group 1998 *Europhysics Conference Abstracts: Proc. 1998 International Congress on Plasma Physics combined with the 25th EPS Conf. on Controlled Fusion and Plasma Physics (Praha, 1998)* (Geneva: European Physical Society) vol 22C (ECA) 675
- [701] Kardaun O.J.W.F. 1999 *Plasma Phys. Control. Fusion* **41** 429
- [702] Cordey J.G. *et al* 2002 *Proc. 19th Int. Conf. on Fusion Energy 2002: (Lyon, 2002)* (Vienna: IAA) CD-ROM file CT/P-02 and <http://www.iaea.org/programmes/ripc/physics/fec2002/html/fec2002.htm>
- [703] Kardaun O.J.W.F. 2002 *Nucl. Fusion* **42** 841
- [704] Kardaun O.J.W.F. 2002 *Garching Report IPP-IR 2002/5 1.1*, Max Planck Institut fuer Plasmaphysik
- [705] Thomsen K. and H-mode Database Working Group 2002 *Fusion Eng. Des.* **60** 347
- [706] Thomsen K. *et al* 2002 *Plasma Phys. Control. Fusion* **44** A429
- [707] Cordey J.G., ITPA H-Mode Database Working Group and ITPA Pedestal Database Working Group 2003 *Nucl. Fusion* **43** 670
- [708] Thomsen K. *et al* 2004 *Europhysics Conference Abstracts: Proc. 31st EPS Conf. on Plasma Physics (London, 2004)* (Geneva: European Physical Society) vol 28G (ECA) paper P-5.145
- [709] Cordey J.G. *et al* 2004 *Proc. 20th Int. Conf. on Fusion Energy 2004: (Vilamoura, 2004)* (Vienna: IAEA) CD-ROM file IT/P3-32 and <http://www-naweb.iaea.org/naweb/physics/fec/fec2004/datasets/index.html>
- [710] Baranov Y. and International ITB Database Working Group 2001 *Bull. Am. Phys. Soc.* **46** 117
- [711] Fukuda T. and JT-60 Team 2002 *Plasma Phys. Control. Fusion* **44** B39
- [712] Hoang G.T. *et al* 2002 *Europhysics Conference Abstracts: Proc. 29th EPS Conf. on Controlled Fusion and Plasma Physics (Montreux, 2002)* (Geneva: European Physical Society) vol 26B (ECA) paper P-4.068
- [713] Fujita T. *et al* 2003 *Europhysics Conference Abstracts: Proc. 30th EPS Conf. on Controlled Fusion and Plasma Physics (St Petersburg, 2003)* (Geneva: European Physical Society) vol 27A (ECA) paper P-2.131
- [714] Gohil P. *et al* 2003 *Nucl. Fusion* **43** 708
- [715] Imbeaux F. *et al* 2004 *Europhysics Conference Abstracts: Proc. 31st EPS Conf. on Plasma Physics (London, 2004)* (Geneva: European Physical Society) vol 28G (ECA) paper P-4.143
- [716] Tala T.J.J. *et al* 2004 *Proc. 20th Int. Conf. on Fusion Energy 2004: (Vilamoura, 2004)* (Vienna: IAEA) CD-ROM file TH/P2-9 and <http://www-naweb.iaea.org/naweb/physics/fec/fec2004/datasets/index.html>
- [717] Bracco G. and Thomsen K. 1997 *Nucl. Fusion* **37** 759
- [718] Bracco G. and Thomsen K. 1997 *Abingdon Report JET-R(97)17*, JET Joint Undertaking
- [719] Bourdelle C. *et al* 2002 *Nucl. Fusion* **42** 892
- [720] Sugihara M., Takizuka T. and International H-Mode Edge Pedestal Expert Group 2002 *Plasma Phys. Control. Fusion* **44** A299
- [721] Onjun T. *et al* 2002 *Phys. Plasmas* **9** 5018
- [722] Kritz A.H. *et al* 2002 *Europhysics Conference Abstracts: Proc. 29th EPS Conf. on Controlled Fusion and Plasma Physics (Montreux, 2002)* (Geneva: European Physical Society) vol 26B (ECA) paper D-5.001

- [723] Lloyd B. *et al* 2002 *Proc. 19th Int. Conf. on Fusion Energy 2002: (Lyon, 2002)* (Vienna: IAEA) CD-ROM file OV/2-3 and <http://www.iaea.org/programmes/ripc/physics/fec2002/html/fec2002.htm>
- [724] LeBlanc B.P. *et al* 2004 *Nucl. Fusion* **44** 513
- [725] Osborne T.H. *et al* 2000 *Plasma Phys. Control. Fusion* **42** A175
- [726] Horton L.D. *et al* 2002 *Plasma Phys. Control. Fusion* **44** A273
- [727] Takizuka T. *et al* 2002 *Plasma Phys. Control. Fusion* **44** A423
- [728] ITER Confinement Database & Modelling Group and Cordey J.G. 1997 *Plasma Phys. Control. Fusion* **39** B115
- [729] Petty C.C. *et al* 2003 *Fusion Sci. Technol.* **43** 1
- [730] Erba M. *et al* 1997 *Plasma Phys. Control. Fusion* **39** 261
- [731] Weiland J. 2000 *Collective Modes in Inhomogeneous Plasmas* (Bristol: Institute of Physics Publishing)
- [732] Zhu P. *et al* 2000 *Phys. Plasmas* **7** 2898
- [733] Bateman G. *et al* 1999 *Proc. 17th Int. Conf. on Fusion Energy 1998: (Yokohama, 1998)* (Vienna: IAEA) CD-ROM file IAEA-F1-CN-69/THP2/19 and <http://www.iaea.org/programmes/ripc/physics/start.htm>
- [734] Lönnroth J.-S. *et al* 2003 *Plasma Phys. Control. Fusion* **45** 1689
- [735] Pankin A.Y. *et al* 2005 *Plasma Phys. Control. Fusion* **47** 483
- [736] Saibene G. *et al* 2001 *Europhysics Conference Abstracts: Proc. 28th EPS Conf. on Controlled Fusion and Plasma Physics (Madeira, 2001)* (Geneva: European Physical Society) vol 25A (ECA) p 1749
- [737] Taroni A. *et al* 1998 *Contrib. Plasma Phys.* **38** 37
- [738] Pereverzev G.V. and Zolotukhin O.V. 2003 *Europhysics Conference Abstracts: Proc. 30th EPS Conf. on Controlled Fusion and Plasma Physics (St Petersburg, 2003)* (European Physical Society) vol 27A (ECA) paper P-3.138
- [739] Weiland J. 2001 *Europhysics Conference Abstracts: Proc. 28th EPS Conf. on Controlled Fusion and Plasma Physics (Madeira, 2001)* (Geneva: European Physical Society) vol 25A (ECA) p 633
- [740] Belo P. *et al* 2004 *Plasma Phys. Control. Fusion* **46** 1299
- [741] Kukushkin A.S. *et al* 1998 *Contrib. Plasma Phys.* **38** 20
- [742] Fichtmüller M. *et al* 1998 *Abingdon Report JET-P(98)69, JET Joint Undertaking*
- [743] Hogan J.T. and Hillis D.L. 1996 *Nucl. Fusion* **36** 1079
- [744] Pacher G.W. *et al* 2005 *Nucl. Fusion* **45** 581
- [745] Leonov V.M. and Zhogolev V.E. 2005 *Plasma Phys. Control. Fusion* **47** 903
- [746] Polevoi A.R. *et al* 2005 *Nucl. Fusion* **45** 1451
- [747] Kishimoto Y. 2000 *J. Plasma Fusion Res.* **76** 1280
- [748] Waltz R.E. *et al* 2005 *Nucl. Fusion* **45** 741
- [749] Evans T.E. *et al* 2004 *Proc. 20th Int. Conf. on Fusion Energy 2004: (Vilamoura, 2004)* (Vienna: IAEA) CD-ROM file EX/2-5Ra and <http://www-naweb.iaea.org/napc/physics/fec/fec2004/datasets/index.html>
- [750] Mukhovatov V. *et al* 2003 *Plasma Phys. Control. Fusion* **45** A235